

# Thermal deposition approaches for graphene growth over various substrates

Von der Fakultät Maschinenwesen der Technischen Universität Dresden

zur Erlangung des akademischen Grades

Doktoringenieur (Dr.-Ing.)

angenommene

DISSERTATION

von

Master of Engineering

Jinbo PANG

geboren am 06.12.1985 in Shandong





Tag der Einreichung: 6. Dezember 2016

Tag der Verteidigung: 7. März 2017

*Supervisors:*

1. Gutachter: Prof. Dr. Jürgen Eckert
2. Gutachter: Prof. Dr. Mark. H. Rümmeli
3. Gutachter: Prof. Dr. Gianaurelio Cuniberti



*“It is inevitable that many ideas of the young mind will later have to give way to the hard realities of life. But these realities will make themselves felt soon enough and while I am certainly not asking you to close your eyes to the experiences of earlier generations, I want to advise you not to conform too soon and to resist the pressure of practical necessity. Free imagination is the inestimable prerogative of youth and it must be cherished and guarded as a treasure. Dream your dream and may they come true.”*

Felix Bloch (physicist who developed the Bloch theorem to describe electrons in solid crystals)



# KURZFASSUNG

Im Zuge dieser Doktorarbeit wurden großflächige und homogene Graphen-Monolagen mittels chemischer Gasphasenabscheidung auf Kupfer- (Cu) und Silizium- (Si) Substraten erfolgreich synthetisiert. Solche monolagigen Graphenschichten wurden mithilfe mikroskopischer und spektrometrischer Methoden gründlich charakterisiert. Außerdem wurde der Wachstumsmechanismus von Graphen anhand eines chemo-thermischen Verfahrens untersucht.

Die Bildung von homogenen Graphenschichten auf Cu erfordert eine sehr saubere Substratoberfläche, weshalb verschiedene Substratvorbehandlungen und dessen Einfluss auf die Substratoberfläche angestellt wurden. Vier Vorbehandlungsarten von Cu-Substraten wurden untersucht: Abwischen mit organischen Lösungsmitteln, Ätzen mit Eisen-(III)-Chloridlösung, Wärmebehandlung an Luft zur Erzeugung von Cu-Oxiden und Wärmebehandlung an Luft mit anschließender Wasserstoffreduktion. Von diesen Vorbehandlungen ist die zuletzt genannte Methode für die anschließende Abscheidung einer großflächigen Graphen-Monolage am effektivsten.

Die chemische Gasphasenabscheidung ist die am meisten verwendete Methode zur Massenproduktion von Graphen. Es besteht aber auch Interesse an alternativen Methoden, die Graphen direkt aus organischen, auf einem Substrat adsorbierten Molekülen, synthetisieren können. Jedoch gibt es derzeit nur wenige Studien zu derartigen alternativen Methoden. Solche Prozessrouten erfordern mehrstufige Reaktionen, welche wiederum die Qualität der erzeugten Graphenschicht limitieren, da nur kleine Korngrößen erreicht werden können. Daher wurde in dieser Arbeit ein deutlich einfacherer Weg entwickelt. Es handelt sich dabei um ein Verfahren, bei dem auf einer Cu-Substratoberfläche adsorbierte, organische Lösungsmittelmoleküle in einer Wasserstoffatmosphäre geglüht werden, um eine direkte Bildung von Graphen auf einem saubereren Cu-Substrat zu gewährleisten.

Der Einfluss von Temperatur, Druck und Gasfluss auf diesen einstufigen chemothermischen Syntheseweg wurde systematisch untersucht. Die temperaturabhängigen Untersuchungen liefern einen Einblick in die Wachstumskinetik und thermodynamische Größen, wie zum Beispiel die Aktivierungsenergie  $E_a$ , für die Synthese von Graphen aus Aceton, Isopropanol oder Ethanol. Diese Studien untersuchen außerdem die Rolle von Wasserstoffradikalen auf die Graphensynthese. Weiterhin wurde ein verbessertes Verständnis der Rolle von Wasserstoff auf die Graphensynthese aus adsorbierten, organischen Lösungsmitteln erlangt (beispielsweise im Vergleich zur konventionellen thermischen Gasphasenabscheidung).

Die direkte Graphensynthese mittels chemischer Gasphasenabscheidung auf Si-Substraten mit einer Oxidschicht ( $\text{Si}/\text{SiO}_x$ ) ist extrem anspruchsvoll in Bezug auf die großflächige und einheitliche Abscheidung (Lagenanzahl) von Graphen-Monolagen. Das direkte Wachstum von Graphen auf  $\text{Si}/\text{SiO}_x$ -Substrat ist interessant, da es frei von unerwünschten Übertragungsverfahren ist und kein Metallsubstrat erfordert, welche die erzeugten Graphenschichten brechen lassen können. Um ein homogenes Graphenwachstum zu erzielen wurde durch den Kontakt zweier Si-Wafer, mit ihren Oxidflächen zueinander zeigend, eine lokale Umgebung im chemischen Gleichgewicht erzeugt. Diese Konfiguration der Si-Wafer ist nötig, um eine einheitliche Graphen-Monolage bilden zu können. Eine gründliche Untersuchung des abgeschiedenen Materials zeigt, dass trotz der anfänglichen Keimbildung von runden Inseln facettierte Körner erzeugt werden. Aufgrund der Bestrebung der Graphenkörner ihre (Oberflächen-) Energie zu minimieren, wird eine Facettierung der Körner in polygonaler Form erzeugt, was darin begründet liegt, dass das System idealerweise eine Anordnung von hexagonal geformten Körnern erzeugen würde (niedrigster Energiezustand). Der Prozess ist vergleichbar mit der sechseckigen Zellstruktur einer Bienenstockwabe, welche ein Minimum an Wachs erfordert. Dieser Prozess führt auch zu einer nahezu minimalen Gesamtkorn-grenzlänge pro Flächeneinheit. Diese Tatsache zusammen mit der hohen Qualität



der resultierenden Graphenschicht spiegelt sich auch in dessen elektrischer Leistungsfähigkeit wider, die in hohem Maße mit der auf anderen Substraten gebildeten Graphenschichten (inklusive Cu-Substrate) vergleichbar ist. Darüber hinaus ist das Graphenwachstum selbstabschliessend, wodurch ein großes Parameterfenster für eine einfache und kontrollierte Synthese eröffnet wird.

Dieser Ansatz zur chemischen Gasphasenabscheidung von Graphen auf Si-Substraten ist leicht skalierbar und gegenüber der Abscheidung auf Metallsubstraten konkurrenzfähig, da keine Substratübertragung nötig ist. Darüber hinaus ist dieser Prozess auch für die direkte Synthese anderer zweidimensionalen Materialien und deren Van-der-Waals-Heterostrukturen anwendbar.



# ABSTRACT

In the course of the PhD thesis large area homogeneous strictly monolayer graphene films were successfully synthesized with chemical vapor deposition over both Cu and Si (with surface oxide) substrates. These synthetic graphene films were characterized with thorough microscopic and spectrometric tools and also in terms of electrical device performance. Graphene growth with a simple chemo thermal route was also explored for understanding the growth mechanisms.

The formation of homogeneous graphene film over Cu requires a clean substrate. For this reason, a study has been conducted to determine the extent to which various pre-treatments may be used to clean the substrate. Four type of pre-treatments on Cu substrates are investigated, including wiping with organic solvents, etching with ferric chloride solution, annealing in air for oxidation, and air annealing with post hydrogen reduction. Of all the pretreatments, air oxidation with post hydrogen annealing is found to be most efficient at cleaning surface contaminants and thus allowing for the formation of large area homogeneous strictly monolayer graphene film over Cu substrate.

Chemical vapor deposition is the most generally used method for graphene mass production and integration. There is also interest in growing graphene directly from organic molecular adsorbents on a substrate. Few studies exist. These procedures require multiple step reactions, and the graphene quality is limited due to small grain sizes. Therefore, a significantly simple route has been demonstrated. This involves organic solvent molecules adsorbed on a Cu surface, which is then annealed in a hydrogen atmosphere in order to ensure direct formation of graphene on a clean Cu substrate. The influence of temperature, pressure and gas flow rate on the one-step chemo thermal synthesis route has been investigated systematically. The temperature-dependent study provides an insight into the growth kinetics, and supplies thermodynamic information such as the activation

energy,  $E_a$ , for graphene synthesis from acetone, isopropanol and ethanol. Also, these studies highlight the role of hydrogen radicals for graphene formation. In addition, an improved understanding of the role of hydrogen is also provided in terms of graphene formation from adsorbed organic solvents (*e.g.*, in comparison to conventional thermal chemical vapor deposition).

Graphene synthesis with chemical vapor deposition directly over Si wafer with surface oxide (Si/SiO<sub>x</sub>) has proven challenging in terms of large area and uniform layer number. The direct growth of graphene over Si/SiO<sub>x</sub> substrate becomes attractive because it is free of an undesirable transfer procedure, necessity for synthesis over metal substrate, which causes breakage, contamination and time consumption. To obtain homogeneous graphene growth, a local equilibrium chemical environment has been established with a facile confinement CVD approach, in which two Si wafers with their oxide faces in contact to form uniform monolayer graphene. A thorough examination of the material reveals it comprises faceted grains despite initially nucleating as round islands. Upon clustering these grains facet to minimize their energy, which leads to faceting in polygonal forms because the system tends to ideally form hexagons (the lowest energy form). This is much like the hexagonal cells in a beehive honeycomb which require the minimum wax. This process also results in a near minimal total grain boundary length per unit area. This fact, along with the high quality of the resultant graphene is reflected in its electrical performance which is highly comparable with graphene formed over other substrates, including Cu. In addition the graphene growth is self-terminating, which enables the wide parameter window for easy control.

This chemical vapor deposition approach is easily scalable and will make graphene formation directly on Si wafers competitive against that from metal substrates which suffer from transfer. Moreover, this growth path shall be applicable for direct synthesis of other two dimensional materials and their Van der Waals heterostructures.

# Contents

Quotation	v
Kurzfassung	vii
Abstract	xi
Contents	xiii
Acronyms	xvii
<b>1 Aims and objectives</b>	<b>1</b>
<b>2 Introduction</b>	<b>5</b>
2.1 Carbon allotropes	6
2.1.1 Hybridized $sp^2$ carbon nanomaterials	6
2.1.2 Graphene	7
2.2 Properties of graphene	8
2.2.1 Crystalline structure	8
2.2.2 Electrical transport	10
2.2.3 Optical transparency	11
2.2.4 Other properties	12
2.3 Graphene deposition methods	13
2.3.1 Synthesis approaches	13
2.3.2 Chemical vapor deposition	14
2.3.3 Substrate selection	15
2.3.4 Substrate pretreatments	16
2.3.5 Carbon feedstock	17
2.3.6 Thermal chemical vapor deposition	17
2.3.7 Plasma chemical vapor deposition	18
2.3.8 Transfer protocol	19
2.4 Chemical vapor deposition for graphene growth	21
2.4.1 Thermodynamics	22
2.4.2 Arrhenius plots	22
2.4.3 Activation energy	24
2.4.4 Growth kinetics	25
2.4.5 Reaction mechanisms over Cu	27

---

2.4.6	Reaction mechanisms over Ni	29
2.4.7	Reaction mechanisms over non-metals	31
2.4.8	Reaction mechanisms of free-standing graphene	35
2.5	Summary	35
2.6	Scope of the thesis	36
<b>3</b>	<b>Experimental setup and characterization techniques</b>	<b>37</b>
3.1	Experimental setup of chemical vapor deposition	37
3.2	Optical microscopy	39
3.3	Scanning electron microscopy	40
3.4	Atomic force microscopy	41
3.5	Transmission electron microscopy	42
3.5.1	Selected area electron diffraction	44
3.5.2	Dark field transmission electron microscopy	46
3.6	Raman spectroscopy	47
3.7	Ultraviolet-Visible spectrophotometry	49
3.8	Electrical transport measurements	49
<b>4</b>	<b>CVD growth of graphene on oxidized Cu substrates</b>	<b>51</b>
4.1	Motivation	52
4.2	Experimental protocol	53
4.3	Influence of Cu pretreatments on graphene formation	54
4.4	Influence of Cu oxidation on graphene growth	60
4.5	Effect of oxidation pretreatment on Cu surface cleaning	64
4.6	Summary	66
<b>5</b>	<b>Chemo-thermal synthesis of graphene from organic adsorbents</b>	<b>67</b>
5.1	Motivation	67
5.2	Experimental protocol	69
5.3	Influence of reaction temperature on graphene growth	75
5.4	Influence of reaction pressure on graphene growth	78
5.5	Influence of reaction flow rate on graphene growth	80
5.6	Summary	81
<b>6</b>	<b>Monolayer graphene synthesis directly over Si/SiO<sub>x</sub></b>	<b>83</b>
6.1	Motivation	83
6.2	Experimental protocol	86
6.3	Influence of substrate confinement configuration	87
6.4	Time dependent evolution for graphene formation	91
6.5	Grain boundaries in graphene film	95
6.6	Bubble clustering of faceted graphene grains	98
6.7	Electrical and optical performance of graphene	100
6.8	Summary	102
<b>7</b>	<b>Conclusions</b>	<b>103</b>

---

<b>8 Outlook</b>	<b>107</b>
<b>A Graphene synthesis over Cu and transfer to Si/SiO<sub>x</sub> substrate</b>	<b>111</b>
<b>B Chemo-thermal synthesis of graphene over Cu</b>	<b>115</b>
<b>C CVD graphene growth directly over Si/SiO<sub>x</sub> substrate</b>	<b>127</b>
<b>Bibliography</b>	<b>147</b>
<b>List of Figures</b>	<b>193</b>
<b>List of Tables</b>	<b>197</b>
<b>Acknowledgements</b>	<b>199</b>
<b>List of publications</b>	<b>203</b>
<b>Erklärung</b>	<b>205</b>





# ACRONYMS

0D	zero Dimensional
1D	one Dimensional
2D	two Dimensional
3D	three Dimensional
AFM	Atomic Force Microscopy
APS	Ammonium Persulfate
BSE	Back-Scattered Electron
BLG	bi-Layer Graphene
CEA	Chemical Equilibrium with Applications, a computer program
C(gr)	Graphitic Carbon
Cox	Oxide Capacitance per unit area
Cs	Spherical aberration
CVD	Chemical Vapor Deposition
DFTEM	Dark Field Transmission Electron Microscopy
Ea	Activation Energy
EDX	Energy Dispersive X-ray spectroscopy
eV	Electron Volt
FeCl <sub>3</sub>	Ferric Chloride
FET	Field Effect Transistor
fLG	few-Layer Graphene
FFT	Fast Fourier Transform
FWHM	Full Width at Half Maximum
GB	Grain Boundary

HRTEM	High Resolution Transmission Electron Microscopy
$I_{DS}$	Drain-Source Current
IPA	Isopropanol
KOH	Potassium Hydroxide
LSI	Large Scale Integrated-circuits
mLG	mono-Layer Graphene
OM	Optical Microscopy
PC	Polycarbonate
PECVD	Plasma Enhanced Chemical Vapor Deposition
PMMA	poly(methyl methacrylate)
RMS	Root Mean Square
SE	Secondary Electron
SEM	Scanning Electron Microscopy
SAED	Selected Area Electron Diffraction
TCO	Transparent Conducting Oxide
TEM	Transmission Electron Microscopy
UV-Vis	Ultraviolet-Visible
$V_{DS}$	Drain-Source Voltage
$V_G$	Gate Voltage

# Chapter 1

## Aims and objectives

Graphene, a one-atom-thick pure carbon crystal with a honeycomb-like structure, has become one of the most intensively studied materials of the 21<sup>st</sup> Century. It remains of great interest to both the scientific and engineering communities, owing to its range of unique properties and potential number of applications. In particular, its potential usage within the electronics industry in such elements as field effect transistors and transparent conducting films holds great promise. However, the mass production of graphene will only prove viable if a cost-effective route for synthesis can be devised, and if such manufacturing techniques yield material which is of sufficiently high quality for future applications. To date, chemical vapor deposition (CVD) appears the most promising means of graphene synthesis, and this method is already well-developed within both the laboratory and industry environments.

In terms of the fabrication of a large area of graphene monolayer film, Cu has been the most widely explored substrate, as its low carbon solubility enables the formation of a homogeneous single-layer graphene sheet. However, the graphene described within the current literatures is not strictly a monolayer, but rather a mixture of monolayer film and second-layer flakes (*cf.* [subsection 2.4.5](#)). Therefore, a principal aim of this thesis is to fabricate a strictly pure graphene

monolayer (illustrated in Figure 1.1), thereby preventing the emergence of any ‘contamination’ by second layer flakes.

To obtain a homogeneous monolayer of graphene over Cu, this thesis focuses upon tracking the origins of the observed second layer flakes in graphene full-coverage film, *i.e.*, investigating at which stage the second layer flakes form in terms of their nucleation, growth or termination stages. After identifying the stage at which flake formation occurs, this thesis will take measurements (*e.g.*, oxidation treatment) to remove these flakes and any related carbon contaminants. Next, after successfully avoiding any formation of these undesirable flakes, the strictly monolayer graphene film is expected to be readily fabricated.

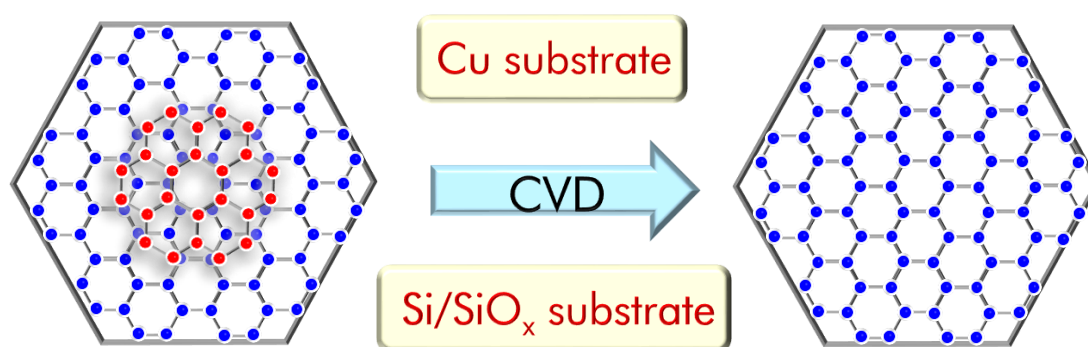


FIGURE 1.1: Towards the formation of strictly monolayer graphene film. (left) Inhomogeneous monolayer graphene mixing with second layer flakes. The previous studies have such problems of inhomogeneity in graphene film. (right) Homogeneous strictly monolayer graphene. The research goal is to obtain strictly monolayer graphene over large area. The methods for synthesis are thermal deposition approaches, mainly chemical vapor deposition and also chemo-thermal route. Various substrates, such as Cu and Si/SiO<sub>x</sub> will be adopted for graphene synthesis.

Ideally, in future electronic applications, where graphene-based devices are fabricated directly onto a dielectric oxide (currently Si/SiO<sub>x</sub> wafers), the graphene monolayer film will no longer require a post-synthetic transfer onto the intended dielectric substrate. It is beneficial that graphene grows on a dielectric substrate directly, *viz.* device integration is highly compatible on the as-produced graphene without any post-synthesis treatment.

Presently, this strategy for graphene growth on metals and post transfer on dielectrics not only leads to undesired damage and contamination of the transferred graphene, which degrades its electrical performance, but also greatly extends the time and cost of fabrication. Compared with its synthesis over metals, this graphene synthesis directly over dielectrics expedite the fabrication process and preserve its electrical performance.

Thus the direct fabrication of uniform graphene on a Si/SiO<sub>x</sub> substrate becomes of considerable importance. However, there are challenging problems facing investigators in the direct synthesis of graphene on Si/SiO<sub>x</sub> substrates. The resulting graphene film reported from recent reports suffers from apparent inhomogeneity in layer numbers (shown in left of [Figure 1.1](#)), *viz.* the synthetic graphene consists of a mixture of monolayer film and second layer flakes (*cf.* [subsection 2.4.7](#)). Therefore, another principal aim of this thesis is to achieve the direct synthesis of a homogeneous graphene film on a Si/SiO<sub>x</sub> substrate (*cf.* [section 2.6](#)).

To realize the direct fabrication of homogenous monolayer graphene, this thesis will seek to contribute knowledge towards an evaluation of the mechanisms for achieving a precise control of the local growth environment on a specially prepared SiO<sub>x</sub> surface to enable equilibrium growth, with new carbon atoms attaching only at the leading edges of the graphene grains rather than on top of them. Such desired control of the growth environment may be satisfied by a confinement of the growth surface, with the substrate embedded within sandwich-like Si wafers, wherein two Si wafers are stacked with their oxide faces in contact with one other. The confinement for the sample configuration thus provides provide an equilibrium environment in which it is expected to be possible to fabricate a strictly homogeneous monolayer of graphene film. The electrical and optical performance properties of the synthetic graphene film is then examined and compared to those of other recent studies.

The direct synthesis of graphene over a non-catalytic Si/SiO<sub>x</sub> substrate yields a different pattern of growth behavior as compared to that found over a catalytic Cu substrate. The thermodynamics and kinetics of graphene synthesis on both

---

substrates is compared in order to obtain the activation energies for both catalytic and non-catalytic substrates. The temperature-dependence of the formation of graphene is determined to yield data on the growth kinetics of grain size and density. Further, thermodynamic calculations for reactive species derived from the thermal decomposition of hydrocarbons is evaluated at the chemical equilibrium state of gas feedstock at the used reaction temperatures.

# Chapter 2

## Introduction

During the course of this decade graphene has become one of the most intensively studied materials. Its extraordinary properties, and their tremendous potential for a wide variety of applications, have attracted much attention. Mass production of graphene is only viable if an economical approach to synthesis can be developed, and if a supply of sufficiently high quality (according to the requirements of the application) can be ensured. Chemical vapor deposition (CVD) is the most promising method of graphene fabrication, as it is already a sophisticated technique used in both laboratories and industries.

This chapter begins by introducing the properties and corresponding applications of graphene, in order to explain why it attracts such a high level of interest. CVD fabrication is then briefly reviewed, including pretreatments of substrates and the growth mechanism. This is followed by a comparison of thermal and plasma-enhanced CVD. The discussion also covers growth kinetics and thermodynamics, selection of catalysts and carbon feedstock, and transfer protocol.

There are still problems which need to be tackled in this area, in terms of how to synthesize graphene on both metals such as Cu and non-metals such as Si/SiO<sub>x</sub> in a controllable manner and how to gain a fundamental understanding of the growth mechanism. This work therefore aims to improve understanding of the synthesis

of high quality graphene using CVD. Accordingly, the scope of this thesis covers both the production of a superior production and an investigation into the growth behavior of graphene.

## 2.1 Carbon allotropes

Carbon materials have various allotropes. One type is crystalline, such as diamond, graphite, and graphene; another is amorphous carbon materials. Of these allotropes, it is  $sp^2$  hybridized graphene which has taken the globe by storm with its novel properties.

### 2.1.1 Hybridized $sp^2$ carbon nanomaterials

In order to discuss  $sp^2$  carbon, it is necessary first to explain atomic orbital hybridization. This is the process which leads to the differences in the physical and chemical properties between the various carbon allotropes [1, 2]. The atomic number of carbon is six, and each carbon atom consists of six electrons. Two electrons fill the  $1s^2$  orbital, which is the inner shell, while the other four electrons occupy the orbitals of  $2s^2$ ,  $2p_x^1$  and  $2p_y^1$  (*cf.* [Figure 2.1a](#)). The hybridization of  $2s$  and  $2p$  orbitals occurs for the four outer electrons. When these electrons contribute equally to the formation of covalent bonds,  $sp^3$  hybridization leads to the formation of diamond (*cf.* [Figure 2.1b](#)).

The bonding energy is strong (3.6 eV) between two  $sp^3$  carbon atoms, which is what gives diamond its great strength. When three electrons ( $2s^2$  and  $2p_x^1$ ) form in-plane covalent bonds and the fourth ( $2p_z^1$ ) forms a weak non-covalent inter-plane  $\pi$  bond (*cf.* [Figure 2.1c](#)),  $sp^2$  hybridization occurs, leading to graphite. The



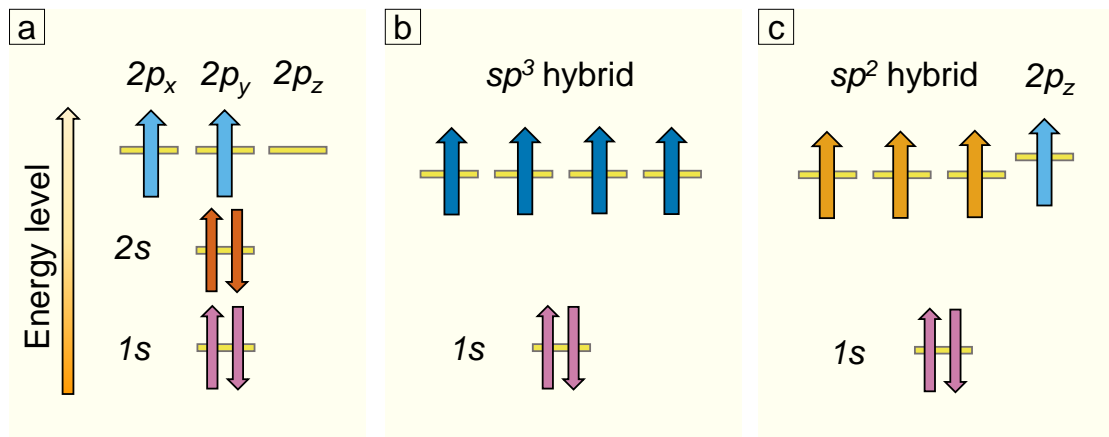


FIGURE 2.1: Atomic orbital diagram of carbon atom. The four valence electrons in the spherical  $2s$  orbital and the dumbbell-shaped  $2p$  orbitals contribute to chemical bonding of the carbon element. (a) Ground state. (b)  $sp^3$  hybridized in diamond. (c)  $sp^2$  hybridized in graphene and graphite

electrons in graphite (graphene) are delocalized, lending them good electrical conductivity. Compared with the in-plane  $\sigma$  bond (6.4 eV), the inter-plane  $\pi$  bond (31 meV) is relatively low [3]. This determines that graphite is a stacked structure with graphene sheets, which is prone to sliding away under pressure; this easy sliding motion allows for the fulfillment of graphical purposes as a graphite pencil.

### 2.1.2 Graphene

The graphite layers can be cleaved into thinner sheets, ultimately forming a monolayer sheet, termed graphene [1–4]. The three equivalent  $\sigma$  orbitals assemble in the X-Y plane at  $120^\circ$ , forming a planar honeycomb lattice.

Graphene has two other derivative allotropes. When a graphene sheet is packed into a ball, this is known as fullerene, in which carbon pentagons are generated amid the hexagons to form curvature, similar to a leather football. A graphene monolayer can also be rolled into a single walled carbon nanotube. When a few layers of graphene sheets are rolled up, multi-walled carbon nanotubes are produced. In terms of morphology, the  $sp^2$  carbon allotropes consist of 3D graphite, 2D graphene, 1D carbon nanotube, and 0D fullerene.

According to morphology, graphene is divided into vertical and planar graphene. The former is free-standing with anchoring over a supporting substrate; in contrast, the latter resides parallel to the substrate. In terms of layer numbers, planar graphene can be classified into monolayer, bilayer, and multilayer graphene.

## 2.2 Properties of graphene

Two-dimensional graphene has attracted a great deal of attention for its unique electronic properties, such as high carrier mobility [5–8], electric field effect [5], and ballistic transport of charge carriers [5]. In the following sections, the electronic transport properties of graphene will be discussed, along with the properties associated with its crystalline structure. This will be followed by a description of the properties relating to the optical transmittance of the material. Other properties of graphene, such as mechanical, thermal, and chemical properties will also receive a brief introduction.

### 2.2.1 Crystalline structure

[Figure 2.2a](#) shows the hexagonal lattice of graphene, with a zigzag and an arm-chair edge. The unit cell has two nonequivalent carbon atoms (A and B) in the grey rhombus. The yellow and blue circles correspond to the atomic sites of the A and B triangular sub-lattices. [Figure 2.2b](#) shows the reciprocal lattice of graphene, which is useful for describing the diffraction data (*cf.* SAED in [subsection 3.5.1](#)). It comprises an array of points, within which each point corresponds to one set of lattice planes in real space.

The two sets of lattice planes seen in [Figure 2.2c](#) have plane distances of 0.21 nm and 0.12 nm, respectively. The diffraction spots in the corners of the

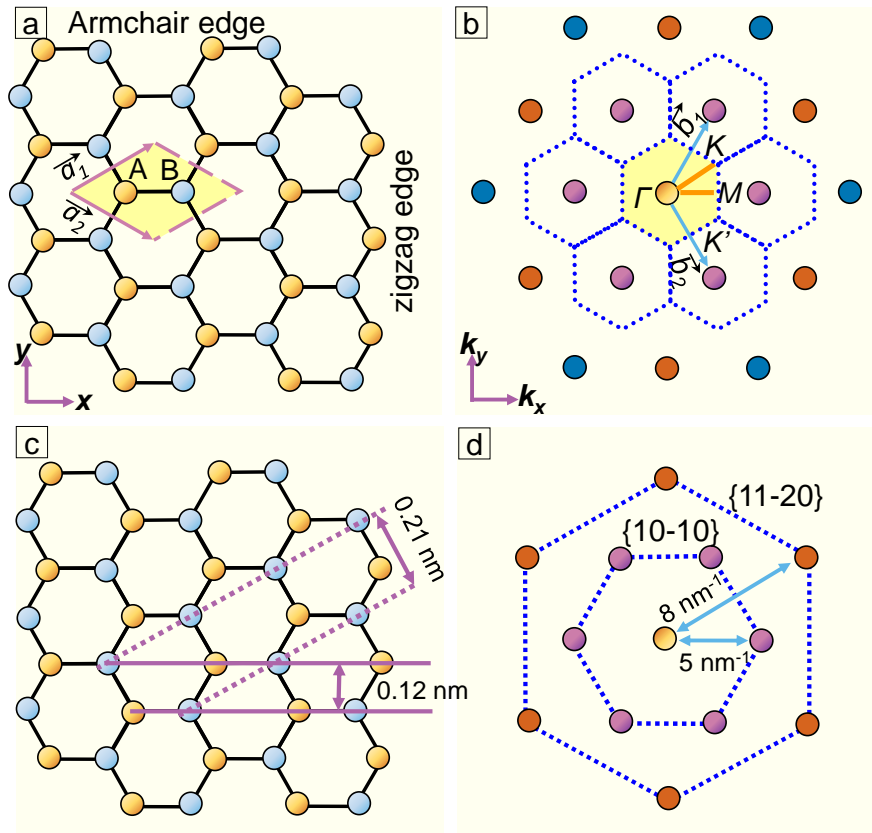


FIGURE 2.2: Hexagonal lattice structure of graphene. (a) 2D planar honeycomb lattice of graphene in real space. The unit cell is indicated as the grey rhombus. It contains two atom bases, A and B, and primitive vectors,  $\vec{a}_1$  and  $\vec{a}_2$ . (b) The hexagonal crystal structure in reciprocal space. The first Brillouin zone is in the grey hexagon. The primitive vectors in the reciprocal space are  $\vec{b}_1$  and  $\vec{b}_2$ , whereas  $\Gamma$ , M, K, and  $K'$  are labeled as the high-symmetry points. (c) The lattice distances in real space are 0.21 nm and 0.12 nm for the two sets of lattice planes, respectively. (d) The corresponding diffraction patterns in reciprocal space are  $\{10-10\}$  and  $\{11-20\}$  as lattice planes, respectively.

inner hexagon represent the lattice plane  $\{10-10\}$  in real space, whereas the six points at the outer hexagon correspond to the lattice plane  $\{11-20\}$  in real space.

Figure 2.2d is a schematic of the graphene diffraction pattern.

The reciprocal lattice is useful in describing the electronic band structure of a solid-state material when plotting the band along specific directions; for example, from  $\Gamma$  to M or from  $\Gamma$  to K in the Brillouin zone of Figure 2.2b.

For graphene, the two points (K and  $K'$ ) are of crucial importance; these are known as the Dirac points. Graphene is a zero-band gap semiconductor in which

the conductance band and valence band are in contact with the Dirac points and exhibit a linear dispersion along the momentum direction [1, 7]. The electron density of states is zero at the Dirac points. The exotic topology of the graphene band structure leads to its unique and exciting electronic transport properties. The charge carriers are massless, having extreme intrinsic carrier mobility [7, 9]. The extraordinary electronic properties of graphene hold great promise for the next generation of molecular electronics, with the possibility of applications such as graphene field-effect transistors.

## 2.2.2 Electrical transport

Graphene has emerged as a promising material, due to its unique electronic and electrical properties. In particular, monolayer graphene has three important properties: zero-carrier density at the Dirac points, relativistic carriers, and pseudo-spin [1, 4]. Together, these provide a platform for novel physical experiments, such as band-gap engineering by assembly of graphene nanoribbons [10, 11], the quantum hall effect [12, 13], and the modulation of carrier density [14] and surface potential [15] with tuning gate voltage. In other words, monolayer graphene is a building block for transistors [16]. Bilayer graphene [17], particularly AB-Bernal stacking [18–20], has a tunable band gap when applying a gate voltage [21, 22]. Few-layered graphene is more suitable in electrochemical energy systems [23–27] as opposed to transistor fabrication. Vertical (normally, multilayered) graphene [28–30] has a folded and curved morphology in comparison to planar graphene; it is typically applied as an electrode in rechargeable batteries, as well as a support for catalysts [31–39].

Intrinsic graphene is a zero band-gap semiconductor or a semi-metal. Measurements of field-effect transistors (FETs) [40] on mechanically exfoliated graphene have revealed that the latter has extremely high mobility and ballistic transport

within a sub-micrometer distance [5]. Its carrier mobility is dependent on charged impurities on the surface of the graphene or between the graphene and substrate, carrier scattering by various extrinsic factors (such as surface phonons) [6, 41–44], and creases and ripples in the planar graphene.

Different factors, such as surface functionality, the concentration of defects, and the average number of layers, are found to result in a range of behaviors, as exhibited by various specimens. Indeed, experiments on mechanically exfoliated graphene (FET) have indicated that the drain current ( $V_D$ , which depends on the gate voltage,  $V_G$ ) first decays to a sharp valley and then rises back to a high current [21, 45–48], leading to an ambipolar behavior in transfer characteristics (the  $V_D$  *vs.*  $V_G$  curve exhibits quasi-symmetry).

However, FETs with CVD graphene after transfer (grown on Cu foil) commonly exhibit a bipolar transfer behavior [49, 50], which is a p-type doping attributed to the trapped water or organic molecules between the graphene and Si/SiO<sub>2</sub> substrate [5, 51, 52]. Boron-doped graphene exhibits a p-type doping transfer characteristic that is analogous to the intrinsic CVD-grown graphene [53]. However, nitrogen-doped graphene exhibits an n-type doping transfer characteristic [54]. To understand these doping transfer behaviors, high vacuum annealing is applied to remove the chemical residue on top of or beneath the CVD-grown graphene and to recover an ambipolar transfer characteristic [51, 55].

It is remarkable that, with the direct growth of graphene on a Si/SiO<sub>2</sub> substrate, FETs can be fabricated without post-synthesis treatments, and that they show ambipolar behavior in the transfer curve [56]. This highlights the importance of growing graphene directly on dielectric substrates, rather than on metal foil.

### 2.2.3 Optical transparency

Graphene is regarded as a next-generation transparent-conducting electrode, due to its outstanding mechanical, chemical, and thermal stability. Monolayer graphene

film has a transmittance of  $> 90\%$  [37, 57], together with a sheet resistance of  $< 200 \Omega$  per square, which is comparable to transparent conducting oxides (TCOs). Therefore, graphene has adequate potential for use as transparent electrodes in photo-electronic devices, such as touchscreens. Research efforts are driven by a burgeoning interest in replacing the current TCOs, due to their resource storage limit (such as in the rare elements In and Ga) and fabrication costs. In addition, the high flexibility of graphene is an advantage, with the material showing no degradation in electric mobility performance with 5% stretching deformation [58]. This constitutes a considerable advantage over TCOs of a fragile ceramic nature. As a result, graphene has paved the way for wearable electronics. Another boon is that the optical conductance of graphene is independent of frequency over a wide range [59, 60].

## 2.2.4 Other properties

Graphene also have unique mechanical, thermal and chemical properties. Graphene possesses the highest intrinsic strength of all known materials [61, 62], due to its strong C-C  $\sigma$  bonds. Accordingly, graphene nano-platelets can blend into a polymer composite to reinforce the latter's mechanical strength and electrical conductivity [63]. The thermal conductivity of graphene can be as high as  $2000 \text{ W m K}^{-1}$ , which is the highest of all the carbon allotropes [1].

A perfect graphene sheet comprises a flawless hexagonal honeycomb network. However, pentagon and heptagon pairs are often observed, with defects such as folded edges [64], grain boundaries [65, 66], and electron-irradiation-induced faults [67, 68]. These defective pairs detract from the graphene in terms of strength [69, 70]. They also degrade its electronic conductivity through the introduction of electron-scattering sites [71, 72].

The functionalization of graphene can modify its chemical properties [73–78].

The external functional radicals or molecules interact with graphene through covalent bonds or van der Waals forces [79, 80]. This chemical exfoliation is a means of obtaining few-layered graphene flakes via the intercalation of molecules between two graphene sheets. Graphene-based complex materials have a large area to volume ratio, which provides a supporting surface for the embedding of functional particles. This has great potential for application in complex anodes for Li ion batteries [81], humidity sensors [82], catalyzed H<sub>2</sub> generation [83] and antibacterial devices [84], along with biological sensors [85].

## 2.3 Graphene deposition methods

There are a number of deposition approaches to obtain graphene. Here a brief comparison between them is given to assist the selection of approach to fabricate large area high quality graphene for electronic applications.

### 2.3.1 Synthesis approaches

Since the first isolation of graphene [5] in year 2004, various synthesis approaches have been developed for obtaining graphene, such as mechanical exfoliation [5, 86, 87], epitaxial growth from silicon carbide decomposition [88], chemical exfoliation [79, 89–92], organic synthesis from aromatic hydrocarbon precursors [93–95], reduced graphene oxide (rGO) [96–101], as well as chemical vapor deposition [102–107].

Mechanical and chemical exfoliation, as well as rGO provide the graphene flakes of hundred micrometer scale, which limits the potential for mass production. Bottom-up organic synthesis requires complicate reaction steps [93] and the yield of graphene is low and thus not suitable for large area graphene formation.

Graphene epitaxy over decomposed SiC has limitation in homogeneity control of the layer numbers over a large area [108–110]. However, CVD is the most promising graphene synthesis technique for both mass production and homogeneity control. Therefore, CVD is adopted as the main deposition approaches to obtain graphene over large area in this thesis.

### **2.3.2 Chemical vapor deposition**

CVD is a well-established synthesis route for both laboratory research and industrial production. It is an important technique in a wide range of areas, such as thin film deposition, crystal growth, and fiber and powder production. The method is well-developed in graphene synthesis. The principals of CVD, in terms of graphene growth, consist of two steps, namely thermal decomposition of carbon feedstock, and graphene assembly with reactive carbon radicals [4].

According to heating principles, CVD techniques consist of conventional thermal CVD and plasma-enhanced CVD. In a thermal CVD furnace, the heat is transferred from a resistance-heating element to the feedstock and the target substrates. In a plasma CVD system, a plasma source is coupled with the thermal process to enhance the cracking of carbon feedstock. Plasma CVD offers certain advantages; for example, it decreases the synthesis temperature. However, while the synthetic graphene derived from plasma CVD is good for growing vertical few-layered graphene it has, to date, been seen to have limitations in fabricating planar nano-crystalline graphene.

In terms of reaction pressure, CVD can be classified into low pressure CVD and ambient pressure CVD. Ambient pressure (ca. 1 bar) is commonly adopted during the CVD process. In general, this is the most economical approach, as it avoids the use of a vacuum system. However, it has slower growth kinetics. In contrast, low pressure (1 mbar - 10 mbar) CVD enables rapid growth, because the



reactive carbon radicals have a greater probability of residing in the substrates and assembling into graphene.

### 2.3.3 Substrate selection

The interaction between graphene and substrates have significant influence on the graphene growth behavior. According to the catalytic capability, the substrates can be classified into two types: catalyst and non-catalysts. Catalytic metals, such as the transition metals Cu and Ni, are commonly chosen for a chemical vapor deposition reaction to enhance the decomposition of carbon feedstock as well as to support graphene assembly. Polycrystalline Cu has proven as an efficient substrate to produce predominantly monolayer graphene [111]. How the weak interaction between Cu and graphene influences the growth behavior is interpreted in greater details next (*cf.* [subsection 2.4.5](#)). In contrast, on polycrystalline Ni, inhomogeneous few layer graphene film of is synthesized due to the difficulty in homogeneity control [112]. The strong interaction between Ni and graphene leads to formation few layer graphene, which is discussed thoroughly in the following introduction (*cf.* [subsection 2.4.6](#)). Hence, Cu is selected as one substrate for the optimization of monolayer graphene synthesis.

However, non-catalytic substrates, such as Si/SiO<sub>2</sub>, have advantages for graphene synthesis in comparison to catalytic substrates. First, the graphene directly grown on dielectric Si/SiO<sub>2</sub> substrate is compatible with subsequent electronic device fabrication. This reduces time cost by avoiding a complicated transfer step, which is necessary for graphene grown over metals. Notes that the transfer step for metal substrates takes several days and even weeks. Second, the direct graphene growth avoids the processing contamination and breakage introduced by the transfer step. Last, the direct graphene growth over Si/SiO<sub>2</sub> can save the cost of using high purity Cu foils. Moreover, the interaction between Si/SiO<sub>2</sub> and graphene determine the

graphene morphology evolution is reviewed in the following (*cf.* [subsection 2.4.7](#)). Therefore, Si/SiO<sub>2</sub> is selected as another substrate for the direct fabrication of large area homogeneous monolayer graphene.

### 2.3.4 Substrate pretreatments

It is vital to apply substrate pretreatment prior to graphene growth by CVD. Substrates can be divided into two types: metals and non-metals. When selecting metals such as Cu, pretreatments include general surface cleaning through organic solvent soaking [113], partial removal of the Cu surface using weak acetic acid [114] or strong nitric acid [115], liquefying the Cu surface at its melting point [116, 117] and increasing the Cu grain with H<sub>2</sub> annealing [4].

In the absence of pretreatment, second-layer flakes are commonly observed above or beneath a first layer complete graphene film [118]. This is attributed to the surface roughness of the Cu substrate and its carbon contamination. With surface-smoothing pretreatments [119–121], the thick second-layer flakes are suppressed, because the polished surface avoids carbon-trapping sites, such as Cu grooves and grease contamination. In addition, oxygen is observed to promote the growth of a graphene single crystal [85, 115], but at a very slow rate.

Ni catalysts have high carbon solubility. The thickness of Ni film on a support (such as Mo foil or Si/SiO<sub>2</sub> wafer) is therefore important in controlling the number of synthetic graphene layers, as well as the homogeneity of the graphene layers, through the adjustable diffusion of carbon into the Ni sections [122–124].

When non-metal substrates, such as silicon oxide are employed, they are initially soak-cleaned in organic solvents [116]. Oxygen pretreatment with air sintering at 800 °C for one hour [50] is applied to increase the nucleation density of graphene grains.

### 2.3.5 Carbon feedstock

Carbon feedstock, typically a hydrocarbon, can be divided into gas, liquid, and solid phases. Gaseous methane ( $\text{CH}_4$ ) [111, 125–127] is most frequently used in Cu-catalyzed CVD. Additionally, acetylene ( $\text{C}_2\text{H}_2$ ) [128, 129] and ethylene ( $\text{C}_2\text{H}_4$ ) [130] are successful feedstocks for growing graphene. Liquid feedstocks are common solvents [131, 132], such as methanol, ethanol, isopropanol, and acetone, large hydrocarbons (pentane and hexane) [83, 85, 113], and aromatic hydrocarbons [133–136]. Liquid feedstock is generally introduced using a carrier gas, such as Ar. Solid carbon feedstocks have been derived from amorphous carbon [137–139], camphor [140–143], DNA [144], insect protein [145], self-assembly-monolayer layer [146], carbon precursors to bulk metals [147, 148], PS polymers [149], PMMA [150–154] and waste plastics [155].

### 2.3.6 Thermal chemical vapor deposition

Thermal CVD is commonly employed in planar graphene synthesis. In a thermal CVD process, Cu and Ni are the two most widely used substrates for synthesizing graphene [4], although a few processors use Ag [156], Ru [157], Co [128] and Fe [158, 159]. Initially, the Ni foil yields multilayered graphene (layer number  $> 10$ ). When the Ni thickness is reduced by, for example, applying Ni thin film on a support, the number of layers of graphene can be brought down (to below 10) in both ambient pressure [103, 112] and low pressure CVD [104]. Single crystalline Ni is good for controlling monolayer graphene growth (purity *ca.* 90%); however, polycrystalline Ni has a lower yield in monolayer graphene (purity *ca.* 72%).

Polycrystalline Cu foil is favored over Ni substrates, because it yields monolayer graphene at a higher purity (*ca.* 90%) far more easily. In addition, the graphene grain size is larger on Cu than that grown on Ni [4]. The former's easy control of monolayer graphene growth is a consequence of the low solubility of carbon in

Cu. It is generally agreed that monolayer graphene grows in a self-limited manner on polycrystalline Cu [111]. A further advantage of using Cu foil as a substrate lies in the scale-up potential for mass production of graphene: A 30-inch graphene sheet has been successfully transferred onto a flexible substrate using a roll-to-roll method [57]. In addition, thin film Cu over a Si/SiO<sub>2</sub> support [160] can be employed in order to avoid having to undergo the transfer step after synthesis, because the support sublimates during the CVD so that only the graphene membrane remains on the substrates.

Another technique employed to avoid transfer (which damages and contaminates the synthetic graphene) is direct graphene synthesis over non-metal substrates. Non-metallic insulators are used to grow graphene, such as MgO crystals [129], Si/SiO<sub>2</sub> [50], Si/Si<sub>3</sub>N<sub>4</sub> film [56], quartz [49], sapphire [161] and hexagonal BN [162–164]. The growth rate on such insulators is slower than on metals. However, direct graphene growth (over Si/Si<sub>3</sub>N<sub>4</sub>) holds promise in improving the electrical properties of graphene, (*e.g.*, providing a higher carrier mobility than transferred graphene (grown on Cu) [56]).

### 2.3.7 Plasma chemical vapor deposition

Plasma CVD differs from its thermal counterpart in several respects. First, plasma-enhanced CVD (PECVD) facilitates the growth of vertical graphene over a range of substrates, such as Si [29, 30] and Si/SiO<sub>2</sub> [165, 166]. In addition, planar graphene film can be synthesized using this type of CVD. Second, it requires a much lower synthesis temperature than thermal CVD. The typical temperature used in plasma CVD is 600 °C, in order to grow good graphene film [167], while the temperature needed for thermal CVD is as hot as 1000 °C or higher [49]. Third, the synthesis time to obtain a graphene film with PECVD is 15 minutes [165], which is much shorter than with thermal CVD (which takes as long as eight hours) [50].

### 2.3.8 Transfer protocol

Graphene grown over metals requires a transfer treatment in order to fabricate a device or carry out further characterization. First, the graphene surface is spin-coated with a supporting polymer, such as PMMA [112, 168, 169]. Second, the PMMA/graphene/Cu layers are floated upon an etching solvent such as ferric chloride ( $\text{FeCl}_3$ ) [169] and ammonium persulfate (APS) [40, 170]. Third, the PMMA/graphene is cleaned with deionized water after thorough removal of Cu [40], before being fished over a target substrate. Next, acetone is employed to dissolve the PMMA. Finally, high vacuum annealing on the graphene/substrate completes the transfer by thorough removal of organic residues.

It is worth noting that the graphene film on the unwanted side of the Cu foil can be pre-etched with nitric acid [40] or APS [170], because graphene can grow on both sides of the Cu foil. The transfer procedure and chemical choices are listed in [Table 2.1](#).

Alternative approaches can also be successfully employed in graphene transfer. Bubbles can be used to intercalate into the graphene/substrate interface before subsequent separation. For example, the  $\text{H}_2$  bubble, which can be generated through an electro-chemical reaction [171], can peel off the PMMA/graphene membrane from the Cu substrate. However, such electro-chemical methods require a conducting metallic substrate, such as Cu [172, 173].

One well-established bubble method, which does not employ an electro-chemical unit, can be used to transfer graphene from non-metals [175]. The approach hinges on the continuous release of  $\text{O}_2$  bubbles, which can intercalate into the graphene/substrate interface and act as a lift-off medium. A schematic of this method is shown in [Figure 2.3](#).

In contrast to the above wet chemistry methods, mechanical force can be employed to peel off sticky epoxy or graphene from the substrate [178]; similarly, thermal release tapes can detach graphene from the substrate in a dry transfer [57].

TABLE 2.1: A review of the chemicals selected for each step in the transfer procedure.

Etching of bottom graphene	Coating polymer support	Etching Cu with reactive agents	Fishing graphene onto substrate	Removing polymer in solvents	Reference
APS	PMMA	FeCl <sub>3</sub> /HCl	Water	Acetone	[112, 168–170]
HNO <sub>3</sub>	PMMA	APS	Isopropanol	Acetone	[40]
No	PC	FeCl <sub>3</sub>	Water	Chloroform	[174]
No	PMMA	H <sub>2</sub> O <sub>2</sub> +NH <sub>3</sub> ·H <sub>2</sub> O +H <sub>2</sub> O	Water	Acetone	[175]
No	PMMA	Electrochemistry	Water	Acetone	[171, 176]
No	No	APS	No	No	[177]

Alternative polymers such as polycarbonate (PC) [174] have the advantage of minimizing the polymer residue without the need for a high vacuum annealing treatment. The PC polymer provides a clean transfer because it can dissolve more thoroughly in chloroform than the PMMA/acetone pair [174].

In addition, when loading a polymer/graphene film onto a substrate, isopropanol may be used to replace water as a medium, in order to achieve improved adhesion over the Si/SiO<sub>2</sub> substrate [179].

For graphene grown on In, Ga, and MgO substrates, HCl solution serves as an etching agent [23, 117, 180]. In terms of graphene grown over Ni, the etching/peeling-off agent can be selected from O<sub>2</sub> bubbles [175], acetic acid [25, 26], hydrochloric acid [112], and nitric acid [25]. A KOH base can be employed to transfer the graphene over Si/SiO<sub>2</sub> and quartz to other arbitrary substrates [181, 182].

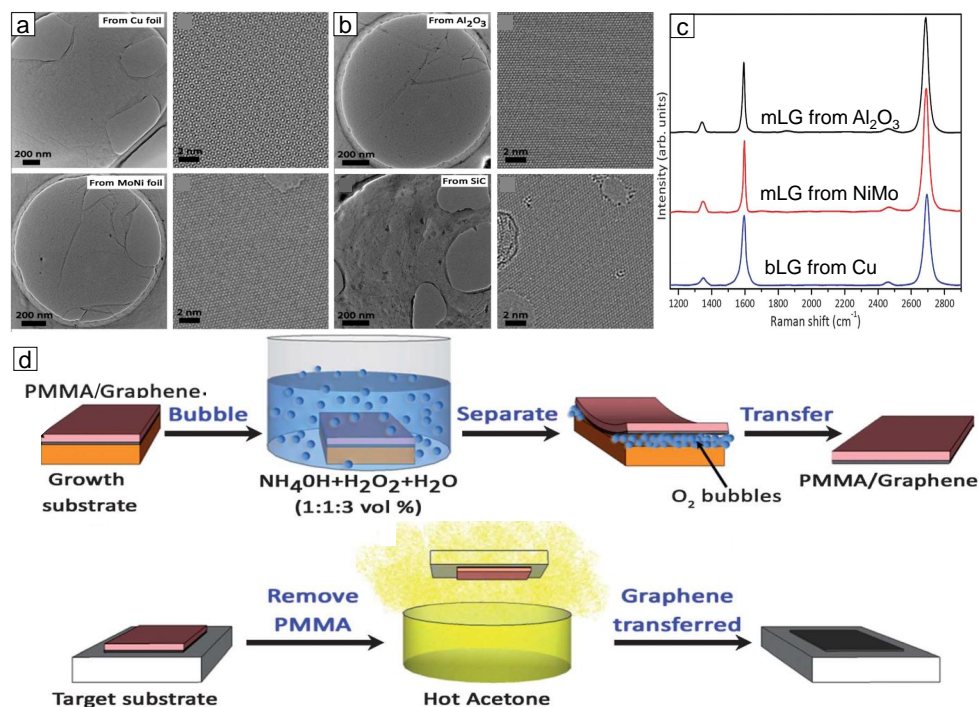


FIGURE 2.3: A bubble transfer protocol that applies to arbitrary substrates. (a) TEM images of a graphene membrane transferred from Cu, Mo/Ni,  $\text{Al}_2\text{O}_3$ , and SiC supports. (b) Raman spectra of the transferred graphene film. (c) Raman spectral mapping of G/D intensity ratio of the transferred graphene (from Cu foil). (d) Photograph of key steps of the transfer: PMMA spin-coating, immersion inside the bubble medium, lift-off of PMMA/graphene from Cu foil and fishing onto Si/SiO<sub>2</sub> substrate. (e) Sketch of the complete transfer procedure. Adapted from reference [175].

## 2.4 Chemical vapor deposition for graphene growth

There is a wide range of techniques for preparing graphene, including mechanical exfoliation [5], chemical exfoliation [174, 175], reduced graphene oxide [97, 98, 183], epitaxial growth on silicon carbide [108, 184], ribbon generation through unzipping carbon nanotubes [185, 186], organic synthesis from aromatic solvents [93], hydrogen annealing over adsorbed organic molecules [187], electron beam-driven graphene formation [188], carbon segregation during cooling of transition metals [122, 123, 181, 182], and chemical vapor deposition [18, 25, 111, 125]. Considering its application in electronic devices, graphene should possess the following features: a large area, high quality, and low cost. As its setups are well-developed

and have great scale-up potential, CVD is one of the most widely used methods for both research into graphene and mass production of graphene film.

### 2.4.1 Thermodynamics

Thermodynamics is used to predict whether a reaction can possibly occur. An energy barrier referred to as the activation energy ( $E_a$ ) must be surmounted for the initialization of a chemical reaction. Usually, the factors needed to start a reaction include a critical temperature, together with a catalyst. Kinetics are used to evaluate the rate of a reaction; in turn, kinetic constants are deployed to assess kinetics. In CVD growth of graphene, the kinetic constants are determined by an increased rate in the radius of the graphene domain, or the enhanced degree of coverage during the formation of full film graphene. The experimental data on growth rate can be used to derive the kinetic constants. When constructing an Arrhenius plot (*i.e.*, the logarithm of kinetic constant versus the reciprocal of the temperature), the activation energy can be calculated experimentally.

### 2.4.2 Arrhenius plots

As in the Atkins Thermodynamics textbook [189], the Arrhenius plot and the activation energy are well described. Here the brief concepts of these two are presented. The most reaction rate increase when the temperature is increased. For many experimental reactions, the plot of  $\ln k$  against  $1/T$  presents a linear behavior,  $\ln k = \ln A - \frac{E_a}{RT}$ , which is normally expressed as Arrhenius equation with two Arrhenius parameters, one standing for the slope and the other the intercept.



The parameter  $E_a$ , is obtained from the slope  $-E_a/R$ , is termed activation energy. The parameter  $A$ , represents the intercept of the straight line, termed pre-exponential factor.  $E_a$  is determined by the slope of the plot of  $\ln k$  against  $1/T$ , which means, the reaction rate constant is more dependent on temperature when activation energy is higher. For example, the graphene growth over  $\text{SiO}_x$  has higher activation energy than over Cu (*cf.* Table 2.2 in next subsection as well as Figure C for  $E_a$  in graphene formation over  $\text{SiO}_x$ ). This activation energy difference can be interpreted as the energy to reach the transition state (which is crucial to form products) from the molecular potential energy of reactants (ground state). If the activation energy is zero, its reaction rate is independent of temperature, *viz.*, it occurs spontaneously without external energy input.

However, when the activation energy is negative (showing positive slope in the Arrhenius plot), it indicates that the rate reduces when temperature is raised (*cf.* Figure 5.6 in  $E_a$  for graphene formation from pre-adsorbed organic solvents). This behavior is a symbol that this reaction presents a complicated mechanism. For this case, graphene flakes form upon thermal annealing on the pre-deposited organic adsorbents. However, the growth mechanism is different with the conventional CVD, where continuous carbon feedstock is introduced. Here in this case, the solvent adsorbents serves as non-continuous carbon feedstock, which will involve a complex growth mechanism, *viz.*, the competence between accelerated thermal decomposition for providing reactive species and the enhanced desorption of these species. The former increases the growth rate, which prefers the increase of the grain size. In contrast, the latter decreases the nucleation rate, which reduces the grain density. This competence between molecule absorption and desorption lead to the complicated behavior of activation energy for both grain growth rate and nucleation rate.

In the following section, the activation energies obtained from various growth conditions are reviewed.

### 2.4.3 Activation energy

The activation energy in this thesis refers to the total activation energy of the graphene growth reaction. The activation energy is influenced by a number of parameters: reaction pressure, carbon feedstock, choices of substrates/catalysts, plasma assistance, and oxygen incorporation. First, at ambient pressure CVD, the activation energy is 5 eV [190], whereas at low pressure CVD the activation energy ranges from 1.5 eV to 3.7 eV [114, 190–192]. Therefore, low pressure CVD is favored in the fabrication of large-area graphene film over Cu, because of the lower activation energy.

Second, the effect of carbon feedstock on activation energy is investigated. When using methane ( $\text{CH}_4$ ) and ethane ( $\text{C}_2\text{H}_2$ ), the activation energies are similar, ranging from 2 to 3.7 eV [185, 186]. When employing general solvents (ethanol, isopropanol, and acetone),  $E_a$  drops to 1.4–1.6 eV [187]. When introducing aromatic hydrocarbons ( $\text{C}_{22}\text{H}_{14}$  and  $\text{C}_{24}\text{H}_{12}$ ),  $E_a$  decreases to 1.46 eV and 1.87 eV, respectively [136]. It seems that ethanol-based CVD offers advantages in the form of lower activation energy and no hazards. Indeed, ethanol is used to grow high quality graphene in CVD [193], but typically requires a bubbling apparatus with Ar as a carrier gas [193, 194]. Meanwhile, methane is most widely employed as a carbon feedstock to grow graphene, perhaps because of its simple apparatus in terms of gas introduction, and perhaps because sufficient resources of methane exist.

Third, the type of substrate significantly influences the activation energy. When selecting catalytic metals, such as Cu, Co, and Ru, the activation energies have similar values (for example, from 1.4 - 2.9 eV) [195, 196]. In terms of non-catalytic substrates, however, the activation energies are notably higher. For Si/SiO<sub>2</sub> substrates [50],  $E_a$  increases to 4.75 eV, while for the Si<sub>3</sub>N<sub>4</sub> substrate [56], it rises to 6.75 eV. This confirms the role of the catalyst in reducing the energy barrier in a CVD reaction.

Last but not least, surface oxygen adsorbed over a Cu substrate can suppress

the activation energy. The surface oxygen, upon hydrogen annealing, results in the formation of OH radicals [114]. These enhance the decomposition of carbon precursors, which contributes to the decrease in  $E_a$ . It is also worth noting that plasma assistance diminishes the activation energy to 1.03 eV by activating the feedstock decomposition [197]. In addition, a so-called Ni promoter reduces the activation energy by 2 eV. Indeed, the Ni foil is typically located in the up-streaming of the hot reaction zone [191], which cracks the carbon precursor into activated radicals before it arrives at the target substrates. The list of  $E_a$  values can be found in [Table 2.2](#), based on the above-mentioned conditions.

#### **2.4.4 Growth kinetics**

The kinetics of graphene growth can be used to predict the time cost of a CVD. The kinetic rates can be increased by: a rise in synthesis temperature, increasing the concentration of carbon precursors, and improving the catalyst's capability.

First, an elevated temperature can reduce the time required to grow graphene full film. At temperatures slightly lower than 1000 °C, the graphene film is complete after 150 minutes of growth [192]. However, at temperatures above 1000 °C (such as 1025 – 1035 °C), the graphene film can be grown within 10 minutes [192, 198]. Second, the reaction rates can be upgraded by increasing the concentration of reactive carbon species. For instance, an increase in the partial pressure of the methane satisfies this need [199]. Meanwhile, the generation of reactive carbon radicals can be enhanced at higher temperatures [200, 201]. Third, the growth kinetics can be improved through the incorporation of catalytic metals, such as Cu and Ni. Indeed, CVD over Cu or Ni substrates completes full-coverage graphene film growth within one hour [104, 111, 112, 125].

TABLE 2.2: The activation energies depending on various growth conditions.

Support\ Substrate	Ea (eV)	Carbon source	Pressure	Temperature (°C)	CVD type	Reference
Cu	5.0	CH <sub>4</sub>	Ambient	950-1080	Thermal	[190]
Cu	3.7	CH <sub>4</sub>	Low	850-1000	Thermal	[191]
Cu	2.74	CH <sub>4</sub>	Ambient	900-1050	Thermal	[202]
Cu	2.6	CH <sub>4</sub>	Low	750-1000	Thermal	[192]
Cu	2.0	CH <sub>4</sub>	Low	950-1080	Thermal	[190]
Cu	1.5, 1.76	CH <sub>4</sub>	Low	835-1035	Thermal	[114, 203]
Cu	1.7	CH <sub>4</sub>	Low	850-1000	Ni promoted thermal	[191]
Cu	1.03	CH <sub>4</sub>	Low	500-900	Plasma enhanced	[197]
Cu	0.92	CH <sub>4</sub>	Low	835-1035	Oxygen thermal	[114]
Cu	2.4-3.1	C <sub>2</sub> H <sub>4</sub>	Low	900-1050	Thermal	[204]
Cu	1.4-1.6	C <sub>3</sub> H <sub>6</sub> O, C <sub>3</sub> H <sub>8</sub> O, C <sub>2</sub> H <sub>6</sub> O	Low	850-1025	Chemo route	Thermal [187]
Cu	1.46,1.87	C <sub>22</sub> H <sub>14</sub> ,C <sub>24</sub> H <sub>12</sub>	Vacuum	550-1000	Thermal	[136]
Co	1.4, 2.9	C <sub>2</sub> H <sub>4</sub>	Vacuum	340-360	Thermal stage	[196]
Ru	2	C film	Vacuum	470-800	Thermal stage	[195]
Si <sub>3</sub> N <sub>4</sub>	6.75	CH <sub>4</sub>	Ambient	1150-1190	Thermal	[56]
SiO <sub>2</sub>	4.75	CH <sub>4</sub>	Ambient	1050-1190	Thermal	[50]

In contrast, CVD on non-metals, such as  $\text{SiO}_2$ , usually requires a long growth time (*e.g.*, from seven hours to three days) [49, 50, 56]. In addition, metal vapor can accelerate the graphene growth. For example, Cu vapor can be confined and employed to enhance the carbon decomposition in an equilibrium environment [125, 205]. With the assistance of Cu vapor, the graphene full film can form within 10 seconds [121, 125]; however, without the vapor, 15 minutes is required [125].

To evaluate the growth kinetics, in-situ imaging and spectroscopic characterization tools are in the process of being established, such as in-situ LEEM [202, 203], SEM [206, 207] and XPS [208].

Growth mechanisms of graphene in CVD are highly dependent on substrate types, such as Cu, Ni, and ceramic oxides. In CVD, the growth conditions include feedstocks, temperature, and catalysts. After the comprehensive study of the role of these three conditions, the detailed growth mechanisms over various substrates will be discussed.

### 2.4.5 Reaction mechanisms over Cu

Cu is the most frequently used substrate in the fabrication of high quality monolayer graphene film. Monolayer graphene accounts for 95% of the coverage [111]; however, secondary layer flakes are present in the monolayer film (*cf.* Figure 2.4ab) in layers of two or three (*cf.* Figure 2.4c). The low carbon solubility of Cu accounts for the so-called self-limiting growth mechanism [104]. When the Cu surface is fully covered with graphene membrane, the catalytic reaction terminates, and graphene synthesis ceases. This self-limiting mechanism has been observed in a number of independent labs [119, 160, 199, 209–211]. However, this mechanism cannot provide an explanation for the formation of second layer patches that emerge in monolayer graphene full film [111].

Indeed, second-layer flakes are present in monolayer graphene film [111, 212–214], either individually or merged into parallel stripes [199, 215], and even occur as full coverage growth of bilayer graphene [18, 20]. Many researchers are interested in understanding why second-layer flakes form. Some propose that the carbon atoms can diffuse through the first layer of graphene to nucleate beneath it, ultimately assembling second-layer flakes. Others argue that these flakes can form above the initial graphene layer. While both camps are able to cite supporting evidence, a definitive answer is yet to emerge.

Liquid Cu substrates have advantages over solid substrates when growing single crystal monolayer graphene [116, 117, 216]. At temperatures above 1080 °C, Cu foils liquefy on a support. When this is followed with CVD, single crystalline graphene domains form with either round or hexagonal shapes. Other liquid metals, such as In [117] and Ga [180], have similar merits for single crystalline graphene growth. However, the liquid metal method usually requires high temperatures (> 1100 °C) from a CVD furnace.

The morphology of synthetic graphene grains has some dependence on the interaction between graphene and the substrates. The geometric morphology of individual graphene grains varies: they can be square, hexagonal, or four- or six-lobed shapes in the early stages of CVD. On the one hand, the graphene shapes probably depend on the crystalline orientation on the surface of solid Cu. On Cu (101) and Cu (110) facets, a four-lobed graphene domain is formed [217]. In addition, a higher growth rate is obtained on Cu (111) facets than on Cu (100) facets [218]. On the other hand, the geometry is also affected by the gas conditions. For example, square-shaped graphene grains can be obtained when gas flows are adjusted (*e.g.*, using larger hydrogen flow rate in comparison to methane flow rate) [219]. However, hexagonal graphene domains are usually formed at a large ratio of hydrogen/methane flow rate [118, 220]. The six-lobe-shaped graphene domains are generally formed in an equilibrium growth environment (such as inside a half-sealed tube or a so-called Cu pocket) [126, 221–223]. A Cu pocket is made manually by folding a Cu square into halves, then sealing the three edges

by pressing them [126].

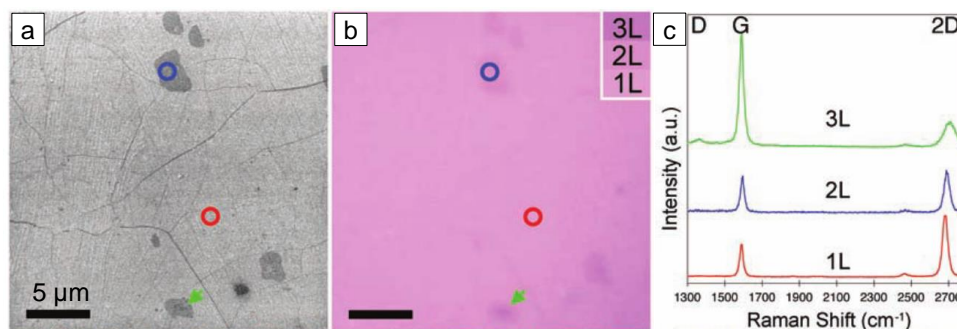


FIGURE 2.4: Predominantly monolayer graphene film growth over Cu via CVD. (a) SEM graph of graphene transferred onto a Si/SiO<sub>x</sub> substrate shows monolayer graphene film with bi- and tri-layer regions. (b) Optical micrograph of the same region as in panel a. (c) Raman spectra from the circled or arrowed position, presenting the mono-, bi-, and triple layers of graphene. Adapted from reference [111].

## 2.4.6 Reaction mechanisms over Ni

Nickel is another important substrate for graphene growth. The growth occurs in three stages: carbon dissolution, carbon segregation, and graphene precipitation [104, 112, 224]. First, in the initial stages of CVD, carbon atoms dissolve and diffuse [225] into the bulk Ni and a carbide forms [226]. Second, when cooling begins, the carbon atoms segregate from meso-stable Ni<sub>2</sub>C [227]. Third, these carbon species precipitate to the surface of Ni and form graphene. However, the number of layers of graphene grown over pure Ni is varies from one to ten.

Based on this last point, Ni substrates should be tailored to obtain graphene with a consistent number of layers. Initially, Ni thin film is employed to suppress the diffusion of carbon atoms into bulk Ni [112, 228]. Second, Ni sub-oxide (from mild oxidation by CO<sub>2</sub>) in the thin surface facilitates the growth of thin few-layer graphene [224]. The NiO<sub>x</sub> surface can both increase the catalytic capability and suppress the carbon diffusion into bulk Ni. The schematic of the CO<sub>2</sub>-enhanced graphene growth over NiO<sub>x</sub> is shown in [Figure 2.5](#).

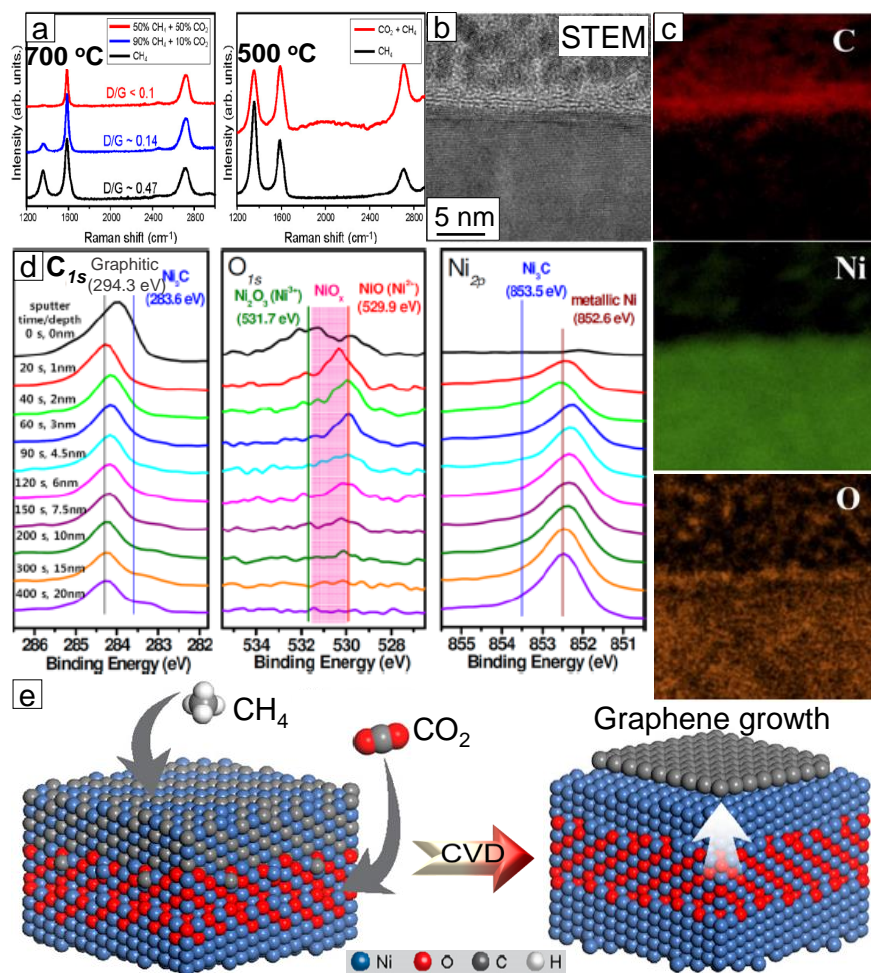


FIGURE 2.5: Graphene synthesis over NiO<sub>x</sub> substrates with CO<sub>2</sub> assistance. (a) Schematic of CVD synthesis of graphene over NiO<sub>x</sub> surface. The middle diagram shows the system energy (on both Ni and NiO<sub>x</sub>) against the reaction pathway of hydrogen detachment from a methane molecule. (b) Raman spectra of graphene grown at 700 oC. The D mode with CO<sub>2</sub> enhancement is lower than that without. (c, d) STEM image and EDX map of C, Ni, and O in the graphene/ NiO<sub>x</sub> interface. (e) XPS of the surface elements of graphene on NiO<sub>x</sub>. The surface oxygen is confirmed in the form of Ni sub-oxide. Adapted from reference [224].

In addition, when using a Ni/Mo alloy [122, 123], the monolayer graphene can be fabricated. Figure 2.6 presents the monolayer growth over a Ni/Mo substrate. Similarly, with Cu/Ni alloys the potential exists to adjust the number of layers of graphene in a CVD, to either monolayer film or bilayer film, by controlling the component ratio of Cu to Ni [173].



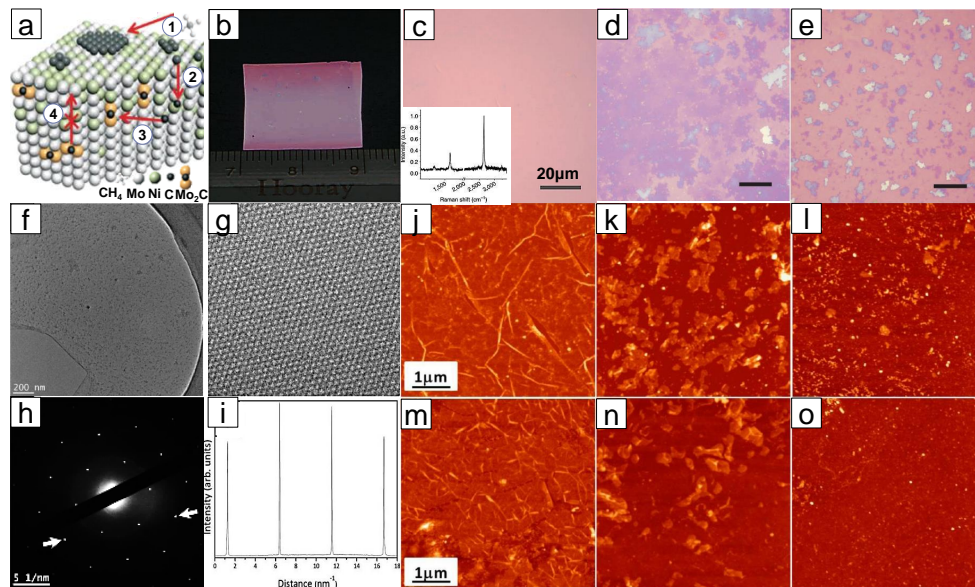


FIGURE 2.6: Monolayer graphene synthesis over binary Ni-Mo substrate. (a) Sketch of the growth mechanism, including the decomposition of methane, carbon diffusion into Ni bulk, carbon suppression through the formation of stable  $\text{Mo}_2\text{C}$ , and carbon precipitation for graphene assembly. (b) Photograph of graphene film (transferred) onto a  $\text{Si}/\text{SiO}_x$  substrate. (c) Optical micrograph of the graphene film. Inset Raman spectrum confirms the monolayer feature. (d,e) Discontinuous film and individual flakes with various cooling protocols. Adapted from reference [122]. (f,g,h,i) TEM characterization of graphene monolayer membrane. (j,k,l,m,n,o) AFM height images of the graphene obtained from different cooling steps. Adapted from reference [123].

### 2.4.7 Reaction mechanisms over non-metals

Graphene can be synthesized over non-metal oxides, such as  $\text{MgO}$  [129],  $\text{Al}_2\text{O}_3$  [161] and  $\text{SiO}_2$  [49, 50]. This usually requires higher temperatures ( $1100^\circ\text{C}$ ) than growth over  $\text{Cu}$  ( $1000^\circ\text{C}$ ) [21, 47]. Graphene growth can be enhanced with additional measures, such as metal vapor [220, 229], plasma assistance [165] and surface oxygen [50].

Graphene formation over  $\text{MgO}$  nanocrystals displays epitaxial growth [129]. The graphene layers are seen to be stacked parallel to the crystal lattice of  $\text{MgO}$  in an HRTEM observation, which confirms that this type of growth occurs (*cf.* Figure 2.7). Graphene growth on sapphire ( $\text{Al}_2\text{O}_3$ ) substrate also proceeds via the epitaxial mechanism. The facet of the resulting graphene has a relative rotation

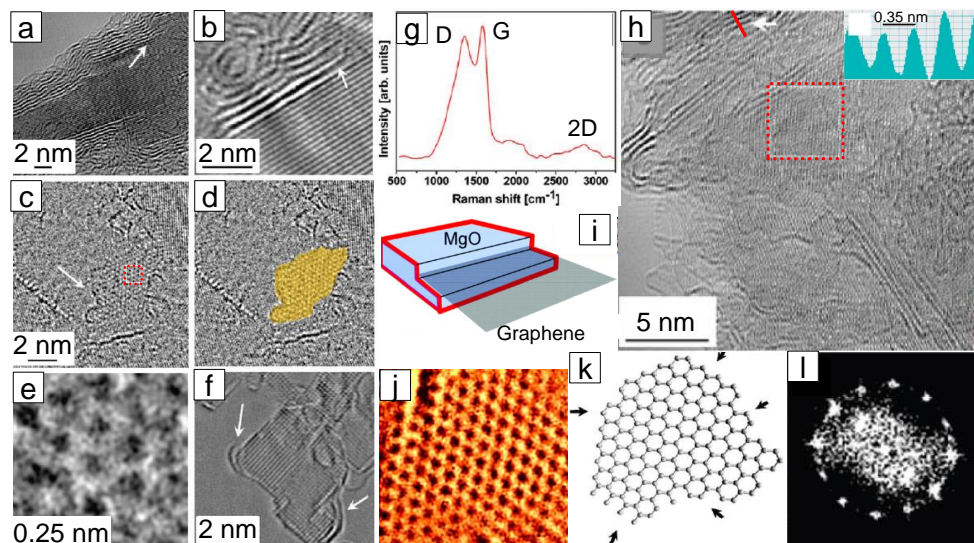


FIGURE 2.7: Graphene growth over MgO support. (a, b) TEM observation of few-layer graphene on MgO crystal. (c, d) Graphene nano-crystal over MgO surface formed in the early stages of CVD. (e) Magnified image from dashed square in Panel C shows the lattice feature of graphene. (f) Cross-section TEM of graphene over MgO support. (g) Raman spectrum of nano-crystalline graphene after removal of MgO. (h) TEM of the purified graphene after MgO removal. (i) Sketch of graphene growth mechanism: nucleation at lattice steps and extrusion. (j) HRTEM of the graphene showing the honeycomb structure. (k) Atomic configuration of a nano-graphene flake with a large ratio of atoms at its edges. (l) Fast Fourier transformation from magnified region of Panel h. Adapted from reference [129].

stacking of  $30^\circ$  in comparison to the sapphire [161]. Hence, the planar graphene growth is driven by the van de Waals attraction between the supporting sapphire and the incubating graphene [161]. In addition, graphene can be synthesized on other crystalline substrates, such as SiC [108], BN [164], graphite [172, 230] and graphene film (over a Cu substrate) [20].

Graphene synthesis over the Si/SiO<sub>2</sub> substrate is of ultimate importance, because the direct growth enables subsequent transistor fabrication without any post-treatments (such as transfer). In addition, the direct synthesis has the benefit of avoiding foreign contamination from the transfer step (such as graphene growth over Cu).

Two types of planar graphene can be grown directly on Si/SiO<sub>2</sub> substrates. One type is polycrystalline film, which is pieced together with nano-crystalline

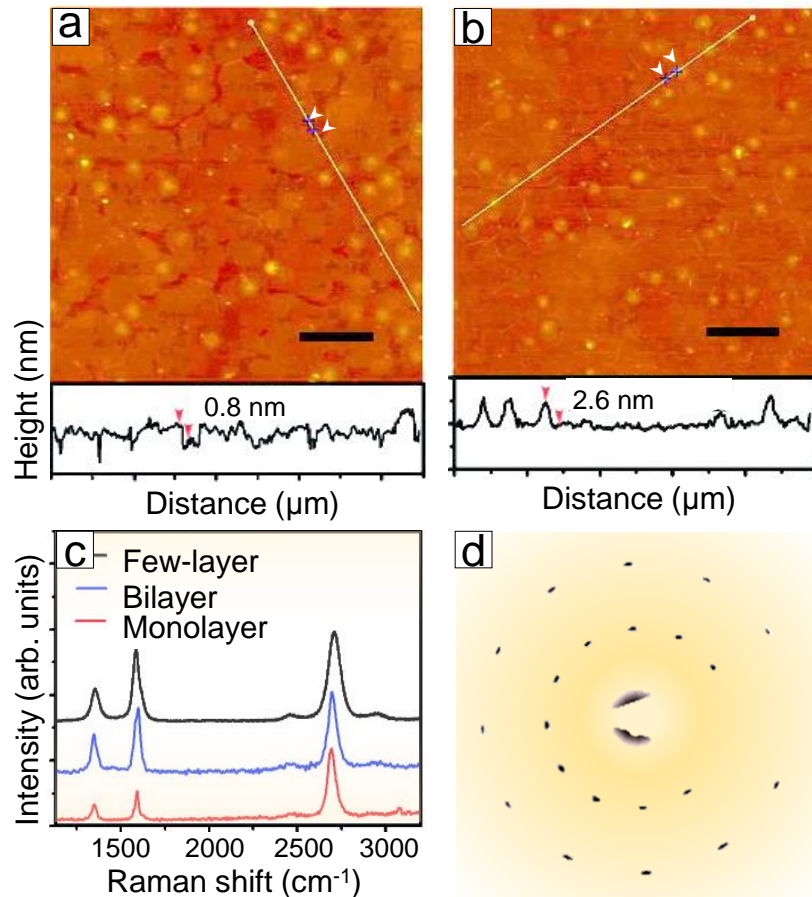


FIGURE 2.8: Graphene grown directly over  $\text{Si}/\text{SiO}_x$  substrates with CVD. (a) Incomplete graphene film with holes (uncovered substrate) and second-layer flakes. The height between graphene film and substrate is 0.8 nm, indicative of monolayer graphene. (b) Complete graphene film but mixing with second-layer flakes. The height between graphene film and substrate is 2.6 nm, indicative of few-layer graphene. (c) Raman spectra showing the features of monolayer, bi-layer and few-layer graphene in the synthetic film. (d) Selected area electron diffraction of the graphene film (transferred on to TEM grid) showing the rotational stacking of bilayer graphene. Adapted from reference [50].

graphene domains of, for example, 300 nm in diameter [50]. The graphene film requires seven hours to form. However, there is a drawback in terms of a large amount of secondary flakes as well as cracks forming in the monolayer film (*cf.*, Figure 2.8). The other type of planar graphene is a single crystalline graphene domain (*e.g.*, 10  $\mu\text{m}$  in diameter) [49]. This type of graphene grain holds promise for electric transistor applications, but requires an extremely long growth times (in the region of 72 hours). The graphene growth rate over the  $\text{SiO}_2$  surface is usually low (for example, 60 - 300 nm/hour in diameter) [50], and some suggest

that it involves a vapor-solid-solid mechanism [21, 47]. It has been posited that graphene nucleates over one intermediate SiC phase rather than directly over the oxide surface [231]. In short, the growth mechanisms over the  $\text{SiO}_x$  substrate are yet to become clear.

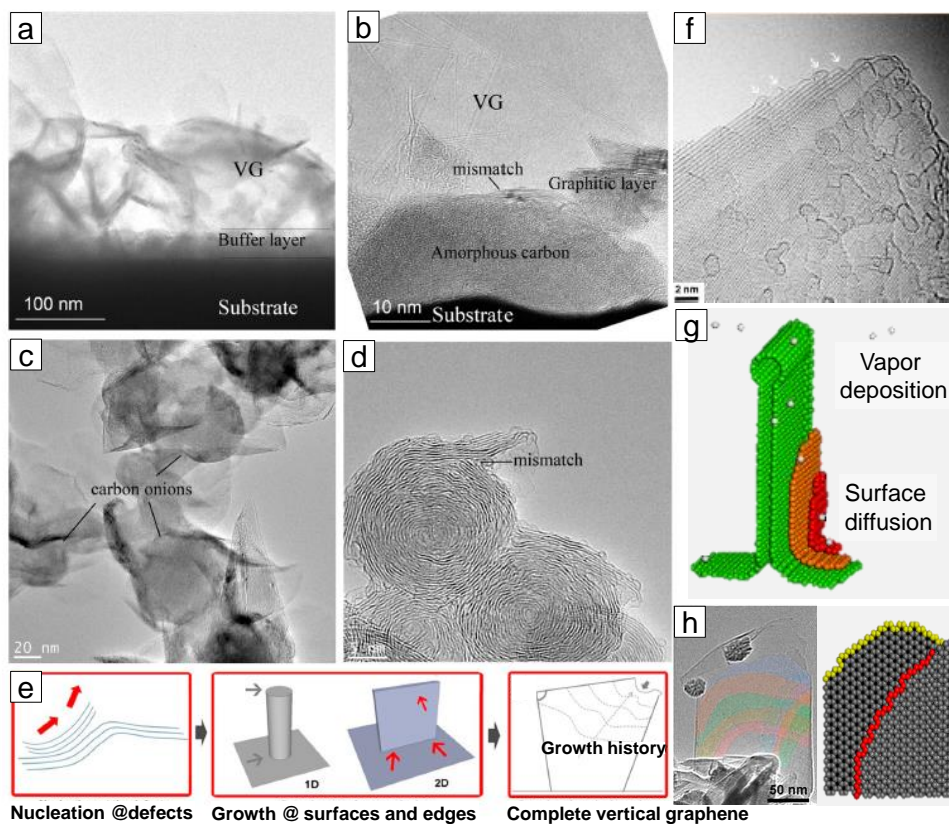


FIGURE 2.9: Vertical graphene growth via plasma-enhanced chemical vapor deposition. (a) TEM overview of vertical graphene, buffer layer, and substrate. (b) High magnification TEM of the bottom of vertical graphene. There is a mismatch in the stacking of graphene supply to the nucleation sites, while the amorphous carbon is the buffer layer. (c) TEM graph for graphitic onions, from which vertical graphene has stemmed and formed. (d) High magnification TEM of the mismatch site on the edge of the graphitic onion. (e) Schematic of growth mechanism, including nucleation on defects and growth along surfaces and edges. (f) HRTEM of the seamlessly folded edge at a graphene enclosure. (g) Atomic configuration of graphene as an enclosure. (h) TEM observation (with fake color) and atomic model of a vertical graphene sheet with curved terraces. Adapted with permission from reference [30].

### 2.4.8 Reaction mechanisms of free-standing graphene

Free-standing vertical graphene can be synthesized in a plasma CVD over non-metal substrates such as silicon [232] and quartz glass [166] or without a substrate [233, 234]. As is shown in [Figure 2.9](#), initially, a buffer layer (such as amorphous carbon) forms over the substrate [30]. Graphene then nucleates at defective sites, and as a consequence, carbon atoms diffuse on the graphene surface and elongate into a vertical (wall-shaped) graphene.

## 2.5 Summary

This chapter covers two main aspects of graphene synthesis: the fundamentals and properties of graphene, and the related aspects of graphene CVD growth and transfer.

The first section refers to the introduction of carbon allotropes, the  $sp^2$  hybridization of carbon into graphene, and the types of graphene. Certain properties of graphene were discussed in detail, namely crystal structure, electrical transport, and optical transmittance. Other properties were covered in brief, such as mechanical, thermal, and chemical properties.

The second section, on CVD, covers the basic concept of a CVD reaction: carbon feedback, choices of catalysts/substrates, pretreatment of substrates, plasma/thermal CVD, and the transfer protocols. The discussion then switches to a detailed review of the thermodynamics and kinetics of CVD growth of graphene.

Last, but not least, there is a detailed review of the growth mechanisms over various substrates (such as Cu, Ni, Si/SiO<sub>x</sub>, and other non-metals). Numerous exciting results have emerged from the study of graphene growth over different substrates. However, a full understanding of the graphene growth mechanisms on

both Cu and Si/SiO<sub>x</sub> substrates is yet to be reached.

## 2.6 Scope of the thesis

The aim of this thesis was to fabricate a large area homogeneous high quality graphene film via the CVD method. Growth mechanisms on Cu and Si/SiO<sub>x</sub> substrates are as yet not well understood and it was therefore necessary to tackle several important problems relating to CVD growth of graphene. Thus, the scope of the thesis may be stated as follows:

- Tracking the origin of the secondary layer flakes in graphene full film over Cu (*i.e.*, to investigate at which stage the secondary layer flakes form: nucleation stage, growth stage, or termination/cessation stage).
- Fabrication of large-area strict monolayer graphene full film (without any second layer flakes) over a Cu substrate.
- Synthesis of graphene with adsorbed organic molecules over Cu (*e.g.*, to study the thermodynamics and extract the activation energy).
- Formation of large-area homogeneous monolayer graphene growth over Si/SiO<sub>x</sub>.

# Chapter 3

## Experimental setup and characterization techniques

This chapter introduces the experimental protocols and characterization techniques used. The first section discusses synthesis of graphene. The synthesis method of chemical vapor deposition (CVD) is described in detail. Further, the main techniques of characterization are briefly introduced, including optical microscopy, scanning and transmission electron microscopy, atomic force microscopy, Raman spectroscopy, ultraviolet-visible spectrophotometry, and electrical transport measurements.

### 3.1 Experimental setup of chemical vapor deposition

For this study, a thermal CVD technique was used for graphene synthesis over a solid substrate (*i.e.*, metallic Cu foil and dielectric Si/SiO<sub>x</sub>).

CVD protocols are carried out on a furnace reactor. A horizontal CVD setup

is employed for this work, which is schematically depicted in Figure 3.1. The parts of the CVD reactor are sequentially described as follows: The reaction chamber is made from a long tube. For graphene synthesis over Cu, the tube material is fused quartz, because graphene synthesis over a Cu substrate requires temperatures up to 1025 °C. The inner diameter of the quartz reactor tube is 2.2 cm and the length of the heating zone of the reactor is 10 cm for the set temperature. However, the tube material for synthesis over Si/SiO<sub>x</sub> is sintered alumina (also termed as corundum), which can tolerate an even higher temperature, namely 1185 °C. The inner diameter of the corundum reactor tube is 4 cm and the length of the heating zone of the reactor is 20 cm for the set temperature. A gas inlet is connected to one side of the tube and an outlet to the other side. The gas feedstock includes methane (CH<sub>4</sub>), hydrogen (H<sub>2</sub>), and argon (Ar). The tube passes through a cylindrical furnace. The substrate is located on the center zone where the temperature gradient is uniform.

The CVD experiments were conducted for nominal times. When the CVD

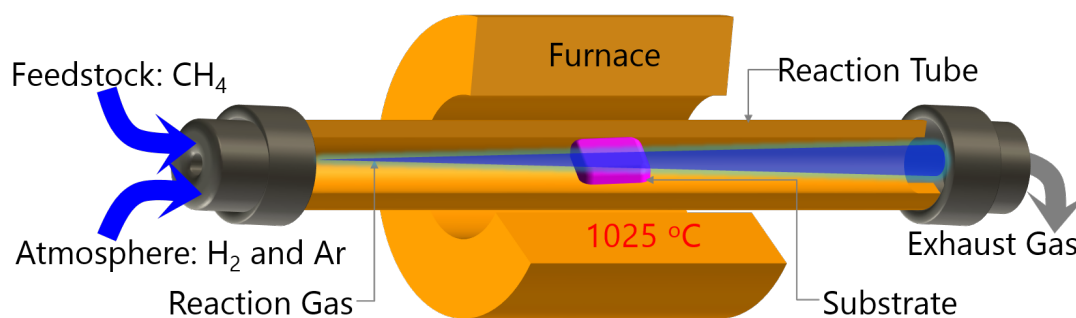


FIGURE 3.1: A horizontal CVD furnace system. A schematic is shown of the CVD reactor for the synthesis of graphene over a substrate. The important materials and components are labeled.

reaction was completed, the gas and the oven were switched off. The substrate temperature decreased to room temperature, naturally. Parameters such as substrate temperature, reaction time, gas flow rate, and gas pressure were each



optimized in these studies.

## 3.2 Optical microscopy

With an optical microscope, the object is illuminated with white light from the condenser, and the reflected light forms a magnified view of the specimen through an objective lens. Light passing through the objective lens can be diverted by a beam splitter either into an eyepiece for binocular observation or through a projection lens into a CCD camera. An optical microscope is a well-established tool that can be used to investigate a large area of graphene film over a substrate, due to the obvious contrast between the two. Graphene can be distinguished from a Si/SiO<sub>2</sub> substrate because interference occurs between the reflection path of SiO<sub>2</sub>-to-Si and air-to-Si/SiO<sub>2</sub> interfaces. With their interface thickness changing, the interfering paths undergo a relative phase shift, which finally contributes to a color (wavelength) shift for eye recognition. When the SiO<sub>2</sub> film thickness is 300 nm, the graphene over SiO<sub>2</sub> allows a direct observation as well as layer determination [1, 235].

In this study, optical microscopy is used for rapid observation of large-area continuity (*i.e.*, to determine whether there is a crack) and homogeneity (*i.e.*, to determine whether the color of the graphene is the same all over) before using more precise but time-consuming microscopy, such as scanning or transmission electron microscopy and atomic force microscopy. The model is a Zeiss Axio microscope equipped with a digital camera and a power-tunable light source.

### 3.3 Scanning electron microscopy

Scanning electron microscopy (SEM) is frequently employed in micro-scale material characterization due to its ease of operation, large depth of focus, wide range of magnification, and good image resolution. Briefly, inside an SEM, electrons are emitted from an electron gun and accelerated by cascaded anodes. The electron beam is converged by electromagnetic condenser lenses to a specific spot. When passing through scanning coils, the electron beam interacts with the sample surface and the beam is deflected in the x and y axes in a raster fashion.

The interaction of an electron beam with the sample surface generates secondary electrons (SE), which are commonly used for imaging the surface morphology of a specimen. The electron detector can collect the SE signal and the program translates into greyscale images after a full raster scan. The electron beam-sample interaction can also generate back-scattered electrons [236]. The BSE are emitted by elastic scattering of electrons at the sample surface. The BSE signal is dependent on the atomic number of the elements that constitute the specimen. Thereafter, it supplies a contrast between two regions that are enriched in different elements. Characteristic X-rays are produced from the specimen when the electron from the inner shell of an atom is removed by excitation by an electron from the primary electron beam. These X-rays are used to determine the type of elements that constitute the sample. [Figure 3.2](#) shows a sketch of the electrons and X-rays that are generated from the electron-beam sample interaction and their related excitation volumes.

The spatial resolution of SEM is dependent on the spot size of an electron probe and the probe's interaction volume close to the specimen surface. The point resolution of sub-nm can be reached on state-of-the-art SEM.

In this work, SEM is employed to determine the grain size and the layer number of the large-area graphene film and of individual graphene flakes when

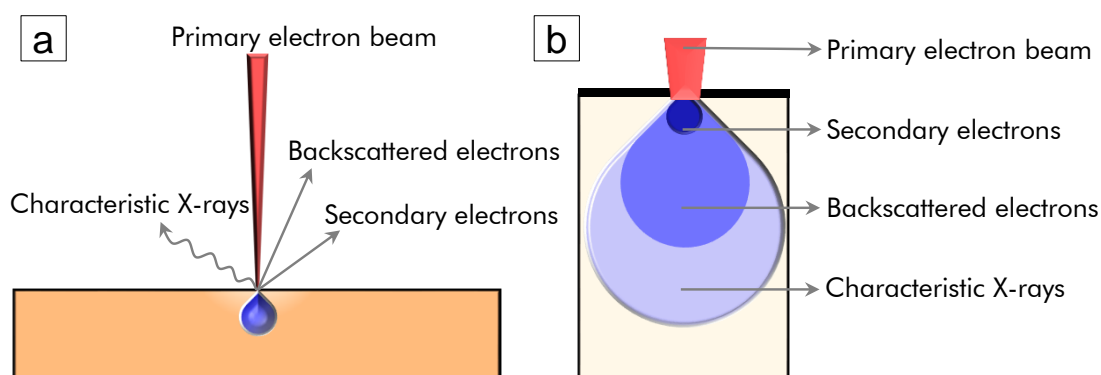


FIGURE 3.2: Schematic of useful signals for sample examination in SEM. (a) The electrons or X-rays generated from electron-specimen interaction. (b) The excitation volume for the generation of each signal.

combined with other microscopy, such as atomic force microscopy (AFM) and transmission electron microscopy (TEM). The SEM images presented in this thesis are collected from a Zeiss Ultra Plus and a FEI quanta 250 microscope with field emission gun. Both microscopes are operated with secondary electron mode at an accelerating voltage of 5 kV.

### 3.4 Atomic force microscopy

AFM illustrates the topography of the sample surface at the nanoscale. Briefly, AFM measures the forces between a sharp tip (usually  $\text{Si}_3\text{N}_4$  or Si) and the sample surface. The tip resides beneath a cantilever from which a laser beam is reflected and collected on a photodiode detector. Through the displacement of the laser beam by cantilever deflection, one can monitor the z deflection between tip and specimen. The AFM in a square region can be constructed in a scanning raster fashion. Tapping mode AFM is predominantly used in imaging graphene

with the cantilever oscillation at its resonant frequency. The cantilever oscillates when the distance between tip and sample ranges is between 0.5 and 2 nm. A piezoelectric system mounted within the tip drives the oscillation. During collection of an image, the oscillation amplitude is controlled at a constant to maintain a tip-specimen interaction. Tapping mode AFM is more suitable for high-resolution imaging when specimens are loosely held on a substrate and so is rarely used in this study.

Within this work AFM is used, in particular, to investigate the number of graphene layers on a Si/SiO<sub>x</sub> support, the shape of flakes, and the level of wrinkle. The AFM images presented in this thesis are collected on an Asylum Research Cypher instrument. The image resolution is 1024 *pixels* by 1024 *pixels* with a line scan rate of 0.8 - 1.4 *Hz*.

### **3.5 Transmission electron microscopy**

The transmission electron microscope is one of the highest resolution characterization tools available for the study of graphene. This section briefly introduces the working principals of the TEM: spherical aberration correction, selected area electron diffraction, dark field imaging, high resolution imaging and fast Fourier transformation.

TEM makes use of the wave nature of electrons and can be used to analyze nanomaterials at the atomic level. Briefly, inside the TEM, electrons are generated by a thermionic or field emission gun and injected into the column with accelerating voltages between 80 kV and 300 kV. The electron beam passes through a double or triple electromagnetic condenser lens before reaching the specimen. The electrons are scattered after the transmission by the electrostatic

potentials of atoms within the specimen. After passing through the object/specimen, the electron beam is focused by the objective lens in an intermediate image plane. The following projector lens projects the image (or diffraction pattern) onto a fluorescent screen. The image (or diffraction pattern) can be collected by the CCD camera and then digitally saved. The simplified TEM schematic is illustrated in [Figure 3.3](#).

With TEM measurement, the sample experiences significant damage, such as

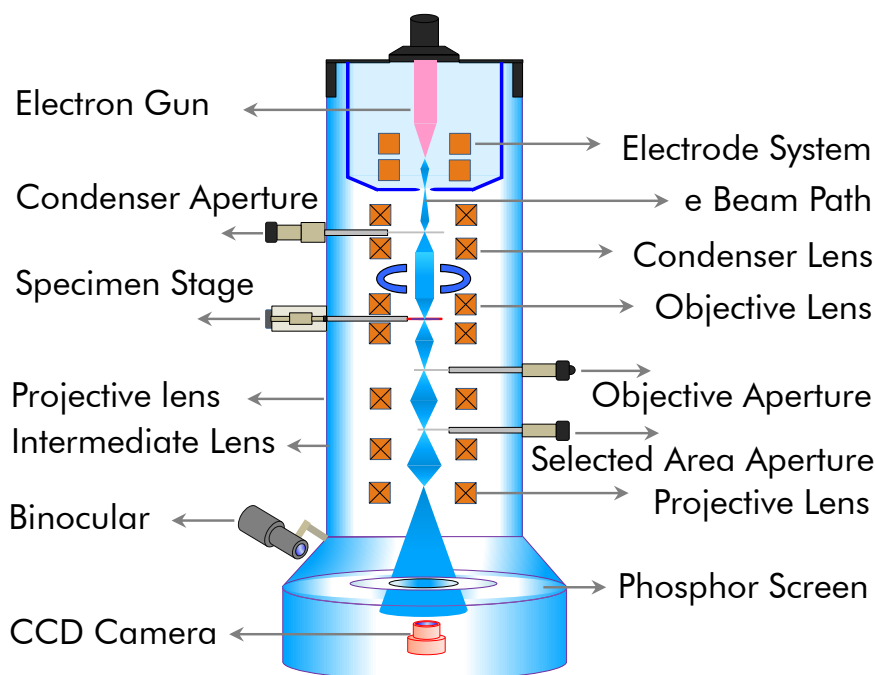


FIGURE 3.3: A schematic of transmission electron microscope with a typical configuration such as various apertures and lenses.

radiolysis, knock-on damage, and electron-stimulated desorption due to electron-specimen interaction. Pristine crystalline graphene is sensitive to knock-on damage at voltages above 86kV [237]. Thus, it requires an acceleration voltage of 80 kV for non-destructive electron beam exposure. At low-acceleration voltage, such as 80 kV, it is hard to obtain atomic resolution imaging in graphene so that a spherical aberration (Cs) corrector is required to overcome the obstacle. With this in place graphene can usually be examined with atomic resolution, not only for imaging, but also for other analytical techniques, such as electron

energy loss spectroscopy and energy dispersion X-ray spectroscopy.

The TEM image at low magnification can provide information on whether or not the transfer of graphene succeeds. The graphene is transferred onto standard Cu grids coated with lacey carbon or holey carbon film.

### 3.5.1 Selected area electron diffraction

In addition to imaging, TEM plays an important role relating to electron diffraction in graphene research. Electron diffraction is intensively used to differentiate monolayer graphene from AB Bernal stacked bilayer graphene. It can also be used to study the stacking order, stacking rotation, and planar sheet roughness. When inserting a selected-area aperture, one can obtain selected-area electron diffraction (SAED) [238] rather than a diffraction pattern for a much larger region. The SAED allows precise determination of structural information in the sub-200 nm region, whereas electron diffraction covers the micro-meter region. The SAED of graphene can confirm the monolayer feature in the hundred-nanometer region.

In the reciprocal space for monolayer graphene lattice, there is only the zero-order Laue zone, so the intensity of diffraction peaks does not vary much with the tuning-in incidence angle of an electron beam. However, with different incident angles, bilayer graphene exhibits changes in total diffraction intensity. Therefore, the monotonic change in diffraction intensity observed with changing the tilt angle is reliable for determining the presence of monolayer graphene [239, 240]. The intensity of the electron diffraction pattern from  $\{10-10\}$  and  $\{11-20\}$  planes is useful to determine the layer number [1, 241]. If  $I_{\{11-20\}}/I_{\{10-10\}}$  is  $>1$ , it is determined as Bernal stacked bilayer graphene, as shown in [Figure 3.4cd](#), and if the ratio is  $<1$ , it is reported as monolayer graphene, as shown in [Figure 3.4ab](#).

In Figure 3.4e, a top layer graphene sheet rotates  $28^\circ$  with respect to the bottom layer graphene and thereby exhibits rotational stacking. The corresponding SAED shows two sets of six-fold reflection symmetry. That is, the SAED in Figure 3.4b duplicates itself, but the new set of SAED follows with a rotational angle of  $28^\circ$ . This overlapping of two sets of diffraction patterns is shown in Figure 3.4f. The rotational angle between stacking layers is illustrated with two arrows in dark orange and light blue.

In some samples, two monolayer graphene grains with a relative rotational

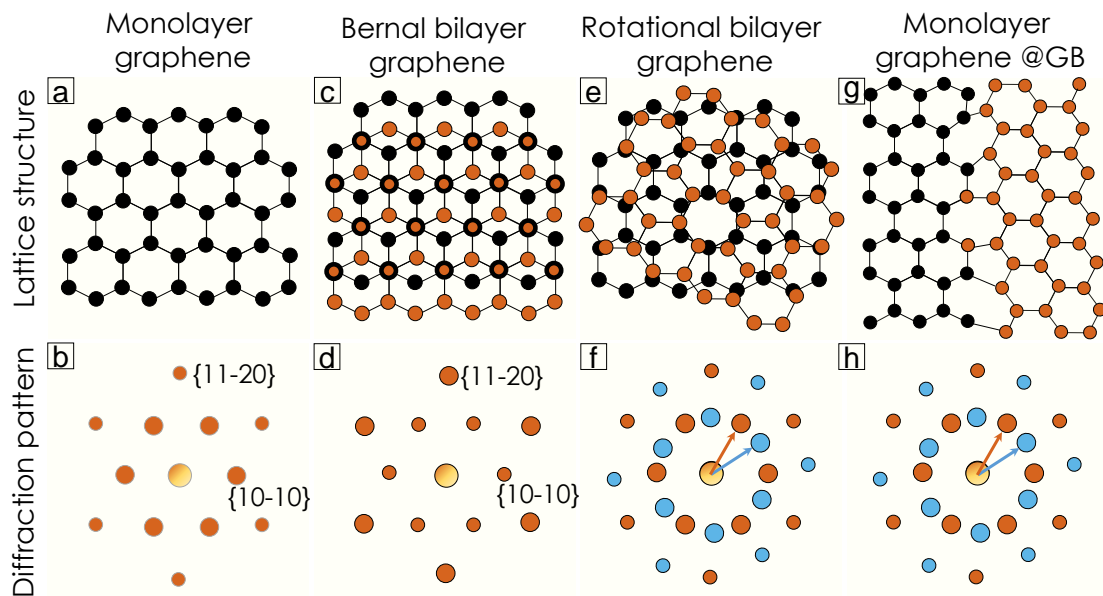


FIGURE 3.4: Schematic of lattice structures of graphene and their corresponding diffraction pattern. (a) Monolayer graphene has one crystalline domain in the lattice structure. (b) In the diffraction pattern sketch, the large spots represent higher intensity in the diffraction peak than the small ones. The diffraction intensity for  $\{10-10\}$  is stronger than that in  $\{11-20\}$ . (c) AB Bernal bilayer graphene has two layers (yellow and black). (d) The diffraction peak  $\{10-10\}$  is weaker than that in  $\{10-20\}$ . (e) Rotational stacking bilayer graphene has a rotational angle of  $28^\circ$  between two graphene sheets. (f) The two sets of diffraction patterns have corresponding rotations. The rotational angle is formed by the two arrows (dark orange and light blue). (g) Two graphene grains merge and form a grain boundary (GB). The relative rotation angle between two grains is  $28^\circ$ . (h) The diffraction pattern is analogous to that of rotational bilayer graphene. However, the high-resolution TEM is straightforward to differentiate the rotational bilayer graphene from two-grain monolayer graphene by Moiré pattern (exhibiting in rotational bilayer graphene).

angle form a grain boundary, as shown in Figure 3.4g. It is remarkable that

SAED exhibits two rotational sets of six reflex spots in [Figure 3.4h](#), which can be easily mixed up with that of rotational stacking bilayer graphene. In this case, one can use HRTEM to observe the Moiré pattern to identify rotational bilayer graphene, because no Moiré pattern is reported in monolayer graphene. Another method involves the use of dark field TEM [242] to distinguish these two monolayer domains. In DF-TEM, monolayer graphene at grain boundary (GB) is illuminated on one crystal domain but darkened on another crystal grain. However, rotational stacking bilayer graphene will be illuminated on the whole tested region when doing DF-TEM and selecting each set of diffraction patterns. Thus, one can also classify the specimen with the DF TEM approach.

### 3.5.2 Dark field transmission electron microscopy

Dark field TEM can determine the grain size and relative rotational angle between two adjacent graphene grains. In conventional TEM, the contrast aperture (*e.g.*, objective aperture) has been adjusted concentrically to let the optical axis pass through, (*i.e.*, only slightly scattered electrons pass the aperture). When shifting the contrast aperture away from the axis point, the strongly scattered electrons can pass the aperture, whereas the slightly scattered electrons cannot. Therefore, an inverse contrast image is captured, which is known as dark field imaging. When inserting the smallest objective aperture, individual reflections can be selected within a diffraction pattern. In the following DF TEM, these grains exhibit bright contrast, which corresponds to the selected reflex [243]. Furthermore, one can select another reflection set to light up the next domain area. When completing all the rotational sets of diffraction patterns, grain mapping can be carried out in order to obtain the relative rotation and size information.

With HR TEM of the rotation stacking graphene, one can get a fast Fourier



transform (FFT) of the image. In small region FFT, one can obtain one or more sets of six-fold reflex similar to [Figure 3.4bh](#), in which one can extract the rotation angle with the drawing line (ROI tools) in Digital Micrograph software. Furthermore, FFT is useful for performing grain mapping for rotational angle and size information [123], which is analogous to the DF TEM approach.

### 3.6 Raman spectroscopy

Raman spectroscopy is a commonly used tool for characterizing graphene because it gives information regarding bonding in molecular nanostructures. In Raman spectroscopy the observed spectrum is mostly generated by inelastic scattering of light within molecules. It is sensitive to the specific vibrational mode of molecules after excitation with a laser. Raman spectroscopy has been extensively applied as a non-destructive approach to determining the electronic and structural characteristics of graphene [1, 8, 244, 245].

A typical Raman spectrum of graphene is shown in [Figure 3.5](#). Raman spectroscopy equipped with optical microscopy can facilitate the spectral mapping in a rectangular region of the specimen.

The Raman spectrum of graphene has three major bands. The G-band, located at approximately  $1580\text{ cm}^{-1}$ , corresponds to in-plane stretching vibrations of the  $sp^2$  carbon atoms. The D band, residing at approximately  $1350\text{ cm}^{-1}$ , is attributed to a double resonant process which involves a scattering by a defect in the graphene lattice. There is only one phonon involving in the D band scattering process. The strongest 2D band (also known as G' band) at  $2700\text{ cm}^{-1}$  is induced by a second-order process that originates from the in-plane breathing-like mode the carbon hexagonal rings [1, 246]. The appearance of the 2D and D bands results from the double resonance Raman scattering process

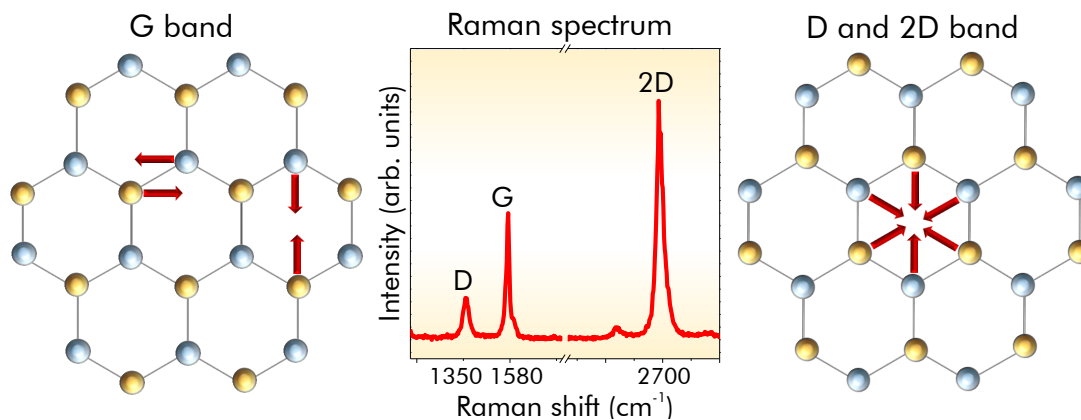


FIGURE 3.5: A typical Raman spectrum of large-area graphene membrane transferred onto Si/SiO<sub>x</sub> substrate. There are three characteristic peaks: D band at 1350 cm<sup>-1</sup>, G band at 1580 cm<sup>-1</sup> and 2D band at 2700 cm<sup>-1</sup>.

[246]. Because two phonons is involved for 2D band, the energy shift for the 2D band is twice of the D band, which derives its name.

Monolayer graphene exhibits a sharp and symmetric 2D band. When increasing layer number (in the case of AB Bernal stacking, such as in the mechanically exfoliated graphene sample), the 2D band becomes broadened and shows blue shifts [247], while the G/2D intensity ratio gets increasingly higher. However, for rotational stacking double-layer graphene, the 2D band gets narrowed and the 2D/G intensity ratio becomes higher than that for monolayer graphene and Bernal bilayer graphene [248].

In this work, the graphene samples are analyzed with Raman spectroscopy after each CVD to determine whether or not graphene has been synthesized. It can also supply information about rotational stacking in bi-layer graphene when complemented with TEM analysis. For Raman spectroscopy analysis, the graphene is first transferred on to a Si/SiO<sub>x</sub> substrate. The analyses are collected on a WiTec Alpha300 R and a Renishaw inVia Raman spectrometer. Both spectrometers are equipped with a laser (514 nm excitation) and an optical microscope. Raman spectroscopy is used to determine the layer number of graphene, the graphene quality (*i.e.*, the presence of defective peaks), and the

homogeneity of large area graphene (Raman spectral mapping).

### 3.7 Ultraviolet-Visible spectrophotometry

Ultraviolet-visible (UV-Vis) spectrophotometry is typically used in determining the optical transmittance of a thin film on a transparent support (*e.g.*, fused quartz). The CVD-grown graphene film is first transferred onto a transparent fused-quartz substrate. In this study, the optical transmittance of graphene film is carried out using an Analytik Specord 250 instrument. The spectrophotometry is equipped with a double-beam within which the light splits into two beams prior to reaching the sample. One beam passing through the pristine quartz support is used as the reference; the other passing through quartz/graphene is used as a sample. The transmittance of graphene is defined as the ratio of the two beam intensities, with the beam intensity for pristine quartz set as 100% transmittance.

### 3.8 Electrical transport measurements

Electrical transport measurements allow the determination of carrier mobility of graphene in a field effect transistor (FET). The graphene (directly grown) on Si/SiO<sub>x</sub> is fabricated in to an FET device. First, a graphene channel was prepared with depositing PMMA electron-resist, e-beam lithography and oxygen plasma cleaning. The graphene channel was formed with e-beam exposure in a Hitachi S400 SEM with a Raith direct writer. Next, the pads and tips for source and drain electrodes were fabricated with e-beam lithography where

Ti(50 nm)/Au(200 nm) were formed subsequently with e-beam deposition. Finally, the graphene device was thoroughly cleaned with acetone after a lift-off step.

The electrical transport measurement of the graphene FET devices in this study was conducted using a Keithley 2612 source meter unit (SMU). The p-doped Si is used as a global back gate electrode. The two Au electrodes on the transferred graphene are used as source and drain electrodes.

With tuning gate voltage from negative bias to positive bias, one can obtain the transfer curve of drain current ( $I_{DS}$ ) versus gate voltage ( $V_G$ ). With linear fitting of drain current against gate voltage, one can obtain the slope ( $\frac{\partial I_{DS}}{\partial V_G}$ ) and thereafter obtain the carrier mobility by multiplying with the constant factor ( $\frac{L}{WC_{OX}V_{DS}}$ ). The graphene channel has a length ( $L$ ) of 2.5  $\mu\text{m}$  and width ( $W$ ) of 15  $\mu\text{m}$ . The dielectric  $\text{SiO}_x$  has a constant electric capacity ( $C_{OX}$ ). Therefore, the formula to derive electrical mobility [54] is  $\mu = \frac{L}{WC_{OX}V_{DS}} \cdot \frac{\partial I_{DS}}{\partial V_G}$ . Moreover, the ON/OFF ratio for drain-source current is defined as  $r = \frac{I_{DS(max)}}{I_{DS(min)}}$ .

## Chapter 4

# CVD growth of graphene on oxidized Cu substrates

Chemical vapor deposition is one of the most common methods of producing graphene. This is attributed to its capability for synthesizing large areas of graphene, and its potential to be scaled up for mass production. In terms of fabrication of large areas of graphene monolayer film, Cu is the most widely explored substrate, because its low carbon solubility enables the formation of a homogenous single-layer graphene sheet. However, the graphene described in the recent literatures is not purely monolayer graphene, but a mixture of monolayer and second-layer flakes. Therefore, the focus of this chapter is on fabricating the production of pure monolayer graphene, *viz.*, on preventing the emergence of second layer flakes.

## 4.1 Motivation

Applications in electrical transistors require large area, good quality, and homogeneous graphene films [4]. Due to these requirements, Cu is more favored than other substrates (*e.g.*, Ni) because the Cu substrate facilitates the growth of predominantly monolayer graphene. Even though uniform graphene synthesis is shown to be easier on a Cu substrate, there are still problems which need to be tackled.

Most methods of graphene synthesis on Cu foils employ pretreatments to suppress organic contaminants [117, 249], tune the surface oxidation level [114, 250], and flatten the surface with polishing [119, 121]. Prior to CVD, the Cu foil is annealed in an H<sub>2</sub> atmosphere so as to reduce any oxide. Recently, it has been shown that surface oxidation can enlarge domain size via suppressive control of the nucleation density [114]. Mechanical and chemical polishing are frequently implemented to decrease the density of graphene nuclei by suppressing the defect sites through the creation of a smooth Cu surface [120, 121]. Organic solvents such as isopropanol are also commonly applied, for the general cleaning of contaminants on Cu surfaces, by rinsing, soaking and sonication [113]. Also, the potential of harsh chemicals (*e.g.*, nitric acid) has been explored; these chemicals may be used to remove the surface layers and expose fresh Cu [115, 249].

In this chapter, the effect of solvents, etching and oxidation are compared with regard to their potential for surface contaminant removal. The results show that solvents have limited effect. Whereas oxidation of Cu foil followed with H<sub>2</sub> reduction is shown to be the most efficient of the three pretreatments.

## 4.2 Experimental protocol

Five types of pretreatment methods were investigated in terms of their effect on CVD growth. The protocols for these pretreatment experiments are listed in [Table 4.1](#). The labeling of the experiments (from a to e) in this table will apply throughout the chapter. These pretreatment steps include wiping the Cu foil with scientific tissue soaked in isopropanol (Alfa Aesar, 99.999% purity), polishing the Cu surface with FeCl<sub>3</sub> solution, annealing in air atmosphere and finally annealing in an H<sub>2</sub> atmosphere.

The chemical vapor deposition synthesis were conducted in a horizontal

TABLE 4.1: Outline of five different pre-treatments on Cu foils prior to chemical vapor deposition. The shortest time required to trigger the initial formation of graphene and the type of graphene produced after the synthesis.

No.	IPA Wipe	FeCl <sub>3</sub> Polish	H <sub>2</sub> Anneal	Air Anneal	H <sub>2</sub> Anneal	CVD Growth	Graphene Formation	Graphene Type
a	No	No	Yes	No	No	Yes	Yes, 10 sec	Mixture*
b	Yes	No	Yes	No	No	Yes	Yes, 10 sec	Mixture
c	Yes	Yes	Yes	No	No	Yes	Yes, 10 sec	Mixture
d	Yes	No	Yes	Yes	No	Yes	Yes, 1 min	Flake**
e	Yes	No	Yes	Yes	Yes	Yes	Yes, 1 min	Film***

(\*Mixture means that the graphene monolayer full film is mixed with second layer flakes. \*\*Flake means that individual graphene grains are present. \*\*\*Film means that a monolayer full film of graphene is produced. IPA is short for isopropanol.)

(quartz-) tube furnace which is demonstrated in [Figure 3.1](#) (*cf.* [chapter 3](#)). Prior to loading the Cu substrates, the Cu foil strip (2.5 cm by 1 cm) is mounted inside a one-end sealed quartz test tube, a so called vapor-trapping sample configuration developed in Rümmeli group [125]. After the pretreatments in [Table 4.1](#)abc, the quartz test tube together with the Cu foil are placed at the center of the reaction tube (as center of heating zone). The tube chamber is then evacuated to a low pressure (0.1 mbar) with a mechanical oil pump. [Figure 4.1](#) shows the typical gas condition and temperature for the H<sub>2</sub> annealing process and the

chemical vapor deposition reaction. First  $H_2$  gas with a 16 sccm flow is introduced into the work tube while the temperature of the furnace is simultaneously increased. When the required temperature has been reached (*e.g.*, 1025 °C) and allowed to stabilize for a short time, the  $CH_4$  gas is introduced with a flow of 16 sccm while maintaining the  $H_2$  (total pressure of  $H_2/CH_4$ : 10 mbar). After the CVD reaction is completed, both  $H_2$  and  $CH_4$  gases are switched off and cooling begins.

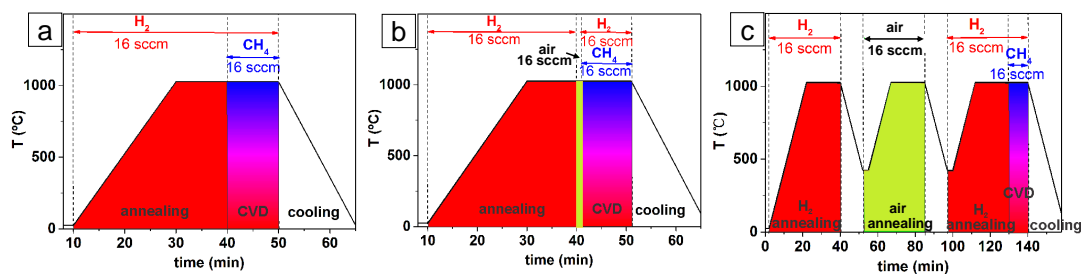


FIGURE 4.1: Temperature profiles and gas conditions for  $H_2$  annealing followed by chemical vapor deposition. Panel (a) represents experiments a, b and c. Panel (b) represents experiment d. And Panel (c) represents experiment e.

Once the graphene has formed on the Cu surface, it is transferred onto a Si/(300nm)  $SiO_x$  wafer or a TEM (lacey carbon film) grid for further characterization. The transfer protocol is depicted previously (*cf.* chapter 2).

### 4.3 Influence of Cu pretreatments on graphene formation

Five types of pretreatment methods, followed by CVD growth, were investigated in this chapter. The protocols for these experiments are listed in Table 4.1 and the labeling for each experiment is established for the entire chapter.

The pretreatment steps include wiping the Cu foil with isopropanol saturated



(lint free) tissue, polishing the Cu surface with  $\text{FeCl}_3$  solution, annealing in an air atmosphere, and eventually annealing in an  $\text{H}_2$  atmosphere.

Scanning electron microscopy graphs (Figure 4.2) show the results of the five different pretreatment experiments, a-e, with four different synthesis times (0.5 min - 10 min). Figure 4.2a, shows the results using Cu foils without any pretreatment. The SEM micrographs indicate full coverage growth of graphene film (later confirmed by Raman spectroscopic mapping images and atomic force microscopy graphs). The black lines are clearly observed as graphene wrinkles (Figure 4.2a), which formed in a cooling step (after CVD) because the thermal coefficients of Cu and graphene are different [1, 215]. In addition, numerous dark islands emerge randomly in the graphene film (Figure 4.2a). Further investigation of these islands (discussed later in relation to AFM and Raman spectroscopy) indicate that they are second layer flakes. From a visual inspection of these SEM images, the size and density of the second layer flakes do not seem to change with increasing growth time.

Figure 4.2b shows similar results when experiment b is carried out. In this experiment the Cu surface is wiped with isopropanol. Again, after  $\text{H}_2$  annealing and CVD reaction, the Cu foil is fully covered with graphene film, even after a short reaction time (0.5 min). However, small graphene patches are still found dotted throughout the sample surface. And the density of flakes increases slightly (shown later in a statistical graph, cf. Figure 4.7), indicating that, being a carbon source, the isopropanol itself may contribute to the flake formation. In this case, no change in the flake size is observed when the growth time is lengthened from 0.5 min - 10 min.

In experiment c, the Cu foil is first cleaned with isopropanol, then polished with  $\text{FeCl}_3$  solution, and then rinsed thoroughly in deionized water and blow dried in  $\text{N}_2$ , prior to undergoing the CVD reaction. As for the other pretreatments, full coverage graphene films are observed for samples produced with the four different growth times, together with the emergence of small second layer

islands randomly dotted on the surface (Figure 4.2c). In addition, the size of the second layer flakes does not change with increasing growth time, and neither does the density.

Experiment d adopts the identical synthesis to experiment b, but with an air oxidation step before the CVD reaction. In this case, no graphene deposit is observed for a 30 sec CVD growth, which is attributed to Cu oxide remaining at the surface (Figure 4.2d). When the reaction time is lengthened to 1 min, individual grains of graphene are observed on the surface and further increase in grain size occurs at a reaction time of 3 min. This is because the gradual reduction of surface oxide leads to more reduced Cu surface, and correspondingly longer growth time (when H<sub>2</sub> remains present).

In experiment e, the pretreatment protocol is analogous to that in experiment d but in this case a H<sub>2</sub> annealing step is carried out (subsequent to air oxidation) before final CVD growth (Table 4.1e). The major advantages of this reduction step are highlighted in Figure 4.2e, in which the foil is deposited with full coverage graphene after a 30 sec CVD reaction.

In this case, no bi-layer flakes emerge on the graphene film. Instead the SEM graphs clearly indicate the presence of pure monolayer graphene film (for 3 min and 10 min growth). Occasionally, very few elongated patches emerge at short reaction times (0.5 min - 1 min). These are attributed to carbon segregation from the grain boundaries of Cu foil [212, 251]. Overall though, homogeneous large area monolayer graphene film is synthesized.

For these experiments atomic force microscopy observations are analogous to SEM analysis. Figure 4.3abc shows full coverage of the substrate with graphene along with typical wrinkle features. Further characterization on the thickness of the graphene film makes it possible to identify whether it is monolayer (*cf.* Figure A.1 in Appendix A), because monolayer graphene has a height of 0.7 nm from substrate [193]. The second layer islands have a height of 0.3 - 0.4 nm above the initial layer of graphene film, which is consistent with a graphitic

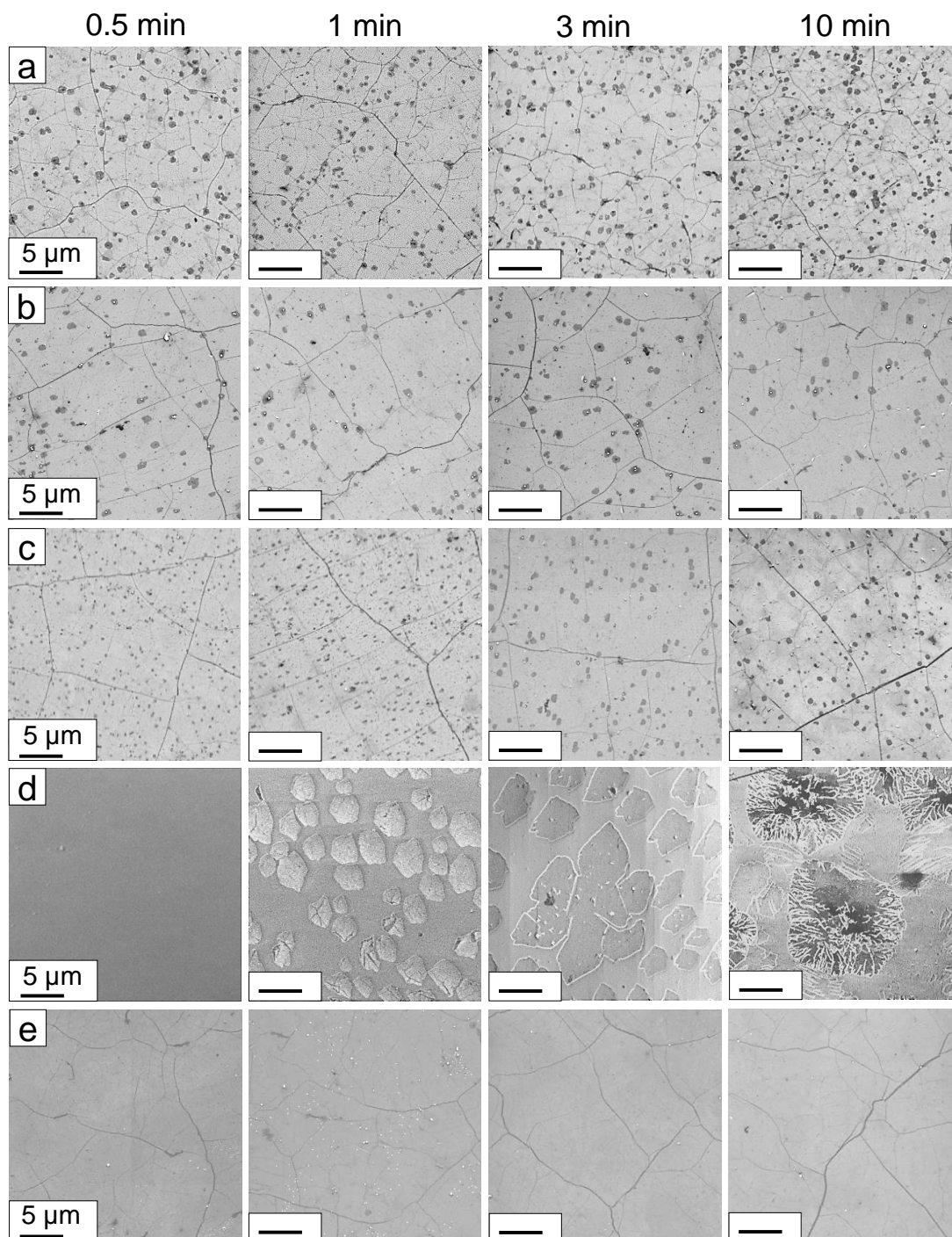


FIGURE 4.2: Scanning electron microscopy graphs for graphene samples synthesized in the pretreatment experiments, a to e, for four different growth times. The labels of pretreatment experiments correspond to the row labels.

sheet-sheet spacing of 0.34 nm [183, 252, 253].

Figure 4.3d indicates no growth of continuous film, instead only individual graphene domains form. The heights of these grains, formed after 1 min and 3 min, range from 0.73 nm to 0.82 nm, which confirms the monolayer feature. However, very little few-layer graphene (layer number  $>3$ ) was observed in the 10 min sample. Again in Figure 4.3e, the height of graphene film is consistent with the monolayer thickness. Experiment e results in clean graphene film formation (*i.e.*, without any additional layer islands).

Raman spectroscopy was employed to confirm the emergence of graphene after the CVD reaction. The Raman spectrum can also supply specific information about the graphene produced, such as the quality and layer number [245, 246, 254, 255]. The three major fingerprints of graphene in the Raman spectrum are the G band at  $1580\text{ cm}^{-1}$  (a double  $E_{2g}$  mode degenerating at zone center), the D band at  $1350\text{ cm}^{-1}$  (a ring breathing mode which is activated near defects in the graphene lattice), and the 2D band at  $2670\text{ cm}^{-1}$  (which is attributed to second order photon scattering). The peak positions, band shapes, and relative intensity ratio of these bands, supply rich information about graphene such as quality and layer number [256–258].

Raman spectra for pretreatment experiments a-c (Figure 4.4), again, confirms that the graphene films have predominantly monolayer features, *e.g.*, 2D/G intensity ratio  $>2$ , full width half maximum (FWHM) of 2D band  $<40\text{ cm}^{-1}$  [123, 125, 160]. The monolayer features remain regardless of CVD growth time (Figure 4.4abc).

Specific investigation into the islands of second layer flakes shows clearly that they are bi-layer or few-layer graphene (Figure 4.4f). Raman spectra for experiment d show no graphene growth in a 0.5 min reaction, predominantly monolayer graphene for 1 min and 3 min growth, and few layer graphene in 10 min growth (Figure 4.4d). In experiment e, monolayer graphene is observed clearly for all growth times (Figure 4.4e).

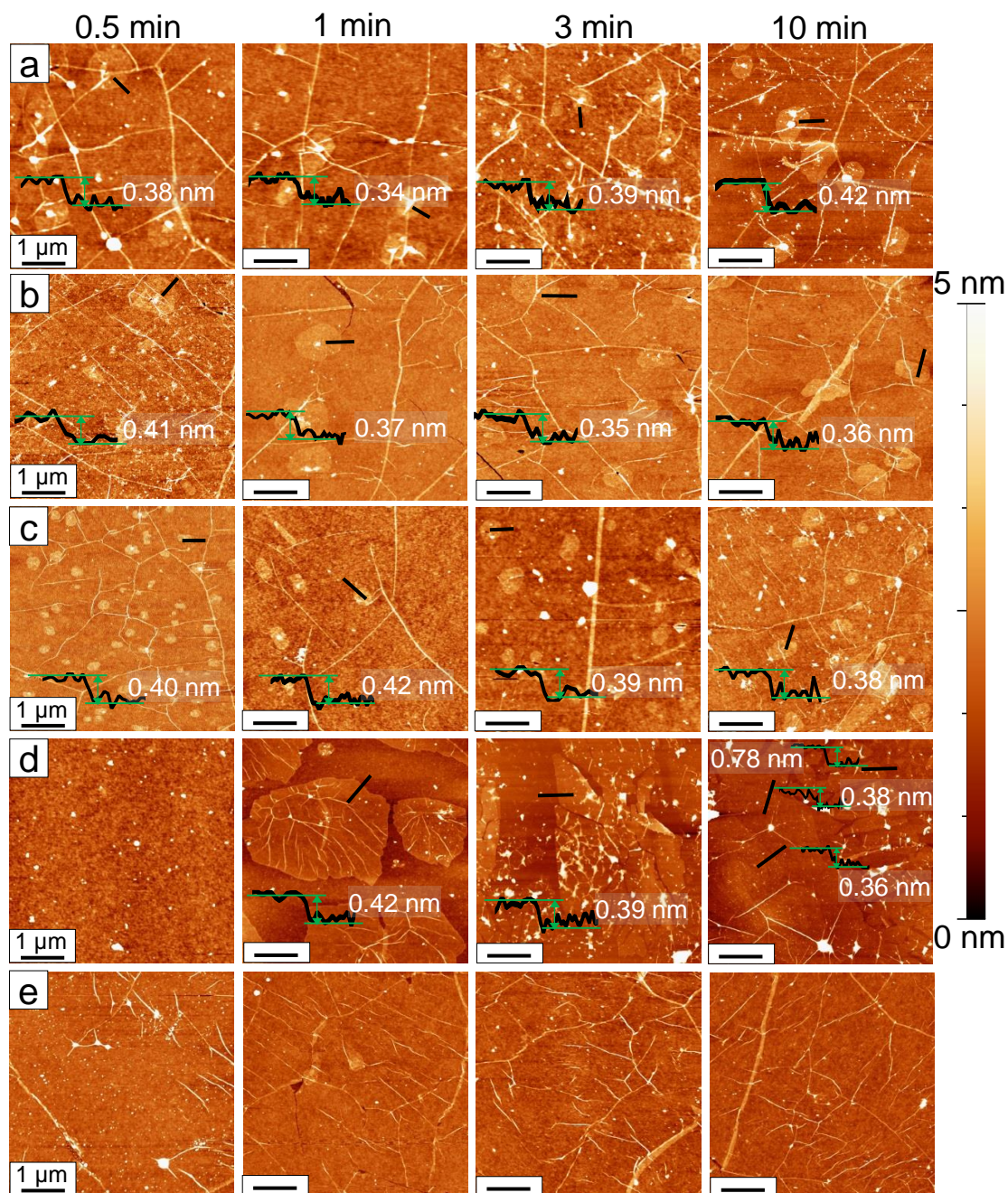


FIGURE 4.3: Atomic force microscopy micrographs of the five experiments, a-e, with different growth times. (a,b,c) The height profiles between second layer flakes and the monolayer graphene full film (as labelled with short black lines) are provided as insets. The height between second layer flake and the monolayer graphene film ranges from 0.3 nm to 0.4 nm. (d,e) The height profiles of individual graphene grains (above the Si/SiO<sub>x</sub> substrate) are present in insets. The typical heights of monolayer graphene are 0.7 - 0.8 nm.

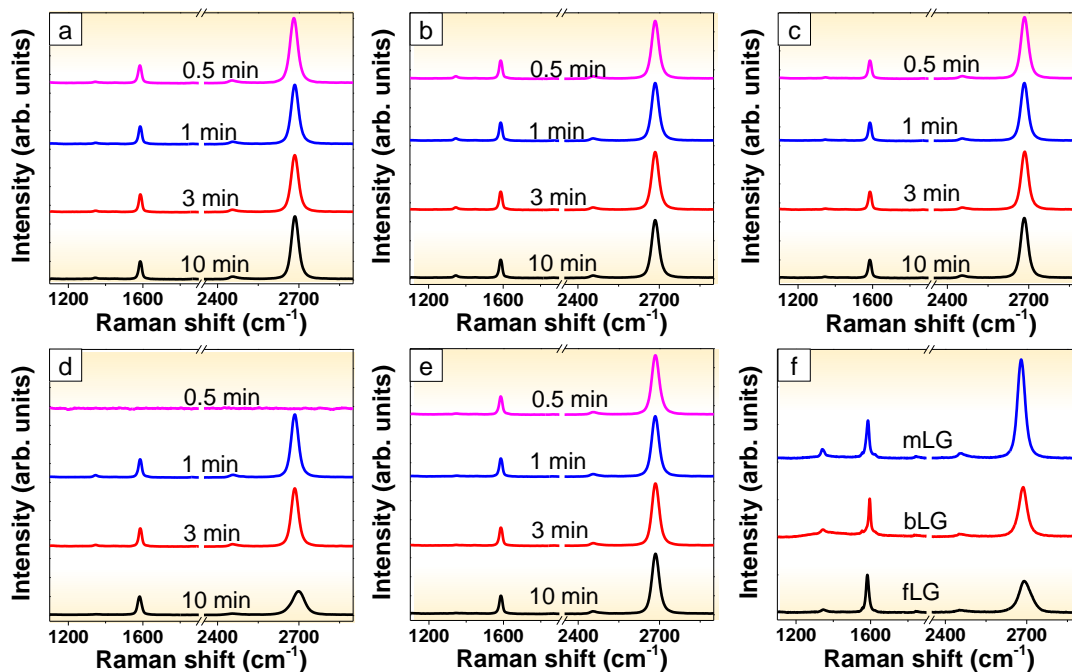


FIGURE 4.4: Raman spectra of the graphene samples. (a-e) Five experiments for four reaction durations. (f) Raman spectra of monolayer, bi-layer and few-layer graphene samples consisting of monolayer film mixing with second layer flakes (*e.g.*, experiment a, b and c).

## 4.4 Influence of Cu oxidation on graphene growth

Raman spectral mapping of 2D band was employed to evaluate the homogeneity of the graphene samples, as shown in Figure 4.5. Again, the monolayer feature (FWHM of 2D band  $<40$  cm<sup>-1</sup>) is predominant in panels a-c but bi-layer islands are also observed, as indicated by the presence of randomly distributed dots (FWHM of 2D band  $>40$  cm<sup>-1</sup>) in the Raman mapping. These Raman mapping images are consistent with previous observations of SEM, AFM and Raman spectra. In particular experiment e produces clean homogeneous monolayer graphene over a large area, *i.e.*, the pretreatments of air oxidation followed by H<sub>2</sub> reduction on Cu completely prevents the formation of second layer flakes.

Experiment e allows clean large scale homogeneous monolayer graphene growth, *e.g.*, a centimeter-size graphene film synthesized and transferred on to Si/SiO<sub>x</sub> substrate for optical imaging (*cf.* Figure A.2 in Appendix A).

Transmission electron microscopy is also employed to evaluate the nature and extent of graphene growth. Figure 4.6a shows a low magnification overview of a typical graphene membrane over a standard lacey carbon TEM grid. The selected area electron diffraction (SAED) pattern (Figure 4.6b) confirms the graphene feature with a six-fold symmetry.

And in Figure 4.6c the intensity ratio of the {11-20} and {10-10} reflexes ( $I_{\{11-20\}}/I_{\{10-10\}} < 1$ ) [237, 259] shows clearly the presence of monolayer graphene. Furthermore, a high resolution TEM image (Figure 4.6d) is employed to check the number of layers. This image confirms that the graphene formed is single layer, which is determined by a layer counting method [260]. This involves counting the layers where holes are formed by electron beam radiation.

With the confirmation of complete graphene film growth, it is necessary to obtain a better understanding of the formation of second layer flakes, *e.g.*, do they form above or beneath the initial monolayer graphene full film which spans the entire foil surface? For experiments a-c, statistical data of the flake size and density are provided in Figure 4.7. No change in the average flake density or size is observed with varying growth times. This indicates that the second layer flakes form in the early stages and do not continue to evolve in the CVD reaction. Hence the initial formation time and the origin of the carbon source are key questions to address. A clue to the answers lies in the fact that no such small islands are observed in experiment d. Neither do they grow in pretreatment experiment e. Both experiments contain a step that involves air oxidation of the Cu foil (which turns into black oxide after the pretreatment). These observations lead to the deduction that organic surface contaminants may be acting as a carbon feedstock during the early stage (*e.g.*, H<sub>2</sub> annealing step) and contributing to the formation of the small flakes.

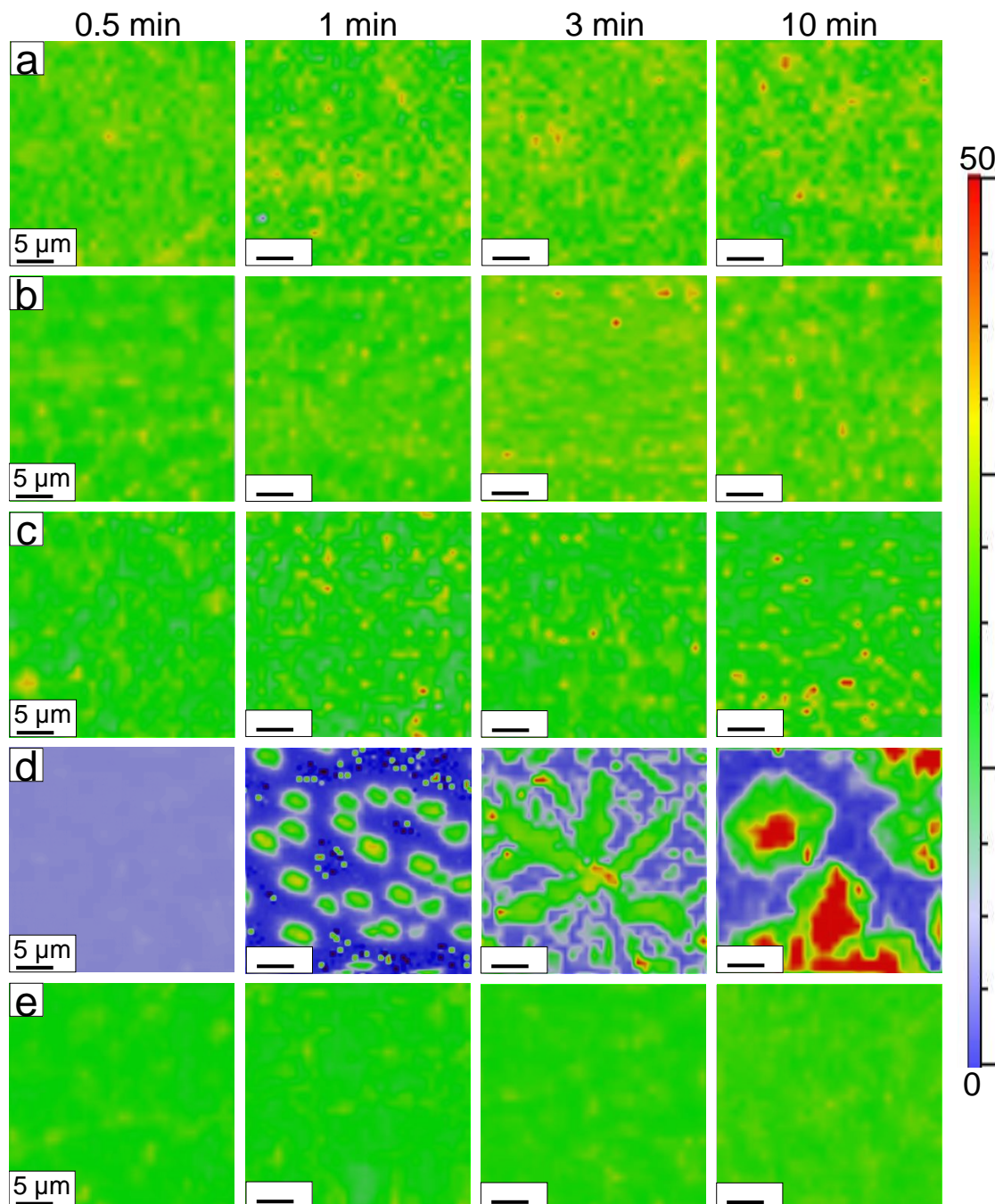


FIGURE 4.5: Raman mapping data of full width at half maximum in 2D band (2D FWHM). The bright green represents monolayer graphene ( $<40 \text{ cm}^{-1}$ ). Deviations in color (from green, yellow to red) correspond to an increase in layer number, except for the first column in experiment d in which no graphene formation is observed. Experiment labels correspond to row labels.



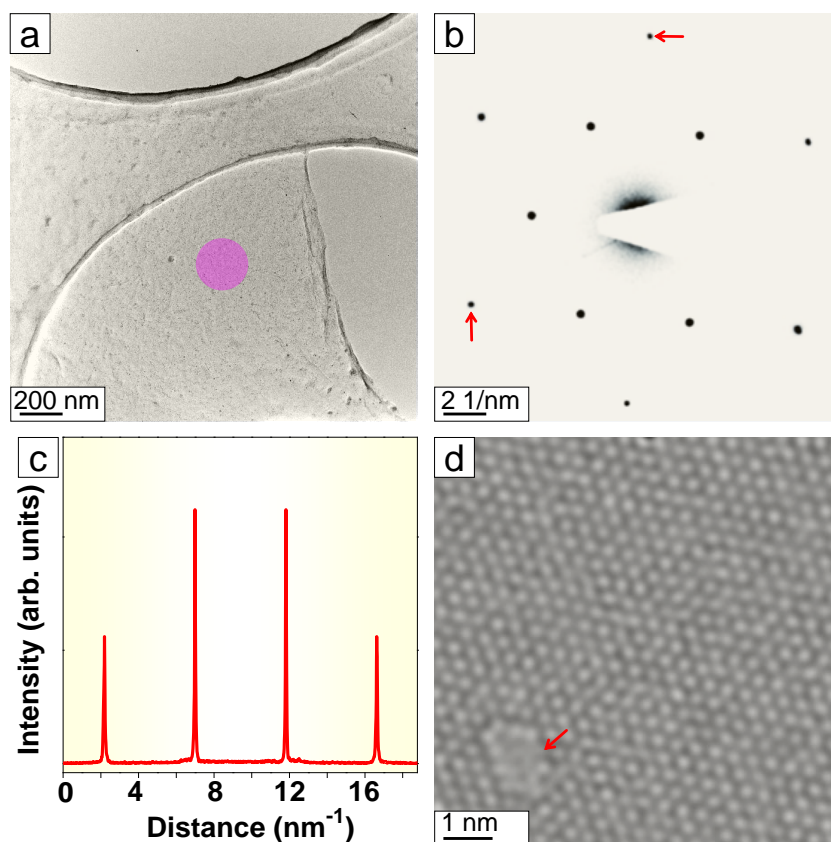


FIGURE 4.6: Transmission electron microscopy images and diffraction pattern from a representative graphene sample in experiment e. (a) Graphene membrane over a large region suspended over a lacey carbon grid. (b) Selected area electron diffraction pattern of the region in a blue mask in panel a. (c) Intensity profile of a line between two white arrows in panel b are across the  $\{11-20\}$  and  $\{10-10\}$  reflexes matching monolayer graphene. (d) High resolution TEM image indicating monolayer graphene by analyzing the layer number when forming a hole (as the white arrow points).

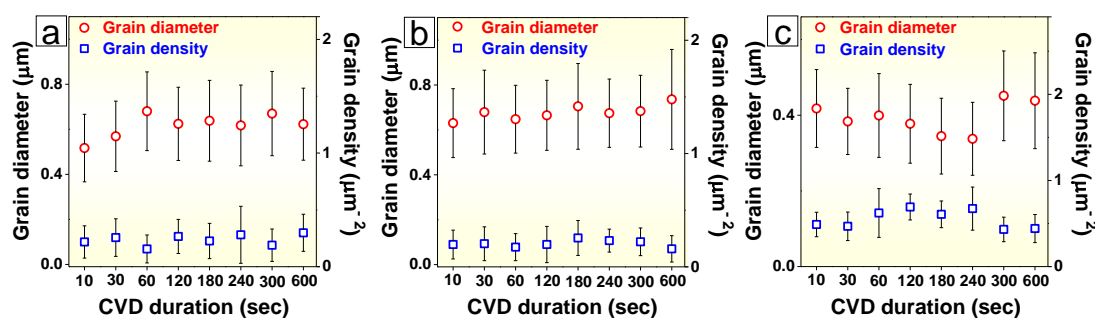


FIGURE 4.7: Statistical data of the size and density of the flakes observed from experiment a, b and c. The flake size is represented by the round markers and the flake density is represented by the square markers. Experiment label matches column label.

## 4.5 Effect of oxidation pretreatment on Cu surface cleaning

Further investigation was conducted on the samples after H<sub>2</sub> annealing (before the CVD reaction, *i.e.*, no CH<sub>4</sub> is introduced). Figure 4.8 shows that small islands (in black contrast) have formed on the Cu surface, and Raman spectroscopy confirms the presence of graphene (*cf.* Figure A.3 in Appendix A).

Analogous results were observed when adopting acetone or ethanol as cleaning solvents (*cf.* Figure A.4 in Appendix A). This shows the limitation of the solvent wiping pretreatment, which either does not remove the organic residues (which consists of a processing grease from the Cu foil supplier), or the solvents themselves, as surface adsorbents, provide the carbon feedstock in the H<sub>2</sub> annealing step.

In Figure 4.8de, no such islands are observed, as would be expected in ex-

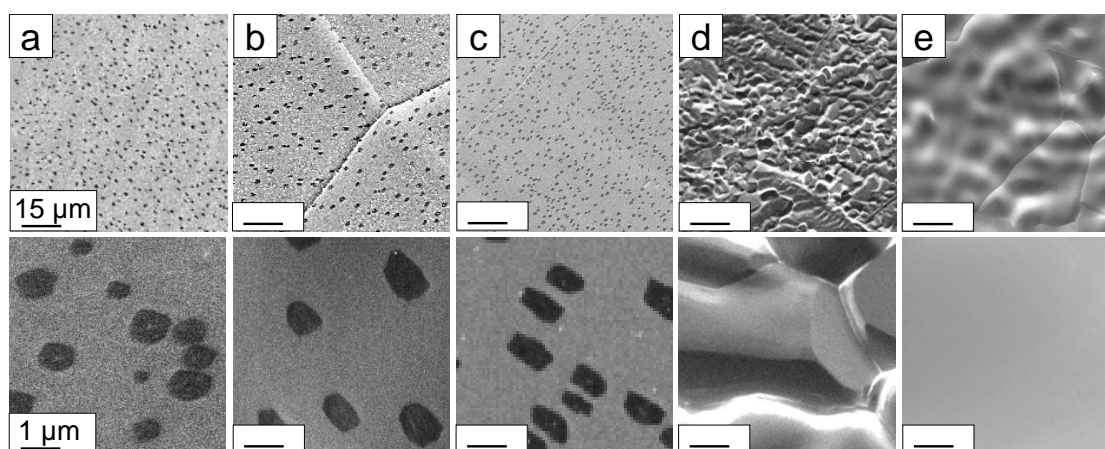


FIGURE 4.8: Scanning electron microscopy images of the samples after H<sub>2</sub> annealing just prior to CVD reaction (*i.e.*, without the introduction of CH<sub>4</sub>). Experiment labels correspond to column labels.

periment d and e. This confirms that the graphene flakes are formed during

the  $H_2$  annealing step (*i.e.*, before the introduction of  $CH_4$  in the process). The large area graphene film forms subsequent to the introduction of  $CH_4$ . This film probably grows on top of the islands (formed in the  $H_2$  annealing step) because these islands do not increase in density or size even for long CVD growth durations.

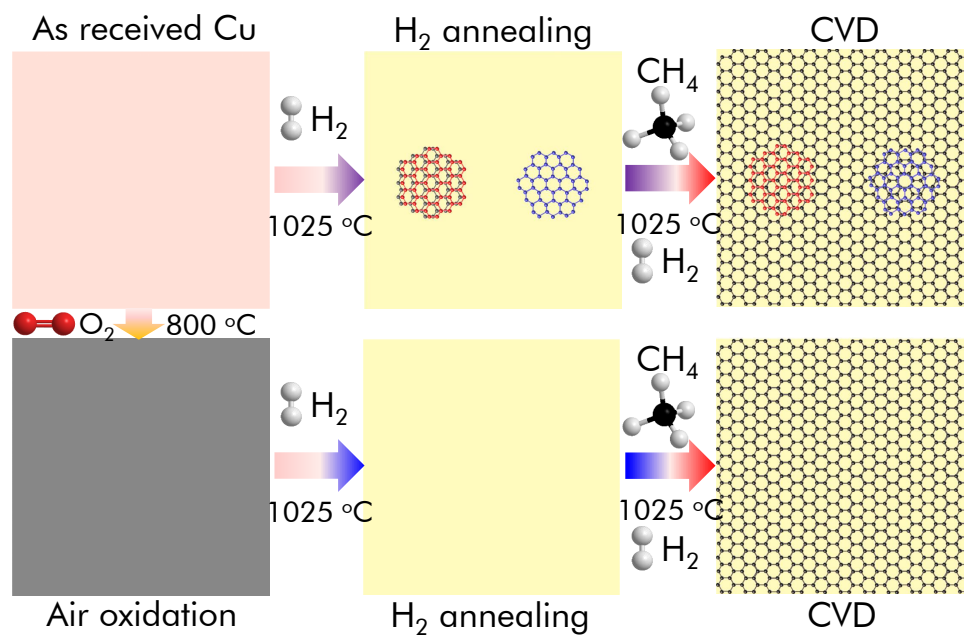


FIGURE 4.9: The mechanism of oxidation pretreatment in the formation of pure monolayer graphene. (Top row) Without oxidation pretreatment, graphene of monolayer film mixed with second layer flakes is produced. (Bottom row) However, with oxidation pretreatment of the Cu foil, pure monolayer graphene is produced.

The mechanism of the air oxidation pretreatment is summarized in [Figure 4.9](#). In brief, the Cu foil without oxidation pretreatment will grow graphene film but with second layer flakes. Whereas with the oxidation pretreatment step the Cu foil supports the formation of large area homogeneous monolayer graphene film without the emergence of second layer islands.

## 4.6 Summary

This chapter covers a comparative study of the five different pretreatments, such as non-pretreatment, solvent wiping, chemical polishing, air annealing as well as air annealing with post hydrogen annealing, to remove organic contaminants on a Cu surface prior to graphene synthesis with CVD. The first three types of pretreatments, which did not involve the air oxidation of Cu foil at high temperature, resulted in the growth of large area single layer graphene film, but with small graphene second layer islands forming randomly on it.

The experimental data shows that these second layer graphene islands form during the H<sub>2</sub> annealing step rather than in the CVD reaction. The carbon feedstock for these flakes is supplied by the surface contaminants on the Cu surface. However, for the experiments involving an air oxidation at 1025 °C, these small flakes were absent in the resultant graphene film.

Thus, air oxidation is considered to thoroughly burn away any surface organic contaminants. Eventually the optimum pretreatment steps (*e.g.*, air oxidation followed by H<sub>2</sub> annealing) allow the formation of large area homogeneous monolayer graphene without any additional layer islands. This oxidation pretreatment approach provides an effective strategy to produce homogeneous strictly monolayer graphene in a large scale.

# Chapter 5

## Chemo-thermal synthesis of graphene from organic adsorbents

After concluding in the previous chapter that carbon species adsorbed on Cu surfaces can result in graphene after thermal annealing, this chapter looks at the synthesis of graphene in a controllable fashion, *viz.* introducing intentionally organic adsorbents on a clean Cu surface and then conduct post thermal annealing. The so-called chemo thermal route includes a controllable deposition of organic molecules (*e.g.*, solvents) and post annealing in hydrogen atmosphere.

### 5.1 Motivation

Graphene demonstrates numerous unique electronic, optical, chemical, thermal and mechanical properties, amongst others [1, 4, 5, 94, 261]. Thus far, there is obvious interest in developing synthesis routes because this is the key to

fully exploiting graphene's properties. Numerous routes have been employed for graphene fabrication. Chemical vapor deposition, where hydrocarbon feedstocks are decomposed on a supporting substrate, is perhaps the most popular route because it is a sophisticated technique adopted both in semiconductor manufacture and also in research labs.

Moreover, this route is highly successful, especially when fabricating graphene on Cu via a surface-mediated growth mechanism [111, 114, 262]. An alternative synthesis route involves another metal, Ni, which has high carbon solubility. This method is based on carbon dissolving through bulk metal [145] and segregating from the bulk so that graphene forms from carbon precipitation on the Ni surface [122, 123, 173, 263]. Graphene can also be obtained via exfoliation, either through mechanical cleavage [5, 86], chemical exfoliation with organic molecule intercalation [79, 90–92], or with the OH functional group through hazardous acid [97–101].

Graphene synthesis by thermal polymerization has also been explored, *e.g.*, the polymerization of Quinone precursors. However this is a complicated route which involves three-step thermal treatments. In another chemo-thermal method graphene nanoribbons can be synthesized via different heating steps from monomer precursors, for example 10,10'-dibromo-9,9'-bianthryl monomer, then dehalogenation of these monomers to finally Cyclodehydrogenation [93]. Besides the dry methods such as CVD and chemo-thermal routes, a bottom-up method has also been developed via organic synthesis. It covers an approach where small aromatic hydrocarbon precursors are pieced together to form a larger graphene structure by coupling reactants [94, 95]. This route holds limited upscale promise because the solubility of polycyclic graphitic products reduces significantly with increasing graphene grains, so that further increase in grain size is negligible.

This chapter discusses a single-step path to synthesize micron-scale graphene monolayer and bilayer flakes on Cu via a significantly simple chemo-thermal

route where three common organic molecules adsorbed on Cu foils serve as carbon precursors.

## 5.2 Experimental protocol

*Pretreatments to Cu substrates:* High purity Cu foil (99.999%) from Alfa Aesar (25  $\mu\text{m}$ ) was adopted as the supporting substrate. Prior to the chemo-thermal graphene synthesis, the Cu substrate was first cleaned. This included a thermal treatment (800  $^{\circ}\text{C}$  for 30 min) of the Cu foil in air after which the foil turns black. The oxidized foil was then reduced through thermal annealing in  $\text{H}_2$  atmosphere (1025  $^{\circ}\text{C}$  for 30 min).

*Direct formation of graphene:* After this step, the Cu foil was cleaned and underwent a dip coating in a general organic solvent, a process that allows organic solvent molecules to be adsorbed on the surface of Cu foil. Three common solvents, acetone, isopropanol and ethanol, were investigated. These solvents were supplied from WMR International with purity for analysis (99.8%). After dip coating, the Cu foil was allowed to dry at ambient conditions. Prior to loading into the reaction tube, the solvent-deposited Cu foil was mounted inside a half-sealed small quartz test tube (inner diameter: 1.8 cm, length: 10 cm). This small quartz test tube, which was previously built up by Rummeli group (*cf.* Ref.[125]), is intended to maintain an organic vapor rich environment when these molecules are volatile upon high temperatures. Then, the quartz test tube (with loaded Cu) was loaded to the reaction chamber, with the sealed side facing the gas flow. The chemo-thermal reactions were operated at temperatures from 700  $^{\circ}\text{C}$  to 1050  $^{\circ}\text{C}$ , pressures from 2 mbar to 1000 mbar, and an  $\text{H}_2$  atmosphere with flow rate between 1 sccm and 100 sccm. In addition, the temperature was measured (with a thermal couple) on the outer wall of the reaction tube, which

is not influenced by the gas flow.

*Calculation of gas equilibrium:* The thermodynamic calculation of the decomposition of carbon precursors was carried out using CEA software (Chemical Equilibrium with Applications, provided by NASA). Initially the program was set on a constant pressure and constant temperature mode. The amount of H<sub>2</sub> was determined by the volume that Cu foil occupied (here using 0.003 μmol as the amount of H<sub>2</sub>). Next, the amount of organic molecules that resided on the Cu surface were determined with an adsorption model described in reference [264, 265], *i.e.*, one acetone molecule adsorbs on one Cu atom on the Cu (111) surface. Therefore the surface area of a Cu surface contributes to 0.003 μmol. Take the acetone precursor for example; the initial condition (*e.g.*, gas condition) was set up with 3 μmol H<sub>2</sub> and 0.003 μmol acetone. Then, the equilibrium state was set at 10 mbar pressure and 1025 °C temperature. Finally, the mole fraction of the resultant gaseous radicals (deriving from both reactants: H<sub>2</sub> and acetone) were presented in an output file from the CEA. For the temperature dependent experiments, the calculation was performed adopting 700 °C - 1025 °C but keeping pressure at 10 mbar. For the pressure dependent experiments, the calculation was carried out at pressures from 2 mbar to 1000 mbar, while maintaining a temperature of 1025 °C. Based on  $PV=nRT$ , the amount of H<sub>2</sub> input increases from 0.6 μmol to 320 μmol with increasing pressure. For solvent variation experiments, isopropanol and ethanol were introduced at the same amount, with other conditions (*e.g.*, pressure and temperature) fixed.

Results are discussed in the following paragraph. In the simple chemo-thermal route clean Cu foil is simply dipped in an organic solvent (or a few droplets are deposited on the Cu surface). This step results in organic molecule precursors adhering to the Cu surface. However, prior to the coating of organic precursors, it is critical to guarantee the cleanliness of the Cu surface. This is because the surface of as-received Cu foils are covered in residual grease which itself serves



as a source of carbon precursors [133]. As [chapter 4](#) demonstrates, the most efficient cleaning method includes first burning the Cu foil in air (oxidization) and then annealing it in H<sub>2</sub> atmosphere (16 sccm H<sub>2</sub> flow rate). Once the cleaning procedure was completed, the clean Cu foils were treated by heating in pure Ar or pure H<sub>2</sub> atmosphere. No graphene or carbon species were observed, confirming that the Cu foil was free of carbon-related contaminants.

To form single crystalline graphene flakes (1 μm in diameter) the clean Cu

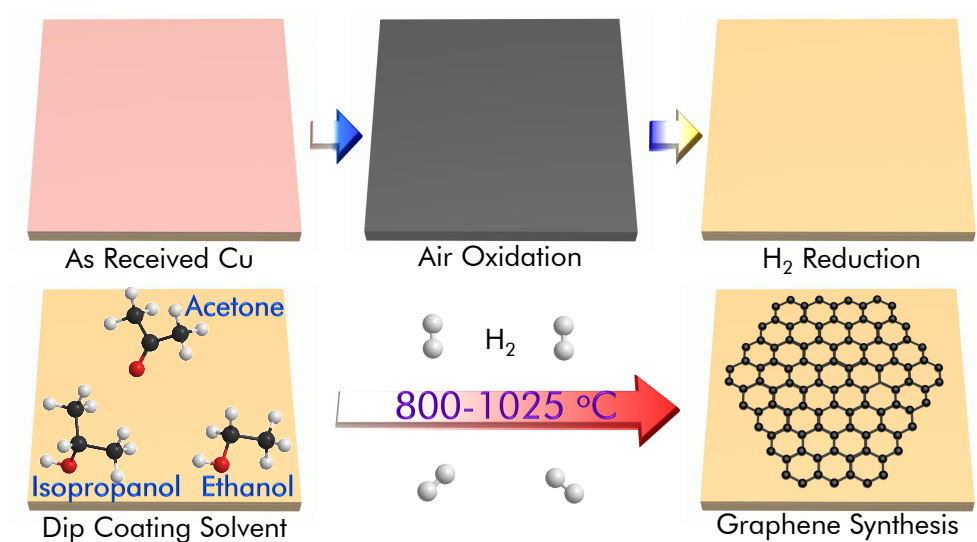


FIGURE 5.1: The procedure of the chemo-thermal route of graphene fabrication. It includes Cu cleaning, organic precursor deposition, and chemo-thermal reaction for graphene formation.

foil was dipped in an organic solvent (acetone, isopropanol or ethanol), followed by drying at ambient conditions. Energy dispersive X-ray spectroscopy (EDX) measurements of the carbon signal relative to measured Cu signal (on both clean Cu and solvent deposited Cu) show elemental C/Cu mass ratios of 0.3, 0.4 and 0.5 (error  $\pm 0.1$ ) for acetone, isopropanol and ethanol, respectively. In a word, the carbon loadings are similar for all three cases, within the acceptable error. Once dry, the Cu foil with organic precursors was loaded in a tube furnace at temperatures from 700 °C to 1050 °C with a H<sub>2</sub> flow of 16 sccm. The complete procedure is demonstrated in [Figure 5.1](#) and the photograph of Cu surface is shown in [Figure B.1](#) of [Appendix B](#). Graphene formation was only observed

between 800 °C and 1025 °C. A variety of reaction pressures and H<sub>2</sub> flow rates were also studied alongside the temperature investigation. No graphene growth was found without the pressure of H<sub>2</sub> in the chemo-thermal treatments. After the reaction was completed, scanning electron microscopy and atomic force microscopy demonstrated the formation of isolated individual graphene flakes on the Cu surface (Figure B.2 and Figure B.3 in Appendix B). For most cases, the graphene flakes had six facets, however at times 4-facet flakes were observed or they were round in shape (*e.g.*, disk-like). The average diameters of these graphene flakes vary from 100 nm to above 1 μm depending on the reaction temperatures. A detailed study of the graphene flakes by both SEM and AFM revealed the typical wrinkle features of graphene grown on Cu substrate (Figure 5.2).

Moreover, the contrast changes in SEM can indicate the number of graphene

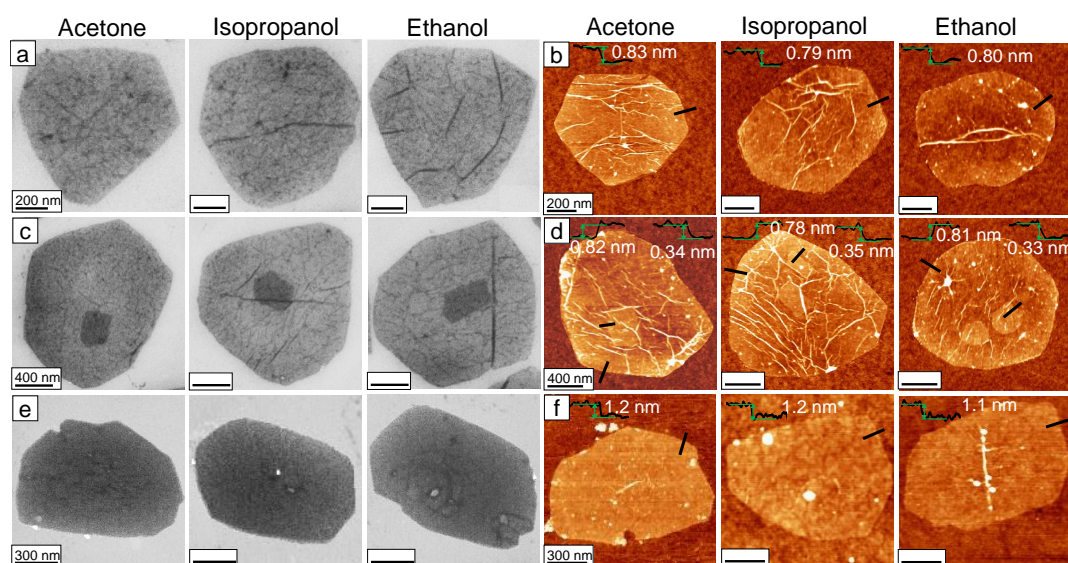


FIGURE 5.2: SEM (a,c,e) and AFM (b,d,f) micrographs for synthetic graphene. Monolayer graphene (top row), monolayer graphene with secondary islands on them (middle row), and bilayer graphene flakes (bottom row). The layer numbers are determined from both relative contrast in SEM and height in AFM graphs.

layers. Indeed a closer examination (Figure B.1) suggests the graphene flakes

are either: monolayer, bilayer, or monolayer with second layer islands. The image contrast  $C$  in SEM can be determined by the equation:

$$C = (I_0 - I)/I_0 \quad (5.1)$$

where  $I$  is the extracted intensity of the graphene flake and  $I_0$  is the intensity of background substrate. The values  $I$  and  $I_0$  were extracted using Gwyddion micrograph analysis software.

The AFM examinations allows measurements of the heights of graphene flakes, where heights ranging from 0.76 nm to 0.82 nm indicate monolayer graphene, while heights ranging from 1.1 nm to 1.3 nm indicate bilayer graphene (right panel, Figure 5.2). Graphene flakes with second layer islands on them are also found (middle row, Figure 5.2).

Raman spectroscopy was also adopted to confirm these flakes are truly

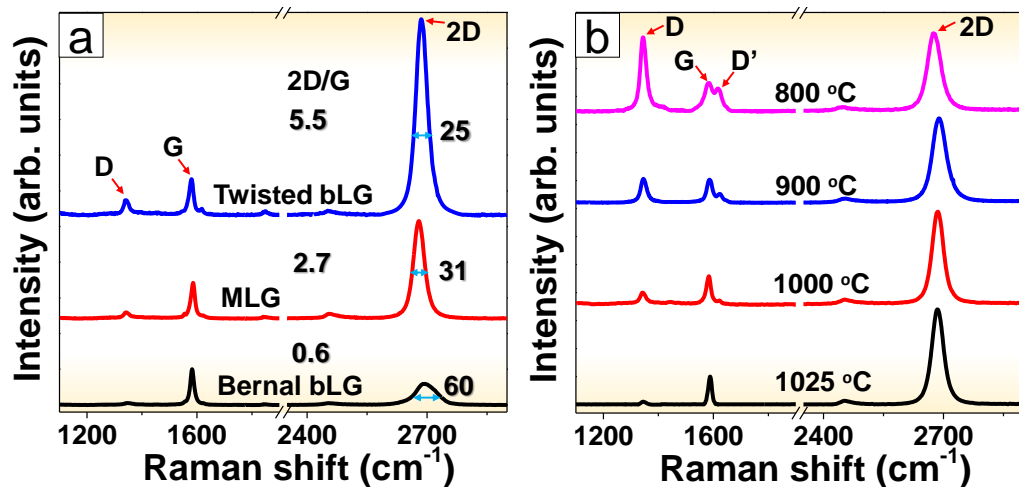


FIGURE 5.3: Raman spectra for synthetic flakes from chemo thermal route. (a) Raman spectra for synthetic flakes of monolayer graphene, AB Bernal stacking bilayer graphene, and twisted bilayer graphene (rotational angle, ca.  $20^\circ$  -  $30^\circ$ ). (b) Evolution of Raman spectra for graphene flakes with respect to thermal annealing/synthesis temperature. The graphene quality improves with a decreasing D band as temperature increases.

graphene. The  $sp^2$  carbon such as graphene can be easily determined by Raman spectrum with their fingerprint Raman shift at  $1350 \text{ cm}^{-1}$  (D band),  $1580$

$\text{cm}^{-1}$  (G band) and  $2700 \text{ cm}^{-1}$  (2D band). For the examined graphene flakes ( $>150$ ), all three bands are present and the typical spectra are shown in [Figure 5.3a](#). In some cases, the intensity ratio of the 2D band and G band (2D/G) range from 2 to 3 and the 2D band is symmetrical with a narrow ( $<40 \text{ cm}^{-1}$ ) full width half maximum (2D FWHM). These spectra are assigned as monolayer graphene (*e.g.*, [Figure 5.3a](#) red spectrum) [246, 266]. In some cases the intensity ratio of 2D/G ranges from 0.5 to 0.7 while the 2D band becomes asymmetrical with a broadening FWHM ( $> 60 \text{ cm}^{-1}$ ) and upshifted by  $3\text{-}5 \text{ cm}^{-1}$ . These spectra suggest the presence of AB Bernal stacked bilayer graphene ([Figure 5.3a](#), black spectrum) [18]. In other cases the 2D/G ratio ranges from 5 to 6 and 2D band with a relatively narrow FWHM (*ca.*  $24 \text{ cm}^{-1}$ ) and 2D position is slightly up-shifted [125, 160, 213, 267]. These final spectra correspond to twisted stacking bilayer graphene with rotational angles between  $20^\circ$  and  $30^\circ$  [268].

Similar to Raman spectroscopy, low voltage transmission electron microscopy is a powerful tool for graphene characterizations [237]. In this chapter, numerous LVTEM studies were performed on the graphene flake specimens. Selected area electron diffraction (SAED) and Fast Fourier Transform (FFT) information show a three-fold symmetry for graphene; and a diffraction spot spacing between the  $\{10\text{-}10\}$  and  $\{11\text{-}20\}$  orientations corresponds to graphene ([Figure 5.4ac](#)).

High resolution TEM images show the graphene honeycomb lattice of monolayer graphene ([Figure 5.4a](#)) and at times the Moiré patterns are observed, indicative of twisted stacking [268] of bi-layer flakes. The layer number of the graphene samples is determined as only monolayer graphene and bilayer graphene using a method [269, 270] to count layer numbers of graphene from vacuum to graphene stacking layers. Furthermore, the intensity profile of the line across the  $\{10\text{-}10\}$  and  $\{11\text{-}20\}$  reflex spots confirm the presence of monolayer ([Figure 5.4d](#)) and bilayer ([Figure 5.4f](#)) graphene.

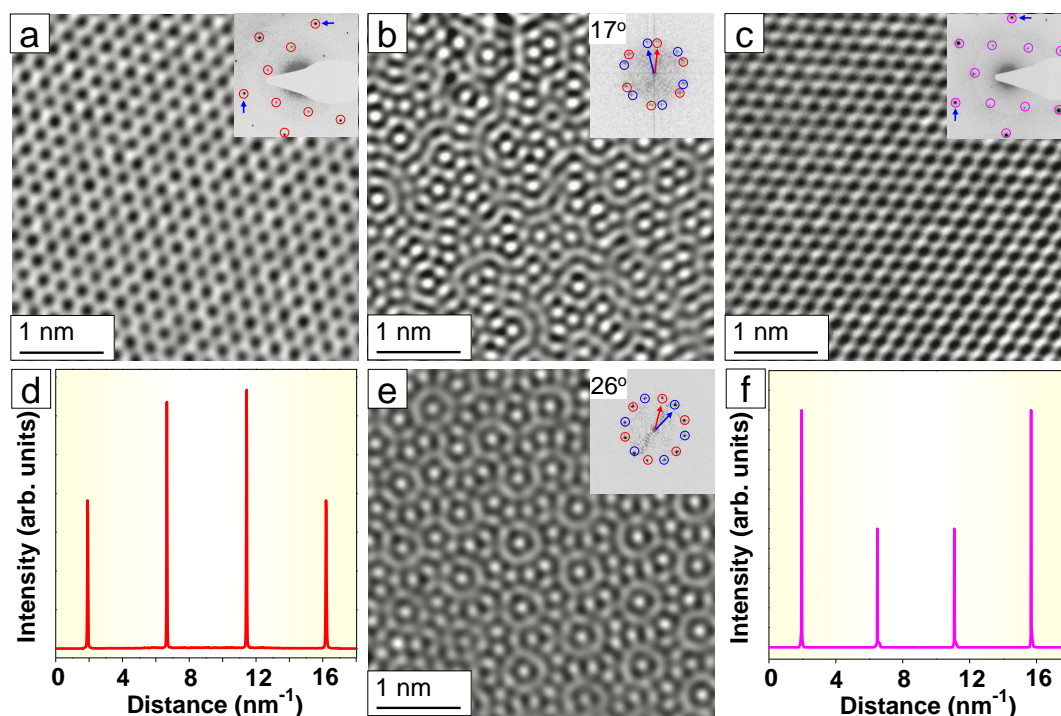


FIGURE 5.4: High resolution TEM images, SAED and FFT for graphene flakes. (a) Monolayer graphene, (b,e) twisted bilayer graphene with Moiré patterns, and (c) AB Bernal stacked bilayer graphene. Insets: diffraction data extracted from SAED (a,c) or Fast Fourier Transform (b, e). Panels d and f reveal the intensity profiles of the  $\{10-10\}$  and  $\{11-20\}$  reflexes, which are in agreement with monolayer and Bernal stacked bilayer graphene, respectively.

### 5.3 Influence of reaction temperature on graphene growth

The graphene synthesis processes were examined with respect to temperature, reaction pressure and flow rate. First, temperature variation was explored from 700 °C to 1050 °C, whilst maintaining pressure at 10 mbar, with a H<sub>2</sub> flow rate of 16 sccm.

Graphene flakes were only found at temperatures between 800 °C and 1025 °C (Figure 5.5). It can be seen from a visual inspection that the flake diameter increases and the flake density falls as temperature increases.

The Raman spectra for graphene samples prepared from different temperatures are shown in Figure 5.3b. The graphene quality improves with increasing

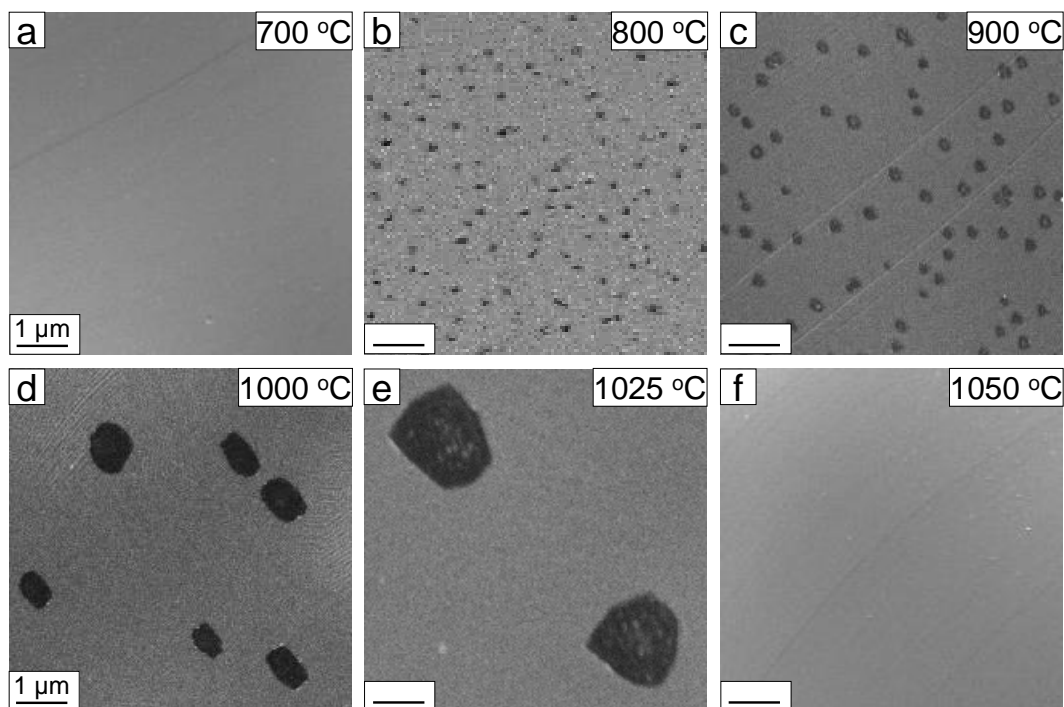


FIGURE 5.5: SEM graphs for graphene formation with respect to reaction temperature. Here acetone serves as organic adsorbent to form graphene.

reaction temperature indicated by the decreasing D band in Raman spectra. The statistics of the Raman spectroscopic band information is listed in Appendix [Table B.1](#). This shows the homogeneity of the predominantly monolayer graphene for these flake samples.

Two Arrhenius plots were presented in [Figure 5.6](#). These plot both the average grain diameter and grain density with respect to the reciprocal temperature. In these plots, changes in grain size and density are both linear so that the activation energies,  $E_a$ , can be extracted based on the Arrhenius equation.

$$k = Ae^{\frac{-E_a}{RT}} \quad (5.2)$$

where  $k$  is a constant of reaction rate,  $A$  is a pre-factor,  $E_a$  is activation energy,  $R$  is gas constant and  $T$  is temperature (Kelvin).

The Arrhenius plots (top row in [Figure 5.6](#)) demonstrate that the graphene growth rate increases with increasing temperature. This reveals an increase in

reactive carbon radicals for graphene formation, *viz.* organic molecule decomposition and carbon species surface diffusion are increased. The activation energies for acetone and ethanol are similar, and slightly higher for isopropanol.

The changes in density show a positive slope with respect to reciprocal

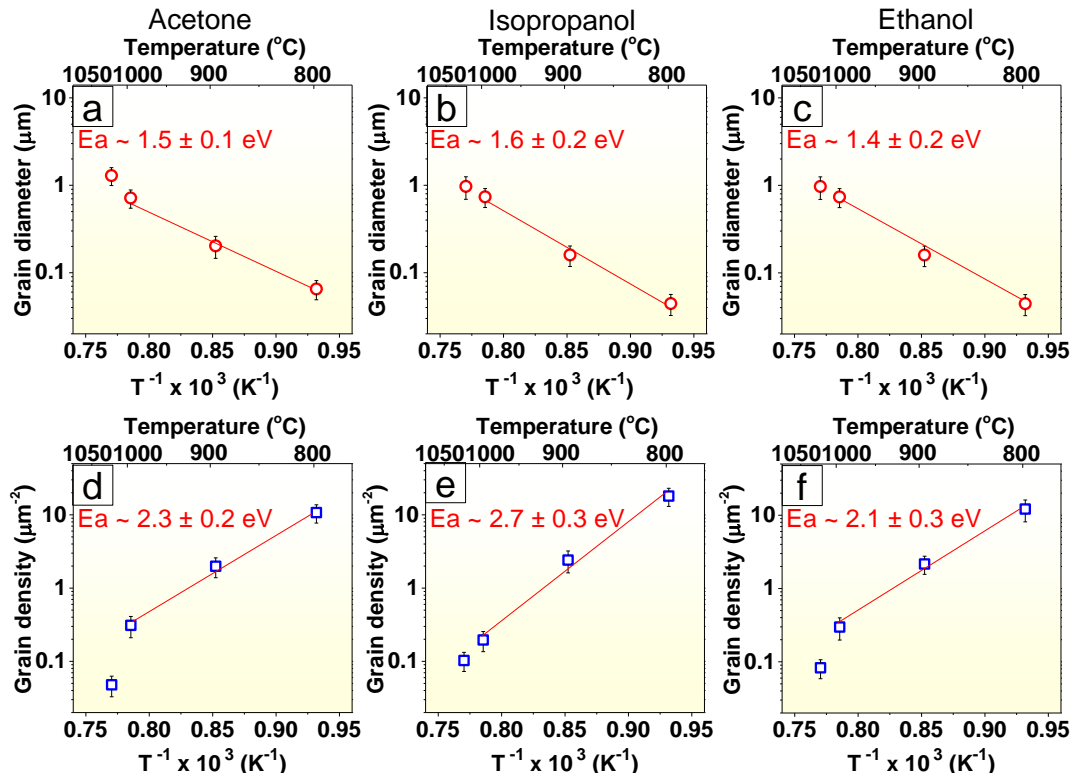


FIGURE 5.6: Arrhenius plots for each solvent precursor for average grain diameter (top row) and grain density (bottom row). The activation energy,  $E_a$ , is listed in red inside each graph.

temperature, which indicates a reduction in density of graphene islands, and therefore a reduction in early nuclei density, when temperature increases. This positive slope indicates a complex reaction mechanism (*cf.* subsection 2.4.2). This could be attributed to the fact that as temperature increases fewer surface defects emerge on the Cu surface, where the defects are assumed to prefer graphene nuclei formation [192, 218, 271–273]. Furthermore, the molar concentration of graphitic carbon species increases, and they then prolong their residence on the Cu surface, which favors graphene formation. In addition, the increase in temperature enhances carbon radical diffusion at the Cu surface and

fewer but larger flakes are formed. The increase in surface desorption of carbon radicals may also account for the decrease in density [118, 192, 274, 275].

The chemical equilibrium calculation (carried out using the CEA program) reveals an increase in all four radicals with respect to temperature (Figure B.5). Indeed experimental data of total graphene area with respect to the underlying Cu surface shows a gradual increase from 800 °C to 1000 °C and a fall when 1025 °C is adopted (Figure B.6). The initial increase is attributed to enhanced solvent precursor decomposition and surface diffusion. However above 1000 °C etching by H\* radicals and surface desorption of carbon species dominate in the reaction, and the graphene area ratio decreases with respect to Cu surface.

The changes in the graphene flakes with respect to temperature were evaluated using Raman spectroscopy. At low temperatures (800 – 900 °C) the D band is bigger than the G band. In addition, close to the G band, there is the presence of an additional peak (1620 cm<sup>-1</sup>), termed the D' band. The D' band is related to graphene defects [254, 276], which indicates that the graphene islands produced at low temperatures are defective. This might be due to the fact that at low temperatures the graphitic carbon radicals are not sufficient, as well as due to slow surface diffusion, so that defects, such as vacancies, will form in the graphene lattice.

## 5.4 Influence of reaction pressure on graphene growth

The role of reaction pressure was investigated from 2 mbar up to 1 bar with a 16 sccm H<sub>2</sub> flow at temperature 1025 °C. SEM graphs demonstrate the trend of graphene growth as reaction pressure increases (Figure 5.7). The density of graphene flakes increases from 2 mbar to 5 mbar, but then falls at 10 mbar, while the grain size increases slightly with respect to pressure (Figure B.7).



With pressure above 10 mbar, no graphene formation was observed. The relative ratio of graphene coverage area in terms of Cu area is nearly 10% for 5 mbar and 10 mbar samples, which are higher than the ratio (1 - 6%) for 2 mbar samples (Figure B.8).

Chemical equilibrium calculations reveal different changes of reactive rad-

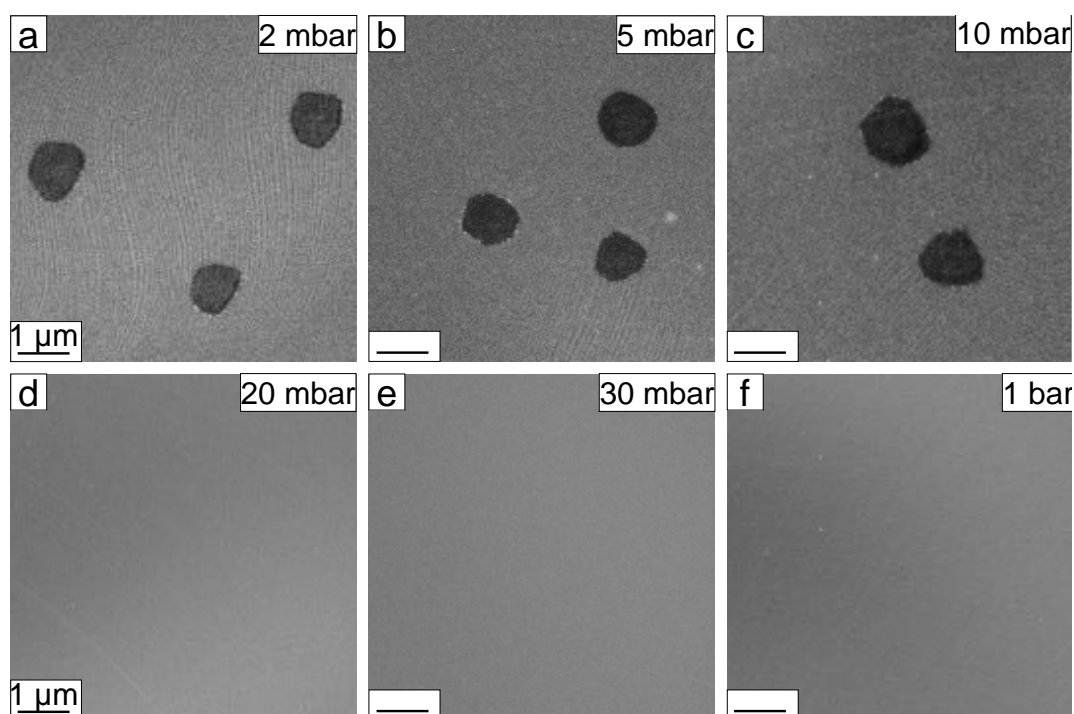


FIGURE 5.7: SEM of graphene flakes formed with different reaction pressures. In these experiments acetone molecules adsorbed on Cu surface prior to the chemo-thermal synthesis.

icals such as  $H^*$ ,  $O^*$ ,  $CH_3$  and graphitic C with respect to reaction pressure (Figure B.9 in appendix B).  $H^*$  radicals as well as graphitic C,  $C(gr)$ , decrease gradually with increasing pressure.  $CH_3$  radicals increase from 2 mbar to 100 mbar and then fall, while  $O^*$  radicals show an inverse trend to  $CH_3$  radicals. Note that the molar fraction of  $O^*$  and  $CH_3$  are much smaller than that of  $H^*$  and  $C(gr)$ . This suggests that  $C(gr)$  and  $H^*$  radicals are determining factors for graphene growth. Indeed, the positive correlation of  $C(gr)$  and  $H^*$  was observed in the pressure section (Figure B.9ab). Again, in the temperature section

(Figure B.5ab), the same positive correlation was found between these two radicals. Moreover, when generalizing both temperature and pressure, a critical mole fraction of graphitic C, C(gr), emerges as 0.001, *viz.* no graphene flakes form below this value.

The combined data from the temperature and pressure investigations suggest that H\* aids the formation of graphitic C fragments. This could be because H\* serves both in assisting organic precursor decomposition and also preventing amorphous carbon formation, which hinders graphene growth [94, 129, 277]. To summarize, the increase in reaction pressure results in changes in chemistry that suppress graphitic carbon generation (Figure B.9b) and matches well with the experimental results (Figure 5.7).

## 5.5 Influence of reaction flow rate on graphene growth

The effect of H<sub>2</sub> flow rate was also investigated, with pressure of 10 mbar at temperature 1025 °C. The SEM graphs of graphene flakes from the three solvent precursors are shown in Figure B.10. The average size of graphene flakes and flake density maximize at a flow rate of 50 sccm and fall at flow rates below or above this value (Figure B.11). The relative ratio of graphene coverage area maximize at 50 sccm (Figure B.12).

Chemical equilibrium calculations for radicals of H\*, C(gr), CH<sub>3</sub> and O\* demonstrate to some extent a significant change with respect to H<sub>2</sub> flow rate (Figure B.13). This may suggest that flow rate plays a dual role in graphene formation in these experiments. First, at low H<sub>2</sub> flow rate (<16 sccm), the H\* is low molar concentration so that thermal decomposition is very low (indicative of low CH<sub>3</sub> concentration), which depends on the role of hydrogen for assistance in thermal decomposition of carbon species. Second, at high H<sub>2</sub> flow rate (>75

sccm), the C(gr) is decreasing due to the role of hydrogen etching effect so that the supply of reactive carbon species are limited and the graphene formation is not favored.

When there is no incorporation of H<sub>2</sub> flow, *i.e.*, using pure Ar flow in the chemo thermal annealing, no graphene is observed (Figure B.14). This shows the essential role of hydrogen in the chemo thermal route for graphene formation.

*The Growth of Bilayer Graphene:* Finally the growth mechanism of bilayer graphene is postulated. Three key arguments have been demonstrated for the formation of bilayer graphene. In the first, gaseous carbon fragments and aromatic species are transported just above a graphene surface (pre-growing on Cu foil) and they may reside on top of graphene and assemble into a second layer graphene flake [268]. In the second argument active carbon species are able to diffuse (*e.g.*, through defects sites) between the initial graphene film and the underlying Cu substrates and form a new layer flake. In the other scenario monolayer graphene and bilayer graphene flakes form spontaneously, (*i.e.*, in an inverted pyramid fashion, topmost layer having larger diameter and bottom layer having smaller diameter) [278]. More experiments are reported to support this scenario [218, 251, 279]. The data in this chapter suggests that the spontaneous growth mode is active because the mixture of monolayer and bilayer graphene is formed spontaneously in one step.

## 5.6 Summary

With this facile chemo thermal route, monolayer and bilayer graphene flakes (with diameter up to 1 μm) have been produced from adsorbed solvent molecules on a clean Cu surface. The influence of temperature, pressure and gas flow rate

have been systematically investigated so that an optical growth window is provided: 1000 - 1025 °C, 16 - 50 sccm flow rate for H<sub>2</sub> and 5 - 10 mbar for reaction pressure, respectively.

The reaction mechanism in the synthesis route has been interpreted thoroughly with both experimental observation and thermodynamic calculation. Upon thermal treatment at high temperature, the adsorbed solvent molecules (*e.g.*, acetone, isopropanol and ethanol) undergo decomposition which provides active carbon species from which graphene can be formed. The H<sub>2</sub> flow is crucial for generating H\* radicals for the synthesis reaction. The equilibrium calculation data shows H\* radicals play two important roles. On the one hand, they activate surface bound C species, *i.e.* they assist the decomposition of organic adsorbents and remove weak carbon bonds to allow for the formation of the preferred strong bonds in graphene. On the other hand, they work as an etchant that can decrease the graphene diameter (with increasing H<sub>2</sub> partial pressure) and finally prevent graphene growth. These dual roles of H<sub>2</sub> observed in this chemo-thermal route provide an insight into the reaction mechanism for graphene formation. This finding also enriches the understanding of conventional thermal CVD approach.

This simple graphene synthesis route, which consists of a one-step thermal treatment, may shed light on the spatial control of graphene formation, *e.g.* using a mask to pattern the targeted region for organic molecule adsorption. Moreover this chapter provides new insights into graphene formation, *e.g.* the thermal dynamics in graphene formation from small organic molecules, and the dual roles of hydrogen with respect to organic precursors in the synthesis reaction.

# Chapter 6

## Monolayer graphene synthesis directly over Si/SiO<sub>x</sub>

Directly grown graphene over dielectrics have great advantages that it avoids undesirable transfer procedures which cause breakage and contamination of the graphene. Hence it is of interest to directly grow graphene directly over non-catalytic Si/Si oxide substrate and thus avoid the need for transfer.

### 6.1 Motivation

It is well over a decade now since Andre Geim and Konstantin Novoselov first isolated graphene and began revealing a whole myriad of graphene's exciting physical properties [5]. Those studies and subsequent studies by others continue to demonstrate great promise in numerous fields from electronics, coatings, composites, bio-medical applications and beyond [280–285]. Of core importance to realizing graphene's success commercially is its production. Large films and small sheets of graphene are the two major forms of graphene used for various

applications [78, 286–288]. In terms of large area graphene, which holds promise for future electronics [33, 55, 210, 285, 289], *e.g.*, field effect transistors (FET), touch panels, displays and photovoltaic devices, there are numerous efforts to achieve uniform monolayer and few-layer in a controlled manner. In the microelectronics industry there is hope that large area graphene may offer solutions beyond just complex devices [290] and transparent electrodes [285] but also as efficient electrical interconnects in large scale integrated circuits (LSI) [291].

In the pursuit of the above, for large area graphene fabrication, the vast body of work has been dedicated to the fabrication of large area graphene over metals using chemical vapor deposition (CVD), mostly using Cu or Ni as catalytic substrates [103–107]. Cu with its low carbon solubility makes achieving uniform monolayer and bi-layer graphene more likely as compared to Ni [104, 111]. Roll-to-roll fabrication of graphene over Cu has also been achieved [57]. However, to use such graphene within microelectronic applications where the devices are built on dielectric substrates (mostly Si/SiO<sub>x</sub> wafers) the as-produced graphene requires post synthesis transfer of the graphene on to a dielectric substrate. This procedure leads to undesired damage and processing contamination of the transferred graphene [37, 112, 169, 292].

To this end, a relatively large body of work has looked at the thermal decomposition of SiC surfaces to yield graphene [88]. While the quality of the obtained graphene is good, it is near impossible to achieve this in large area and with uniform layer number [108–110]. Other dielectric substrates have also been explored, such as quartz, sapphire, SrTiO<sub>3</sub>, Si<sub>3</sub>N<sub>4</sub> and borosilicate glass [49, 56, 161, 293, 294]. Indeed, recent developments of direct graphene growth over glass are remarkable [295]. Of course, given that Si/SiO<sub>x</sub> technology is so successful and very well established it makes sense that graphene be formed on Si wafer material in a more direct manner. There are two approaches to achieve this, the first is termed pseudo-direct, and this includes techniques in which a metal catalyst upstream helps decompose the carbon feedstock enabling

graphene to form on a Si/SiO<sub>x</sub> substrate downstream [296, 297].

Alternatively, one can form a thin metallic film on a Si/SiO<sub>x</sub> substrate that evaporates away during the synthesis process [298]. The use of liquid metal films (which also evaporate away) on Si/SiO<sub>x</sub> for uniform graphene formation has been particularly successful [117, 229]. The second approach is to fabricate synthetic graphene directly on Si/SiO<sub>x</sub>. The team from Yunqi Liu completed a variety of pioneering works showing large graphene grain formation on Si/SiO<sub>x</sub> [49]. They and others went on to developed film coverage over Si/SiO<sub>x</sub> [50, 230, 299, 300].

However, homogeneous and uniform graphene layering for large area coverage directly over Si/SiO<sub>x</sub> has remained a challenge. Moreover, the challenges facing homogeneous and uniform graphene coverage over Si/SiO<sub>x</sub> have led to the direct CVD synthesis of graphene over Si wafers being largely ignored in favor of the far easier and more developed approaches, namely CVD fabrication over Cu and SiC decomposition. This fact is easily seen in [Figure C.1](#) in [Appendix C](#) in which published articles from the different synthesis approaches are presented in a bar chart. Clearly CVD grown graphene dominates and the number of publications on this theme is several orders magnitude large than that for the direct fabrication of graphene over Si/SiO<sub>x</sub>. The difference is surprising given that the direct graphene fabrication over Si/SiO<sub>x</sub> is highly desirable due to the potential lower cost, compatibility with current Si based technology and better process control [301].

In this chapter, the direct fabrication of graphene over Si/SiO<sub>x</sub> is revisited. Ideas originally developed for uniform graphene fabrication over Cu are borrowed in which confinement of the substrate is implemented [125, 126]. The synthesis of graphene directly on Si/SiO<sub>x</sub> both without and with confinement are compared and this work demonstrates, for the first time, that large area uniform monolayer graphene directly over Si/SiO<sub>x</sub> is feasible.

Indeed, this approach is remarkably simple and involves simply sandwiching

two Si/SiO<sub>x</sub> wafers together (which in essence produces a uniform single layer graphene film at each surface). The resultant graphene when characterized is shown to have faceted grain boundaries in the form of polygons despite nucleating in the form of disks. This faceting process occurs as the system aims to minimize its energy and moves towards the ideal case of forming hexagonal polygons, much like a beehive forming hexagonal cells to minimize wax use. In this way, the grain boundary periphery is minimized and as such the optical and electric performance is highly competitive when compared to monolayer graphene produced over metals and other substrates. The work should pave the way for large area uniform graphene production directly over Si wafers.

## 6.2 Experimental protocol

*Graphene growth.* Si/SiO<sub>x</sub> (300nm oxide) wafer after sonication in acetone and drying in N<sub>2</sub> was used for the synthesis experiments. The graphene grains and films were synthesized in a horizontal (Al<sub>2</sub>O<sub>3</sub> corundum) tube furnace. CVD synthesis is performed at a temperature of 1185 °C in ambient pressure with a gas mix of Ar/H<sub>2</sub>/CH<sub>4</sub> with flow rates of 120/30/1.5 sccm, respectively. The growth times varied according to the specific experiment in question. The samples were typically heated up in an Ar/H<sub>2</sub> flow (120 sccm/30sccm) to the synthesis temperature. After the temperature stabilized (10 min), the Ar/H<sub>2</sub>/CH<sub>4</sub> gas mix was introduced for a nominal growth time. It was found that a post treatment under Ar/H<sub>2</sub> for *ca.* 20 min followed by cooling in an Ar atmosphere yielded the cleanest (minimal surface contamination) graphene.

*Transfer.* For TEM and optical transmittance investigations the graphene was transferred using KOH aqueous solution to detach graphene from the Si/SiO<sub>x</sub> surface. The protocol steps are spin-coating PMMA, detaching the film in KOH



(2M), fishing onto TEM grid in isopropanol medium [179], and then PMMA removal using acetone. Finally, high vacuum annealing is employed to remove any organic residues.

*Characterizations.* SEM measurements were performed on Zeiss Ultra plus and FEI Quanta 250 (5kV) with secondary electron detector. AFM was performed using an Asylum Research Cypher in the tapping mode (0.8 Hz for 1024 pixels by 1024 pixels). DF-TEM was performed on a Tecnai F30 (at an acceleration voltage of 80 kV). HR-TEM was performed on a Titan 80-300 with Cs corrector for the primary objective lens (at an acceleration voltage of 80 kV). Raman spectra and mapping were performed on a WiTec alpha 300 (514 nm laser excitation). Optical transmittance was performed on a UV/Vis spectrophotometer (Analytik Jena Specord 250). The electrical transistor measurements were conducted using a dual channel source-meter unit (Keithley 2612B). The transistor devices were fabricated using lithography, electrode deposition and peeling off steps.

### 6.3 Influence of substrate confinement configuration

Initially, three Si/SiO<sub>x</sub> (300 nm oxide) substrate configurations are adopted, the schematics of which are presented in [Figure 6.1](#). The three configurations from left to right are; Si/SiO<sub>x</sub> with the oxide facing up (exposed), Si/SiO<sub>x</sub> with the oxide facing down on a sintered alumina support and two Si/SiO<sub>x</sub> wafers with their oxide faces sandwiched together.

After individually subjecting these different configurations to an atmospheric thermal CVD reaction for nominal periods of time, the samples were cooled and then initially examined using scanning electron microscopy (SEM) and Raman

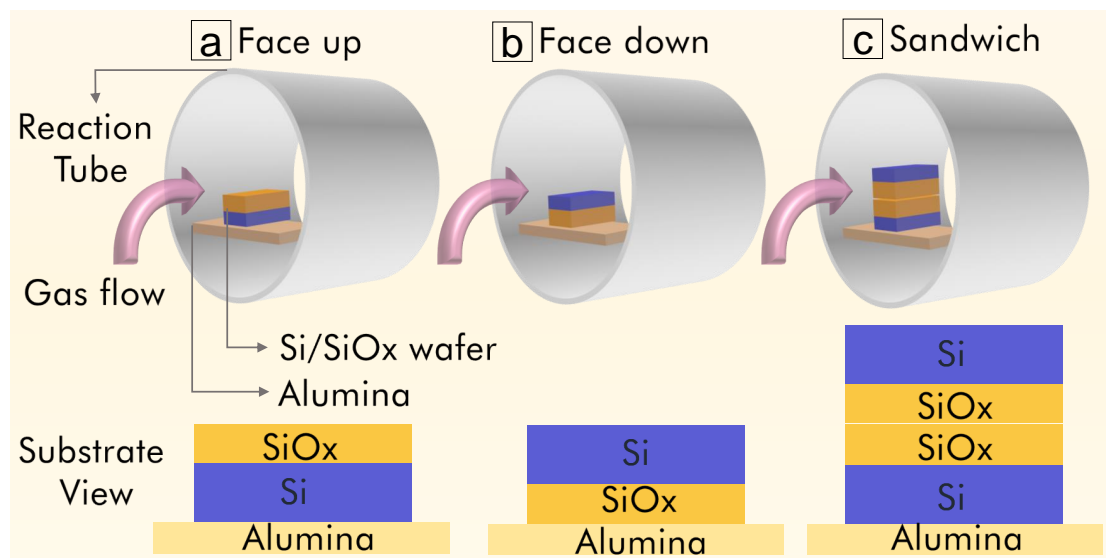


FIGURE 6.1: Schematic illustrating the substrate configurations explored for the direct synthesis of graphene over Si/SiO<sub>x</sub> using thermal CVD. (a) SiO<sub>x</sub> facing up, (b) SiO<sub>x</sub> facing down and (c) a sandwiched Si/SiO<sub>x</sub> - SiO<sub>x</sub>/Si configuration. The oxide layer is desired substrate surface for graphene growth. The substrate is commercially available Si wafer with a polished thermally-grown oxide (layer thickness *c.a.* 300 nm). The supporting plate is sintered alumina.

spectroscopy. The data show full coverage on the oxide face after 4 to 5 hours. This preparation features a short time frame when compared against full film coverage in other works (6 – 8 hours) [50, 294].

Figure 6.2 presents representative data from the samples after a reaction time of 5 hours in which the substrates are fully covered by a graphene film. Clear differences between the different substrate configurations are observed. For the upward facing oxide layer from the substrate (*cf.* Figure 6.1a) one sees full or near full coverage of graphene and numerous randomly located secondary and ternary layers. The secondary layers show up as dark contrast spots in the SEM micrographs while Raman maps of the full width at half maximum (FWHM) of the 2D peak, which is used to differentiate between monolayer graphene and few layer graphene [246, 266] confirm the inhomogeneity in layer numbers. Local Raman spectroscopy on the clear patches of the as-produced film indicate monolayer graphene. A similar outcome is observed for the samples in which the oxide layer lies face down on an (polycrystalline) alumina base

(*cf.* Figure 6.1b). However, both the SEM data and the Raman data indicate fewer secondary layers as opposed to the face up case. For the samples in which two Si/SiO<sub>x</sub> substrates with their oxide faces sandwiched together the graphene layer showed homogeneous monolayer large area graphene (see Figure C.2 in Appendix C), *viz.*, secondary layer formation is avoided. Moreover, the Raman spectroscopy data showed a 2D/G ratio of 2 indicating that the as-grown film of strictly monolayer graphene directly formed on a Si/SiO<sub>x</sub> substrate is of high quality. These data are presented in Figure 6.2.

To gain insight into why there is such a large difference between the face-

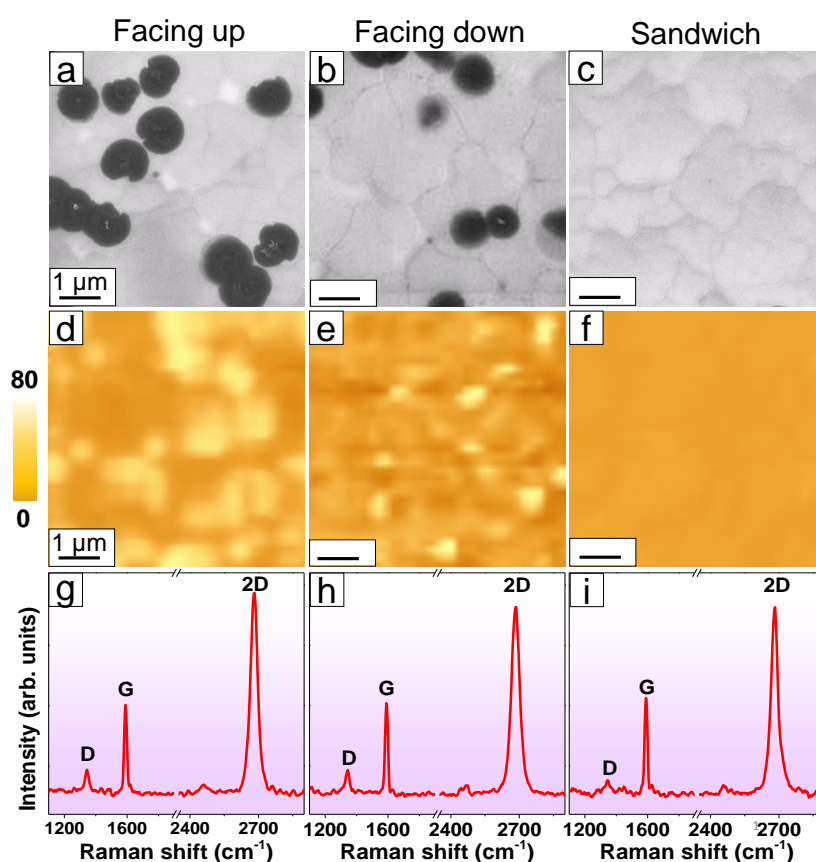


FIGURE 6.2: Characterization of the synthetic graphene for the three substrate configurations explored for the direct growth of graphene over Si/SiO<sub>x</sub>. (a,b,c) SEM micrographs of the post-synthesis sample surfaces. (d,e,f) Raman spectral mapping of the full width at half-maximum of 2D band. The units for the color scale bar are cm<sup>-1</sup>. (g,h,i) Raman spectra showing representative G, 2D and D bands for the graphene samples.

down sample on an alumina base and the sandwich (SiO<sub>x</sub>/SiO<sub>x</sub>) samples (*cf.*

Figure 6.1c), atomic force microscopy (AFM) topography investigations are conducted for the Si/SiO<sub>x</sub> faces as well as the Al<sub>2</sub>O<sub>3</sub> support base surface (Figure C.3). The AFM data shows the SiO<sub>x</sub> surface has a roughness of  $0.18 \pm 0.02$  nm. In contrast, the alumina has a surface roughness of  $101 \pm 8$  nm, which is more than 500 times that of the polished SiO<sub>x</sub> surface. This means that the confined space in the sandwiched SiO<sub>x</sub>/SiO<sub>x</sub> interface is significantly less than that found at the SiO<sub>x</sub>/alumina interface. In short, the space between the two polished SiO<sub>x</sub> faces confines or restricts the diffusion of feedstock species to the SiO<sub>x</sub> surface where graphene forms. Previous reports in which synthetic graphene was fabricated by CVD over Cu have also shown that restricting the feedstock supply through space confinement in essence controls the C supply rate and can favor homogeneous single layer graphene formation [125, 126]. To some degree this behavior can also be achieved by limiting the CH<sub>4</sub>/H<sub>2</sub> ratio and flow [127, 302]. In short, in this work, confining the gap space between the sandwiched Si/SiO<sub>x</sub> substrate helps limit the carbon supply and reduces the nucleation density. In the case of the substrate lying face down on the alumina base (Figure 6.1b) the gap is limited because of the rather large roughness of the alumina surface, while for a Si/SiO<sub>x</sub> face down on another polished SiO<sub>x</sub> surface (Figure 6.1c) the gap is significantly lower and so the C supply is sufficiently reduced to favor single graphene layer formation and limit secondary layer formation. Hence, the carbon species limitation is demonstrated by space confinement for homogeneous high-grade monolayer graphene can also be achieved with non-metallic Si/SiO<sub>x</sub> substrates using a simple sandwich technique which importantly overcomes what has been a challenge for the direct growth of large area graphene growth over Si/SiO<sub>x</sub>, namely, homogeneous large area graphene growth directly on Si/SiO<sub>x</sub>. Here samples of 2 x 2 cm<sup>2</sup> (Figure C.2) are produced however this size can easily be scaled up depending on the size of the CVD reactor.

## 6.4 Time dependent evolution for graphene formation

To understand the evolution of the graphene growth for the sandwich substrate configuration, the CVD reactions are performed with growth times from 1 to 5 hours. Figure 6.3 are typical data for time dependent samples. After 1 hour round graphene islands are randomly located on the substrate surface (Figure 6.3a). The average diameter of the flakes is  $375 \pm 30$  nm. The formation of round islands is in keeping with previous work [50] and occurs because the lowest energy atomic configuration at nucleating graphene island edges favors iso-directional (disk-like) growth for non-metal substrates [303]. With increasing growth time (2 hours), the islands enlarge (mean diameter  $670 \pm 45$  nm) and start to merge (Figure 6.3b). After 4 hours a nearly complete film has formed with only a few small open patches remaining (Figure 6.3c) and after 5 hours a full graphene film is obtained which is free of secondary layers. Similar data to that from SEM are found with the AFM studies. In addition, AFM allows us to measure the height of the islands and forming film at open edges. The heights are typically  $0.80 \pm 0.02$  nm, which is concomitant with monolayer graphene over Si/SiO<sub>x</sub> substrates [187, 193].

Raman spectroscopy investigations confirm the presence of monolayer graphene through the G mode (*ca.*  $1580 \text{ cm}^{-1}$ ) and 2D mode (*ca.*  $2700 \text{ cm}^{-1}$ ) locations, relative intensities and 2D FWHM (single Lorentzian fit of  $34 \text{ cm}^{-1}$ ) [126, 168]. The D mode (*ca.*  $1350 \text{ cm}^{-1}$ ) intensity relative to the G mode decreases with increasing growth time. The D mode is associated with defects. Open graphene edges are also defects that increase the D mode [129]. Hence, in this case as the number of free edges reduce as the individual grains grow and merge so does the D mode, such that once full coverage is obtained only a minute D mode remains present.

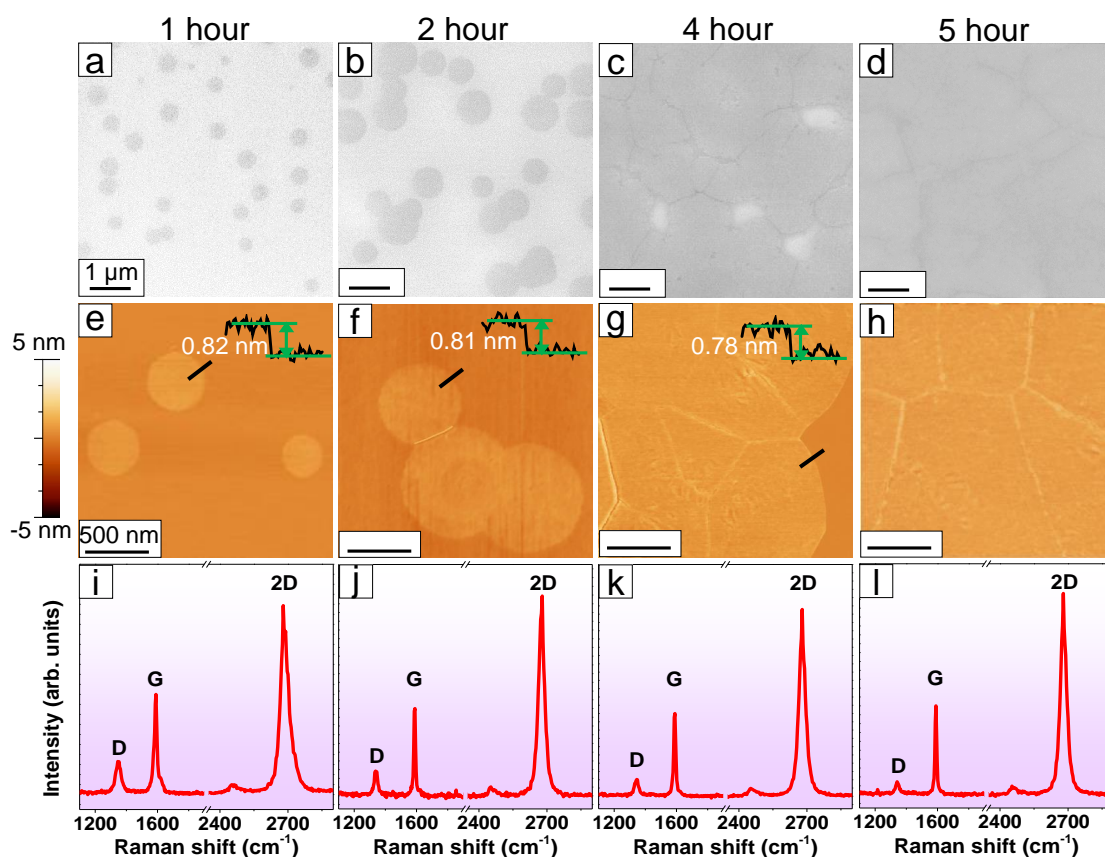


FIGURE 6.3: Time dependent growth evolution of the graphene from individual domains, adjacent grains merging to form a continuous monolayer graphene for the sandwich configuration. (a,b,c,d) SEM micrographs for the time-dependent graphene formation. (e,f,g,h) AFM height images of the corresponding samples. (i,j,k,l) Representative Raman spectra for the samples with reducing D band as full monolayer coverage is achieved.

By forming a plot of individual grain sizes for low growth times and grain sizes of merging flakes for longer growth times, it is shown how the grain size depend on temperature (Figure C.4a). One can also determine the growth rate change with respect to the growth time (Figure C.4b). The growth rate is seen to be approximately linear initially and then rapidly slows and stops. This behavior is attributed to the merging of the individual flakes and reduction in free edges as the film grows to eventually encompass the entire substrate surface. A comparison of grain size and growth rate in this work as compared with other reports is listed in Table C.1. In the table, it is seen that initial growth

rate of 375 nm/hour found in this work is the highest among similar works for direct graphene synthesis over Si/SiO<sub>x</sub> substrates. Moreover, here this chapter demonstrates, for the first time, large area homogeneous monolayer directly formed over Si/SiO<sub>x</sub> substrates using thermal CVD and, importantly, a sandwich or confinement technique.

Examination is also conducted on the diameter of the individual disk shaped islands during early growth and their temperature dependence (Figure C). SEM evaluations show the graphene disk diameter increases with increasing temperature for a given reaction time (2 hours). In addition, the density of the disks increases with increasing temperature indicating an increase in nucleation rate with increasing temperature. From the data, Arrhenius plots are prepared from which the activation energies are extracted for the disk diameter and disk density (nucleation density) [189, 304]. They are  $7.2 \pm 1.5$  eV and  $4.6 \pm 0.6$  eV, respectively. The activation energies for the grain/disk diameter are comparable with other works for the direct formation of graphene over dielectrics [304] and these values are much higher than found for graphene growth over Cu [114, 192, 203]. On the one hand, the non-catalytic feature of SiO<sub>x</sub> surface determines the larger energy barrier to overcome prior to the reaction initialization than over catalytic Cu. On the other hand, the gaseous diffusion in the micro pores (*cf.*, Figure C.3) is suppressed in the SiO<sub>x</sub> sandwich configuration in comparison to the open surface configuration (facing up). Therefore, the activation energy for gas diffusion is increased. This will increase the total activation energy because in this work the activation energy are extracted from the total reaction, *viz.*, from carbon feedstock to the graphene (without considering the middle transitional processes).

The increasing growth rates of the graphene disks with respect to increasing temperature are attributed to improved thermal decomposition of the feedstock

at higher temperatures. This finding is supported by thermodynamics calculations which show and increase in mole fraction for C with increasing temperature, as well as an increase for the two most prominent radicals, H\* and CH<sub>3</sub> (Figure C.6). The thermodynamic calculations also confirm that thermal CH<sub>4</sub> decomposition occurs at the growth temperatures used in this study, *viz.*, decomposition occurs without a catalyst.

Now the large area homogeneous single layer graphene directly formed over Si/SiO<sub>x</sub> with the sandwich configuration are characterized using low voltage (80 kV) Cs corrected high resolution transmission electron microscopy (HRTEM), selected area electron diffraction (SAED) and dark-field transmission electron microscopy (DF-TEM). Figure 6.4a shows a low magnification micrograph of a typical (transferred) graphene film covering over a holey carbon/Cu TEM grid. A representative SAED pattern from this region (Figure 6.4b) shows the three-fold diffraction symmetry of the material and the reflex spacing's are indicative of crystalline graphene. The relative intensities of the reflex spots across the {11-20} and {10-10} directions confirm monolayer graphene [1, 237]. High resolution micrographs (Figure 6.4c,d) present the honeycomb-like graphene lattice. In areas where a hole exists (data not presented), layer counting from the edge also confirms the presence of monolayer graphene [260].

DF-TEM allows one to determine the domain size, shape and relative rotation angles of the graphene grains forming the single-layer polycrystalline film [65, 66, 242, 305]. Examples are provided in Figure 6.4e, Figure C.7, Figure C.8 and Figure C.9 in Appendix C. False color is used to aid the eye to easily see the grain shape and relative grain orientations in Figure 6.4e and Figure C.7. The DF-TEM data consistently show the grains are faceted, *i.e.*, the single-layer graphene film comprises stitched polygonal graphene grains and this observation differs significantly to the grain shapes found in polycrystalline monolayer graphene formed over Cu using common CVD routes [66, 305].



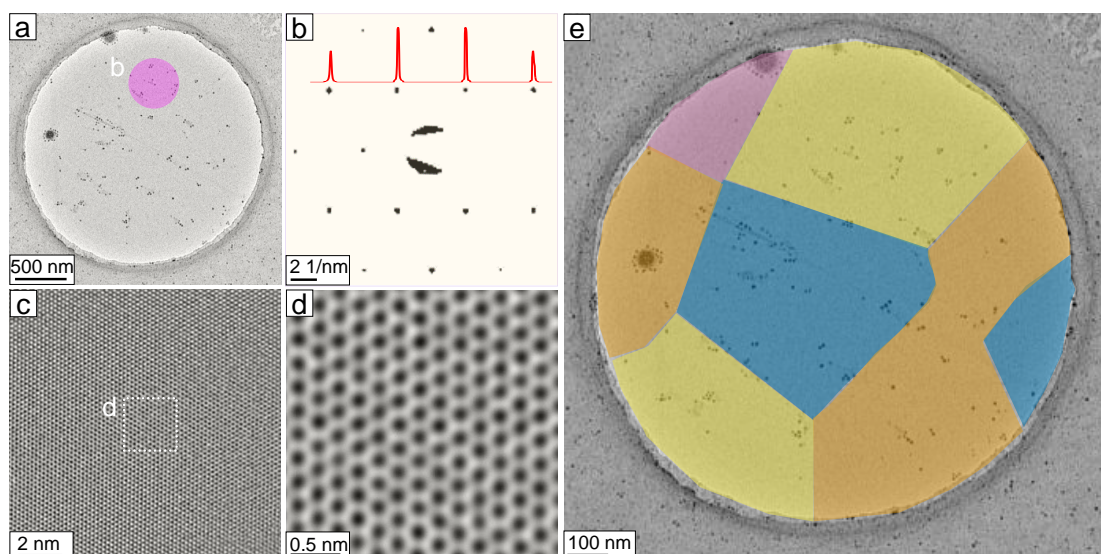


FIGURE 6.4: TEM characterizations of the large area synthetic monolayer graphene (from sandwich configuration). (a) Low magnification micrograph of graphene film transferred onto a holey carbon TEM grid. (b) SAED pattern of the region circled in (a). The inset profile shows the intensity profile of the diffraction spots. (c,d) High resolution TEM images showing the honeycomb atomic configuration of graphene. (e) False color composite micrograph highlighting the different domain (grain) orientations and faceted grain-boundaries. Corresponding DF-TEM images showing how the composite image is formed are provided in the [Appendix C](#) in [Figure C.7](#).

## 6.5 Grain boundaries in graphene film

In order to better understand the grain boundaries, complementary studies are conducted by employing atomic force microscopy (AFM), scanning electron microscopy (SEM) and low voltage HRTEM studies. [Figure 6.5a](#) shows a typical AFM topography image of monolayer graphene film. The tomography images show regions of lines of bright contrast (increased height) concomitant with the faceting of the grains as shown in [Figure 6.5a-c](#). Phase imaging ([Figure C.10](#)) makes observation of the facets easier [306] and also allows one to determine where grain boundaries with no height change most probably are (using WSXM processing software). Height measurement statistics show boundary heights varying between 0 and 1.4 nm (average 0.30.04 nm and are discussed in detail

below. The faceted grain boundaries are mostly visible by SEM and show up as lines of reduced intensity relative the monolayer graphene on the Si/SiO<sub>x</sub> substrate (Figure 6.5e-f).

The reduced contrast in SEM occurs because the local curvature of a raised graphene grain boundary provides more shielding for the secondary electron emission (from the Si/SiO<sub>x</sub> substrate) so that the facets look darker than the overall flat graphene film lying flush with the substrate [307, 308]. The reduction in contrast is determined to be as much as  $22 \pm 4\%$  (as extracted by Gwyddion image analysis software). In both the AFM and SEM data the faceted grain boundaries are analogous to those found with DF-TEM mapping, as for example shown in Figure 6.5g in which the faceted grains are presented in false color along with their relative rotation angles.

With HR-TEM the grain boundaries are observed at high magnification and at this scale the boundaries do not appear straight but have a degree of curvature and form through pentagon-heptagon pairs, much as with graphene grain boundaries in general as this arrangement exhibits the lowest energy configuration [309, 310]. The amplitude of the (in plane) undulations in the grain boundaries ranges from 0.6 to 1.2 nm (see also Figure C.11). A fuller analysis of the grain boundary heights and their relative rotation angles show a correlation as presented in Figure C.12 in Appendix C in the supplementary information.

The collected statistics of the grain boundary heights do not fit a Gaussian profile; indeed the profile seems to have three peaks (Figure C.12a). Moreover, a statistical analysis of the relative rotation angles between grains also shows three peaks in the distribution (Figure C.12b). These data are in excellent agreement with a theoretical study by Carlsson et al. [308] which correlates grain boundary (out of plane) heights with relative rotation angles. The theoretical study showed that the most common rotation angle is  $28^\circ$  in agreement with the experimental data in this work as well as that from others [65, 311]. The relative height for relative rotations of  $28^\circ$  were predicted to be between 0 and

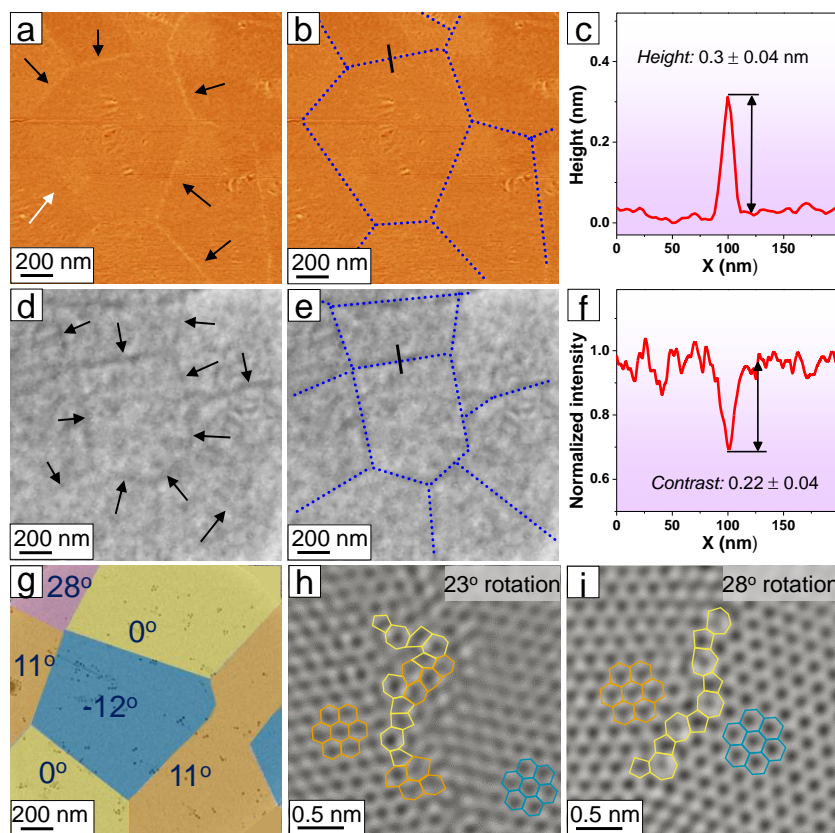


FIGURE 6.5: Complementary microscopy investigation of faceted graphene film for sandwich substrate configuration. (a) AFM height image showing the facets of graphene domains, with black arrows indicating grain boundaries. (b) Outlining the grain boundaries. The height profile (c) across the black bar in (b) showing the local curvature with a height of 0.3 nm. (d) SEM graph of the graphene film showing darker contrast of the grain boundaries and (e) its outline and (f) the intensity profile across the black bar. (g) False color composited TEM image indicating the facets and rotational misorientations between two adjacent grains. (h,i) HR TEM graphs for the grain boundaries of  $23^\circ$  and  $28^\circ$ , respectively. The grain boundaries are stitched with carbon pentagon-heptagon pairs.

0.3 nm; it is experimentally observed *ca.* 0.2 nm in this work. The theoretical work also claimed heights between 0.6 to 0.8 nm and 1.0 to 2.0 nm for relative grain rotations of around  $10^\circ$  to  $20^\circ$  and  $0^\circ$  to  $10^\circ$ , respectively. Again, this experimental data are in good agreement with the theoretical study.

## 6.6 Bubble clustering of faceted graphene grains

Analysis comes to the evolution mechanism, *i.e.*, merging of the individual disk like islands that ultimately yield faceted grains in the large area homogeneous monolayer graphene film. The formation of facets with merging disks occurs as they seek to minimize their perimeter and hence minimize energy. Much like multiple bubbles clustering, their minimal configuration is achieved when the shape of the cluster is faceted [312–314].

This process ideally leads to the formation of hexagons. By analogy the hexagon cells in a beehive which require the minimum possible amount of wax. In this large area homogenous single layer graphene are for the most part hexagonal although at times deviations, such as 4, 5 and 7 sided polyhedral, are seen (Figure C.13), which is attributed to the non-uniform spatial distribution of the nucleating islands. The faceting process of clustering islands is illustrated in Figure 6.6.

A key advantage of this approximation toward hexagonal faceting of the grain, is that the sum length of grain boundaries per unit area  $\sum L_{GB}/\pi r^2$  is less than for most large-area graphene films grown over metal where grains usually complex grain shapes are obtained and so the sum length of grain boundaries per unit area in these cases is larger.

Grain boundaries are scattering sites that can reduce electrical performance [305], and hence, as is shown below, because of the faceting and hence minimization of grain boundaries this large area homogeneous single layer graphene competes very favorably with single crystal graphene grown over non-metals and large-area graphene grown over Cu.

The growth mechanism is summarized in Figure 6.7. After a thermal CVD procedure, the sandwiched two Si wafers result in strictly monolayer graphene films on both the oxide surface.

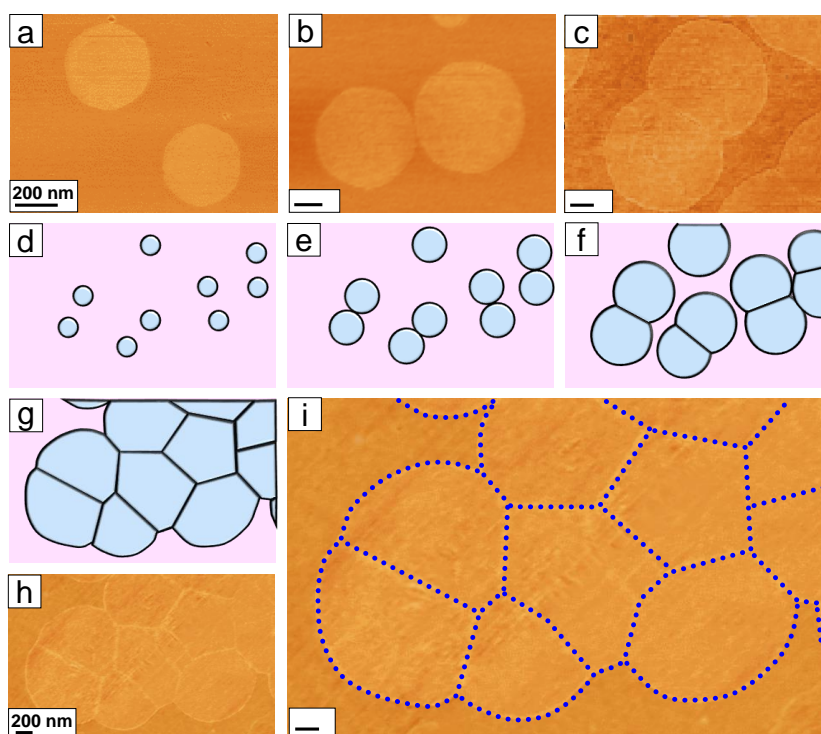


FIGURE 6.6: The growth evolution of graphene monolayer film in a bubble-merging fashion. AFM imaging for different stages. (a) Early formation of graphene nuclei. (b) Two adjacent graphene grains increase in size and both their frontier edges contact initially at tangential point. (c) The graphene domains continue growing and their grain boundaries become elongated. (d,e,f) Schematics of merging disk grains. (g,h) Sketch and AFM image for clustering of graphene disks. (i) Outline of the faceted grain boundaries of the monolayer graphene.

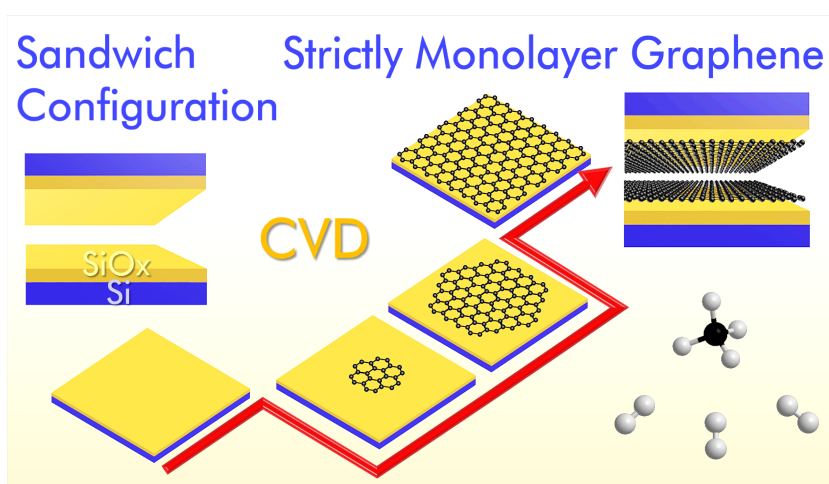


FIGURE 6.7: The growth schematic of strictly monolayer graphene film on both oxide surface of the Si wafers in sandwich configuration.

## 6.7 Electrical and optical performance of graphene

Hence, the optical and electrical performance are examined for the large area single layer graphene film directly fabricated over Si/SiO<sub>x</sub>. [Figure 6.8a](#) shows the optical transmittance of the graphene films after transfer on to a transparent quartz substrate. Starting from 450 nm, a 97% transmittance is achieved with  $97.9 \pm 0.5\%$  at 550 nm, which agrees well with the published data for monolayer graphene [37]. This further confirms the large area full coverage of the synthetic film is single layer graphene. [Figure 6.8b](#) shows a similar result ( $97.7 \pm 0.4\%$  at 550 nm) for 6-hour CVD growth. The fact that similar transmittance results are obtained for both 5 and 6 hours CVD growth shows that once a full coverage layer of graphene has formed (5 hours), continued CVD for extended periods does not lead to additional graphene layer formation *i.e.*, the growth reaction is self-limiting, probably because there are no available sites for new adatom formation due to depletion of active grain edges via stitching at the grain boundaries [315, 316]. The self-limiting growth is further supported by Raman spectroscopy studies on samples grown between 6 and 8 hours. All samples shows homogeneous monolayer graphene (*e.g.*, [Figure C.14](#)).

[Figure 6.8c](#) shows the output drain-source current characteristics of a graphene field effect transistor from this large area graphene with a back gate for tuning. [Figure 6.8d](#) shows the transfer characteristics (gate voltage manipulated drain current) for a drain source voltage of 0.1 V. The ambipolar transfer curve shows p type doping, which is attributed to adsorbents from the air [317, 318] and/or chemical residue from the device fabrication process [40]. The carrier mobility from 20 fabricated transistors using this monolayer graphene grown directly over Si/SiO<sub>x</sub> ranged from 410 to 760 cm<sup>2</sup> V<sup>-1</sup> s<sup>-1</sup> (extracted from the middle linear region [54] of the transfer characteristics).

The FET mobility in this work is the best ever measured in a back-gated transistor for direct synthetic graphene monolayer full coverage films formed

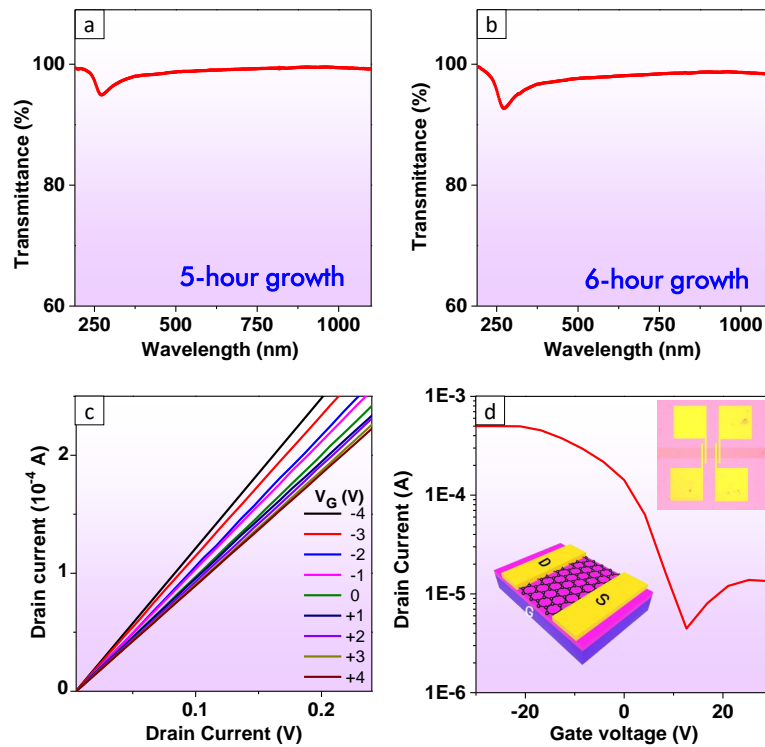


FIGURE 6.8: Optical and electrical performance of large area monolayer graphene (from the sandwich configuration, *cf.* Figure 6.1c). (a,b) Optical transmittance of graphene film (transferred onto a fused quartz substrate) for samples from 5 and 6 hours growth, respectively. (c) Output drain current for drain voltage while tuning gate voltage. (d) Transfer characteristics of the graphene transistor at a drain source voltage 0.1 V (p doping is observed). Insets are optical graph and the sketch of a graphene field effect transistor with a global p-doped Si back gate.

over a Si/SiO<sub>x</sub> substrate. A comparative study with other works can be found in Figure C.15a and Table C.2. Moreover, the mobility of direct synthetic graphene in this work approaches the performance of monolayer graphene full coverage films grown over Cu [127, 251]. To highlight the competitiveness of this large area monolayer graphene grown directly over Si/SiO<sub>x</sub> its electrical performance data are compared with published values, including graphene grown over Cu and present that in a graphical format (Figure C.15b) and in tabular form (Table C.3). Moreover, the ON/OFF ratio for drain-source current has a relatively high value as  $112 \pm 10$ .

## 6.8 Summary

In this chapter large scale homogeneous strictly monolayer graphene have been successfully fabricated with CVD growth directly over Si/SiO<sub>x</sub>. The large area uniform single-layer graphene films are fabricated by implementing a substrate confinement approach, in which the Si wafers are simply sandwiched together.

The space confinement provides an equilibrium in local chemical environment, in which carbon adatom preferably attaches at graphene grain edges other than the top of them. The edge-attaching grain growth allows for formation of strictly monolayer graphene grains which lead to strictly monolayer graphene film upon grain merging.

The cluster faceting mechanism has been proposed for graphene film formation directly over dielectric substrate. Initially during the formation circular or disk-like graphene islands form. As they grow and merge (cluster) faceted grain boundaries form and this arrangement is attributed to energy minimization, much like layers of bubbles clustering together. This behavior leads to a near minimal total length of grain boundaries per unit area, which is reflected in the optical and electrical characteristics of the as-produced film that is as competitive as equivalent large area graphene fabricated over Cu. Once full coverage of the film is obtained new graphene formation stops indicating the process is self-terminating. This termination mechanism provides a wide parameter window for laboratory synthesis as well as mass production.

This confinement approach for strictly monolayer graphene can be scaled up by simply stacking sandwiched Si/SiO<sub>x</sub> wafers on top of each other ([Figure C.16](#)). One should reinvigorate efforts for the direct synthesis of uniform graphene over Si/SiO<sub>x</sub> which has the key advantage of not requiring transfer as compared to CVD over Cu. Moreover, the technique holds promise in improvement for synthesis of other 2D materials and their van der Waals heterostructures.



# Chapter 7

## Conclusions

The primary aim of this thesis was to develop novel approaches for the synthesis of large area homogeneous monolayer graphene films over such substrates as Cu foils and Si wafers with an oxide surface. The graphene monolayers that were synthesized and characterized within this body of work represent an advance for large area continuous and strictly monolayer film over both Cu and Si/SiO<sub>x</sub> substrates, achieving a precision in control in terms of layer homogeneity. The optical and electrical performance of the resulting synthetic graphene films achieve an advanced level.

The synthesis of a strictly monolayer graphene film over a Cu substrate was successfully achieved by employing an oxidation pretreatment step prior to graphene synthesis by means of a chemical vapor deposition reaction. This systematic study of different pretreatments on a Cu substrate reveals that prior oxidation is the most efficient approach in providing a clean Cu surface following the H<sub>2</sub> annealing step, thereby facilitating the formation of a strictly monolayer graphene deposition within the subsequent CVD reaction. Conversely, other pretreatments without oxidation (*e.g.*, using organic solvent rinsing, FeCl<sub>3</sub> polishing, or non-pretreatment of Cu), result in a mixing of monolayer films and second layer flakes. Such second layer flakes were found to be formed during

the H<sub>2</sub> annealing step. By tracking the carbon sources for graphene flake formation, the organic contaminants were identified to have served as the precursors. Therefore, oxidation in air at 800 °C has proven to be the most efficient means so far of removing any organic contaminants which is necessary for the formation of strictly monolayer graphene films.

For the investigation of the thermodynamic and kinetic properties of graphene growth over a Cu substrate, a simple chemo-thermal method was established. Using this single step synthesis path, micro-sized graphene flakes over Cu were formed as a result of the pre-adsorption and post thermal annealing of organic molecules. This facilitates a more detailed understanding of the temperature-dependent growth behavior arising from three adsorbed solvents, namely acetone, isopropanol and ethanol, in which reaction activation energies for size growth and nucleation density are extracted from the Arrhenius plots as 1.4 - 1.6 eV and 2.1 - 2.7 eV, respectively. Obtaining these activation energies has enriched our understanding of graphene growth from a variety of carbon sources. Through a comparison of the experimental data obtained for graphene formation, with an associated thermodynamic calculation for fractions of reactive species at a chemical equilibrium state, a critical parameter window has been observed for graphene formation (*i.e.* 800 - 1025 °C, 2 - 10 mbar and a flow rate of 16 - 75 sccm H<sub>2</sub>). In addition, the quality of synthetic graphene flakes was found to improve with increasing reaction temperature, as indicated by the decreasing D band in the resultant Raman spectra. The effects of growth pressure and gas flow were studied and the optimal growth windows for obtaining larger grain sizes and densities were obtained as 1025 °C, 5 mbar, and a flow rate of 50 sccm H<sub>2</sub>, respectively.

The direct formation of a large area homogeneous monolayer graphene film was also successful over a Si/SiO<sub>x</sub> wafer substrate. A confinement approach in which a simple ‘sandwich’ of two Si/SiO<sub>x</sub> substrates, in which their oxide faces were in contact with each other, was developed. Within this confinement

approach, strictly monolayer graphene films were grown over a relatively large area ( $2 * 2 \text{ cm}^2$ ), and a precise control was achieved in terms of monolayer number and homogeneity. The optical transmittance of the resulting synthetic graphene film was in good agreement with the standard monolayer graphene film. The electrical carrier mobility of a transistor derived from the synthetic graphene film achieved an electron mobility of  $760 \text{ cm}^2 \text{ V}^{-1} \text{ s}^{-1}$ , exceeding that previously reported for graphene films which were directly grown on a Si/SiO<sub>x</sub> substrate (*cf.* [section 6.7](#)). Such a sandwich confinement employs the advantage of minimal roughness of the SiO<sub>x</sub> surface in comparison to the supporting plate (alumina). This allows for the control of small gas flow, possibly providing an equilibrium chemical environment for atom attachment at the grain edges rather than on top of them.

A time-dependent evolution of direct graphene growth over Si/SiO<sub>x</sub> was observed and interpreted as being of a faceting cluster nature. The faceting graphene grains have a minimum length for grain boundaries (known as scattering sites for charge carriers), which directly contribute to the improvement of electrical carrier mobility owing to the resultant decrease in scattering sites (grain boundaries).

The temperature dependence of the thermodynamic and kinetic properties of direct graphene growth over a Si/SiO<sub>x</sub> substrate was investigated. The statistical data enables the extraction of the growth activation energies, 7.2 eV and 4.6 eV for growth size and density, respectively. This confirms the higher temperatures which are required for graphene formation over non-catalytic dielectrics in comparison to catalytic metals such as Cu. These findings enrich and further our understanding of growth energy barriers in graphene monolayer formation and shed additional light on the exploration of the possibility of employing more ‘gentle’ parameters, such as a decrease in reaction temperatures, in future research.



# Chapter 8

## Outlook

Despite the novel insights afforded by this thesis in relation to the prospects for growing large areas of homogeneous monolayer graphene films, many avenues remain opportune for future investigation, and in particular the use of alternate substrates.

Based upon the findings presented with this thesis, a number of potential experiments are proposed for future investigation, including the:

- Early nucleation mechanism in the chemo-thermal synthesis route. It is a newly proposed growth mechanism for one-step thermal annealing to obtain graphene from adsorbed organic molecules (*cf.* Chapter 5). More experimental data on the early stages of the growth would provide more insights into how such graphene islands initially nucleate and how their growth can be controlled. In addition, an even deeper investigation of influence of other synthesis variables could be conducted to obtain more understanding such as underlying Cu grain orientations and textures.
- Thorough study of the nucleation mechanism of graphene over a Si/SiO<sub>x</sub> substrate. With a more detailed understanding of the nucleation sites

and density for early nuclei formation, it may be possible to employ pre-treatment steps to modify the substrate surface to control (decrease) the nucleation density so that average grain diameter can be increased within a complete graphene film.

- Further studies on the structure of the grain boundaries. The increase in average grain size holds promise in minimizing the total grain boundary length. Hence one can expect the improvement of electric carrier mobility performance. Moreover, one can plot the correlation of graphene grain boundaries (average grain sizes) with the electric transport performance. In addition, the grain boundaries themselves can be studied in greater details, *e.g.*, the correlation between GB height, the curvatures of graphene lattice, as well as the TEM imaging of atomic resolution.
- Systematic investigation of the influence of gas pressure and flow ratio (of the Ar/H<sub>2</sub>/CH<sub>4</sub> mixture) on the growth of graphene monolayers over Si/SiO<sub>x</sub> substrates. With an optimal parameter for large methane flow, the growth kinetics could be enhanced so that the total growth time can be reduced. However, the nucleation density will be expected to spontaneously increase, resulting in a decrease in average grain size. Therefore, there may be an optimal balance between growth rate and grain size that remains to be determined.
- Exploration of factors that may decrease the growth temperature. For example, the assistance of hydrocarbon decomposition by external forces (*e.g.*, plasma and/or catalyst), selecting a hydrocarbon that decomposes at lower temperatures, and the incorporation of oxygen (and other weak oxidants CO<sub>2</sub> and H<sub>2</sub>O) could enable the efficient synthesis of graphene at reduced temperatures.
- Transferability of graphene synthesized over Si/SiO<sub>x</sub> to other dielectric substrates such as sapphire and quartz, which have wider applications in

the fabrication of transparent conducting glasses and defoggers. To confirm the universal validity of the growth path proposed within this thesis, it will be important to synthesize graphene films over other substrates and to investigate their growth behavior.





# Appendix A

## Graphene synthesis over Cu and transfer to Si/SiO<sub>x</sub> substrate

The appendix A is supporting information for [chapter 4](#).

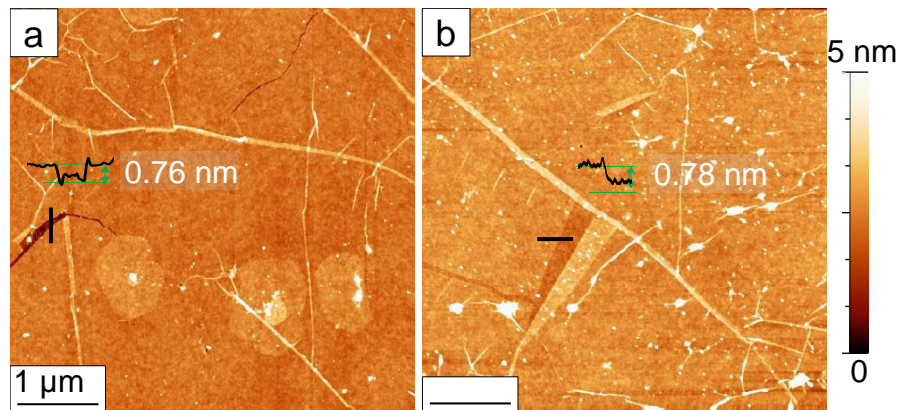


FIGURE A.1: AFM height determining the graphene thickness (starting from the substrate surface). (a) The height profile (black curve) is plotted from a graphene edge (labelled with black line). A typical height is 0.76 nm, indicative of monolayer graphene. (b) The height profile in experiment e is plotted, with a height of 0.78 nm, which again confirms a monolayer graphene film over the substrate. This height from substrate surface to the graphene surface is a straightforward way of determining the layer thickness and layer number.

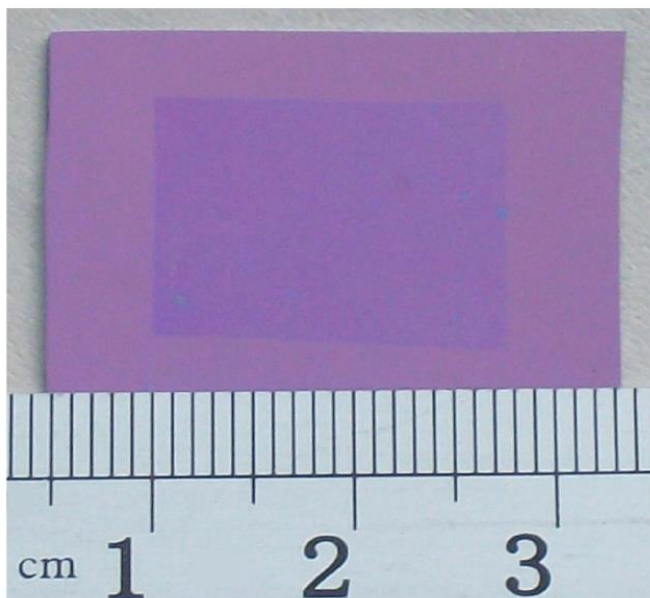


FIGURE A.2: Large area, clean, homogeneous monolayer graphene after transfer on to a Si/SiO<sub>x</sub> (300 nm oxide) wafer. The graphene sample was synthesized in experiment e.

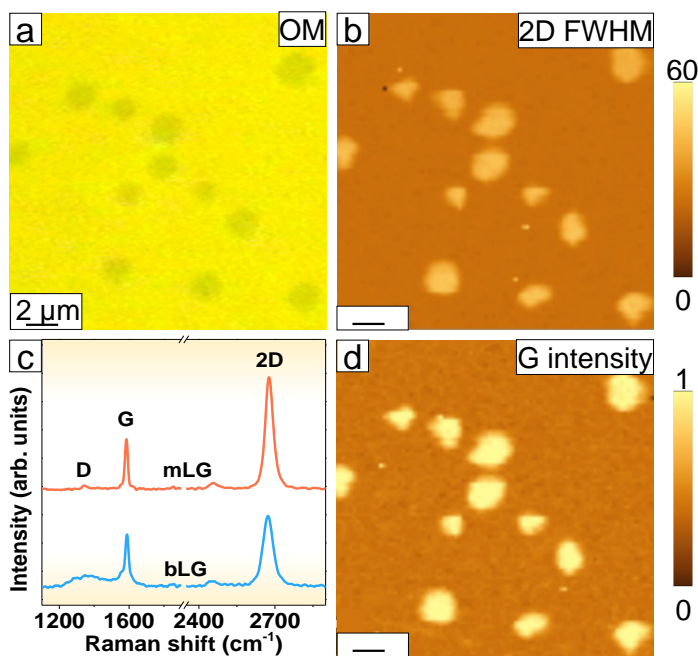
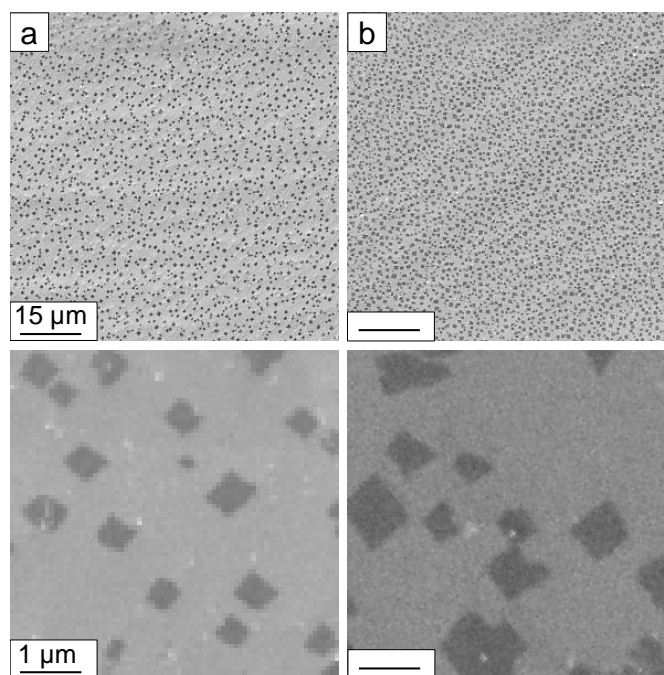


FIGURE A.3: Identification of ‘flakes’ on H<sub>2</sub> annealed Cu without any pre-treatment. (a) Flakes (in black) were clearly observed after transferred onto Si/(300 nm) SiO<sub>x</sub>. Raman mapping of 2D intensity (b) and G intensity (d) confirm that the graphene are isolated and randomly distributed on the substrate. (c) Raman spectra from two flakes displays the typical graphene feature of three bands: D band, G band and 2D band. The 2D/G intensity ratios range from 1 to 2, indicative of a mixing of monolayer graphene and bilayer graphene.



---

FIGURE A.4: SEM graphs of graphene flakes on H<sub>2</sub> annealed Cu foil (before the CVD synthesis, *i.e.*, prior to introducing CH<sub>4</sub>). (a) Pretreatment analogous to experiment b but wiping with acetone instead of isopropanol. (b) Pretreatment similar to experiment b but using ethanol for wiping the Cu surface.



# Appendix B

## Chemo-thermal synthesis of graphene over Cu

The appendix B is supporting information for [chapter 5](#).

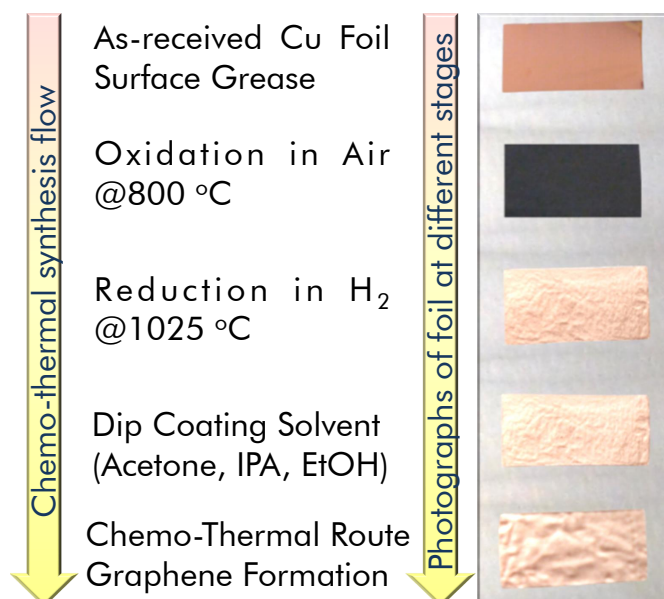


FIGURE B.1: The chemo thermal approach for graphene flake formation. (left) various steps in the synthesis procedure. (right) photographs of the Cu foils at different stages.

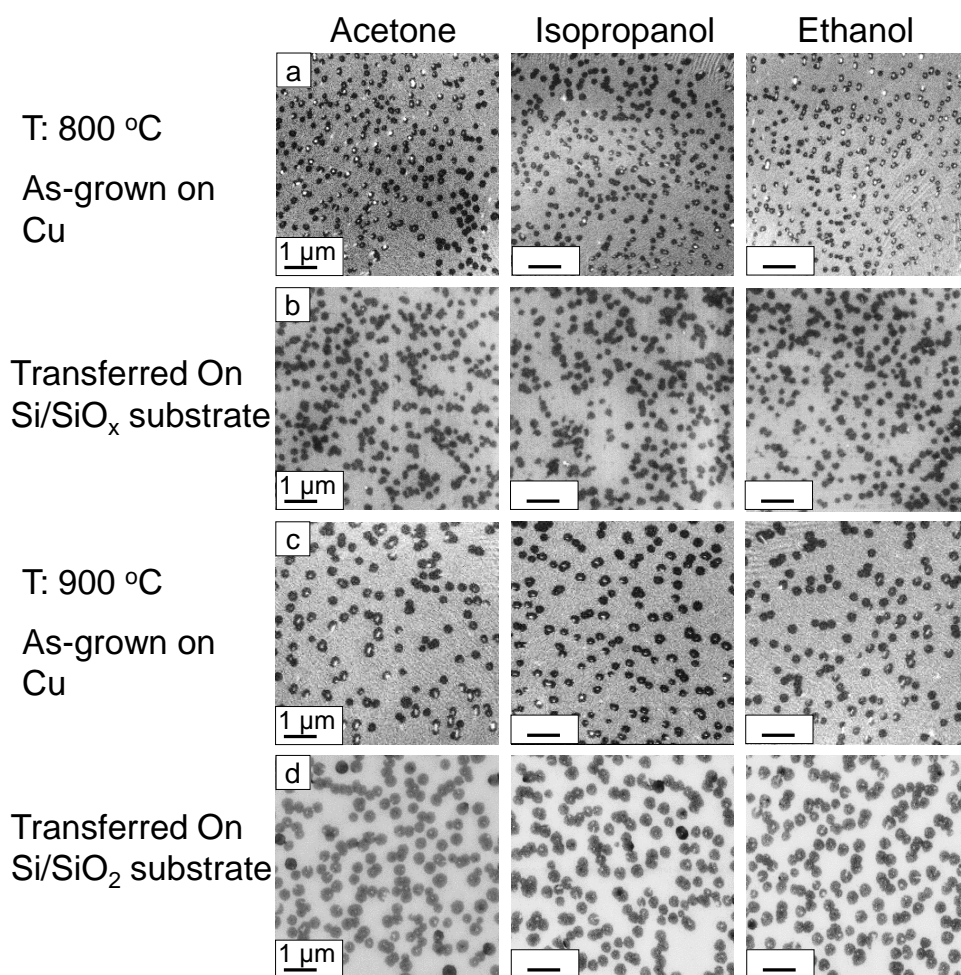


FIGURE B.2: Typical graphene flake synthesis over Cu and transferred on to Si/ (300 nm) SiO<sub>x</sub>. (Chemo-thermal synthesis parameters: temperature=800 °C and 900 °C, reaction pressure =10 mbar, H<sub>2</sub> flow rate =16 sccm).

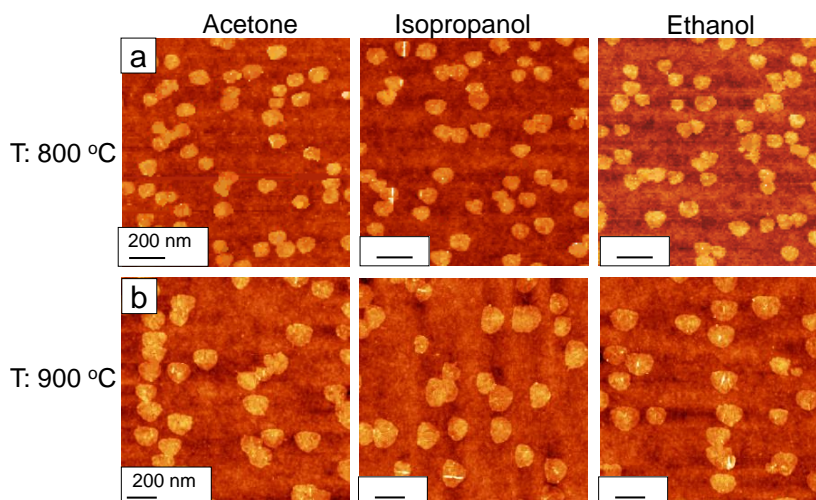


FIGURE B.3: AFM images of synthetic graphene flakes synthesis over Cu. These flakes are transferred on to Si/SiO<sub>x</sub> substrates for characterization. (Chemo-thermal synthesis parameters: temperature=800 °C) and 900 °C, reaction pressure =10 mbar, H<sub>2</sub> flow rate =16 sccm).

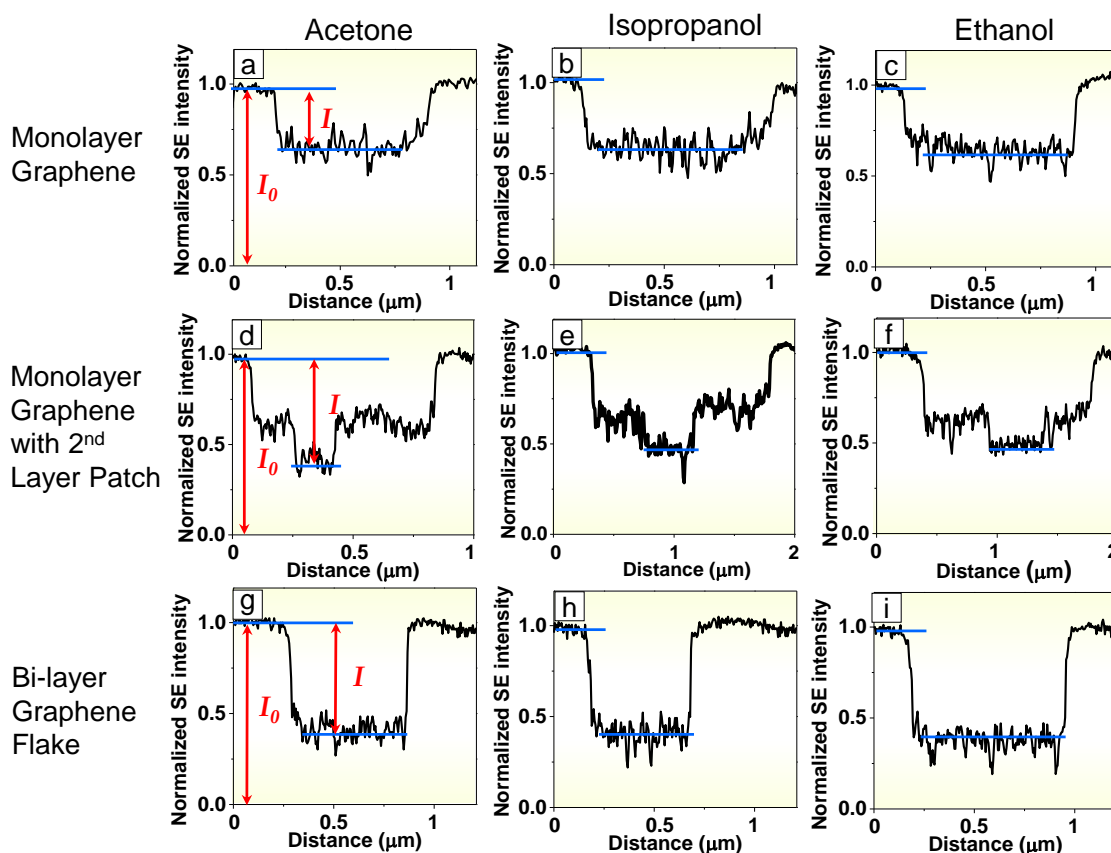


FIGURE B.4: Relative contrast of graphene flakes in SEM graphs in comparison to Si/SiO<sub>x</sub> background substrate in SEM micrographs from Figure 4.2 (using Gwyddion analysis software) for all three studied organic solvents.

TABLE B.1: Raman spectral information of graphene flakes from temperature experiments.

Temperature (°C)	Solvent type	D/G intensity ratio	2D/G intensity ratio	2D position (cm <sup>-1</sup> )
800	Acetone	2.9 ± 0.2	3 ± 0.1	2676 ± 3
	Isopropanol	3.0 ± 0.2	3 ± 0.2	2683 ± 4
	Ethanol	3.1 ± 0.2	3 ± 0.2	2696 ± 5
900	Acetone	0.9 ± 0.10	3 ± 0.1	2690 ± 5
	Isopropanol	0.72 ± 0.14	3 ± 0.1	2687 ± 4
	Ethanol	0.39 ± 0.08	3 ± 0.3	2685 ± 3
1000	Acetone	0.49 ± 0.11	3 ± 0.4	2681 ± 4
	Isopropanol	0.34 ± 0.06	3 ± 0.1	2688 ± 4
	Ethanol	0.26 ± 0.09	3 ± 0.2	2690 ± 5
1025	Acetone	0.16 ± 0.2	3 ± 0.2	2688 ± 4
	Isopropanol	0.20 ± 0.5	3 ± 0.2	2690 ± 5
	Ethanol	0.17 ± 0.3	3 ± 0.3	2686 ± 4

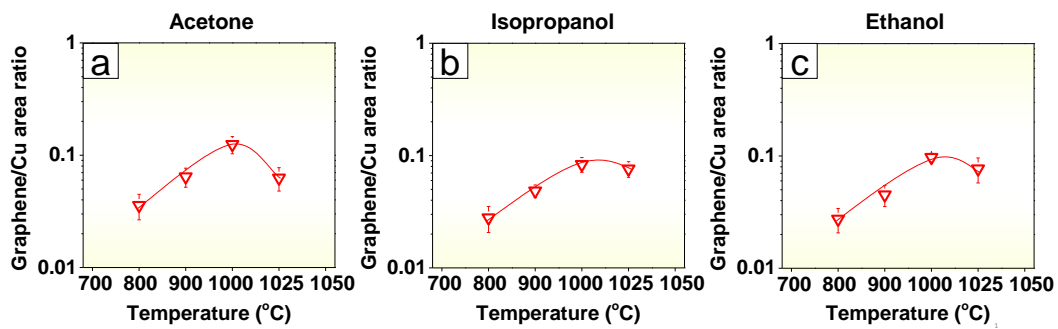


FIGURE B.5: Relative ratio of Graphene coverage area to Cu area in temperature experiments for adsorbed solvents such as acetone, isopropanol and ethanol (from left to right).



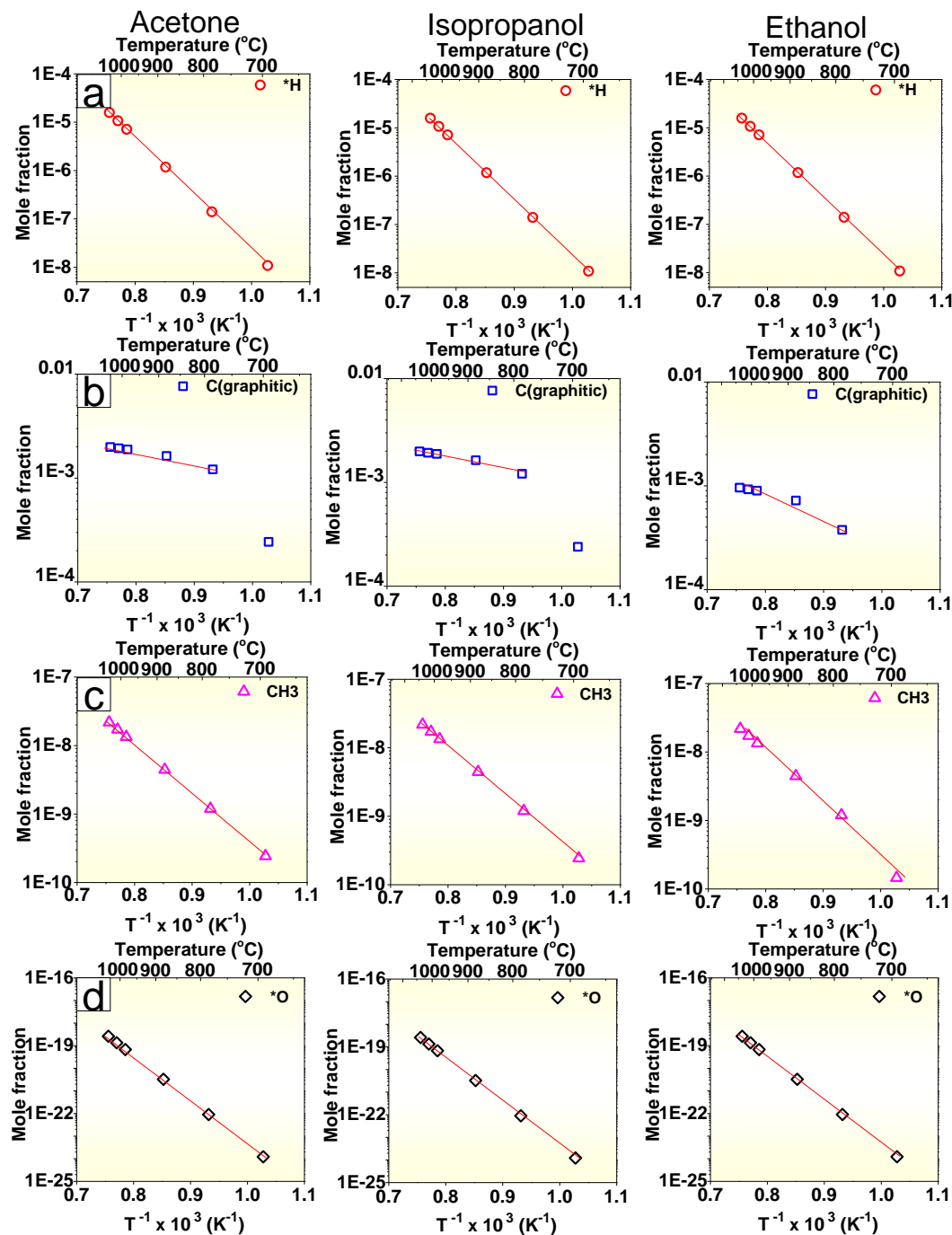


FIGURE B.6: Thermodynamic calculation at the chemical equilibrium state show the relative mole fractions for the four key radicals generated in the chemo-thermal reaction (top row:  $\text{H}^*$ ), (first middle row: graphitic carbon), (second middle row:  $\text{CH}_3$ ) and (bottom row:  $\text{O}^*$ ).

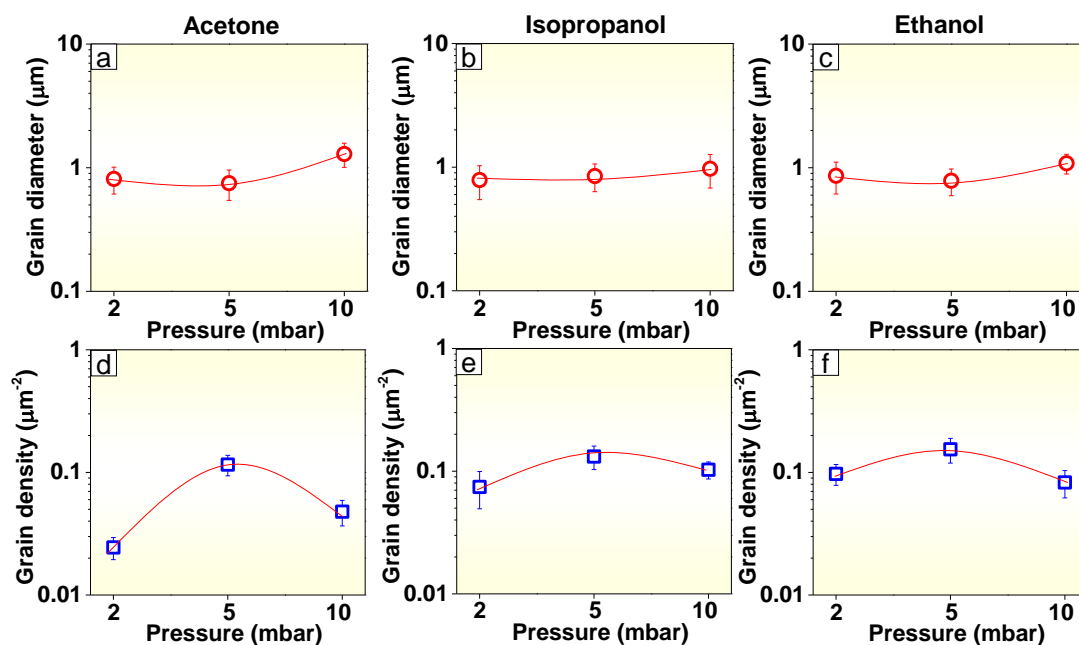


FIGURE B.7: Statistical information plots of grain diameter and grain density of the synthetic graphene flakes. Top row: average diameter and bottom row: average density with respect to reaction pressure.

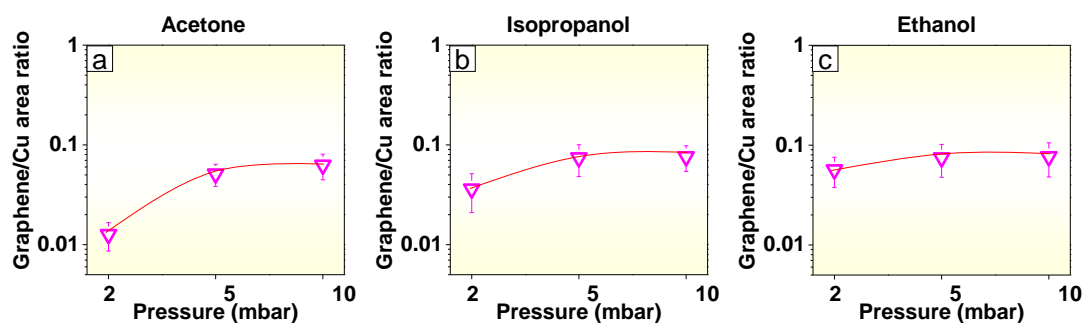


FIGURE B.8: Relative ratio of graphene coverage area to Cu area (pressure experiments) for adsorbed solvents such as acetone, isopropanol and ethanol (from left to right) for the pressure-dependent growth experiments.

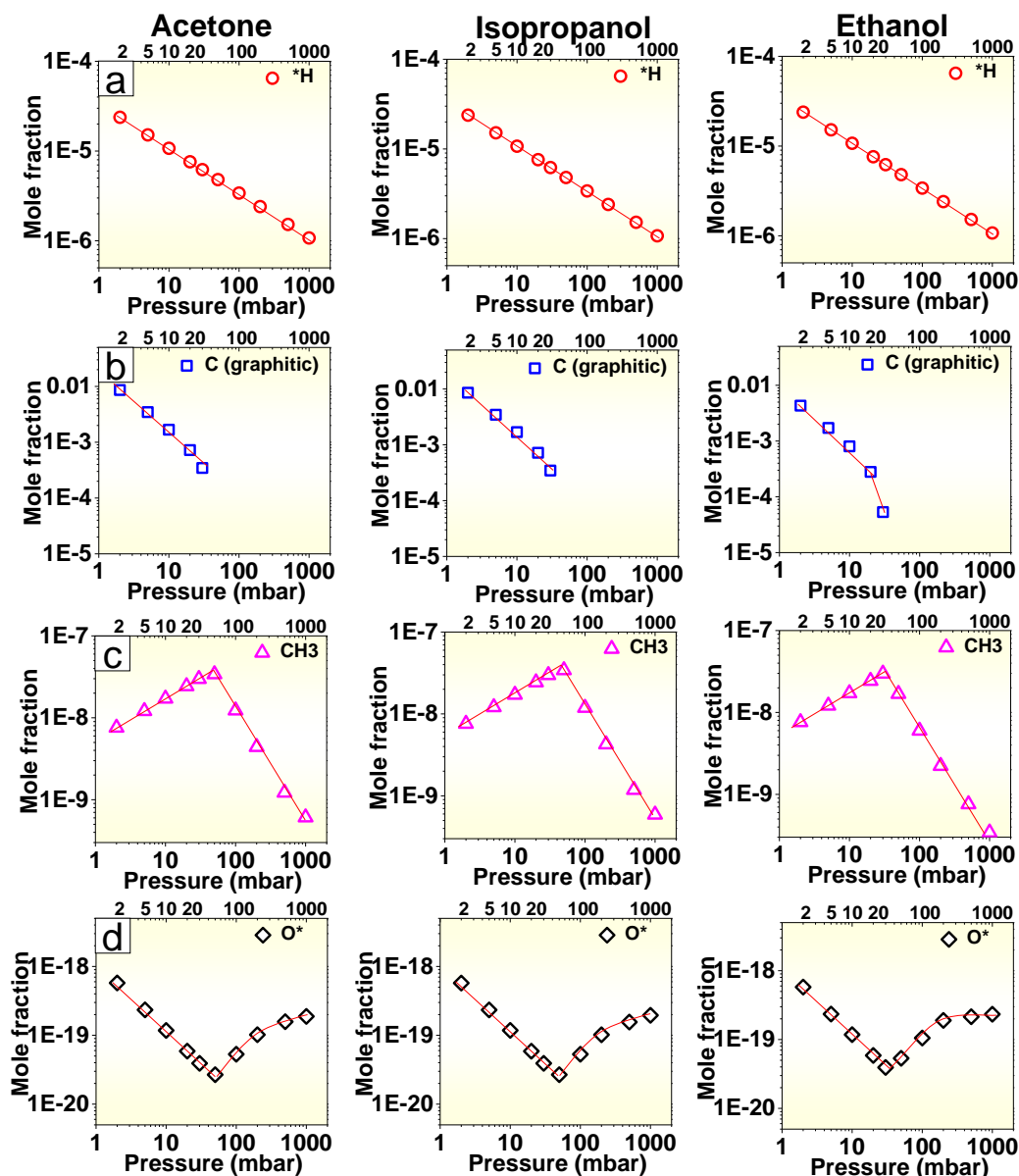


FIGURE B.9: The plots of mole fraction of radicals at chemical equilibrium state (pressure experiments) from thermal decomposition of acetone, isopropanol and ethanol (plus  $\text{H}_2$ ) with respect to reaction pressure. When pressure is higher than 50 mbar, no graphitic carbon is formed. When pressure goes above 10 mbar, only negligible mole fraction of graphitic carbon is generated.

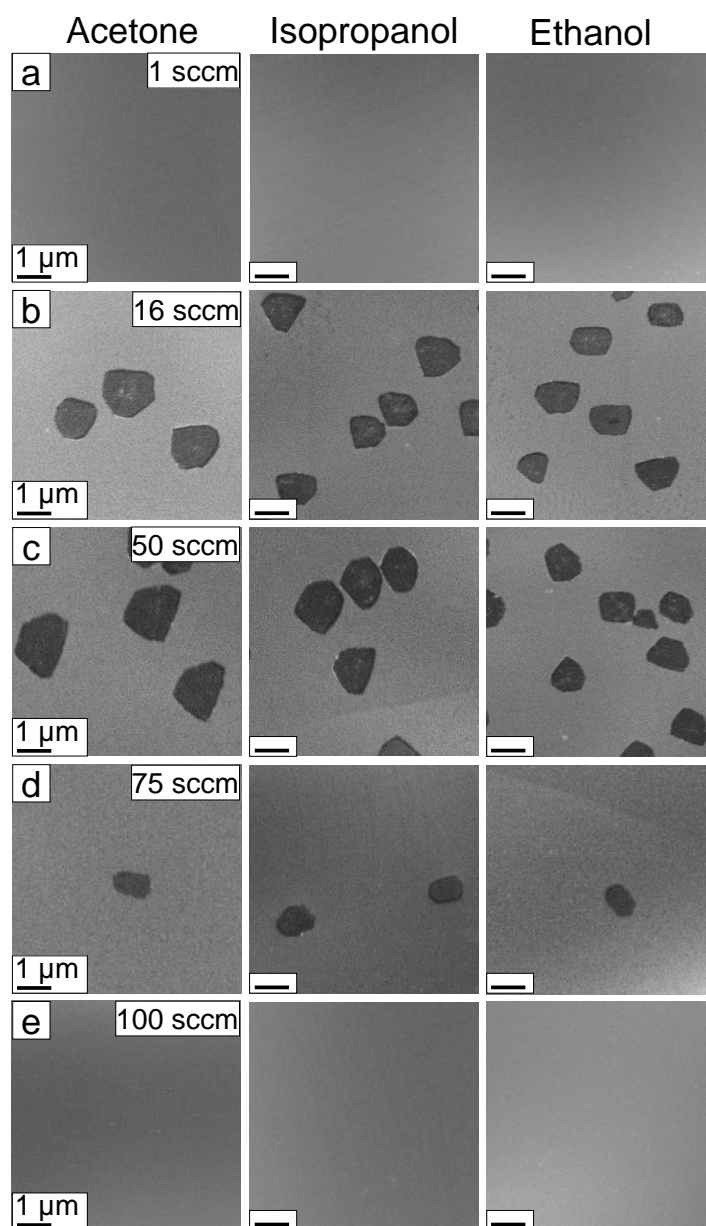


FIGURE B.10: SEM micrographs of the synthetic graphene flakes (H<sub>2</sub> flow dependent experiments).

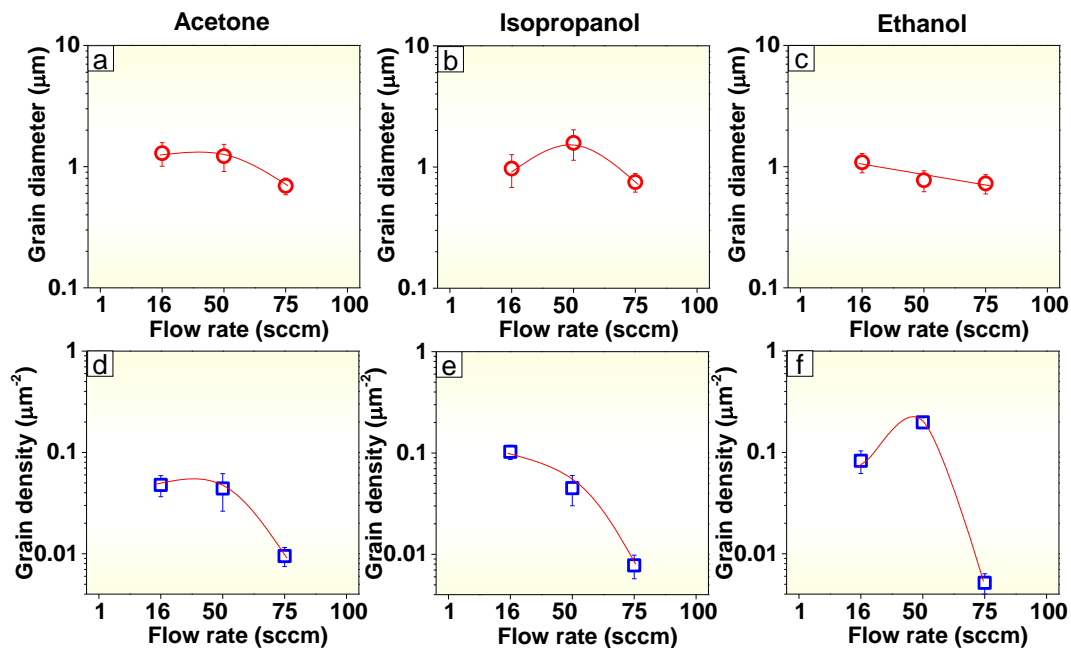


FIGURE B.11: Statistical information plots of average diameter and grain density of the synthetic graphene flakes ( $\text{H}_2$  flow dependent experiments). Top row: average diameter and bottom row: average density with respect to reaction  $\text{H}_2$  flow.

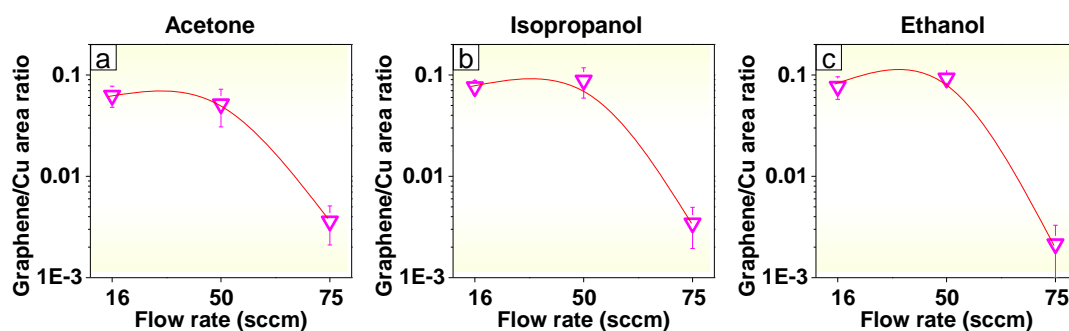


FIGURE B.12: Relative ratio of graphene coverage area to Cu area ( $\text{H}_2$  flow experiments) for adsorbed solvents such as acetone, isopropanol and ethanol (from left to right) for the  $\text{H}_2$  flow rate-dependent growth experiments.

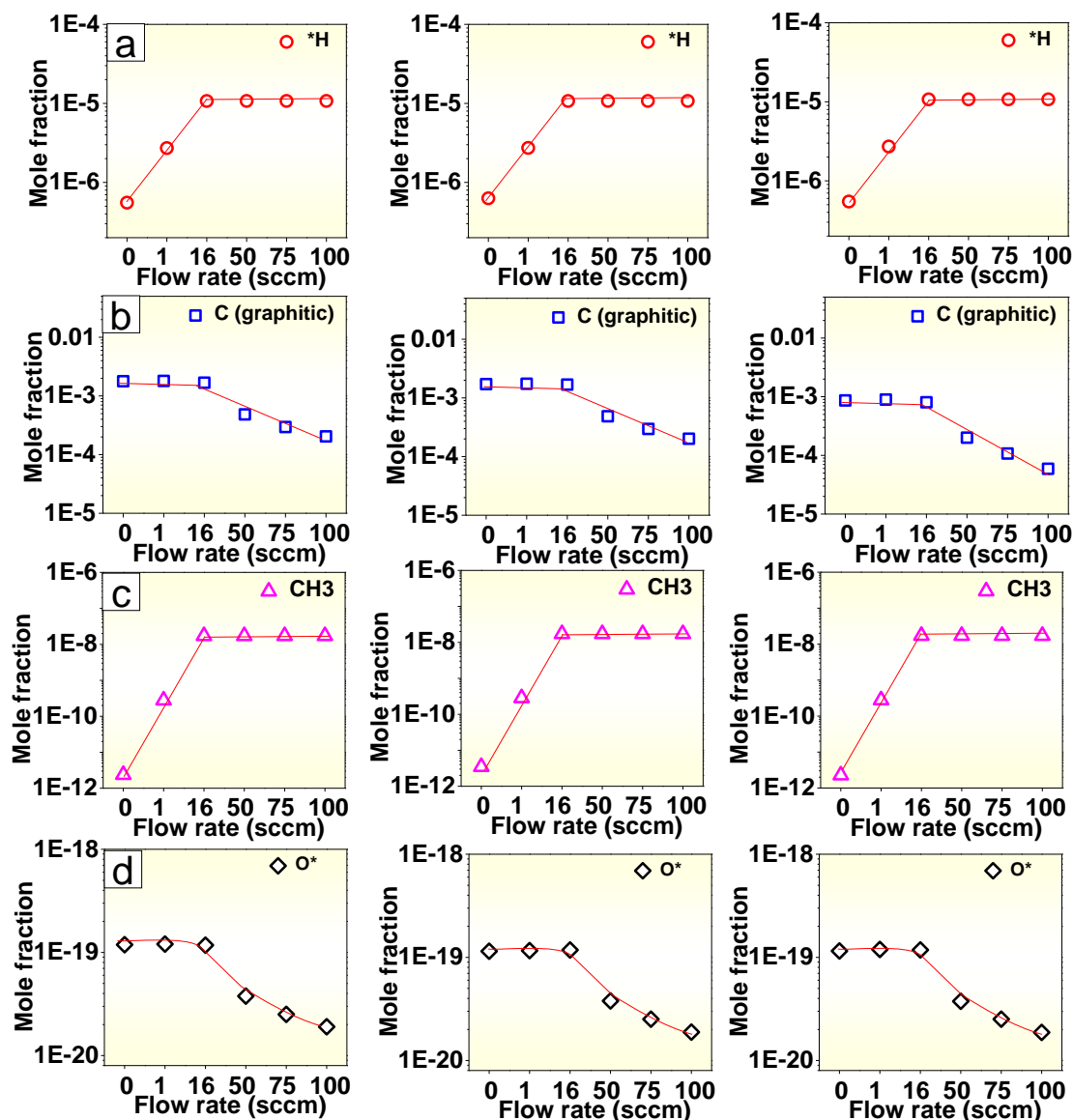


FIGURE B.13: The plots of mole fraction of radicals at chemical equilibrium state ( $H_2$  flow experiments) from thermal decomposition of acetone, isopropanol and ethanol (plus  $H_2$ ) with respect to  $H_2$  flow rate. When the  $H_2$  flow rate increases, the mole fraction of graphitic carbon decreases. This is due to the increasing ratio of hydrogen in comparison to the organic solvent molecules.

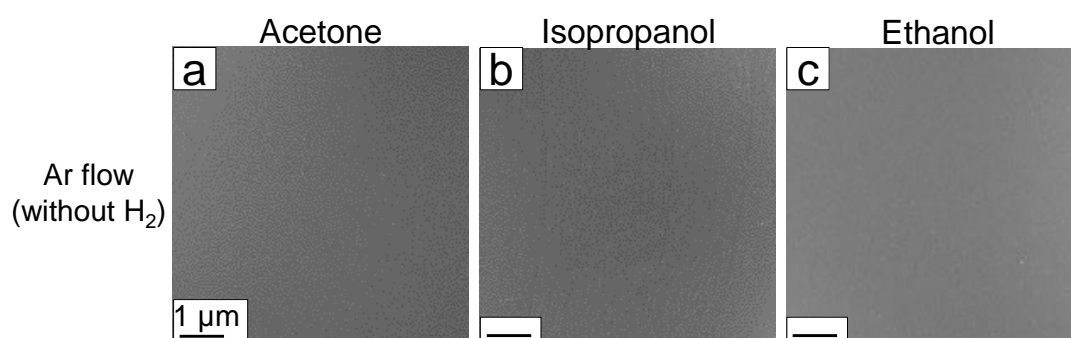


FIGURE B.14: SEM micrographs of the synthetic graphene flakes in the pure Ar flow (without any H<sub>2</sub>).





# Appendix C

## CVD graphene growth directly over Si/SiO<sub>x</sub> substrate

The appendix C is supporting information for [chapter 6](#). It includes: Materials and methods, publication statistics for graphene synthesis over various substrates, AFM of the surface of Si/SiO<sub>x</sub> and alumina substrates, a photograph of a large area graphene film, statistics for the growth rate, detailed dark field TEM analysis, AFM height and phase images, HRTEM of undulation at graphene grain boundary, statistics of the grain diameter and rotational angle and comparison of height and rotational angles at grain boundaries.

This appendix also cover the comparison of the electrical mobility in this work with that in the literature for metal and non-metal substrates, temperature-dependent graphene evolution and Arrhenius plots of grain diameter and density, chemical equilibrium calculations on the gas decomposition at different temperatures, and a schematic for the multi-stacking of the sandwich configuration for scale-up production.

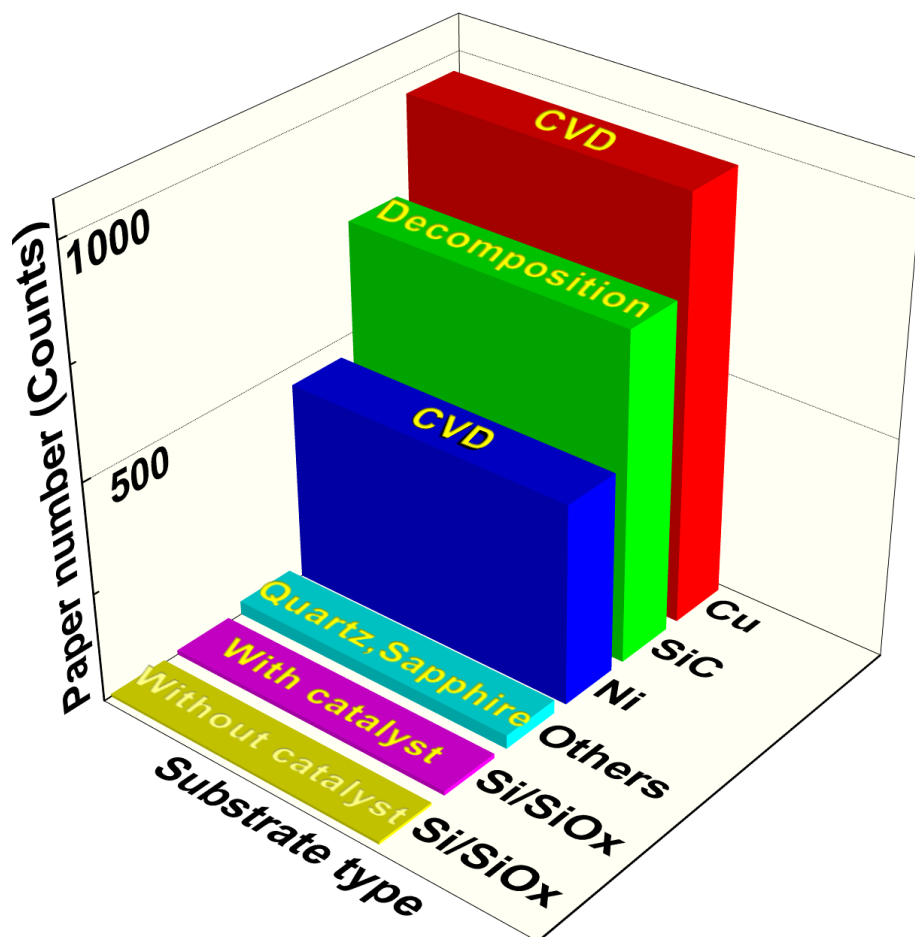
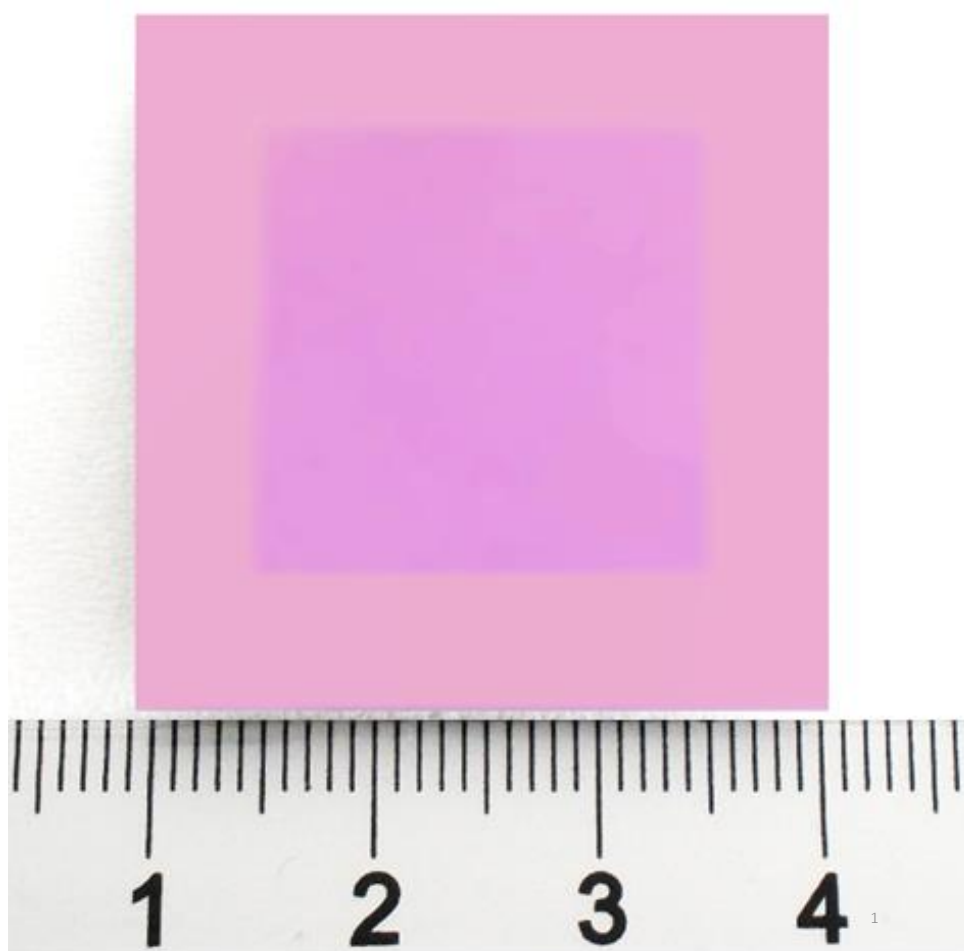


FIGURE C.1:

Comparison of the paper numbers of the study in graphene synthesis over various substrates. The papers of graphene growth on Cu substrates contributes to the highest counts. The research of graphene synthesis over SiC and Ni have decreasing but still large paper numbers. The research of graphene over Si/SiO<sub>x</sub> attract the least attention so the paper number is smallest. This suggests that more research efforts should be attracted on the Si/SiO<sub>x</sub> substrates. In addition, there are some papers on other substrates, *e.g.*, quartz, glass, sapphire, Si<sub>3</sub>N<sub>4</sub>, SrTiO<sub>3</sub> and Ge. The database in Web of Science (Thomson Reuters) is adopted to determine the paper number of graphene synthesis over various substrates. For example, we search the key words for ‘graphene’ and ‘Cu’ (and also ‘copper’) to determine the graphene growth over Cu substrates and so forth for other substrates.



---

FIGURE C.2:

Optical photograph of a centimeter-size large graphene film after transfer. The graphene was originally synthesized on a Si wafer containing a 300 nm-thick SiO<sub>x</sub> layer. This technique renders homogeneous and large area graphene.

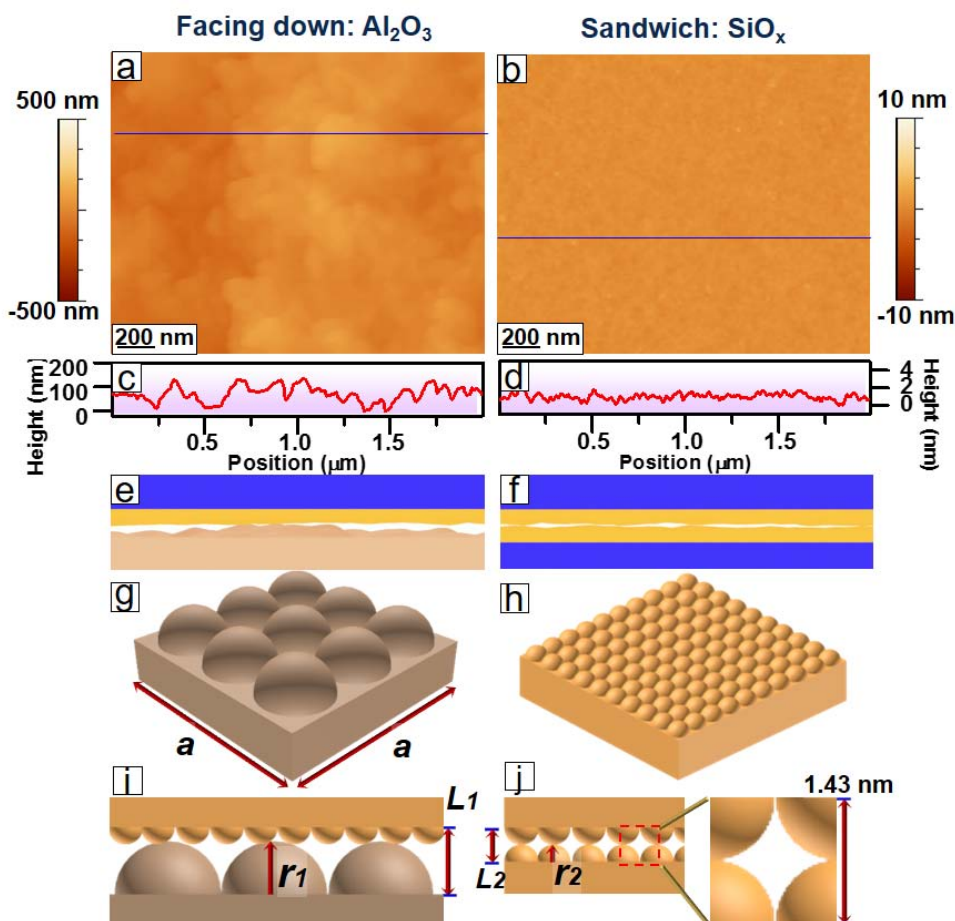


FIGURE C.3: AFM images showing a comparison of the topographic features of sintered alumina (Al<sub>2</sub>O<sub>3</sub>) in panel a and silicon/silicon oxide (Si/SiO<sub>x</sub>) wafer in panel b. The Si wafer has a 300 nm thick layer of SiO<sub>x</sub> (polished). The typical height profiles of both substrates are shown in (c) and (d) below the images. Each of the substrate has a different root mean square (RMS) roughness. The RMS was used to characterize the surface roughness by doing the statistics of the height of each pixel in the AFM images. The sintered alumina has a larger surface roughness (RMS  $101 \pm 8$  nm) than the polished SiO<sub>x</sub> layer over the Si wafer (RMS  $0.18 \pm 0.02$  nm). (e,f) The schematic of the cross section view of the reaction interfaces for graphene growth on the SiO<sub>x</sub>/Al<sub>2</sub>O<sub>3</sub>. (e) SiO<sub>x</sub>/SiO<sub>x</sub> sandwich (f), respectively. (g, h) Simplified models for the surfaces of Al<sub>2</sub>O<sub>3</sub> and SiO<sub>x</sub>, respectively. (i, j) A cross section view of the gap between the interfaces of SiO<sub>x</sub>/Al<sub>2</sub>O<sub>3</sub> and SiO<sub>x</sub>/SiO<sub>x</sub> configurations, respectively. There is larger space in SiO<sub>x</sub>/Al<sub>2</sub>O<sub>3</sub> interface (147 nm) than a SiO<sub>x</sub>/SiO<sub>x</sub> interface (1.43 nm) from the peak-valley height difference estimation (in AFM height image). When comparing with the relevant reactive species: C<sub>2</sub> dimer (0.3 nm) and C<sub>6</sub> graphitic hexagon (0.45 nm), the gap space is much larger. Therefore, the sandwich configuration provides sufficient gap space that allows for all reactive species to diffuse through (the micro-pores and the macro-pores).

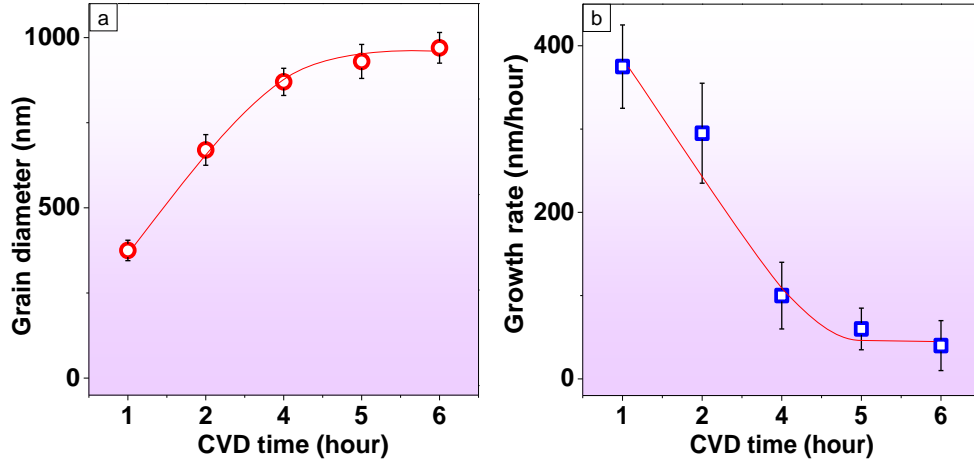


FIGURE C.4:

Statistics for time dependent evolution (grain diameter and growth rate) in graphene formation. (a) The grain diameter increasing with time and reaching its saturation point after 5 hours. (b) The growth rate is the highest ( $350 \pm 25$  nm/hour) at 1 hour. After 2 hours it is lower ( $320 \pm 20$  nm/hour) than the initial hour. After 4 hours it reaches  $100 \pm 15$  nm/hour and after 5 hours it reaches its minimum growth rate at  $40 \pm 8$  nm/hour and the grain stops growth.

TABLE C.1: Comparison of grain diameter and growth rate from this work and others in the literature for graphene over dielectric substrates.

No.	Grain size ( $\mu\text{m}$ )	Type of graphene	Growth time (hour)	Growth rate (nm/hour)	Substrate	Temperature ( $^{\circ}\text{C}$ )	Reference
1	1	Monolayer film	5	375	Si/SiO <sub>x</sub>	1185	This work
2	0.9	Monolayer film	6	100	Molten glass	1000	[294]
3	0.2	Monolayer film	8	60 - 300	Si/SiO <sub>x</sub>	1100	[50]
4	0.1	Monolayer film	0.05	800	Sapphire	1650	[161]
5	n.a.	Monolayer film	1	n.a.	Si/SiO <sub>x</sub>	1100	[299]
6	10	Individual grain	72	14	Si/SiO <sub>x</sub>	1180	[49]

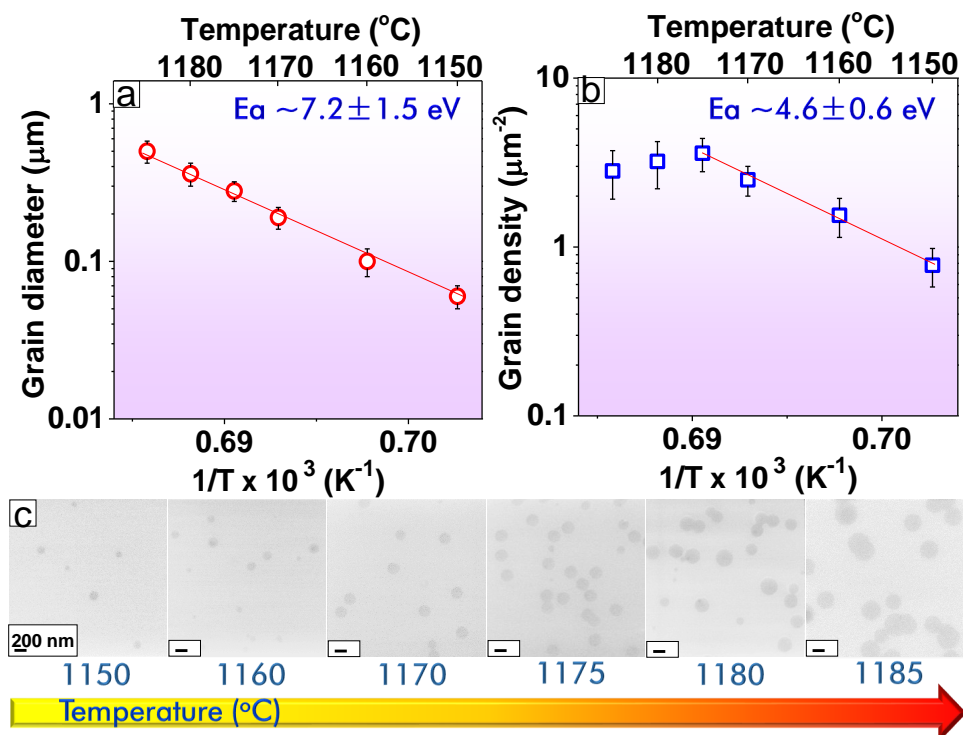


FIGURE C.5:

Temperature-dependent growth evolution of graphene disks (for sandwich configuration). (a, b) Arrhenius plots of the statistical grain diameter and grain density for different temperatures. Insets: the activation energies,  $E_a$ , are extracted based on the slope of the Arrhenius plots. (c) SEM graphs for graphene formation at different temperatures. The implemented equation is  $k = Ae^{-E_a/RT}$ , where  $k$  is the growth rate,  $A$  is a pre-factor,  $E_a$  is the activation energy for the total graphene formation reaction,  $R$  is the gas constant,  $T$  is the temperature (Kelvin). The activation energy for the grain diameter indicates the energy consumed to add one carbon atom to a growing grain; the activation energy for grain density represents the energy consumed to form a new nucleus. The growth conditions for the CVD reaction were: Ar 120 sccm, H<sub>2</sub> 30 sccm, CH<sub>4</sub> 1.5 sccm, 2-hour reaction time at various temperatures from 1150 °C to 1185 °C. This efficient temperature window has been carefully investigated and selected based on two points: first, at higher temperature (>1200 °C, approaching the melting point), the silicon sublimation was observed to contaminate the sample surface and thus introduce more complex variables, which prevents from the evaluation of the reaction activation energy; second, at lower temperature (<1140 °C), negligible graphene formation was observed. Therefore, the fine tuning in the temperature range (<1185 °C) was conducted in the selected range.

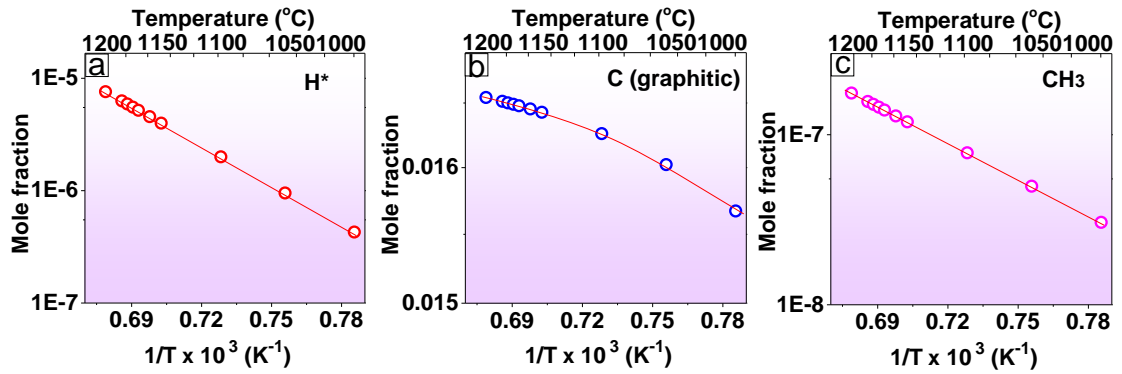


FIGURE C.6:

Thermodynamic calculations of the mole fractions of the active radicals in the chemical equilibrium state for various temperatures: (a) H\*, (b) C (graphitic), (c) CH<sub>3</sub> are the concentration of active radicals that contribute to the reaction rates in the thermal decomposition process. With a temperature increase, the mole fraction of H\*, C(graphitic) and CH<sub>3</sub> increase rapidly. All these curves show the importance of evaluated temperature on enhancing the growth kinetics (*e.g.*, increasing growth rate). The parameters used in the CEA program were 1 atm. pressure for different temperatures. The initial gases: Ar 120: H<sub>2</sub> 30: CH<sub>4</sub> 1.5 (mole ratio).

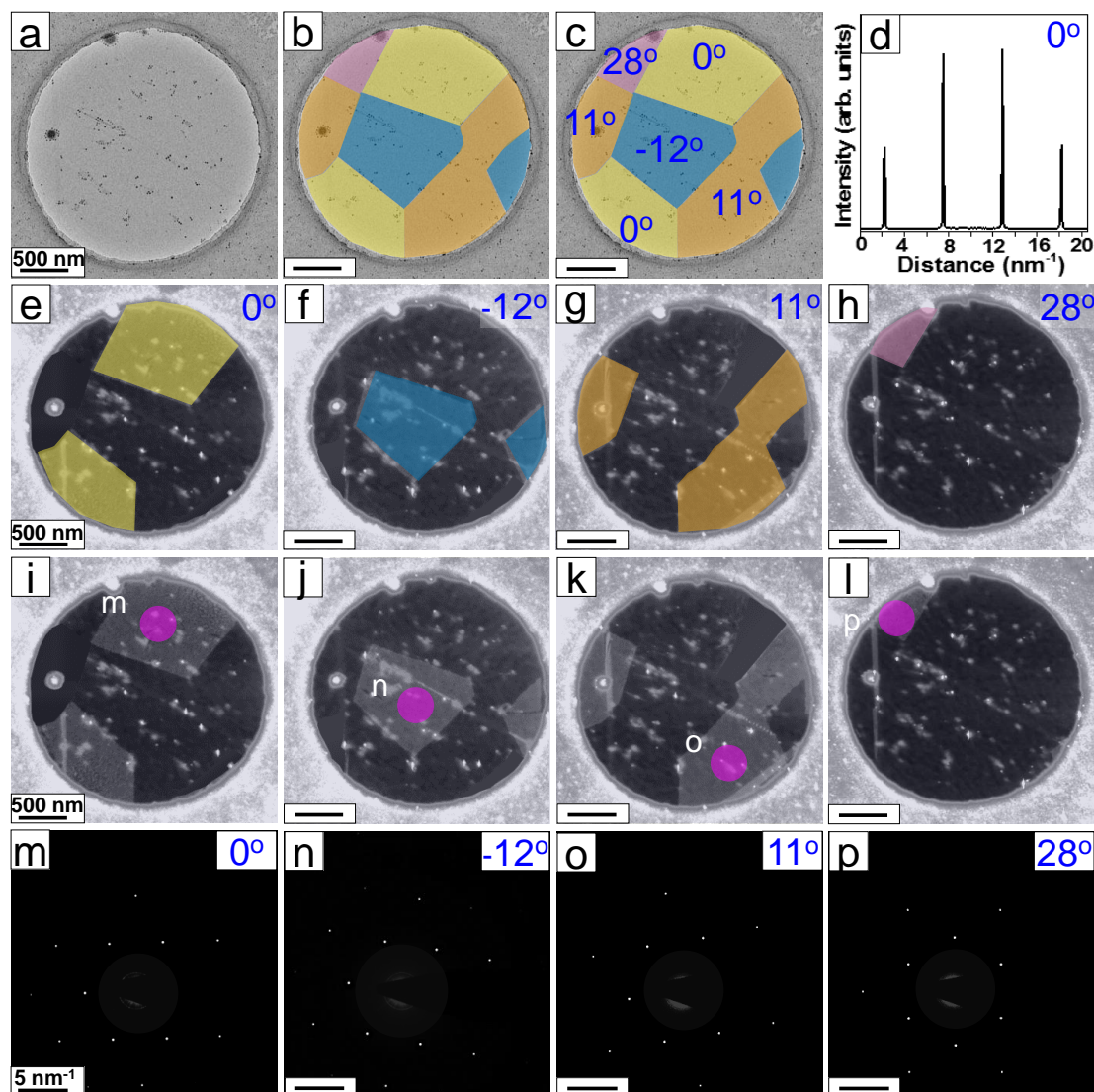


FIGURE C.7:

DF-TEM determination of the relative rotation angles and grain sizes of the grains forming monolayer graphene (sandwich configuration). (a) Homogeneous monolayer graphene (transferred) on to a TEM grid. (b) False color composite TEM image and (c) labelling of the relative rotation angles. (d) Intensity profile of line crossing the SAED pattern spots. (e-h) False color composite DF-TEM images with relative rotation angles. (i-l) Pristine DF-TEM images. (m-p) SAED for the regions circled in (i-l), respectively.



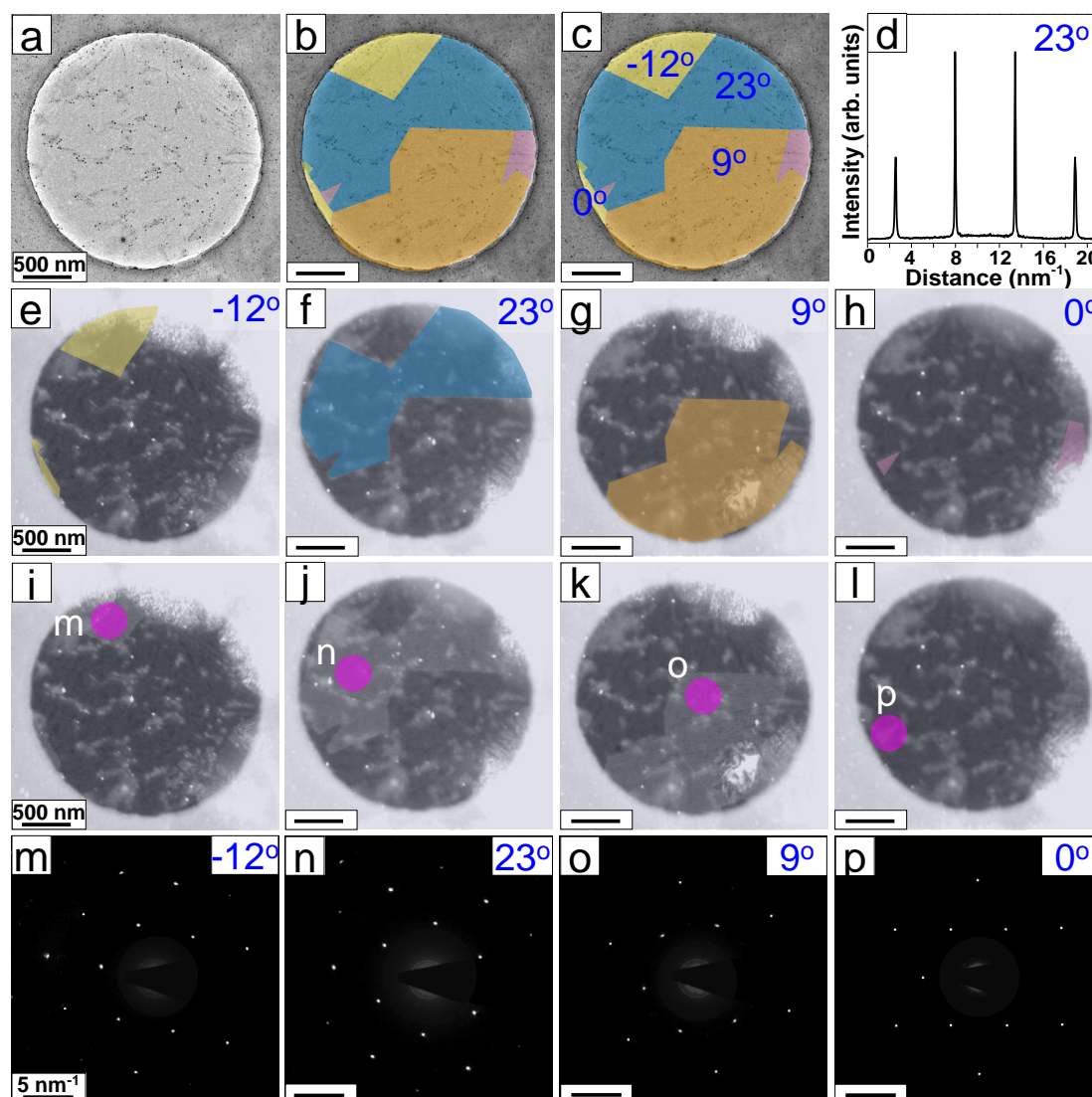


FIGURE C.8:

DF-TEM determination of monolayer graphene film for sandwich configuration in another sample showing the same faceting features of merging grains. (a) Homogeneous monolayer graphene (transferred) on to a TEM grid. (b) False color composite TEM image and (c) labelling of the relative rotation angles. (d) Intensity profile of line crossing the SAED pattern spots. (e-h) False color composite DF-TEM images with relative rotation angles. (i-l) Pristine DF-TEM images. (m-p) SAED for the regions circled in (i-l), respectively.

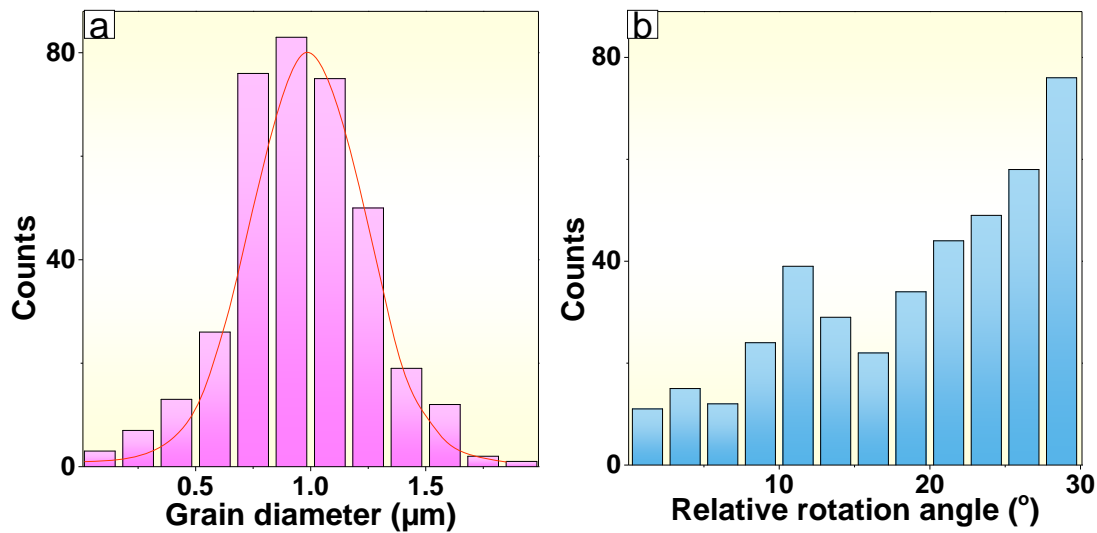


FIGURE C.9: Statistics of the measured grain diameter and relative rotation angles as obtained from DF-TEM (as shown in [Figure C.7](#) and [Figure C.8](#)). (a) and (b) show the statistics of the measured grain diameter and relative rotation angle. The size of the graphene grain is in average about 1  $\mu\text{m}$ , and it varies from about 0.25 to 1.5  $\mu\text{m}$ . In terms of the relative rotation angle, the most common angle between two neighboring grains is  $28^\circ$ . Other smaller angles varying from  $5^\circ$  to  $23^\circ$  could also be observed. Typically  $28^\circ$  is the most frequently observed relative rotation angle because it has the lowest energy configuration.

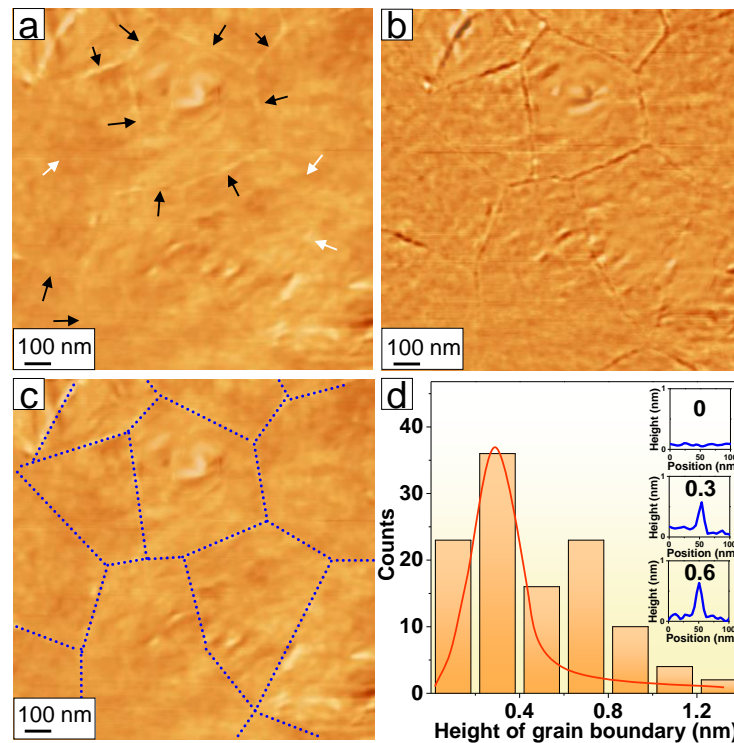


FIGURE C.10: Complementary height contrast and phase contrast image from AFM for the same region in a graphene sample using the sandwich configuration. (a) AFM topography image showing the visible grain boundaries (black arrows) and the white arrows depict grain boundaries that cannot be easily observed in this AFM mode. (b) AFM phase micrograph assisting the assignment of the grain boundaries. (c) The dashed lines labeling the grain boundaries to guide the eyes. (d) The histogram of the height of more than 100 grain boundaries. Most of the heights range from 0 to 0.8 nm and there are little amount of height above 1 nm. The inset of d are three typical height profiles across the grain boundaries. They are 0 nm, 0.3 nm and 0.6 nm, respectively. Note that AFM phase imaging (imaged simultaneously with the AFM topography) is more sensitive due to its direct measure of changes in the cantilever oscillation (resonant frequency) and is not affected by neighboring height differences. Therefore, the AFM phase image enhances contrast of fine structures such as grain boundary edges, as seen in (b).

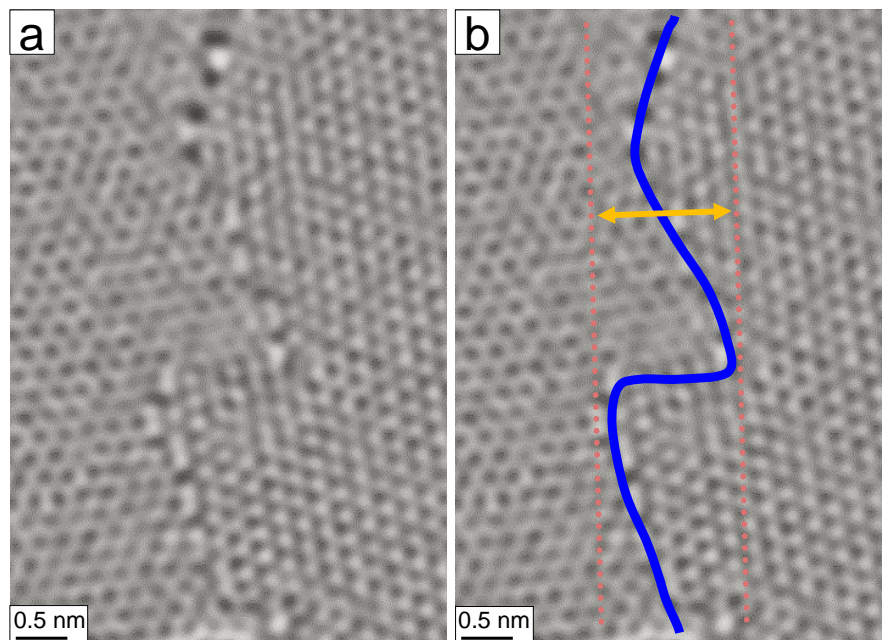


FIGURE C.11:

HRTEM image showing undulation of a grain boundary (a) and its outline (b), respectively. The range of amplitude of the undulations is typically from 0.6 - 1.2 nm. Note that at a low magnification view (*e.g.*, SEM, DF-TEM, and AFM), the grain boundaries look straight. However at an atomic scale the grain boundaries show undulation as exemplified in the pristine HRTEM image.

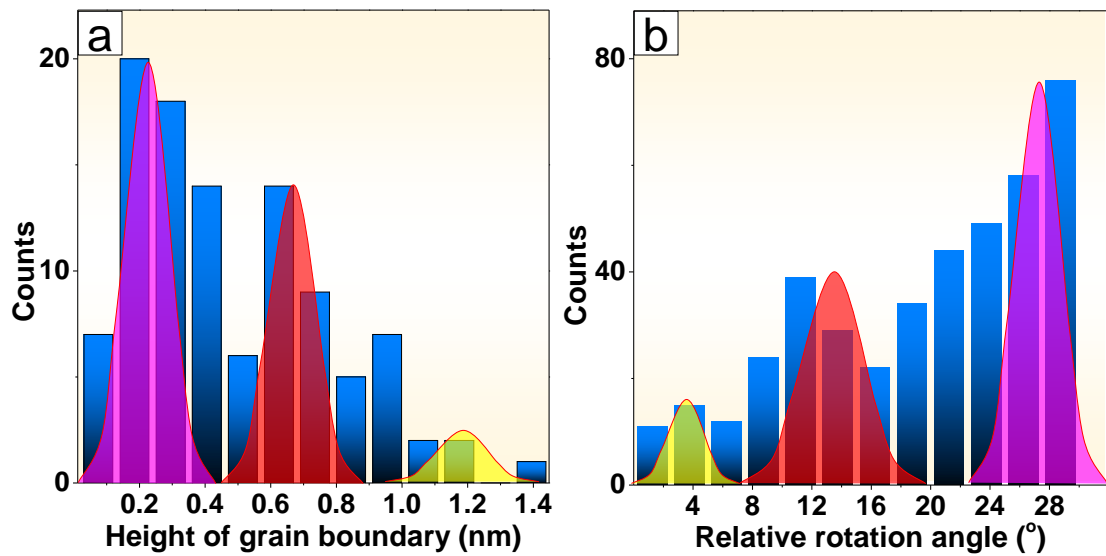


FIGURE C.12:

Complementary study from AFM and DF-TEM of grain boundaries. (a) Statistics of AFM height of the grain boundaries and (b) the relative rotation angle between two adjacent grains determined with DF-TEM method. Each show three peaks as aided by the fits (with coloring) for height and relative rotational angles, respectively.

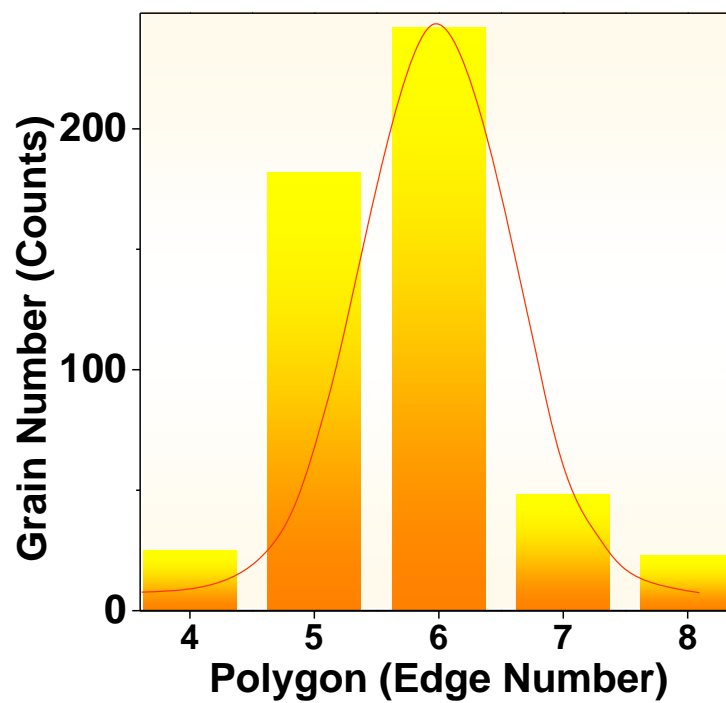


FIGURE C.13:

Statistics of the grain number for graphene polygons of different edge numbers (such as 4-8 edges).

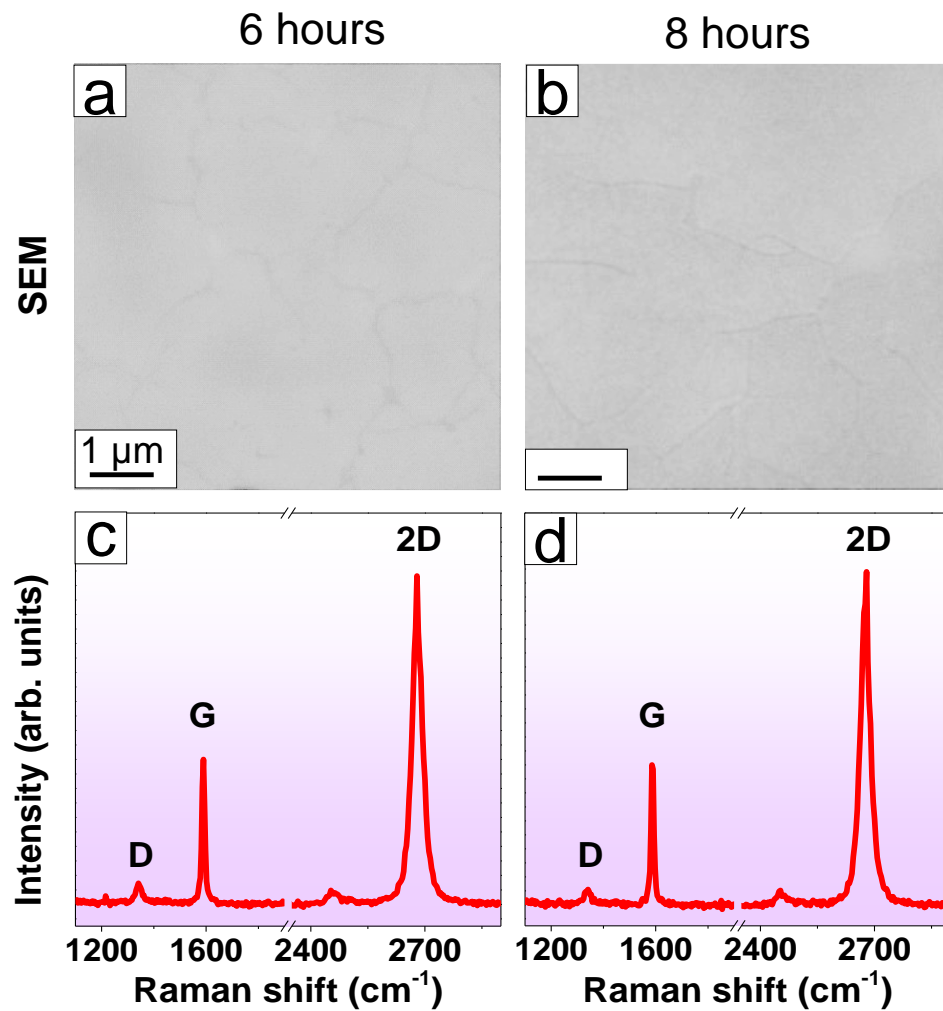


FIGURE C.14:

SEM (a, b) and Raman spectra (c,d) for monolayer graphene film after 6 and 8 hour growth. The homogeneity of synthetic monolayer graphene film are confirmed by SEM and layer number by Raman spectra (collected at numerous locations).

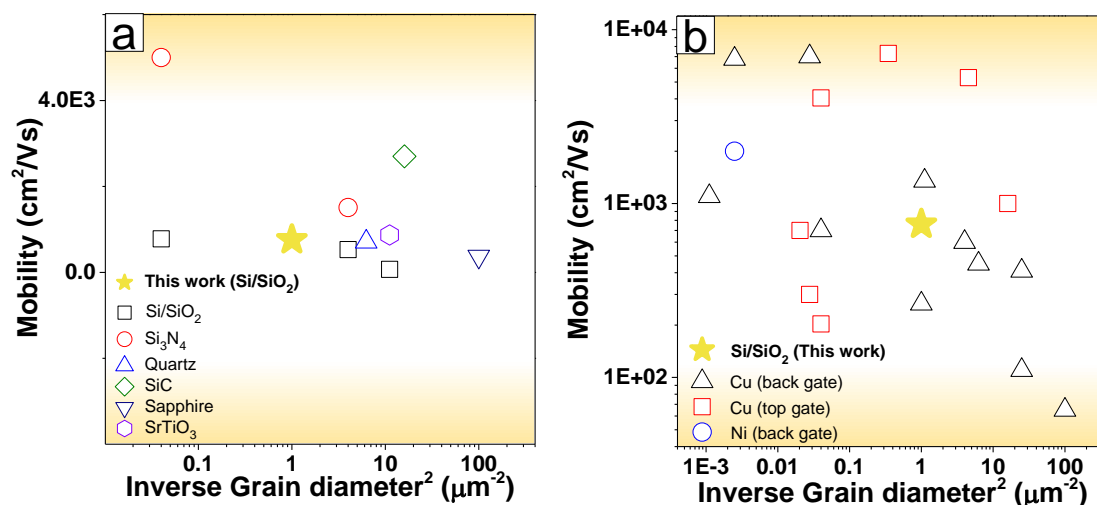


FIGURE C.15:

Comparison of carrier mobility of synthetic monolayer graphene film directly grown on Si/SiO<sub>x</sub> in this work (filled star) with other reports (a) graphene directly grown on dielectric substrates and (b) graphene grown on Cu substrates. This work shows the highest hole mobility in back-gated field effect transistors for the monolayer graphene film directly grown over Si/SiO<sub>x</sub> substrates. Also, this direct grown graphene over Si/SiO<sub>x</sub> is catching (and even exceeding) the performance of graphene grown over Cu in other reports. The mobility data are from [Table C.2](#) and [Table C.3](#), respectively.



TABLE C.2: Comparison of transistor mobility for graphene of this work and other reports over dielectrics.

No.	Substrate ( $\mu\text{m}$ )	Type of graphene	Grain size ( $\mu\text{m}$ )	Carrier mobility ( $\text{cm}^2 \text{V}^{-1} \text{s}^{-1}$ )	Reference
1	Si/SiO <sub>x</sub>	Monolayer film	1	410-760	This work
2	Si/SiO <sub>x</sub>	Monolayer film	0.5	531	[50]
3	Si/SiO <sub>x</sub>	Monolayer film	0.3	70	[319]
4	Si/SiO <sub>x</sub> /Si <sub>3</sub> N <sub>4</sub>	Monolayer film	0.5	1510	[56]
5	Quartz	Monolayer film	0.4	553-710	[295]
6	SrTiO <sub>3</sub>	Monolayer film	0.3	870	[293]
7	Sapphire	Monolayer film	0.1	370	[320]
8	Si/SiO <sub>x</sub>	Individual grain	5	780	[49]
9	Si/SiO <sub>x</sub> /Si <sub>3</sub> N <sub>4</sub>	Individual grain	5	5000	[49]
10	SiC decomposition	Monolayer ribbon	0.25	900-2700	[110]

TABLE C.3: Comparison of transistor mobility from this work with graphene grown by CVD over metal substrates.

No.	Substrate	Device configuration	Grain size	Carrier mobility (cm <sup>2</sup> V <sup>-1</sup> s <sup>-1</sup> )	Growth time (hour)	Type of graphene	Reference
1	Cu	Back gate	20	1000-6780	2	Monolayer film	[251]
2	Cu	Back gate	6	800-7000	0.1	Monolayer film	[127]
3	Si/SiO <sub>x</sub>	Back gate	1	410-760	5	Monolayer film	This work
4	Cu	Back gate	5	700	0.5	Monolayer film	[321]
5	Cu	Back gate	1	265-900	0.2	Monolayer film	[322]
6	Cu	Back gate	0.95	500-1350	0.5	Monolayer film	[323]
7	Cu	Back gate	0.5	400-600	0.6	Monolayer film	[121]
8	Cu	Back gate	n.a.	200-450	0.2	Monolayer film	[54]
9	Cu	Back gate	0.2	410	0.3	Monolayer film	[324]
10	Cu	Back gate	0.2	110	0.5	Monolayer film	[325]
11	Cu	Back gate	0.1	65	0.5	Monolayer film	[325]
12	Cu	Top gate	20-40	1100	0.2	Monolayer film	[160]
13	Cu	Top gate	5	4050	0.5	Monolayer film	[111]
14	Cu	Top gate	0.25, 0.47, 1.70	1000, 5300, 7300	0.5	Monolayer film	[65]
15	Cu	Top gate	7	700	0.3	Monolayer film	[326]
16	Cu	Top gate	6	260-300	0.8	Monolayer film	[327]
17	Cu	Top gate	5	203	0.5	Monolayer film	[328]
18	Ni	Back gate	<20	100-2000	0.2	Monolayer film	[112]

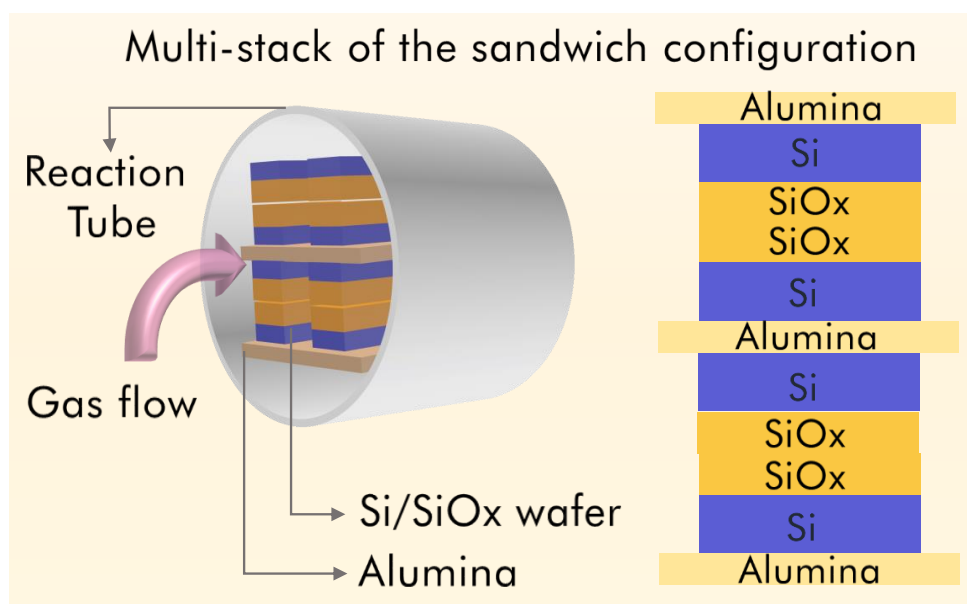


FIGURE C.16:

Schematic of multi-stacking of sandwich configuration allowing for the scale-up production of large area homogeneous strict monolayer graphene films in a single CVD reaction.



# Bibliography

- [1] J.H. Warner, F. Schäffel, A. Bachmatiuk, and M.H. Rümmeli. *Graphene Fundamentals and Emergent Applications*. Elsevier, Waltham, MA, 1th edition, 2013.
- [2] M.H. Rümmeli, P. Ayala, and T. Pichler. *Chapter 1. Carbon Nanotubes and Related Structures: Production and Formation*, pages 1–21. WILEY-VCH Verlag GmbH & Co., KGaA, Weinheim, 1th edition, 2010.
- [3] Z. Liu, J.Z. Liu, Y. Cheng, Z. Li, L. Wang, and Q. Zheng. Interlayer binding energy of graphite: A mesoscopic determination from deformation. *Phys. Rev. B*, 85(20):205418, 2012.
- [4] M.H. Rümmeli, C.G. Rocha, F. Ortman, I. Ibrahim, H. Sevincli, F. Börrnert, J. Kunstmann, A. Bachmatiuk, M. Pötschke, M. Shiraishi, M. Meyyappan, B. Büchner, S. Roche, and G. Cuniberti. Graphene: Piecing it together. *Adv. Mater.*, 23(39):4471–4490, 2011.
- [5] K.S. Novoselov, A.K. Geim, S.V. Morozov, D. Jiang, Y. Zhang, S.V. Dubonos, I.V. Grigorieva, and A.A. Firsov. Electric field effect in atomically thin carbon films. *Science*, 306(5696):666–669, 2004.
- [6] J.H. Chen, C. Jang, S. Xiao, M. Ishigami, and M.S. Fuhrer. Intrinsic and extrinsic performance limits of graphene devices on sio<sub>2</sub>. *Nat. Nanotechnol.*, 3(4):206–209, 2008.

- 
- [7] K.S. Novoselov, A.K. Geim, S.V. Morozov, D. Jiang, M.I. Katsnelson, I.V. Grigorieva, S.V. Dubonos, and A.A. Firsov. Two-dimensional gas of massless dirac fermions in graphene. *Nature*, 438(7065):197–200, 2005.
- [8] C.N.R. Rao, A.K. Sood, K.S. Subrahmanyam, and A. Govindaraj. Graphene: The new two-dimensional nanomaterial. *Angew. Chem. Int. Ed.*, 48(42):7752–7777, 2009.
- [9] S.V. Morozov, K.S. Novoselov, M.I. Katsnelson, F. Schedin, D.C. Elias, J.A. Jaszczak, and A.K. Geim. Giant intrinsic carrier mobilities in graphene and its bilayer. *Phys. Rev. Lett.*, 100(1):016602, 2008.
- [10] P. Han, K. Akagi, F. Federici C., H. Mutoh, S. Shiraki, K. Iwaya, P.S. Weiss, N. Asao, and T. Hitosugi. Bottom-up graphene-nanoribbon fabrication reveals chiral edges and enantioselectivity. *ACS Nano*, 8(9):9181–9187, 2014.
- [11] V.K. Sangwan, D. Jariwala, K. Everaerts, J.J. McMorrow, J. He, M. Grayson, L.J. Lauhon, T.J. Marks, and M.C. Hersam. Wafer-scale solution-derived molecular gate dielectrics for low-voltage graphene electronics. *Appl. Phys. Lett.*, 104(8):083503, 2014.
- [12] B. Fallahazad, Y. Hao, K. Lee, S. Kim, R.S. Ruoff, and E. Tutuc. Quantum hall effect in bernal stacked and twisted bilayer graphene grown on cu by chemical vapor deposition. *Phys. Rev. B*, 85(20):201408, 2012.
- [13] K.S. Novoselov, Z. Jiang, Y. Zhang, S.V. Morozov, H.L. Stormer, U. Zeitler, J.C. Maan, G.S. Boebinger, P. Kim, and A.K. Geim. Room-temperature quantum hall effect in graphene. *Science*, 315(5817):1379, 2007.

- [14] J. Yan, Y. Zhang, P. Kim, and A. Pinczuk. Electric field effect tuning of electron-phonon coupling in graphene. *Phys. Rev. Lett.*, 98(16):166802, 2007.
- [15] Y.J. Yu, Y. Zhao, S. Ryu, L.E. Brus, K.S. Kim, and P. Kim. Tuning the graphene work function by electric field effect. *Nano Lett.*, 9(10):3430–3434, 2009.
- [16] P.K. Ang, A. Li, M. Jaiswal, Y. Wang, H.W. Hou, J.T.L. Thong, C.T. Lim, and K.P. Loh. Flow sensing of single cell by graphene transistor in a microfluidic channel. *Nano Lett.*, 11(12):5240–5246, 2011.
- [17] Z. Yan, Z. Peng, Z. Sun, J. Yao, Y. Zhu, Z. Liu, P.M. Ajayan, and J.M. Tour. Growth of bilayer graphene on insulating substrates. *ACS Nano*, 5(10):8187–8192, 2011.
- [18] L. Liu, H. Zhou, R. Cheng, W.J. Yu, Y. Liu, Y. Chen, J. Shaw, X. Zhong, Y. Huang, and X. Duan. High-yield chemical vapor deposition growth of high-quality large-area ab-stacked bilayer graphene. *ACS Nano*, 6(9):8241–8249, 2012.
- [19] Y. Wu, H. Chou, H. Ji, Q. Wu, S. Chen, W. Jiang, Y. Hao, J. Kang, Y. Ren, R.D. Piner, and R.S. Ruoff. Growth mechanism and controlled synthesis of ab-stacked bilayer graphene on cu-ni alloy foils. *ACS Nano*, 6(9):7731–7738, 2012.
- [20] K. Yan, H. Peng, Y. Zhou, H. Li, and Z. Liu. Formation of bilayer bernal graphene: layer-by-layer epitaxy via chemical vapor deposition. *Nano Lett.*, 11(3):1106–1110, 2011.
- [21] F. Xia, D.B. Farmer, Y.M. Lin, and P. Avouris. Graphene field-effect transistors with high on/off current ratio and large transport band gap at room temperature. *Nano Lett.*, 10(2):715–718, 2010.

- [22] W.J. Yu, L. Liao, S.H. Chae, Y.H. Lee, and X. Duan. Toward tunable band gap and tunable dirac point in bilayer graphene with molecular doping. *Nano Lett.*, 11(11):4759–4763, 2011.
- [23] A. Bachmatiuk, R.G. Mendes, C. Hirsch, C. Jahne, M.R. Lohe, J. Grothe, S. Kaskel, L. Fu, R. Klingeler, J. Eckert, P. Wick, and M.H. Rümmeli. Few-layer graphene shells and nonmagnetic encapsulates: a versatile and nontoxic carbon nanomaterial. *ACS Nano*, 7(12):10552–10562, 2013.
- [24] J.W. Deng, L.F. Chen, Y.Y. Sun, M.H. Ma, and L. Fu. Interconnected mmo2 nanoflakes assembled on graphene foam as a binder-free and long-cycle life lithium battery anode. *Carbon*, 92:177–184, 2015.
- [25] J. Guo, T. Zhang, C. Hu, and L. Fu. A three-dimensional nitrogen-doped graphene structure: a highly efficient carrier of enzymes for biosensors. *Nanoscale*, 7(4):1290–1295, 2015.
- [26] X. Hu, M. Ma, M. Zeng, Y. Sun, L. Chen, Y. Xue, T. Zhang, X. Ai, R.G. Mendes, M.H. Rümmeli, and L. Fu. Supercritical carbon dioxide anchored fe3o4 nanoparticles on graphene foam and lithium battery performance. *ACS Appl. Mater. Inter.*, 6(24):22527–22533, 2014.
- [27] J. Liu, X. Leng, Y. Xiao, C. Hu, and L. Fu. 3d nitrogen-doped graphene/beta-cyclodextrin: host-guest interactions for electrochemical sensing. *Nanoscale*, 7(28):11922–11927, 2015.
- [28] A. Bachmatiuk, J. Boeckl, H. Smith, I. Ibrahim, T. Gemming, S. Oswald, W. Kazmierczak, D. Makarov, O.G. Schmidt, J. Eckert, L. Fu, and M.H. Rümmeli. Vertical graphene growth from amorphous carbon films using oxidizing gases. *J. Phys. Chem. C*, 119(31):17965–17970, 2015.



- [29] K. Davami, M. Shaygan, N. Kheirabi, J. Zhao, D.A. Kovalenko, M.H. Rummeli, J. Opitz, G. Cuniberti, J.-S. Lee, and M. Meyyappan. Synthesis and characterization of carbon nanowalls on different substrates by radio frequency plasma enhanced chemical vapor deposition. *Carbon*, 72:372–380, 2014.
- [30] J. Zhao, M. Shaygan, J. Eckert, M. Meyyappan, and M.H. Rummeli. A growth mechanism for free-standing vertical graphene. *Nano Lett.*, 14(6):3064–3071, 2014.
- [31] H. Park, S. Chang, J. Jean, J.J. Cheng, P.T. Araujo, M. Wang, M.G. Bawendi, M.S. Dresselhaus, V. Bulović, J. Kong, and S. Gradečak. Graphene cathode-based zno nanowire hybrid solar cells. *Nano Lett.*, 13(1):233–239, 2013.
- [32] S. Chattopadhyay, A.L. Lipson, H.J. Karmel, J.D. Emery, T.T. Fister, P.A. Fenter, M.C. Hersam, and M.J. Bedzyk. In situ x-ray study of the solid electrolyte interphase (sei) formation on graphene as a model li-ion battery anode. *Chem. Mater.*, 24(15):3038–3043, 2012.
- [33] Y. Cheng, S. Lu, H. Zhang, C.V. Varanasi, and J. Liu. Synergistic effects from graphene and carbon nanotubes enable flexible and robust electrodes for high-performance supercapacitors. *Nano Lett.*, 12(8):4206–4211, 2012.
- [34] Y.T. Liang, B.K. Vijayan, K.A. Gray, and M.C. Hersam. Minimizing graphene defects enhances titania nanocomposite-based photocatalytic reduction of co<sub>2</sub> for improved solar fuel production. *Nano Lett.*, 11(7):2865–2870, 2011.

- [35] S. Lu, Y. Cheng, X. Wu, and J. Liu. Significantly improved long-cycle stability in high-rate li-s batteries enabled by coaxial graphene wrapping over sulfur-coated carbon nanofibers. *Nano Lett.*, 13(6):2485–2489, 2013.
- [36] Y. Ma, P. Li, J.W. Sedloff, X. Zhang, H. Zhang, and J. Liu. Conductive graphene fibers for wire-shaped supercapacitors strengthened by unfunctionalized few-walled carbon nanotubes. *ACS Nano*, 9(2):1352–1359, 2015.
- [37] Y. Wang, S.W. Tong, X.F. Xu, Barbaros Özyilmaz, and K.P. Loh. Interface engineering of layer-by-layer stacked graphene anodes for high-performance organic solar cells. *Adv. Mater.*, 23(13):1514–1518, 2011.
- [38] A.R.B.M. Yusoff, L. Dai, H.-M. Cheng, and J. Liu. Graphene based energy devices. *Nanoscale*, 7(16):6881–6882, 2015.
- [39] J. Zang, C. Cao, Y. Feng, J. Liu, and X. Zhao. Stretchable and high-performance supercapacitors with crumpled graphene papers. *Sci. Rep.*, 4:6492, 2014.
- [40] A. Pirkle, J. Chan, A. Venugopal, D. Hinojos, C.W. Magnuson, S. McDonnell, L. Colombo, E.M. Vogel, R.S. Ruoff, and R.M. Wallace. The effect of chemical residues on the physical and electrical properties of chemical vapor deposited graphene transferred to sio<sub>2</sub>. *Appl. Phys. Lett.*, 99(12):122108, 2011.
- [41] E.H. Hwang and S. Das Sarma. Acoustic phonon scattering limited carrier mobility in two-dimensional extrinsic graphene. *Phys. Rev. B*, 77(11):115449, 2008.

- [42] T. Stauber, N.M.R. Peres, and F. Guinea. Electronic transport in graphene: A semiclassical approach including midgap states. *Phys. Rev. B*, 76(20):205423, 2007.
- [43] F.T. Vasko and V. Ryzhii. Voltage and temperature dependencies of conductivity in gated graphene. *Phys. Rev. B*, 76(23):233404, 2007.
- [44] A.H. Castro Neto, F. Guinea, N.M.R. Peres, K.S. Novoselov, and A.K. Geim. The electronic properties of graphene. *Rev. Mod. Phys.*, 81(1):109–162, 2009.
- [45] S.J. Han, K.A. Jenkins, A. Valdes Garcia, A.D. Franklin, A.A. Bol, and W. Haensch. High-frequency graphene voltage amplifier. *Nano Lett.*, 11(9):3690–3693, 2011.
- [46] Y.M. Lin, K.A. Jenkins, A. Valdes-Garcia, J.P. Small, D.B. Farmer, and P. Avouris. Operation of graphene transistors at gigahertz frequencies. *Nano Lett.*, 9(1):422–426, 2009.
- [47] I. Meric, C.R. Dean, A.F. Young, N. Baklitskaya, N.J. Tremblay, C. Nuckolls, P. Kim, and K.L. Shepard. Channel length scaling in graphene field-effect transistors studied with pulsed current-voltage measurements. *Nano Lett.*, 11(3):1093–1097, 2011.
- [48] F. Schwierz. Graphene transistors. *Nat. Nanotechnol.*, 5(7):487–496, 2010.
- [49] J. Chen, Y. Guo, L. Jiang, Z. Xu, L. Huang, Y. Xue, D. Geng, B. Wu, W. Hu, G. Yu, and Y. Liu. Near-equilibrium chemical vapor deposition of high-quality single-crystal graphene directly on various dielectric substrates. *Adv. Mater.*, 26(9):1348–1353, 2014.
- [50] J. Chen, Y. Wen, Y. Guo, B. Wu, L. Huang, Y. Xue, D. Geng, D. Wang, G. Yu, and Y. Liu. Oxygen-aided synthesis of polycrystalline graphene

- on silicon dioxide substrates. *J. Am. Chem. Soc.*, 133(44):17548–17551, 2011.
- [51] P. Joshi, H.E. Romero, A.T. Neal, V.K. Toutam, and S.A. Tadigadapa. Intrinsic doping and gate hysteresis in graphene field effect devices fabricated on sio2 substrates. *J. Phys. Condens. Matter.*, 22(33):334214, 2010.
- [52] F. Schedin, A.K. Geim, S.V. Morozov, E.W. Hill, P. Blake, M.I. Katsnelson, and K.S. Novoselov. Detection of individual gas molecules adsorbed on graphene. *Nat. Mater.*, 6(9):652–655, 2007.
- [53] D.J. Late, A. Ghosh, K.S. Subrahmanyam, L.S. Panchakarla, S.B. Krupanidhi, and C.N.R. Rao. Characteristics of field-effect transistors based on undoped and b- and n-doped few-layer graphenes. *Solid State Commun.*, 150(15-16):734–738, 2010.
- [54] D. Wei, Y. Liu, Y. Wang, H. Zhang, L. Huang, and G. Yu. Synthesis of n-doped graphene by chemical vapor deposition and its electrical properties. *Nano Lett.*, 9(5):1752–1758, 2009.
- [55] J.U. Park, S. Nam, M.S. Lee, and C.M. Lieber. Synthesis of monolithic graphene-graphite integrated electronics. *Nat. Mater.*, 11(2):120–125, 2011.
- [56] J. Chen, Y. Guo, Y. Wen, L. Huang, Y. Xue, D. Geng, B. Wu, B. Luo, G. Yu, and Y. Liu. Two-stage metal-catalyst-free growth of high-quality polycrystalline graphene films on silicon nitride substrates. *Adv. Mater.*, 25(7):992–997, 2013.
- [57] S. Bae, H. Kim, Y. Lee, X. Xu, J.S. Park, Y. Zheng, J. Balakrishnan, T. Lei, H.R. Kim, Y.I. Song, Y.J. Kim, K.S. Kim, B. Ozyilmaz, J.H. Ahn, B.H. Hong, and S. Iijima. Roll-to-roll production of 30-inch

- graphene films for transparent electrodes. *Nat. Nanotechnol.*, 5(8):574–578, 2010.
- [58] H. Jang, Y.J. Park, X. Chen, T. Das, M.S. Kim, and J.H. Ahn. Graphene-based flexible and stretchable electronics. *Adv. Mater.*, 28(22):4184–4202, 2016.
- [59] Q. Bao, H. Zhang, B. Wang, Z. Ni, Y. Lim, C.H.Y.X. and Wang, D.Y. Tang, and K.P. Loh. Broadband graphene polarizer. *Nat. Photonics*, 5(7):411–415, 2011.
- [60] R.R. Nair, P. Blake, A.N. Grigorenko, K.S. Novoselov, T.J. Booth, T. Stauber, N.M. Peres, and A.K. Geim. Fine structure constant defines visual transparency of graphene. *Science*, 320(5881):1308, 2008.
- [61] C. Lee, X. Wei, J.W. Kysar, and J. Hone. Measurement of the elastic properties and intrinsic strength of monolayer graphene. *Science*, 321(5887):385–388, 2008.
- [62] H. Zhao, K. Min, and N.R. Aluru. Size and chirality dependent elastic properties of graphene nanoribbons under uniaxial tension. *Nano Lett.*, 9(8):3012–3015, 2009.
- [63] K. Kalaitzidou, H. Fukushima, P. Askeland, and L.T. Drzal. The nucleating effect of exfoliated graphite nanoplatelets and their influence on the crystal structure and electrical conductivity of polypropylene nanocomposites. *J. Mater. Sci.*, 43(8):2895–2907, 2008.
- [64] Z. Liu, K. Suenaga, P.J. Harris, and S. Iijima. Open and closed edges of graphene layers. *Phys. Rev. Lett.*, 102(1):015501, 2009.
- [65] P.Y. Huang, C.S. Ruiz-Vargas, A.M. van der Zande, W.S. Whitney, M.P. Levendorf, J.W. Kevek, S. Garg, J.S. Alden, C.J. Hustedt, Y. Zhu,

- J. Park, P. L. McEuen, and D.A. Muller. Grains and grain boundaries in single-layer graphene atomic patchwork quilts. *Nature*, 469(7330): 389–392, 2011.
- [66] K. Kim, Z. Lee, W. Regan, C. Kisielowski, M.F. Crommie, and A. Zettl. Grain boundary mapping in polycrystalline graphene. *ACS Nano*, 5(3): 2142–2146, 2011.
- [67] A. Hashimoto, K. Suenaga, A. Gloter, K. Urita, and S. Iijima. Direct evidence for atomic defects in graphene layers. *Nature*, 430(7002):870–873, 2004.
- [68] J.C. Meyer, C. Kisielowski, R. Erni, M.D. Rossell, M.F. Crommie, and A. Zettl. Direct imaging of lattice atoms and topological defects in graphene membranes. *Nano Lett.*, 8(11):3582–3586, 2008.
- [69] F. Banhart, J. Kotakoski, and A.V. Krasheninnikov. Structural defects in graphene. *ACS Nano*, 5(1):26–41, 2011.
- [70] J.H. Warner, E.R. Margine, M. Mukai, A.W. Robertson, F. Giustino, and A.I. Kirkland. Dislocation-driven deformations in graphene. *Science*, 337(6091):209–12, 2012.
- [71] A. Cortijo and M.A.H. Vozmediano. Electronic properties of curved graphene sheets. *Europhys. Lett.*, 77(4):47002, 2007.
- [72] A. Cortijo and M.A.H. Vozmediano. Effects of topological defects and local curvature on the electronic properties of planar graphene. *Nucl. Phys. B*, 763(3):293–308, 2007.
- [73] Q. Bao, H. Zhang, J.-x. Yang, S. Wang, D.Y. Tang, R. Jose, S. Ramakrishna, C.T. Lim, and K.P. Loh. Graphene-polymer nanofiber membrane for ultrafast photonics. *Adv. Funct. Mater.*, 20(5):782–791, 2010.

- [74] M.Z. Hossain, J.E. Johns, K.H. Bevan, H.J. Karmel, Y.T. Liang, S. Yoshimoto, K. Mukai, T. Koitaya, J. Yoshinobu, M. Kawai, A.M. Lear, L.L. Kesmodel, S.L. Tait, and M.C. Hersam. Chemically homogeneous and thermally reversible oxidation of epitaxial graphene. *Nat. Chem.*, 4:305–309, 2012.
- [75] M.Z. Hossain, M.A. Walsh, and M.C. Hersam. Scanning tunneling microscopy, spectroscopy, and nanolithography of epitaxial graphene chemically modified with aryl moieties. *J. Am. Chem. Soc.*, 132(43):15399–15403, 2010.
- [76] K.K. Manga, S. Wang, M. Jaiswal, Q. Bao, and K.P. Loh. High-gain graphene-titanium oxide photoconductor made from inkjet printable ionic solution. *Adv. Mater.*, 22(46):5265–5270, 2010.
- [77] R.G. Mendes, B. Koch, A. Bachmatiuk, X. Ma, S. Sanchez, C. Damm, O.G. Schmidt, T. Gemming, J. Eckert, and M.H. Rummeli. A size dependent evaluation of the cytotoxicity and uptake of nanographene oxide. *J. Mater. Chem. B*, 3(12):2522–2529, 2015.
- [78] L. Yan, Y.B. Zheng, F. Zhao, S. Li, X. Gao, B. Xu, P.S. Weiss, and Y. Zhao. Chemistry and physics of a single atomic layer: strategies and challenges for functionalization of graphene and graphene-based materials. *Chem. Soc. Rev.*, 41(1):97–114, 2012.
- [79] J.E. Johns and M.C. Hersam. Atomic covalent functionalization of graphene. *Accounts Chem. Res.*, 46(1):77–86, 2013.
- [80] R.G. Mendes, A. Bachmatiuk, B. Büchner, G. Cuniberti, and M.H. Rummeli. Carbon nanostructures as multi-functional drug delivery platforms. *J. Mater. Chem. B*, 1(4):401–428, 2013.

- [81] H. Wang, L.F. Cui, Y. Yang, H. Sanchez Casalongue, J.T. Robinson, Y. Liang, Y. Cui, and H. Dai. Mn<sub>3</sub>O<sub>4</sub>-graphene hybrid as a high-capacity anode material for lithium ion batteries. *J. Am. Chem. Soc.*, 132(40):13978–13980, 2010.
- [82] H. Bi, K. Yin, X. Xie, J. Ji, S. Wan, L. Sun, M. Terrones, and M.S. Dresselhaus. Ultrahigh humidity sensitivity of graphene oxide. *Sci. Rep.*, 3(5):2714, 2013.
- [83] Y. Li, H. Wang, L. Xie, Y. Liang, G. Hong, and H. Dai. MoS<sub>2</sub> nanoparticles grown on graphene: An advanced catalyst for the hydrogen evolution reaction. *J. Am. Chem. Soc.*, 133(19):7296–7299, 2011.
- [84] S. Liu, T.H. Zeng, M. Hofmann, E. Burcombe, J. Wei, R. Jiang, J. Kong, and Y. Chen. Antibacterial activity of graphite, graphite oxide, graphene oxide, and reduced graphene oxide: Membrane and oxidative stress. *ACS Nano*, 5(9):6971–6980, 2011.
- [85] H.S. Choi, T.J. Park, M.H. Yang, Kim J.S., N.S. Heo, S.Y. Lee, J. Kong, and W.H. Hong. Solution chemistry of self-assembled graphene nanohybrids for high-performance flexible biosensors. *ACS Nano*, 4(5):2910–2918, 2010.
- [86] Y. Zhang, J.P. Small, M.E. Amori, and P. Kim. Electric field modulation of galvanomagnetic properties of mesoscopic graphite. *Phys. Rev. Lett.*, 94(17):176803, 2005.
- [87] M. Yi and Z. Shen. A review on mechanical exfoliation for the scalable production of graphene. *J. Mater. Chem. A*, 3:11700–11715, 2015.
- [88] C. Berger, Z. Song, X. Li, X. Wu, N. Brown, C. Naud, D. Mayou, T. Li, J. Hass, A.N. Marchenkov, E.H. Conrad, P.N. First, and W.A. de Heer.



- Electronic confinement and coherence in patterned epitaxial graphene. *Science*, 312(5777):1191–1196, 2006.
- [89] K.R. Paton, E. Varrla, C. Backes, R.J. Smith, U. Khan, A. O’Neil, C. Boland, M. Lotya, O.M. Istrate, P. King, T. Higgins, S. Barwich, P. May, P. Puczkarski, I. Ahmed, M. Moebius, H. Pettersson, E. Long, J. Coelho, S.E. O’Brien, E.K. McGuire, B.M. Sanchez, G.S. Duesberg, N. McEvoy, T.J. Pennycook, C. Downing, A. Crossley, V. Nicolosi, and J.N. Coleman. Scalable production of large quantities of defect-free few-layer graphene by shear exfoliation in liquids. *Nat. Mater.*, 13:624–630, 2014.
- [90] V. Nicolosi, M. Chhowalla, M.G. Kanatzidis, M.S. Strano, and J.N. Coleman. Liquid exfoliation of layered materials. *Science*, 340(6139):1226419, 2013.
- [91] A.A. Green and M.C. Hersam. Solution phase production of graphene with controlled thickness via density differentiation. *Nano Lett.*, 9(12):4031–4036, 2009.
- [92] J.M. Englert, J. Rohrl, C.D. Schmidt, R. Graupner, M. Hundhausen, F. Hauke, and A. Hirsch. Soluble graphene: Generation of aqueous graphene solutions aided by a perylenebisimide-based bolaamphiphile. *Adv. Mater.*, 21(42):4265–4269, 2009.
- [93] J. Cai, P. Ruffieux, R. Jaafar, M. Bieri, T. Braun, S. Blankenburg, M. Muoth, A.P. Seitsonen, M. Saleh, X. Feng, K. Mullen, and R. Fasel. Atomically precise bottom-up fabrication of graphene nanoribbons. *Nature*, 466(7305):470–473, 2010.

- [94] J. Scott Bunch, A.M. van der Zande, S.S. Verbridge, I.W. Frank, D.M. Tanenbaum, J.M. Parpia, H.G. Craighead, and P.L. McEuen. Electromechanical resonators from graphene sheets. *Science*, 315(5811):490–493, 2007.
- [95] X. Yan and L.-S. Li. Solution-chemistry approach to graphene nanostructures. *J. Mater. Chem.*, 21:3295–3295, 2011.
- [96] D. Voiry, J. Yang, J. Kupferberg, R. Fullon, C. Lee, H.Y. Jeong, H.S. Shin, and M. Chhowalla. High-quality graphene via microwave reduction of solution-exfoliated graphene oxide. *Science*, 353(6306):1413–1416, 2016.
- [97] S. Makharza, G. Cirillo, A. Bachmatiuk, I. Ibrahim, N. Ioannides, B. Trzebicka, S. Hampel, and M.H. Rummeli. Graphene oxide-based drug delivery vehicles: functionalization, characterization, and cytotoxicity evaluation. *J. Nanopart. Res.*, 15(12):2099, 2013.
- [98] S.H. Tamboli, B.S. Kim, G. Choi, H. Lee, D. Lee, U.M. Patil, J. Lim, S.B. Kulkarni, C.J. Seong, and H.H. Cho. Post-heating effects on the physical and electrochemical capacitive properties of reduced graphene oxide paper. *J. Mater. Chem. A*, 2(14):5077–5086, 2014.
- [99] Q. Tang, Z. Zhou, and Z. Chen. Graphene-related nanomaterials: tuning properties by functionalization. *Nanoscale*, 5(11):4541–4583, 2013.
- [100] R.S. Edwards and K.S. Coleman. Graphene synthesis: relationship to applications. *Nanoscale*, 5(1):38–51, 2013.
- [101] X. Cui, C. Zhang, R. Hao, and Y. Hou. Liquid-phase exfoliation, functionalization and applications of graphene. *Nanoscale*, 3(5):2118–2126, 2011.

- [102] L. Gao, H. Xu, L. Li, Y. Yang, Q. Fu, X. Bao, and K.P. Loh. Heteroepitaxial growth of wafer scale highly oriented graphene using inductively coupled plasma chemical vapor deposition. *2D Mater.*, 3:021001, 2016.
- [103] A. Reina, S. Thiele, X.T. Jia, S. Bhaviripudi, M.S. Dresselhaus, J.A. Schaefer, and J. Kong. Growth of large-area single- and bi-layer graphene by controlled carbon precipitation on polycrystalline ni surfaces. *Nano Res.*, 2(6):509–516, 2009.
- [104] X. Li, W. Cai, L. Colombo, and R.S. Ruoff. Evolution of graphene growth on ni and cu by carbon isotope labeling. *Nano Lett.*, 9(12):4268–4272, 2009.
- [105] H.Q. Ta, D.J. Perello, D.L. Duong, G.H. Han, S. Gorantla, V.L. Nguyen, A. Bachmatiuk, S.V. Rotkin, Y.H. Lee, and M. H. Rummeli. Stranski-krastanov and volmer-weber cvd growth regimes to control the stacking order in bilayer graphene. *Nano Lett.*, 16(10):6403–6410, 2016.
- [106] S.J. Chae, F. Gunes, K.K. Kim, E.S. Kim, G.H. Han, S.M. Kim, H.J. Shin, S.M. Yoon, J.Y. Choi, M.H. Park, C.W. Yang, D. Pribat, and Y.H. Lee. Synthesis of large-area graphene layers on poly-nickel substrate by chemical vapor deposition: Wrinkle formation. *Adv. Mater.*, 21(22):2328–2333, 2009.
- [107] J. Pang, A. Bachmatiuk, L. Fu, C. Yan, M. Zeng, J. Wang, B. Trzebicka, T. Gemming, J. Eckert, and M.H. Rummeli. Oxidation as a means to remove surface contaminants on cu foil prior to graphene growth by chemical vapor deposition. *J. Phys. Chem. C*, 119(23):13363–13368, 2015.
- [108] K.V. Emtsev, A. Bostwick, K. Horn, J. Jobst, G.L. Kellogg, L. Ley, J.L. McChesney, T. Ohta, S.A. Reshanov, J. Rohrl, E. Rotenberg, A.K.

- Schmid, D. Waldmann, H.B. Weber, and T. Seyller. Towards wafer-size graphene layers by atmospheric pressure graphitization of silicon carbide. *Nat. Mater.*, 8(3):203–207, 2009.
- [109] M. Kruskopf, K. Pierz, S. Wundrack, R. Stosch, T. Dziomba, C.C. Kalmbach, A. Muller, J. Baringhaus, C. Tegenkamp, F.J. Ahlers, and H.W. Schumacher. Epitaxial graphene on sic: modification of structural and electron transport properties by substrate pretreatment. *J. Phys. Condens. Matter.*, 27(18):185303, 2015.
- [110] M. Sprinkle, M. Ruan, Y. Hu, J. Hankinson, M. Rubio-Roy, B. Zhang, X. Wu, C. Berger, and W.A. de Heer. Scalable templated growth of graphene nanoribbons on sic. *Nat. Nanotechnol.*, 5(10):727–731, 2010.
- [111] X. Li, W. Cai, J. An, S. Kim, J. Nah, D. Yang, R. Piner, A. Velamakanni, I. Jung, E. Tutuc, S.K. Banerjee, L. Colombo, and R.S. Ruoff. Large-area synthesis of high-quality and uniform graphene films on copper foils. *Science*, 324(5932):1312–1314, 2009.
- [112] A. Reina, X. Jia, J. Ho, D. Nezich, H. Son, V. Bulovic, M.S. Dresselhaus, and J. Kong. Large area, few-layer graphene films on arbitrary substrates by chemical vapor deposition. *Nano Lett.*, 9(1):30–35, 2009.
- [113] J. Riikonen, W. Kim, C. Li, O. Svensk, S. Arpiainen, M. Kainlauri, and H. Lipsanen. Photo-thermal chemical vapor deposition of graphene on copper. *Carbon*, 62:43–50, 2013.
- [114] Y. Hao, M.S. Bharathi, L. Wang, Y. Liu, H. Chen, S. Nie, X. Wang, H. Chou, C. Tan, B. Fallahazad, H. Ramanarayan, C.W. Magnuson, E. Tutuc, B.I. Yakobson, K.F. McCarty, Y.W. Zhang, P. Kim, J. Hone, L. Colombo, and R.S. Ruoff. The role of surface oxygen in the growth of large single-crystal graphene on copper. *Science*, 342(6159):720–723, 2013.

- [115] S.M. Kim, A. Hsu, Y.-H. Lee, M. Dresselhaus, K.K. Kim, J. Kong, T. Palacios, K.K. Kim, and J. Kong. The effect of copper pre-cleaning on graphene synthesis. *Nanotechnology*, 24(36):365602, 2013.
- [116] L. Tan, M. Zeng, T. Zhang, and L. Fu. Design of catalytic substrates for uniform graphene films: from solid-metal to liquid-metal. *Nanoscale*, 7(20):9105–9121, 2015.
- [117] M. Zeng, L. Tan, J. Wang, L. Chen, M.H. Rummeli, and L. Fu. Liquid metal: An innovative solution to uniform graphene films. *Chem. Mater.*, 26(12):3637–3643, 2014.
- [118] I. Vlassiouk, M. Regmi, P. Fulvio, S. Dai, P. Datskos, G. Eres, and S. Smirnov. Role of hydrogen in chemical vapor deposition growth of large single-crystal graphene. *ACS Nano*, 5(7):6069–6076, 2011.
- [119] G.H. Han, F. Güneş, J.J. Bae, E.S. Kim, S.J. Chae, H.-J. Shin, J.-Y. Choi, D. Pribat, and Y.H. Lee. Influence of copper morphology in forming nucleation seeds for graphene growth. *Nano Lett.*, 11(10):4144–4148, 2011.
- [120] P. Procházka, J. Mach, D. Bischoff, Z.A. Lišková, P. Dvořák, M. Vaňatka, P. Simonet, A. Varlet, D. Hemzal, M. Petrenec, L. Kalina, M. Bartošík, K. Ensslin, P. Varga, J. Čechal, and T. Šikola. Ultra-smooth metallic foils for growth of high quality graphene by chemical vapor deposition. *Nanotechnology*, 25(18):185601, 2014.
- [121] Z. Luo, Y. Lu, D.W. Singer, M.E. Berck, L.A. Somers, B.R. Goldsmith, and A.T.C. Johnson. Effect of substrate roughness and feedstock concentration on growth of wafer-scale graphene at atmospheric pressure. *Chem. Mater.*, 23(6):1441–1447, 2011.

- [122] B. Dai, L. Fu, Z. Zou, M. Wang, H. Xu, S. Wang, and Z. Liu. Rational design of a binary metal alloy for chemical vapour deposition growth of uniform single-layer graphene. *Nat. Commun.*, 2:522, 2011.
- [123] M.H. Rümmeli, M. Zeng, S. Melkhanova, S. Gorantla, A. Bachmatiuk, L. Fu, C. Yan, S. Oswald, R.G. Mendes, D. Makarov, O. Schmidt, and J. Eckert. Insights into the early growth of homogeneous single-layer graphene over ni-mo binary substrates. *Chem. Mater.*, 25(19):3880–3887, 2013.
- [124] K.S. Kim, Y. Zhao, H. Jang, S.Y. Lee, J.M. Kim, K.S. Kim, J.H. Ahn, P. Kim, J.Y. Choi, and B.H. Hong. Large-scale pattern growth of graphene films for stretchable transparent electrodes. *Nature*, 457(7230):706–710, 2009.
- [125] M.H. Rümmeli, S. Gorantla, A. Bachmatiuk, J. Phieler, N. Geißler, I. Ibrahim, J. Pang, and J. Eckert. On the role of vapor trapping for chemical vapor deposition (cvd) grown graphene over copper. *Chem. Mater.*, 25(24):4861–4866, 2013.
- [126] X. Li, C.W. Magnuson, A. Venugopal, R.M. Tromp, J.B. Hannon, E.M. Vogel, L. Colombo, and R.S. Ruoff. Large-area graphene single crystals grown by low-pressure chemical vapor deposition of methane on copper. *J. Am. Chem. Soc.*, 133(9):2816–2819, 2011.
- [127] X. Li, C.W. Magnuson, A. Venugopal, J. An, J.W. Suk, B. Han, M. Borysiak, W. Cai, A. Velamakanni, Y. Zhu, L. Fu, E.M. Vogel, E. Voelkl, L. Colombo, and R.S. Ruoff. Graphene films with large domain size by a two-step chemical vapor deposition process. *Nano Lett.*, 10(11):4328–4334, 2010.

- [128] M.E. Ramon, A. Gupta, C. Corbet, D.A. Ferrer, H.C. Movva, G. Carpenter, L. Colombo, G. Bourianoff, M. Doczy, D. Akinwande, E. Tutuc, and S.K. Banerjee. Cmos-compatible synthesis of large-area, high-mobility graphene by chemical vapor deposition of acetylene on cobalt thin films. *ACS Nano*, 5(9):7198–7204, 2011.
- [129] M.H. Rummeli, A. Bachmatiuk, A. Scott, F. Borrnert, J.H. Warner, V. Hoffman, J.H. Lin, G. Cuniberti, and B. Buchner. Direct low-temperature nanographene cvd synthesis over a dielectric insulator. *ACS Nano*, 4(7):4206–4210, 2010.
- [130] H. Mehdipour and K.K. Ostrikov. Kinetics of low-pressure, low-temperature graphene growth: toward single-layer, single-crystalline structure. *ACS Nano*, 6(11):10276–10286, 2012.
- [131] G. Radhakrishnan, P.M. Adams, A.D. Stapleton, H.G. Muller, and B.J. Foran. Large single-crystal monolayer graphene by decomposition of methanol. *Appl. Phys. A*, 105(1):31–37, 2011.
- [132] N. Lisi, F. Buonocore, T. Dikonimos, E. Leoni, G. Faggio, G. Messina, V. Morandi, L. Ortolani, and A. Capasso. Rapid and highly efficient growth of graphene on copper by chemical vapor deposition of ethanol. *Thin Solid Films*, 571:139–144, 2014.
- [133] S. Gadipelli, I. Calizo, J. Ford, G. Cheng, A.R. Hight Walker, and T. Yildirim. A highly practical route for large-area, single layer graphene from liquid carbon sources such as benzene and methanol. *J. Mater. Chem.*, 21(40):16057–16065, 2011.
- [134] X. Gan, H. Zhou, B. Zhu, X. Yu, Y. Jia, B. Sun, M. Zhang, X. Huang, J. Liu, and T. Luo. A simple method to synthesize graphene at 633k by dechlorination of hexachlorobenzene on cu foils. *Carbon*, 50(1):306–310, 2012.

- [135] G.-P. Dai, P.H. Cooke, and S. Deng. Direct growth of graphene films on tem nickel grids using benzene as precursor. *Chem. Phys. Lett.*, 531:193–196, 2012.
- [136] X. Wan, K. Chen, D. Liu, J. Chen, Q. Miao, and J. Xu. High-quality large-area graphene from dehydrogenated polycyclic aromatic hydrocarbons. *Chem. Mater.*, 24(20):3906–3915, 2012.
- [137] J. Hackley, D. Ali, J. DiPasquale, J.D. Demaree, and C.J.K. Richardson. Graphitic carbon growth on si(111) using solid source molecular beam epitaxy. *Appl. Phys. Lett.*, 95(13):133114, 2009.
- [138] H. Ji, Y. Hao, Y. Ren, M. Charlton, W.H. Lee, Q. Wu, H. Li, Y. Zhu, Y. Wu, R. Piner, and R.S. Ruoff. Graphene growth using a solid carbon feedstock and hydrogen. *ACS Nano*, 5(9):7656–7661, 2011.
- [139] R.S. Weatherup, C. Baetz, B. Dlubak, B.C. Bayer, P.R. Kidambi, R. Blume, R. Schloegl, and S. Hofmann. Introducing carbon diffusion barriers for uniform, high-quality graphene growth from solid sources. *Nano Lett.*, 13(10):4624–4631, 2013.
- [140] G. Kalita, S. Sharma, K. Wakita, M. Umeno, Y. Hayashi, and M. Tanemura. Synthesis of graphene by surface wave plasma chemical vapor deposition from camphor. *Phys. Status Solidi A*, 209(12):2510–2513, 2012.
- [141] G. Kalita, K. Wakita, and M. Umeno. Monolayer graphene from a green solid precursor. *Physica E*, 43(8):1490–1493, 2011.
- [142] S. Sharma, G. Kalita, M.E. Ayhan, K. Wakita, M. Umeno, and M. Tanemura. Synthesis of hexagonal graphene on polycrystalline cu foil from solid camphor by atmospheric pressure chemical vapor deposition. *J. Mater. Sci.*, 48(20):7036–7041, 2013.



- [143] S. Sharma, G. Kalita, R. Hirano, Y. Hayashi, and M. Tanemura. Influence of gas composition on the formation of graphene domain synthesized from camphor. *Mater. Lett.*, 93:258–262, 2013.
- [144] A.N. Sokolov, F.L. Yap, N. Liu, K. Kim, L. Ci, O.B. Johnson, H. Wang, M. Vosgueritchian, A.L. Koh, J. Chen, J. Park, and Z. Bao. Direct growth of aligned graphitic nanoribbons from a dna template by chemical vapour deposition. *Nat. Commun.*, 4:2402, 2013.
- [145] G. Ruan, Z. Sun, Z. Peng, and J.M. Tour. Growth of graphene from food, insects, and waste. *ACS Nano*, 5(9):7601–7607, 2011.
- [146] H.-J. Shin, W.M. Choi, S.-M. Yoon, G.H. Han, Y.S. Woo, E.S. Kim, S.J. Chae, X.-S. Li, A. Benayad, D.D. Loc, F. Gunes, Y.H. Lee, and J.-Y. Choi. Transfer-free growth of few-layer graphene by self-assembled monolayers. *Adv. Mater.*, 23(38):4392–4397, 2011.
- [147] D. Kang, W.-J. Kim, J.A. Lim, and Y.-W. Song. Direct growth and patterning of multilayer graphene onto a targeted substrate without an external carbon source. *ACS Appl. Mater. Inter.*, 4(7):3663–3666, 2012.
- [148] J.S. Lee, C.W. Jang, J.M. Kim, D.H. Shin, S. Kim, S.-H. Choi, K. Belay, and R.G. Elliman. Graphene synthesis by c implantation into cu foils. *Carbon*, 66:267–271, 2014.
- [149] S. Suzuki, Y. Takei, K. Furukawa, G. Webber, S. Tanabe, and H. Hibino. Graphene growth from spin-coated polymers without a gas. *Jpn. J. Appl. Phys.*, 51:06FD01, 2012.
- [150] N. Hong, W. Yang, C. Bao, S. Jiang, L. Song, and Y. Hu. Facile synthesis of graphene by pyrolysis of poly(methyl methacrylate) on nickel particles in the confined microzones. *Mater. Res. Bull.*, 47(12):4082–4088, 2012.

- [151] J. Kwak, T.-Y. Kwon, J.H. Chu, J.-K. Choi, M.-S. Lee, S.Y. Kim, H.-J. Shin, K. Park, J.-U. Park, and S.-Y. Kwon. In situ observations of gas phase dynamics during graphene growth using solid-state carbon sources. *Phys. Chem. Chem. Phys.*, 15(25):10446–10452, 2013.
- [152] S. Lee, J. Hong, J.H. Koo, H. Lee, S. Lee, T. Choi, H. Jung, B. Koo, J. Park, H. Kim, Y.-W. Kim, and T. Lee. Synthesis of few-layered graphene nanoballs with copper cores using solid carbon source. *ACS Appl. Mater. Inter.*, 5(7):2432–2437, 2013.
- [153] T. Lin, Y. Wang, H. Bi, D. Wan, F. Huang, X. Xie, and M. Jiang. Hydrogen flame synthesis of few-layer graphene from a solid carbon source on hexagonal boron nitride. *J. Mater. Chem.*, 22(7):2859–2862, 2012.
- [154] R.N. Tiwari, M. Ishihara, J.N. Tiwari, and M. Yoshimura. Transformation of polymer to graphene films at partially low temperature. *Polym. Chem.*, 3(10):2712–2715, 2012.
- [155] S. Sharma, G. Kalita, R. Hirano, S.M. Shinde, R. Papon, H. Ohtani, and M. Tanemura. Synthesis of graphene crystals from solid waste plastic by chemical vapor deposition. *Carbon*, 72:66–73, 2014.
- [156] B. Kiraly, E.V. Iski, A.J. Mannix, B.L. Fisher, M.C. Hersam, and N.P. Guisinger. Solid-source growth and atomic-scale characterization of graphene on ag(111). *Nat. Commun.*, 4:2804, 2013.
- [157] P. Sutter, M.S. Hybertsen, J.T. Sadowski, and E. Sutter. Electronic structure of few-layer epitaxial graphene on ru(0001). *Nano Lett.*, 9(7):2654–2660, 2009.
- [158] H. An, W.-J. Lee, and J. Jung. Graphene synthesis on fe foil using thermal cvd. *Curr. Appl. Phys.*, 11(4):S81–S85, 2011.

- [159] R. John, A. Ashokreddy, C. Vijayan, and T. Pradeep. Single- and few-layer graphene growth on stainless steel substrates by direct thermal chemical vapor deposition. *Nanotechnology*, 22(16):165701, 2011.
- [160] L. Tao, J. Lee, H. Chou, M. Holt, R.S. Ruoff, and D. Akinwande. Synthesis of high quality monolayer graphene at reduced temperature on hydrogen-enriched evaporated copper (111) films. *ACS Nano*, 6(3):2319–2325, 2012.
- [161] J. Hwang, M. Kim, D. Campbell, H.A. Alsalman, J.Y. Kwak, S. Shivaraman, A.R. Woll, A.K. Singh, R.G. Hennig, S. Gorantla, M.H. Rummeli, and M.G. Spencer. van der waals epitaxial growth of graphene on sapphire by chemical vapor deposition without a metal catalyst. *ACS Nano*, 7(1):385–395, 2013.
- [162] X. Ding, G. Ding, X. Xie, F. Huang, and M. Jiang. Direct growth of few layer graphene on hexagonal boron nitride by chemical vapor deposition. *Carbon*, 49(7):2522–2525, 2011.
- [163] J.M. Garcia, U. Wurstbauer, A. Levy, L.N. Pfeiffer, A. Pinczuk, A.S. Plaut, L. Wang, C.R. Dean, R. Buizza, A.M. Van Der Zande, J. Hone, K. Watanabe, and T. Taniguchi. Graphene growth on h-bn by molecular beam epitaxy. *Solid State Commun.*, 152(12):975–978, 2012.
- [164] S. Tang, G. Ding, X. Xie, J. Chen, C. Wang, X. Ding, F. Huang, W. Lu, and M. Jiang. Nucleation and growth of single crystal graphene on hexagonal boron nitride. *Carbon*, 50(1):329–331, 2012.
- [165] S. Chugh, R. Mehta, N. Lu, F.D. Dios, M.J. Kim, and Z.H. Chen. Comparison of graphene growth on arbitrary non-catalytic substrates using low-temperature pecvd. *Carbon*, 93:393–399, 2015.

- [166] J.Y. Sun, Y.B. Chen, X. Cai, B.J. Ma, Z.L. Chen, M.K. Priyadarshi, K. Chen, T. Gao, X.J. Song, Q.Q. Ji, X.F. Guo, D.C. Zou, Y.F. Zhang, and Z.F. Liu. Direct low-temperature synthesis of graphene on various glasses by plasma-enhanced chemical vapor deposition for versatile, cost-effective electrodes. *Nano Res.*, 8(11):3496–3504, 2015.
- [167] T. Kato and R. Hatakeyama. Direct growth of doping-density-controlled hexagonal graphene on sio<sub>2</sub> substrate by rapid-heating plasma cvd. *ACS Nano*, 6(10):8508–8515, 2012.
- [168] X. Li, Y. Zhu, W. Cai, M. Borysiak, B. Han, D. Chen, R.D. Piner, L. Colombo, and R.S. Ruoff. Transfer of large-area graphene films for high-performance transparent conductive electrodes. *Nano Lett.*, 9(12):4359–4563, 2009.
- [169] J.W. Suk, A. Kitt, C.W. Magnuson, Y. Hao, S. Ahmed, J. An, A.K. Swan, B.B. Goldberg, and R.S. Ruoff. Transfer of cvd-grown monolayer graphene onto arbitrary substrates. *ACS Nano*, 5(9):6916–6924, 2011.
- [170] S.C. O’Hern, C.A. Stewart, M.S. Boutilier, J.C. Idrobo, S. Bhaviripudi, S.K. Das, J. Kong, T. Laoui, M. Atieh, and R. Karnik. Selective molecular transport through intrinsic defects in a single layer of cvd graphene. *ACS Nano*, 6(11):10130–10138, 2012.
- [171] L. Gao, W. Ren, H. Xu, L. Jin, Z. Wang, T. Ma, L.-P. Ma, Z. Zhang, Q. Fu, L.-M. Peng, X. Bao, and H.-M. Cheng. Repeated growth and bubbling transfer of graphene with millimetre-size single-crystal grains using platinum. *Nat. Commun.*, 3:699, 2012.
- [172] L. Zhang, Z. Shi, D. Liu, R. Yang, D. Shi, and G. Zhang. Vapour-phase graphene epitaxy at low temperatures. *Nano Res.*, 5(4):258–264, 2012.

- [173] X. Liu, L. Fu, N. Liu, T. Gao, Y. Zhang, L. Liao, and Z. Liu. Segregation growth of graphene on cu-ni alloy for precise layer control. *J. Phys. Chem. C*, 115(24):11976–11982, 2011.
- [174] Y.C. Lin, C. Jin, J.C. Lee, S.F. Jen, K. Suenaga, and P.W. Chiu. Clean transfer of graphene for isolation and suspension. *ACS Nano*, 5(3):2362–2368, 2011.
- [175] S. Gorantla, A. Bachmatiuk, J. Hwang, H.A. Alsalman, J.Y. Kwak, T. Seyller, J. Eckert, M.G. Spencer, and M.H. Rümmeli. A universal transfer route for graphene. *Nanoscale*, 6(2):889–896, 2014.
- [176] Y. Wang, Y. Zheng, X. Xu, E. Dubuisson, Q. Bao, J. Lu, and K.P. Loh. Electrochemical delamination of cvd-grown graphene film: toward the recyclable use of copper catalyst. *ACS Nano*, 5(12):9927–9933, 2011.
- [177] W.H. Lin, T.H. Chen, J.K. Chang, J.I. Taur, Y.Y. Lo, W.L. Lee, C.S. Chang, W.B. Su, and C.I. Wu. A direct and polymer-free method for transferring graphene grown by chemical vapor deposition to any substrate. *ACS Nano*, 8(2):1784–1791, 2014.
- [178] S.R. Na, J.W. Suk, L. Tao, D. Akinwande, R.S. Ruoff, R. Huang, and K.M. Liechti. Selective mechanical transfer of graphene from seed copper foil using rate effects. *ACS Nano*, 9(2):1325–1335, 2015.
- [179] L. Gao, G.X. Ni, Y. Liu, B. Liu, A.H. Castro Neto, and K.P. Loh. Face-to-face transfer of wafer-scale graphene films. *Nature*, 505(7482):190–194, 2014.
- [180] J. Wang, M. Zeng, L. Tan, B. Dai, Y. Deng, M.H. Rümmeli, H. Xu, Z. Li, S. Wang, L. Peng, J. Eckert, and L. Fu. High-mobility graphene on liquid p-block elements by ultra-low-loss cvd growth. *Sci. Rep.*, 3:2670, 2013.

- [181] L. Ding, A. Tselev, J. Wang, D. Yuan, H. Chu, T.P. McNicholas, Y. Li, and J. Liu. Selective growth of well-aligned semiconducting single-walled carbon nanotubes. *Nano Lett.*, 9(2):800–805, 2009.
- [182] K.R. Williams, K. Gupta, and M. Wasilik. Etch rates for micromachining processing - part ii. *J. Microelectromech. S.*, 12(6):761–778, 2003.
- [183] S. Stankovich, A.D. Dikin, D.R. Piner, A.K. Kohlhaas, A. Kleinhammes, Y. Jia, Y. Wu, T.S. Nguyen, and R.S. Ruoff. Synthesis of graphene-based nanosheets via chemical reduction of exfoliated graphite oxide. *Carbon*, 45(7):1558–1565, 2007.
- [184] K.V. Emtsev, F. Speck, T. Seyller, L. Ley, and J.D. Riley. Interaction, growth, and ordering of epitaxial graphene on sic0001 surfaces: A comparative photoelectron spectroscopy study. *Phys. Rev. B*, 77(15):155303, 2008.
- [185] L. Jiao, L. Zhang, L. Ding, J. Liu, and H. Dai. Aligned graphene nanoribbons and crossbars from unzipped carbon nanotubes. *Nano Res.*, 3(6):387–394, 2010.
- [186] X. Li, X. Wang, L. Zhang, S. Lee, and H. Dai. Chemically derived, ultrasmooth graphene nanoribbon semiconductors. *Science*, 319(5867):1229–1232, 2008.
- [187] J. Pang, A. Bachmatiuk, L. Fu, R.G. Mendes, M. Libera, D. Placha, G.S. Martynková, B. Trzebicka, T. Gemming, J. Eckert, and M.H. Rummeli. Direct synthesis of graphene from adsorbed organic solvent molecules over copper. *RSC Adv.*, 5(75):60884–60891, 2015.
- [188] R.G. Mendes, A. Bachmatiuk, A.A. El-Gendy, S. Melkhanova, R. Klingeler, B. Büchner, and M.H. Rummeli. A facile route to coat iron

- oxide nanoparticles with few-layer graphene. *J. Phys. Chem. C*, 116(44):23749–23756, 2012.
- [189] P. Atkins and J. de Paula. *Physical Chemistry: Thermodynamics, Structure, and Change*. W. H. Freeman, 10th edition, 2014.
- [190] I. Vlassiouk, S. Smirnov, M. Regmi, S.P. Surwade, N. Srivastava, R. Feenstra, G. Eres, C. Parish, N. Lavrik, P. Datskos, S. Dai, and P. Fulvio. Graphene nucleation density on copper: Fundamental role of background pressure. *J. Phys. Chem. C*, 117(37):18919–18926, 2013.
- [191] Y.-P. Hsieh, M. Hofmann, and J. Kong. Promoter-assisted chemical vapor deposition of graphene. *Carbon*, 67:417–423, 2014.
- [192] H. Kim, C. Mattevi, M.R. Calvo, J.C. Oberg, L. Artiglia, S. Agnoli, C.F. Hirjibehedin, M. Chhowalla, and E. Saiz. Activation energy paths for graphene nucleation and growth on cu. *ACS Nano*, 6(4):3614–3623, 2012.
- [193] P. Zhao, A. Kumamoto, S. Kim, X. Chen, B. Hou, S. Chiashi, E. Einarsson, Y. Ikuhara, and S. Maruyama. Self-limiting chemical vapor deposition growth of monolayer graphene from ethanol. *J. Phys. Chem. C*, 117(20):10755–10763, 2013.
- [194] P. Zhao, S. Kim, X. Chen, E. Einarsson, M. Wang, Y. Song, H. Wang, S. Chiashi, R. Xiang, and S. Maruyama. Equilibrium chemical vapor deposition growth of bernal-stacked bilayer graphene. *ACS Nano*, 8(11):11631–11638, 2014.
- [195] E. Loginova, N.C. Bartelt, P.J. Feibelman, and K.F. McCarty. Evidence for graphene growth by c cluster attachment. *New J. Phys.*, 10(9):093026, 2008.

- [196] L. Xu, Y. Jin, Z. Wu, Q. Yuan, Z. Jiang, Y. Ma, and W. Huang. Transformation of carbon monomers and dimers to graphene islands on co(0001): Thermodynamics and kinetics. *J. Phys. Chem. C*, 117(6): 2952–2958, 2013.
- [197] Y.S. Kim, K. Joo, S.K. Jerng, J.H. Lee, D. Moon, J. Kim, E. Yoon, and S.H. Chun. Direct integration of polycrystalline graphene into light emitting diodes by plasma-assisted metal-catalyst-free synthesis. *ACS Nano*, 8(3):2230–2236, 2014.
- [198] H. Kim, E. Saiz, M. Chhowalla, and C. Mattevi. Modeling of the self-limited growth in catalytic chemical vapor deposition of graphene. *New J. Phys.*, 15(5):053012, 2013.
- [199] S. Bhaviripudi, X. Jia, M.S. Dresselhaus, and J. Kong. Role of kinetic factors in chemical vapor deposition synthesis of uniform large area graphene using copper catalyst. *Nano Lett.*, 10(10):4128–4133, 2010.
- [200] C.J. Chen, M.H. Back, and R.A. Back. The thermal decomposition of methane. i. kinetics of the primary decomposition to  $c_2h_6+h_2$  ; rate constant for the homogeneous unimolecular dissociation of methane and its pressure dependence. *Can. J. Chem.*, 53(23):3580–3590, 1975.
- [201] I. Alstrup, I. Chorkendorff, and S. Ullmann. The interaction of  $ch_4$  at high temperatures with clean and oxygen precovered  $cu(100)$ . *Surf. Sci.*, 264(1-2):95–102, 1992.
- [202] S. Xing, W. Wu, Y. Wang, J. Bao, and S.-S. Pei. Kinetic study of graphene growth: Temperature perspective on growth rate and film thickness by chemical vapor deposition. *Chem. Phys. Lett.*, 580:62–66, 2013.



- [203] L. Colombo, X. Li, B. Han, C. Magnuson, W. Cai, Y. Zhu, and R.S. Ruoff. Growth kinetics and defects of cvd graphene on cu. *ECS Trans.*, 28(5):109–114, 2010.
- [204] K. Celebi, M.T. Cole, J.W. Choi, F. Wyczisk, P. Legagneux, N. Rupesinghe, J. Robertson, K.B.K. Teo, and H.G. Park. Evolutionary kinetics of graphene formation on copper. *Nano lett.*, 13(3):967–974, 2013.
- [205] Y. Zhang, L. Zhang, P. Kim, M. Ge, Z. Li, and C. Zhou. Vapor trapping growth of single-crystalline graphene flowers: synthesis, morphology, and electronic properties. *Nano Lett.*, 12(6):2810–2816, 2012.
- [206] P.R. Kidambi, B.C. Bayer, R. Blume, Z.J. Wang, C. Baehtz, R.S. Weatherup, M.G. Willinger, R. Schloegl, and S. Hofmann. Observing graphene grow: catalyst-graphene interactions during scalable graphene growth on polycrystalline copper. *Nano Lett.*, 13(10):4769–4778, 2013.
- [207] Z.J. Wang, G. Weinberg, Q. Zhang, T. Lunkenbein, A. Klein-Hoffmann, M. Kurnatowska, M. Plodinec, Q. Li, L. Chi, R. Schloegl, and M.G. Willinger. Direct observation of graphene growth and associated copper substrate dynamics by in situ scanning electron microscopy. *ACS Nano*, 9(2):1506–1519, 2015.
- [208] R.S. Weatherup, B.C. Bayer, R. Blume, C. Ducati, C. Baehtz, R. Schlögl, and S. Hofmann. In situ characterization of alloy catalysts for low-temperature graphene growth. *Nano Lett.*, 11(10):4154–4160, 2011.
- [209] L. Gao, W. Ren, J. Zhao, L.P. Ma, Z. Chen, and H.-M. Cheng. Efficient growth of high-quality graphene films on cu foils by ambient pressure chemical vapor deposition. *Appl. Phys. Lett.*, 97(18):183109, 2010.

- [210] L. Gomez De Arco, Y. Zhang, C.W. Schlenker, K. Ryu, M.E. Thompson, and C. Zhou. Continuous, highly flexible, and transparent graphene films by chemical vapor deposition for organic photovoltaics. *ACS Nano*, 4(5):2865–2873, 2010.
- [211] C.Y. Su, A.Y. Lu, C.Y. Wu, Y.T. Li, K.K. Liu, W. Zhang, S.Y. Lin, Z.Y. Juang, Y.L. Zhong, F.R. Chen, and L.J. Li. Direct formation of wafer scale graphene thin layers on insulating substrates by chemical vapor deposition. *Nano Lett.*, 11(9):3612–3616, 2011.
- [212] S. Nie, W. Wu, S. Xing, Q. Yu, J. Bao, S.-S. Pei, and K.F. McCarty. Growth from below: bilayer graphene on copper by chemical vapor deposition. *New J. Phys.*, 14(9):093028, 2012.
- [213] P.R. Kidambi, C. Ducati, B. Dlubak, D. Gardiner, R.S. Weatherup, M.-B. Martin, P. Seneor, H. Coles, and S. Hofmann. The parameter space of graphene chemical vapor deposition on polycrystalline cu. *J. Phys. Chem. C*, 116(42):22492–22501, 2012.
- [214] E. Mikmeková, L. Frank, I. Müllerová, B. W. Li, R.S. Ruoff, and M. Lejeune. Study of multi-layered graphene by ultra-low energy sem/stem. *Diam. Relat. Mater.*, 63:136–142, 2016.
- [215] Z. Pan, N. Liu, L. Fu, and Z. Liu. Wrinkle engineering: A new approach to massive graphene nanoribbon arrays. *J. Am. Chem. Soc.*, 133(44):17578–17581, 2011.
- [216] D. Geng, B. Wu, Y. Guo, L. Huang, Y. Xue, J. Chen, G. Yu, L. Jiang, W. Hu, and Y. Liu. Uniform hexagonal graphene flakes and films grown on liquid copper surface. *Proc. Natl. Acad. Sci. U. S. A.*, 109(21):7992–7996, 2012.

- [217] A.T. Murdock, A. Koos, T.B. Britton, L. Houben, T. Batten, T. Zhang, A.J. Wilkinson, R.E. Dunin-Borkowski, C.E. Lekka, and N. Grobert. Controlling the orientation, edge geometry, and thickness of chemical vapor deposition graphene. *ACS Nano*, 7(2):1351–1359, 2013.
- [218] J.D. Wood, S.W. Schmucker, A.S. Lyons, E. Pop, and J.W. Lyding. Effects of polycrystalline cu substrate on graphene growth by chemical vapor deposition. *Nano Lett.*, 11(11):4547–4554, 2011.
- [219] G.-P. Dai, M.H. Wu, D.K. Taylor, and K. Vinodgopal. Square-shaped, single-crystal, monolayer graphene domains by low-pressure chemical vapor deposition. *Mater. Res. Lett.*, 1(2):67–76, 2013.
- [220] A.W. Robertson and J.H. Warner. Hexagonal single crystal domains of few-layer graphene on copper foils. *Nano Lett.*, 11(3):1182–1189, 2011.
- [221] V. Miseikis, D. Convertino, N. Mishra, M. Gemmi, T. Mashoff, S. Heun, N. Haghighian, F. Bisio, M. Canepa, V. Piazza, and C. Coletti. Rapid cvd growth of millimetre-sized single crystal graphene using a cold-wall reactor. *2D Mater.*, 2:014006, 2015.
- [222] X. Chen, P. Zhao, R. Xiang, S. Kim, J. Cha, S. Chiashi, and S. Maruyama. Chemical vapor deposition growth of 5 mm hexagonal single-crystal graphene from ethanol. *Carbon*, 94:810–815, 2015.
- [223] Z. Zhao, Z. Shan, C. Zhang, Q. Li, B. Tian, Z. Huang, W. Lin, X. Chen, H. Ji, W. Zhang, and W. Cai. Study on the diffusion mechanism of graphene grown on copper pockets. *Small*, 11(12):1418–1422, 2015.
- [224] I.H. Son, H.J. Song, S. Kwon, A. Bachmatiuk, S.J. Lee, A. Benayad, J.H. Park, J.Y. Choi, H. Chang, and M.H. Rummeli. Co<sub>2</sub> enhanced chemical vapor deposition growth of few-layer graphene over niox. *ACS Nano*, 8(9):9224–9232, 2014.

- [225] K. Natesan and T.F. Kassner. Thermodynamics of carbon in nickel, iron-nickel and iron-chromium-nickel alloys. *Metall. Trans.*, 4(11):2557–2566, 1973.
- [226] A. Delamoreanu, C. Rabot, C. Vallee, and A. Zenasni. Wafer scale catalytic growth of graphene on nickel by solid carbon source. *Carbon*, 66:48–56, 2014.
- [227] J. Lahiri, T. Miller, L. Adamska, II Oleynik, and M. Batzill. Graphene growth on ni(111) by transformation of a surface carbide. *Nano Lett.*, 11(2):518–522, 2011.
- [228] S. Thiele, A. Reina, P. Healey, J. Kedzierski, P. Wyatt, P.-L. Hsu, C. Keast, J. Schaefer, and J. Kong. Engineering polycrystalline ni films to improve thickness uniformity of the chemical-vapor-deposition-grown graphene films. *Nanotechnology*, 21(1):015601, 2010.
- [229] L. Tan, M. Zeng, Q. Wu, L. Chen, J. Wang, T. Zhang, J. Eckert, M.H. Rümmeli, and L. Fu. Direct growth of ultrafast transparent single-layer graphene defoggers. *Small*, 11(15):1840–1846, 2015.
- [230] D. Wei, Y. Lu, C. Han, T. Niu, W. Chen, and A.T. Wee. Critical crystal growth of graphene on dielectric substrates at low temperature for electronic devices. *Angew. Chem. Int. Ed.*, 52(52):14121–14126, 2013.
- [231] A. Bachmatiuk, F. Börrnert, M. Grobosch, F. Schäffel, U. Wolff, A. Scott, M. Zaka, J.H. Warner, R. Klingeler, M. Knupfer, B. Büchner, and M.H. Rümmeli. Investigating the graphitization mechanism of sio<sub>2</sub> nanoparticles in chemical vapor deposition. *ACS Nano*, 3(12):4098–4104, 2009.

- [232] Z. Bo, W. Zhu, W. Ma, Z. Wen, X. Shuai, J. Chen, J. Yan, Z. Wang, K. Cen, and X. Feng. Vertically oriented graphene bridging active-layer/current-collector interface for ultrahigh rate supercapacitors. *Adv. Mater.*, 25(40):5799–5806, 2013.
- [233] A. Dato, V. Radmilovic, Z. Lee, J. Phillips, and M. Frenklach. Substrate-free gas-phase synthesis of graphene sheets. *Nano Lett.*, 8(7):2012–2016, 2008.
- [234] J.J. Wang, M.Y. Zhu, R.A. Outlaw, X. Zhao, D.M. Manos, B.C. Holloway, and V.P. Mammana. Free-standing subnanometer graphite sheets. *Appl. Phys. Lett.*, 85(7):1265–1267, 2004.
- [235] P. Blake, E.W. Hill, A.H. Castro Neto, K.S. Novoselov, D. Jiang, R. Yang, T.J. Booth, and A.K. Geim. Making graphene visible. *Appl. Phys. Lett.*, 91(6):063124, 2007.
- [236] F.M. Koehler, A. Jacobsen, K. Ensslin, C. Stampfer, and W.J. Stark. Selective chemical modification of graphene surfaces: Distinction between single- and bilayer graphene. *Small*, 6(10):1125–1130, 2010.
- [237] A. Bachmatiuk, J. Zhao, I.G.G. Gorantla, S.M. and Martinez, J. Wiedermann, C. Lee, J. Eckert, and M.H. Rummeli. Low voltage transmission electron microscopy of graphene. *Small*, 11(5):515–542, 2015.
- [238] S. Horiuchi, T. Gotou, M. Fujiwara, R. Sotoaka, M. Hirata, K. Kimoto, T. Asaka, T. Yokosawa, Y. Matsui, K. Watanabe, and M. Sekita. Carbon nanofilm with a new structure and property. *Jpn. J. Appl. Phys.*, 42(9ab):L1073–L1076, 2003.
- [239] Y.H. Wu, T. Yu, and Z.X. Shen. Two-dimensional carbon nanostructures: Fundamental properties, synthesis, characterization, and potential applications. *J. Appl. Phys.*, 108(7):071301, 2010.

- [240] J.C. Meyer, A.K. Geim, M.I. Katsnelson, K.S. Novoselov, T.J. Booth, and S. Roth. The structure of suspended graphene sheets. *Nature*, 446 (7131):60–63, 2007.
- [241] Y. Hernandez, V. Nicolosi, M. Lotya, F.M. Blighe, Z. Sun, S. De, I.T. McGovern, B. Holland, M. Byrne, Y.K. Gun'Ko, J.J. Boland, P. Niraj, G. Duesberg, S. Krishnamurthy, R. Goodhue, J. Hutchison, V. Scardaci, A.C. Ferrari, and J.N. Coleman. High-yield production of graphene by liquid-phase exfoliation of graphite. *Nat. Nanotechnol.*, 3(9):563–568, 2008.
- [242] J. An, E. Voelkl, J.W. Suk, X. Li, C.W. Magnuson, L. Fu, P. Tiemeijer, M. Bischoff, B. Freitag, E. Popova, and R.S. Ruoff. Domain (grain) boundaries and evidence of "twinlike" structures in chemically vapor deposited grown graphene. *ACS Nano*, 5(4):2433–2439, 2011.
- [243] J. Thomas and T. Gemming. *Analytical Transmission Electron Microscopy An Introduction for Operators*. Springer-Verlag, Wien, 1th edition, 2013.
- [244] A.C. Ferrari and D.M. Basko. Raman spectroscopy as a versatile tool for studying the properties of graphene. *Nat. Nanotechnol.*, 8(4):235–246, 2013.
- [245] M.S. Dresselhaus, A. Jorio, and R. Saito. Characterizing graphene, graphite, and carbon nanotubes by raman spectroscopy. *Ann. Rev. Cond. Matt. Phys.*, 1(1):89–108, 2010.
- [246] A.C. Ferrari, J.C. Meyer, V. Scardaci, C. Casiraghi, M. Lazzeri, F. Mauri, S. Piscanec, D. Jiang, K.S. Novoselov, S. Roth, and A.K. Geim. Raman spectrum of graphene and graphene layers. *Phys. Rev. Lett.*, 97(18):187401, 2006.

- [247] L.M. Malard, J. Nilsson, D.C. Elias, J.C. Brant, F. Plentz, E.S. Alves, A.H. Castro Neto, and M.A. Pimenta. Probing the electronic structure of bilayer graphene by raman scattering. *Phys. Rev. B*, 76:201401, 2007.
- [248] K. Kim, S. Coh, L.Z. Tan, W. Regan, J.M. Yuk, E. Chatterjee, M.F. Crommie, M.L. Cohen, S.G. Louie, and A. Zettl. Raman spectroscopy study of rotated double-layer graphene: misorientation-angle dependence of electronic structure. *Phys. Rev. Lett.*, 108(24):246103, 2012.
- [249] I. Vlassiouk, P. Fulvio, H. Meyer, N. Lavrik, S. Dai, P. Datskos, and S. Smirnov. Large scale atmospheric pressure chemical vapor deposition of graphene. *Carbon*, 54:58–67, 2013.
- [250] G. Eres, M. Regmi, C.M. Rouleau, J. Chen, I.N. Ivanov, A.A. Puretzky, and D.B. Geohegan. Cooperative island growth of large-area single-crystal graphene on copper using chemical vapor deposition. *ACS Nano*, 8(6):5657–5669, 2014.
- [251] Z. Han, A. Kimouche, D. Kalita, A. Allain, H. Arjmandi-Tash, A. Reserbat-Plantey, L. Marty, S. Pairis, V. Reita, N. Bendiab, J. Coraux, and V. Bouchiat. Homogeneous optical and electronic properties of graphene due to the suppression of multilayer patches during cvd on copper foils. *Adv. Funct. Mater.*, 24(7):964–970, 2014.
- [252] S. Stankovich, D.R. Piner, T.S. Nguyen, and S.R. Ruoff. Synthesis and exfoliation of isocyanate-treated graphene oxide nanoplatelets. *Carbon*, 44(15):3342–3347, 2006.
- [253] E. Hernandez, C. Goze, P. Bernier, and A. Rubio. Elastic properties of c and bxcynz composite nanotubes. *Phys. Rev. Lett.*, 80(20):4502–4505, 1998.

- [254] M.S. Dresselhaus, A. Jorio, A.G. Souza Filho, and R. Saito. Defect characterization in graphene and carbon nanotubes using raman spectroscopy. *Philos. T. Roy. Soc. A*, 368(1932):5355–5377, 2010.
- [255] A. Jorio, R. Saito, G. Dresselhaus, and M.S. Dresselhaus. *Raman Spectroscopy in Graphene Related Systems*. Wiley-VCH Verlag GmbH & Co. KGaA, Weinheim, Germany, 2011.
- [256] L. Cançado, A Reina, J. Kong, and M. Dresselhaus. Geometrical approach for the study of g band in the raman spectrum of monolayer graphene, bilayer graphene, and bulk graphite. *Phys. Rev. B*, 77(24):245408, 2008.
- [257] M. Kalbac, J. Kong, and M.S. Dresselhaus. Raman spectroscopy as a tool to address individual graphene layers in few-layer graphene. *J. Phys. Chem. C*, 116(35):19046–19050, 2012.
- [258] M.A. Pimenta, G. Dresselhaus, M.S. Dresselhaus, L.G. Cançado, A. Jorio, and R. Saito. Studying disorder in graphite-based systems by raman spectroscopy. *Phys. Chem. Chem. Phys.*, 9(11):1276–1291, 2007.
- [259] J.C. Meyer, A.K. Geim, M.I. Katsnelson, K.S. Novoselov, D. Oberfell, S. Roth, C. Girit, and A. Zettl. On the roughness of single- and bi-layer graphene membranes. *Solid State Commun.*, 143(1-2):101–109, 2007.
- [260] J.H. Warner, M.H. Rummeli, L. Ge, T. Gemming, B. Montanari, N.M. Harrison, B. Büchner, and G.A.D. Briggs. Structural transformations in graphene studied with high spatial and temporal resolution. *Nat. Nanotechnol.*, 4(8):500–504, 2009.
- [261] J. Wu, W. Pisula, and K. Mullen. Graphenes as potential material for electronics. *Chem. Rev.*, 107(3):718–747, 2007.



- [262] L. Fan, Z. Li, X. Li, K. Wang, M. Zhong, J. Wei, D. Wu, and H. Zhu. Controllable growth of shaped graphene domains by atmospheric pressure chemical vapour deposition. *Nanoscale*, 3(12):4946–4946, 2011.
- [263] H. Bong, S.B. Jo, B. Kang, S.K. Lee, H.H. Kim, S.G. Lee, and K. Cho. Graphene growth under knudsen molecular flow on a confined catalytic metal coil. *Nanoscale*, 7(4):1314–1324, 2015.
- [264] M.M. Yang, X.H. Bao, and W.X. Li. First principle study of ethanol adsorption and formation of hydrogen bond on rh(111) surface. *J. Phys. Chem. C*, 111(20):7403–7410, 2007.
- [265] K. Sun, M. Zhang, and L. Wang. Effects of catalyst surface and hydrogen bond on ethanol dehydrogenation to ethoxy on cu catalysts. *Chem. Phys. Lett.*, 585:89–94, 2013.
- [266] L.M. Malard, M.A. Pimenta, G. Dresselhaus, and M.S. Dresselhaus. Raman spectroscopy in graphene. *Phys. Rep.*, 473(5-6):51–87, 2009.
- [267] R.S. Weatherup, B. Dlubak, and S. Hofmann. Kinetic control of catalytic cvd for high-quality graphene at low temperatures. *ACS Nano*, 6(11):9996–10003, 2012.
- [268] R.W. Havener, H. Zhuang, L. Brown, R.G. Hennig, and J. Park. Angle-resolved raman imaging of interlayer rotations and interactions in twisted bilayer graphene. *Nano Lett.*, 12(6):3162–3167, 2012.
- [269] J.H. Warner. The influence of the number of graphene layers on the atomic resolution images obtained from aberration-corrected high resolution transmission electron microscopy. *Nanotechnology*, 21(25):255707, 2010.

- [270] J.H. Warner, M.H. Rummeli, T. Gemming, B. Buchner, and G.A. Briggs. Direct imaging of rotational stacking faults in few layer graphene. *Nano Lett.*, 9(1):102–106, 2009.
- [271] J.M. Wofford, S. Nie, K.F. McCarty, N.C. Bartelt, and O.D. Dubon. Graphene islands on cu foils: The interplay between shape, orientation, and defects. *Nano Lett.*, 10:4890–4896, 2010.
- [272] H. Wang, G. Wang, P. Bao, S. Yang, W. Zhu, X. Xie, and W.-J. Zhang. Controllable synthesis of submillimeter single-crystal monolayer graphene domains on copper foils by suppressing nucleation. *J. Am. Chem. Soc.*, 134(8):3627–3630, 2012.
- [273] W. Wu, L.A. Jauregui, Z. Su, Z. Liu, J. Bao, Y.P. Chen, and Q. Yu. Growth of single crystal graphene arrays by locally controlling nucleation on polycrystalline cu using chemical vapor deposition. *Adv. Mater.*, 23(42):4898–4903, 2011.
- [274] M. Losurdo, M.M. Giangregorio, P. Capezzuto, and G. Bruno. Graphene cvd growth on copper and nickel: role of hydrogen in kinetics and structure. *Phys. Chem. Chem. Phys.*, 13(46):20836–20843, 2011.
- [275] W. Zhang, P. Wu, Z. Li, and J. Yang. First-principles thermodynamics of graphene growth on cu surfaces. *J. Phys. Chem. C*, 115(36):17782–17787, 2011.
- [276] R. Nemanich and S. Solin. First- and second-order raman scattering from finite-size crystals of graphite. *Phys. Rev. B*, 20(2):392–401, 1979.
- [277] A. Bachmatiuk, F. Börrnert, V. Hoffmann, D. Lindackers, J.-H. Lin, B. Buchner, and M.H. Rummeli. Hydrogen-induced self-assembly of

- helical carbon nanostructures from ethanol over  $\text{SiO}_2$  catalysts. *J. Appl. Phys.*, 109(9):094317, 2011.
- [278] Q. Li, H. Chou, J.-H. Zhong, J.-Y. Liu, A. Dolocan, J. Zhang, Y. Zhou, R.S. Ruoff, S. Chen, and W. Cai. Growth of adlayer graphene on Cu studied by carbon isotope labeling. *Nano Lett.*, 13(2):486–490, 2013.
- [279] W. Fang, A.L. Hsu, R. Caudillo, Y. Song, A.G. Birdwell, E. Zakar, M. Kalbac, M. Dubey, T. Palacios, M.S. Dresselhaus, P.T. Araujo, and J. Kong. Rapid identification of stacking orientation in isotopically labeled chemical-vapor grown bilayer graphene by Raman spectroscopy. *Nano Lett.*, 13(4):1541–1548, 2013.
- [280] Q. Chen, J.M. Smith, J. Park, K. Kim, D. Ho, H.I. Rasool, A. Zettl, and A.P. Alivisatos. 3D motion of DNA-Au nanoconjugates in graphene liquid cell electron microscopy. *Nano Lett.*, 13(9):4556–4561, 2013.
- [281] J.M. Yuk, J. Park, P. Ercius, K. Kim, D.J. Hellebusch, M.F. Crommie, J.Y. Lee, A. Zettl, and A.P. Alivisatos. High-resolution EM of colloidal nanocrystal growth using graphene liquid cells. *Science*, 336(6077):61–64, 2012.
- [282] T. Cohen-Karni, Q. Qing, Q. Li, Y. Fang, and C.M. Lieber. Graphene and nanowire transistors for cellular interfaces and electrical recording. *Nano Lett.*, 10(3):1098–1102, 2010.
- [283] S. Pang, Y. Hernandez, X. Feng, and K. Mullen. Graphene as transparent electrode material for organic electronics. *Adv. Mater.*, 23(25):2779–2795, 2011.
- [284] X. Sun, Z. Liu, K. Welsher, J.T. Robinson, A. Goodwin, S. Zaric, and H. Dai. Nano-graphene oxide for cellular imaging and drug delivery. *Nano Res.*, 1(3):203–212, 2008.

- [285] A.C. Ferrari, F. Bonaccorso, V. Fal'ko, K.S. Novoselov, S. Roche, P. Boggild, S. Borini, F.H. Koppens, V. Palermo, N. Pugno, J.A. Garrido, R. Sordan, A. Bianco, L. Ballerini, M. Prato, E. Lidorikis, J. Kivioja, C. Marinelli, T. Ryhanen, A. Morpurgo, J.N. Coleman, V. Nicolosi, L. Colombo, A. Fert, M. Garcia-Hernandez, A. Bachtold, G.F. Schneider, F. Guinea, C. Dekker, M. Barbone, Z. Sun, C. Galiotis, A.N. Grigorenko, G. Konstantatos, A. Kis, M. Katsnelson, L. Vandersypen, A. Loiseau, V. Morandi, D. Neumaier, E. Treossi, V. Pellegrini, M. Polini, A. Tredicucci, G.M. Williams, B.H. Hong, J.H. Ahn, J.M. Kim, H. Zirath, B.J. van Wees, H. van der Zant, L. Occhipinti, A. Di Matteo, I.A. Kinloch, T. Seyller, E. Quesnel, X. Feng, K. Teo, N. Rupesinghe, P. Hakonen, S.R. Neil, Q. Tannock, T. Lofwander, and J. Kinaret. Science and technology roadmap for graphene, related two-dimensional crystals, and hybrid systems. *Nanoscale*, 7(11):4598–4810, 2015.
- [286] W. Ren and H.M. Cheng. The global growth of graphene. *Nat. Nanotechnol.*, 9(10):726–730, 2014.
- [287] Y. Zhu, S. Murali, W. Cai, X. Li, J.W. Suk, J.R. Potts, and R.S. Ruoff. Graphene and graphene oxide: synthesis, properties, and applications. *Adv. Mater.*, 22(35):3906–3924, 2010.
- [288] S. Chen, W. Cai, R.D. Piner, J.W. Suk, Y. Wu, Y. Ren, J. Kang, and R.S. Ruoff. Synthesis and characterization of large-area graphene and graphite films on commercial cu-ni alloy foils. *Nano Lett.*, 11(9):3519–3525, 2011.
- [289] A. Zhang and C.M. Lieber. Nano-bioelectronics. *Chem. Rev.*, 116(1): 215–257, 2016.

- [290] M.P. Levendorf, C.J. Kim, L. Brown, P.Y. Huang, R.W. Havener, D.A. Muller, and J. Park. Graphene and boron nitride lateral heterostructures for atomically thin circuitry. *Nature*, 488(7413):627–632, 2012.
- [291] A. Naeemi and J.D. Meindl. Compact physics-based circuit models for graphene nanoribbon interconnects. *IEEE T. Electron. Dev.*, 56(9):1822–1833, 2009.
- [292] J.W. Suk, W.H. Lee, J. Lee, H. Chou, R.D. Piner, Y. Hao, D. Ak-inwande, and R.S. Ruoff. Enhancement of the electrical properties of graphene grown by chemical vapor deposition via controlling the effects of polymer residue. *Nano Lett.*, 13(4):1462–1467, 2013.
- [293] J. Sun, T. Gao, X. Song, Y. Zhao, Y. Lin, H. Wang, D. Ma, Y. Chen, W. Xiang, J. Wang, Y. Zhang, and Z. Liu. Direct growth of high-quality graphene on high-k dielectric srtio3 substrates. *J. Am. Chem. Soc.*, 136(18):6574–6577, 2014.
- [294] Y. Chen, J. Sun, J. Gao, F. Du, Q. Han, Y. Nie, Z. Chen, A. Bachmatiuk, M. K. Priydarshi, D. Ma, X. Song, X. Wu, C. Xiong, M.H. Rummeli, F. Ding, Y. Zhang, and Z. Liu. Growing uniform graphene disks and films on molten glass for heating devices and cell culture. *Adv. Mater.*, 27(47):7839–7846, 2015.
- [295] J. Sun, Y. Chen, M.K. Priydarshi, Z. Chen, A. Bachmatiuk, Z. Zou, Z. Chen, X. Song, Y. Gao, M.H. Rummeli, Y. Zhang, and Z. Liu. Direct chemical vapor deposition-derived graphene glasses targeting wide ranged applications. *Nano Lett.*, 15(9):5846–5854, 2015.
- [296] H. Kim, I. Song, C. Park, M. Son, M. Hong, Y. Kim, J.S. Kim, H. J. Shin, J. Baik, and H.C. Choi. Copper-vapor-assisted chemical vapor deposition for high-quality and metal-free single-layer graphene on amorphous sio2 substrate. *ACS Nano*, 7(8):6575–6582, 2013.

- [297] P.Y. Teng, C.C. Lu, K. Akiyama-Hasegawa, Y.C. Lin, C.H. Yeh, K. Suenaga, and P.W. Chiu. Remote catalyzation for direct formation of graphene layers on oxides. *Nano Lett.*, 12(3):1379–1384, 2012.
- [298] A. Ismach, C. Druzgalski, S. Penwell, A. Schwartzberg, M. Zheng, A. Javey, J. Bokor, and Y. Zhang. Direct chemical vapor deposition of graphene on dielectric surfaces. *Nano Lett.*, 10(5):1542–1548, 2010.
- [299] S.C. Xu, B.Y. Man, S.Z. Jiang, C.S. Chen, C. Yang, M. Liu, X.G. Gao, Z.C. Sun, and C. Zhang. Direct synthesis of graphene on sio2 substrates by chemical vapor deposition. *CrystEngComm*, 15(10):1840–1844, 2013.
- [300] J. Sun, N. Lindvall, M.T. Cole, K.B. K. Teo, and A. Yurgens. Large-area uniform graphene-like thin films grown by chemical vapor deposition directly on silicon nitride. *Appl. Phys. Lett.*, 98(25):252107, 2011.
- [301] J. Sun, M.E. Schmidt, M. Muruganathan, H.M. Chong, and H. Mizuta. Large-scale nanoelectromechanical switches based on directly deposited nanocrystalline graphene on insulating substrates. *Nanoscale*, 8(12):6659–6665, 2016.
- [302] S. Chen, H. Ji, H. Chou, Q. Li, H. Li, J.W. Suk, R. Piner, L. Liao, W. Cai, and R.S. Ruoff. Millimeter-size single-crystal graphene by suppressing evaporative loss of cu during low pressure chemical vapor deposition. *Adv. Mater.*, 25(14):2062–2065, 2013.
- [303] J. Gao, J. Zhao, and F. Ding. Transition metal surface passivation induced graphene edge reconstruction. *J. Am. Chem. Soc.*, 134(14):6204–6209, 2012.
- [304] J. Pang, A. Bachmatiuk, I. Ibrahim, L. Fu, D. Placha, G.S. Martynkova, B. Trzebicka, T. Gemming, J. Eckert, and M.H. Rümmeli. Cvd growth

- of 1d and 2d sp<sup>2</sup> carbon nanomaterials. *J. Mater. Sci.*, 51(2):640–667, 2016.
- [305] A.W. Tsen, L. Brown, M.P. Levendorf, F. Ghahari, P.Y. Huang, R.W. Havener, C.S. Ruiz-Vargas, D.A. Muller, P. Kim, and J. Park. Tailoring electrical transport across grain boundaries in polycrystalline graphene. *Science*, 336(6085):1143–1146, 2012.
- [306] G.K. Pang, K.Z. Baba-Kishi, and A. Patel. Topographic and phase-contrast imaging in atomic force microscopy. *Ultramicroscopy*, 81(2):35–40, 2000.
- [307] S.T. Skowron, I.V. Lebedeva, A.M. Popov, and E. Bichoutskaia. Energetics of atomic scale structure changes in graphene. *Chem. Soc. Rev.*, 44(10):3143–3176, 2015.
- [308] J.M. Carlsson, L.M. Ghiringhelli, and A. Fasolino. Theory and hierarchical calculations of the structure and energetics of [0001] tilt grain boundaries in graphene. *Phys. Rev. B*, 84(16):165423, 2011.
- [309] W. Guo, B. Wu, Y. Li, L. Wang, J. Chen, B. Chen, Z. Zhang, L. Peng, S. Wang, and Y. Liu. Governing rule for dynamic formation of grain boundaries in grown graphene. *ACS Nano*, 9(6):5792–5798, 2015.
- [310] B.I. Yakobson and F. Ding. Observational geology of graphene, at the nanoscale. *ACS Nano*, 5(3):1569–1574, 2011.
- [311] S. Kurasch, J. Kotakoski, O. Lehtinen, V. Skakalova, J. Smet, 3rd Krill, C.E., A.V. Krasheninnikov, and U. Kaiser. Atom-by-atom observation of grain boundary migration in graphene. *Nano Lett.*, 12(6):3168–3173, 2012.

- [312] M.F. Vaz, S.J. Cox, and M.D. Alonso. Minimum energy configurations of small bidisperse bubble clusters. *J. Phys. Condens. Matter*, 16(23):4165–4175, 2004.
- [313] S.J. Cox and F. Graner. Large two-dimensional clusters of equal-area bubbles: the influence of the boundary in determining the minimum-energy configuration. *Philos. Mag.*, 83(22):2573–2584, 2003.
- [314] S.J. Cox, F. Graner, M.F. Vaz, C. Monnereau-Pittet, and N. Pittet. Minimal perimeter for  $n$  identical bubbles in two dimensions: calculations and simulations. *Philos. Mag.*, 83(11):1393–1406, 2003.
- [315] F. Ding, A.R. Harutyunyan, and B.I. Yakobson. Dislocation theory of chirality-controlled nanotube growth. *Proc. Natl. Acad. Sci. U. S. A.*, 106(8):2506–2509, 2009.
- [316] V.I. Artyukhov, Y. Liu, and B.I. Yakobson. Equilibrium at the edge and atomistic mechanisms of graphene growth. *Proc. Natl. Acad. Sci. U. S. A.*, 109(38):15136–15140, 2012.
- [317] H. Li, Q. Zhang, C. Liu, S. Xu, and P. Gao. Ambipolar to unipolar conversion in graphene field-effect transistors. *ACS Nano*, 5(4):3198–3203, 2011.
- [318] T. Feng, D. Xie, Y. Lin, H. Tian, H. Zhao, T. Ren, and H. Zhu. Unipolar to ambipolar conversion in graphene field-effect transistors. *Appl. Phys. Lett.*, 101(25):253505, 2012.
- [319] D. Liu, W. Yang, L. Zhang, J. Zhang, J. Meng, R. Yang, G. Zhang, and D. Shi. Two-step growth of graphene with separate controlling nucleation and edge growth directly on  $\text{SiO}_2$  substrates. *Carbon*, 72:387–392, 2014.



- [320] H.J. Song, M. Son, C. Park, H. Lim, M.P. Levendorf, A.W. Tsen, J. Park, and H.C. Choi. Large scale metal-free synthesis of graphene on sapphire and transfer-free device fabrication. *Nanoscale*, 4(10):3050–3054, 2012.
- [321] Y.J. Ren, C.F. Zhu, W.W. Cai, H.F. Li, Y.F. Hao, Y.P. Wu, S.S. Chen, Q.Z. Wu, R.D. Piner, and R.S. Ruoff. An improved method for transferring graphene grown by chemical vapor deposition. *Nano*, 7(1):1150001, 2012.
- [322] C.M. Orofeo, H. Hibino, K. Kawahara, Y. Ogawa, M. Tsuji, K. Ikeda, S. Mizuno, and H. Ago. Influence of cu metal on the domain structure and carrier mobility in single-layer graphene. *Carbon*, 50(6):2189–2196, 2012.
- [323] J.Y. Hwang, C.C. Kuo, L.C. Chen, and K.H. Chen. Correlating defect density with carrier mobility in large-scaled graphene films: Raman spectral signatures for the estimation of defect density. *Nanotechnology*, 21(46):465705, 2010.
- [324] Z. Sun, Z. Yan, J. Yao, E. Beitler, Y. Zhu, and J.M. Tour. Growth of graphene from solid carbon sources. *Nature*, 468(7323):549–552, 2010.
- [325] X. Dong, P. Wang, W. Fang, C.-Y. Su, Y.-H. Chen, L.-J. Li, W. Huang, and P. Chen. Growth of large-sized graphene thin-films by liquid precursor-based chemical vapor deposition under atmospheric pressure. *Carbon*, 49(11):3672–3678, 2011.
- [326] M.P. Levendorf, C.S. Ruiz-Vargas, S. Garg, and J. Park. Transfer-free batch fabrication of single layer graphene transistors. *Nano Lett.*, 9(12):4479–4483, 2009.

- 
- [327] C.C. Lu, Y.C. Lin, C.H. Yeh, J.C. Huang, and P.W. Chiu. High mobility flexible graphene field-effect transistors with self-healing gate dielectrics. *ACS Nano*, 6(5):4469–4474, 2012.
- [328] B.J. Kim, H. Jang, S.K. Lee, B.H. Hong, J.H. Ahn, and J.H. Cho. High-performance flexible graphene field effect transistors with ion gel gate dielectrics. *Nano Lett.*, 10(9):3464–3466, 2010.

# List of Figures

1.1	Towards the formation of strictly monolayer graphene film. . .	2
2.1	Atomic orbital diagram of carbon atom. . . . .	7
2.2	Hexagonal lattice structure of graphene. . . . .	9
2.3	A bubble transfer protocol that applies to arbitrary substrates. . . . .	21
2.4	Predominantly monolayer graphene film growth over Cu via CVD. . . . .	29
2.5	Graphene synthesis over NiO <sub>x</sub> substrates with CO <sub>2</sub> assistance. . . . .	30
2.6	Monolayer graphene synthesis over binary Ni-Mo substrate. . . . .	31
2.7	Graphene growth over MgO support. . . . .	32
2.8	Graphene grown directly over Si/SiO <sub>x</sub> substrates with CVD. . . . .	33
2.9	Vertical graphene growth via plasma-enhanced chemical vapor deposition. . . . .	34
3.1	Schematic of horizontal CVD furnace system. . . . .	38
3.2	Schematic of useful signals for sample examination in SEM. . . . .	41
3.3	Schematic of TEM with a typical configuration . . . . .	43
3.4	Schematic of lattice structures of graphene and their corresponding diffraction pattern . . . . .	45
3.5	A typical Raman spectrum of monolayer graphene. . . . .	48
4.1	Temperature profiles and gas conditions in a CVD reaction. . . . .	54
4.2	SEM graphs of graphene grown on Cu with different pretreatments. . . . .	57
4.3	AFM graphs of graphene grown on Cu with different pretreatments. . . . .	59
4.4	Raman spectra of graphene grown on Cu with different pretreatments. . . . .	60
4.5	Raman mapping of graphene grown on Cu with different pretreatments. . . . .	62
4.6	TEM characterization of graphene grown on Cu with oxidation pretreatments. . . . .	63
4.7	Statistics of the flakes formed from three pretreatments without oxidation . . . . .	63
4.8	SEM graphs of the samples after H <sub>2</sub> annealing step . . . . .	64
4.9	The oxidation pretreatment for the formation mechanism of pure monolayer graphene. . . . .	65

---

5.1	Chemo-thermal route for graphene fabrication from adsorbed organic molecules. . . . .	71
5.2	SEM and AFM graphs for graphene flakes from chemo-thermal route. . . . .	72
5.3	Raman spectra for synthetic graphene flakes from chemo thermal route. . . . .	73
5.4	TEM examination for synthetic graphene flakes from chemo thermal route. . . . .	75
5.5	SEM graphs for graphene formation with respect to reaction temperature. . . . .	76
5.6	Arrhenius plots for the diameter and density of graphene flakes for each solvent precursor. . . . .	77
5.7	SEM of graphene flakes formed at different reaction pressures. . . . .	79
6.1	Si/SiO <sub>x</sub> substrate configurations for the direct synthesis of graphene. . . . .	88
6.2	Characterization of the graphene for different substrate configurations. . . . .	89
6.3	Time dependent growth evolution of the synthetic graphene. . . . .	92
6.4	TEM characterizations of the large area synthetic monolayer graphene. . . . .	95
6.5	Faceted graphene film for sandwich substrate configuration. . . . .	97
6.6	Growth evolution of grains in a bubble-merging fashion. . . . .	99
6.7	Schematic of strictly monolayer graphene directly grown over Si/SiO <sub>x</sub> . . . . .	99
6.8	Optical and electrical performance of the directly grown graphene. . . . .	101
A.1	AFM height determining the graphene thickness. . . . .	111
A.2	Large area, clean, homogeneous monolayer graphene after transfer. . . . .	112
A.3	Identification of ‘flakes’ on H <sub>2</sub> annealed Cu. . . . .	112
A.4	Graphene flakes on H <sub>2</sub> annealed Cu foil. . . . .	113
B.1	The chemo-thermal approach for graphene flake formation. . . . .	115
B.2	Typical graphene flake synthesis over Cu and transferred on to Si/SiO <sub>x</sub> . . . . .	116
B.3	AFM images of synthetic graphene flakes synthesis over Cu. . . . .	117
B.4	Relative contrast of graphene flakes in SEM graphs. . . . .	117
B.5	Thermodynamic calculation for the reactive species (temperature). . . . .	118
B.6	Coverage ratio of graphene area to Cu area (temperature). . . . .	119
B.7	Statistics of grain diameter and density (pressure). . . . .	120
B.8	coverage ratio of graphene area to Cu area (pressure). . . . .	120
B.9	Molar fraction of radicals at chemical equilibrium state (pressure). . . . .	121
B.10	SEM micrographs of the synthetic graphene flakes (H <sub>2</sub> flow). . . . .	122

---

B.11	Statistics plots of average diameter and grain density ( $H_2$ flow).	123
B.12	Relative ratio of graphene coverage area to Cu area ( $H_2$ flow).	123
B.13	Molar fraction of radicals at chemical equilibrium state ( $H_2$ flow).	124
B.14	SEM of graphene flakes in the pure Ar flow (without any $H_2$ ).	125
C.1	Publication numbers for studies on graphene synthesis over various substrates. . . . .	128
C.2	Photograph of large area graphene film directly grown over Si/SiO <sub>x</sub> . . . . .	129
C.3	AFM topography images of the Al <sub>2</sub> O <sub>3</sub> plate and Si/SiO <sub>x</sub> surface.	130
C.4	Statistics for time dependent evolution in graphene formation.	131
C.5	Temperature-dependent growth evolution of graphene disks. . .	132
C.6	Thermodynamic calculations of the mole fractions of the active radicals in the chemical equilibrium state for various temperatures. . . . .	133
C.7	DF-TEM determination of the relative rotation angles and grain sizes of the grains forming monolayer graphene. . . . .	134
C.8	DF-TEM imaging of faceted graphene film from another sample.	135
C.9	Statistics of the measured grain diameter and relative rotation angles as obtained from DF-TEM. . . . .	136
C.10	Complementary height contrast and phase contrast image from AFM for the same region in a graphene sample using the sandwich configuration. . . . .	137
C.11	HRTEM image showing undulation of a grain boundary. . . .	138
C.12	Complementary study from AFM and DF-TEM of grain boundaries. . . . .	139
C.13	Statistics for the number of faces in the graphene grains. . . .	140
C.14	SEM and Raman spectra for monolayer graphene film after 6 and 8 hours growth. . . . .	141
C.15	Comparison of carrier mobility of synthetic monolayer graphene film directly grown on Si/SiO <sub>x</sub> in this work with other reports.	142
C.16	Schematic of multi-stacking of sandwich configuration allowing for the scale-up production of large area homogeneous monolayer graphene films. . . . .	145



# List of Tables

2.1	A review of the chemicals selected for each step in the transfer procedure. . . . .	20
2.2	The activation energies depending on various growth conditions. . . . .	26
4.1	Outline of five different pre-treatments on Cu foils prior to chemical vapor deposition. . . . .	53
B.1	Raman spectral information of graphene flakes from temperature experiments. . . . .	118
C.1	Comparison of grain diameter and growth rate from this work and others in the literature for graphene over dielectric substrates. . . . .	131
C.2	Comparison of transistor mobility for graphene of this work and other reports over dielectrics. . . . .	143
C.3	Comparison of transistor mobility from this work with graphene grown by CVD over metal substrates. . . . .	144





# *Acknowledgements*

I was fortunate to obtain funding from the China Scholarship Council (CSC), **Prof. Dr. Mark H Rümmeli** and the Institute for Complex Materials (IKM), and I appreciate the support of these funding bodies. I would like to thank Center of Polymer and Carbon Materials (CMPW), Polish Academy of Sciences (PAN) for covering the accommodation during my research there. More importantly, there have been numerous individuals who helped me complete this PhD thesis, and I am indeed grateful for their support:

- First I would express my gratitude to **Prof. Dr. Jürgen Eckert** as my Doktorvater for the opportunity he gave me to initiate the PhD thesis. I was allowed to take responsibility for the project, and this played a large part in developing my scientific career. His advice, of always starting with easy things, enabled me to solve many problems.
- Second I want to thank **Prof. Dr. Mark H Rümmeli** as direct supervisor for introducing me to the topic of graphene synthesis and transmission electron microscopy. I am greatly indebted to him for his always being available for discussions on the difficulties and progresses in the course of my research. His broad knowledge, insight into carbon nanomaterials, dynamic mind and positive attitude always shed light on the path of my work. I am very appreciative of his enormous input all through my PhD study.
- Third I would like to thank **Prof. Dr. Gianaurelio Cuniberti** for being so kind-hearted and enthusiastic as to serve as the third referee and supervisor of this thesis.

- I would like to thank **Dr. Thomas Gemming** as direct supervisor for his frequent support. I thank him for teaching me about TEM and its operations, and for always being available to help.
- I would like to thank **Dr. Alicja Bachmatiuk** as direct supervisor for supervising me all through my PhD study in Poland and Germany. She has been teaching me CVD methods, characterization techniques (including Raman spectroscopy) and data presentation skills. Her courage and determination always encouraged me to make progress.
- **CMPW PAN** (Centre of Polymer and Carbon Materials, Polish Academy of Sciences), Poland for hosting the graphene synthesis with various depositions approaches as well as all kinds of characterizations, namely, TEM, SEM, AFM and Raman spectroscopy.
- **Dr. Rafael G Mendes** for teaching me data presentation and TEM operation skills, patience in TEM measurements, and for his friendship.
- The members of our group at the Institut für Komplexe Materialien (IKM): **Dr. Imad Ibrahim, Dr. Sandeep Gorantla, Dr. Jiong Zhao, Ignacio Gonzalez** and **Elisabeth Preuße** and our technical staff **Dina Bieberstein, Matthias Uhlemann, Nicole Geißler, Steffi Kaschube, Romy Keller, Andrea Voß** and **Kerstin Hennig**.
- The colleagues in CMPW Zabrze for fruitful collaborations: **Prof. Dr. Barbara Trzebicka, Dr. Alicja Bachmatiuk, Pawel S Wrobel** and **Michal D Wlodarski**.
- **Dr. Lars Giebeler** for the optical transmittance measurements.

- **Prof. Dr. Lei Fu, Mengqi Zeng and Jiao Wang** of Wuhan University for fruitful collaborations.
- **Dr. Annett Gebert** for allowing me to use the optical microscope.
- **Dr. Horst Wendrock** for teaching me SEM and EDX operations.
- **Dr. Siegfried Menzel** for enhancing my SEM skills.
- **Dr. Ulrike Wolff** for teaching me AFM operations.
- **Dr. Jürgen Thomas** for TEM teaching in the Praktikum (exercise).
- **Dr. Grazyna S Martynkova and Dr. Daniela Placha** at VSB Ostrava.
- **Huy Quang Ta, Liang Zhao, Prof. Dr. Chenglin Yan and Prof. Dr. Zhongfan Liu** of Soochow University.
- My office colleagues, **Subhash, Beom Seok, Hamed, Alexander, Nawaz, Omar and Promote**, for the active and friendly atmosphere in our office.
- The Chinese community in the institute for easing daily life and sharing weekly sports: **Dr. Yongheng Huo, Dr. Shilong Li, Dr. Yang Zhang, Dr. Kaikai Song, Dr. Zhi Wang, Dr. Libo Ma, Dr. Shaozhuan Huang, Xiaolei Sun, Xueyi Lu, Yin Yin, Yan Chen, Lixia Xi and Lixiang Liu.**
- Last but not the least I want to thank my parents **Zengxue** and **Lingyan** for their infinite love and continuous support.



# LIST OF PUBLICATIONS

1. **Jinbo Pang**, Rafael G. Mendes, Pawel S. Wrobel, Michal D. Wlodarski, Huy Quang Ta, Liang Zhao, Lars Giebeler, Barbara Trzebicka, Thomas Gemming, Lei Fu, Zhongfan Liu, Jürgen Eckert, Alicja Bachmatiuk and Mark H. Rümmeli. A Self Terminating Confinement Approach for Large Area Uniform Monolayer Graphene Directly over Si/SiO<sub>x</sub> via Chemical Vapor Deposition. *ACS Nano*, 11 (2),1946-1956, 2017.
2. **Jinbo Pang**, Alicja Bachmatiuk, Lei Fu, Chengli Yan, Mengqi Zeng, Jiao Wang, Barbara Trzebicka, Thomas Gemming, Jürgen Eckert and Mark H. Rümmeli. Oxidation as a means to remove surface contaminants on cu foil prior to graphene growth by chemical vapor deposition. *J. Phys. Chem. C*, 119 (23), 13363-13368, 2015.
3. **Jinbo Pang**, Alicja Bachmatiuk, Lei Fu, Rafael G. Mendes, Marcin Libera, Daniela Placha, Grazyna Simha Martynkova, Barbara Trzebicka, Thomas Gemming, Jürgen Eckert and Mark H. Rümmeli. Direct synthesis of graphene from adsorbed organic solvent molecules over copper. *RSC Adv.*, 5 (75), 60884-60891, 2015.
4. **Jinbo Pang**, Alicja Bachmatiuk, Imad Ibrahim, Lei Fu, Daniela Placha, Grazyna S. Martynkova, Barbara Trzebicka, Thomas Gemming, Jürgen Eckert and Mark H. Rümmeli. CVD growth of 1D and 2D *sp*<sup>2</sup> carbon nanomaterials. *J. Mater. Sci.*, 51 (2):640-667, 2016.
5. Imad Ibrahim, Jana Kalbacova, Vivienne Engemaier, **Jinbo Pang**, Raul D. Rodriguez, Daniel Grimm, Thomas Gemming, Dietrich R. T. Zahn, Oliver G. Schmidt, Jürgen Eckert and Mark H. Rümmeli. Confirming the Dual Role of Etchants during the Enrichment of Semiconducting Single Wall Carbon Nanotubes by Chemical Vapor Deposition. *Chem. Mater.*, 27 (17), 5964-5973, 2015.

6. Mark H. Rümmeli, Sandeep Gorantla, Alicja Bachmatiuk, Johannes Phieler, Nicole Geißler, Imad Ibrahim, **Jinbo Pang** and Jürgen Eckert. On the role of vapor trapping for chemical vapor deposition (CVD) grown graphene over copper. *Chem. Mater.*, 25(24), 4861-4866, 2013.
7. Huy Quang Ta, Liang Zhao, Darius Pohl, **Jinbo Pang**, Barbara Trzebicka, Bernd Rellinghaus, Didier Pribat, Thomas Gemming, Zhongfan Liu, Alicja Bachmatiuk and Mark H. Rümmeli. Graphene-Like ZnO: A Mini Review. *Crystals*, 6 (8), 100, 2016.
8. **Jinbo Pang**, Yongan Cai, Qing He, He Wang, Weilong Jiang, Jingjing He, Tao Yu, Wei Liu, Yi Zhang and Yun Sun. Preparation and Characteristics of MoSe<sub>2</sub> Interlayer in Bifacial Cu(In,Ga)Se<sub>2</sub> Solar Cells. *Physics Procedia*, 32, 372-378, 2012.
9. Wei Liu, Jingjing He, Zhiguo Li, Weilong Jiang, **Jinbo Pang**, Yi Zhang and Yun Sun. Effect of Na on lower open circuit voltage of flexible CIGS thin-film solar cells prepared by the low-temperature process. *Physica Scripta*, 85 (5), 055806, 2012.
10. He Wang, Yi Zhang, Xiaolu Kou, Yongan Cai, Wei Liu, Tao Yu, **Jinbo Pang**, Changjian Li and Yun Sun. Effect of substrate temperature on the structural and electrical properties of CIGS films based on the one-stage co-evaporation process. *Semiconductor Science and Technology*, 25 (5), 055007, 2010.

# ERKLÄRUNG

Hiermit versichere ich, dass ich die vorliegende Arbeit ohne unzulässige Hilfe Dritter und ohne Benutzung anderer als der angegebenen Hilfsmittel angefertigt habe; die aus fremden Quellen direkt oder indirekt übernommenen Gedanken sind als solche kenntlich gemacht.

Weitere Personen waren an der geistigen Herstellung der vorliegenden Arbeit nicht beteiligt. Insbesondere habe ich nicht die Hilfe eines kommerziellen Promotionsberaters in Anspruch genommen. Dritte haben von mir keine geldwerten Leistungen für Arbeiten erhalten, die in Zusammenhang mit dem Inhalt der vorgelegten Dissertation stehen.

Die Arbeit wurde bisher weder im Inland noch im Ausland in gleicher oder ähnlicher Form einer anderen Prüfungsbehörde vorgelegt und ist auch noch nicht veröffentlicht worden. Diese Promotionsordnung wird anerkannt.

Datum: 6. Dezember 2016

Unterschrift:

*Junbo Pang*